Experimental study of the coupled dynamics of forces and pressure and velocity fields in complex and turbulent flows

Naz Turankök

université PARIS-SACLAY

Experimental study of the coupled dynamics of forces and pressure and velocity fields in complex and turbulent flows

Etude expérimentale de la dynamique couplée des forces et champs de pression et de vitesse en écoulements complexes et turbulents

Thèse de doctorat de l'université Paris-Saclay

École doctorale n°579 Sciences mécaniques et énergétiques, matériaux et géosciences (SMEMAG)
Spécialité de doctorat : Mécanique des fluides
Graduate School : Sciences de l'ingénierie et des systèmes
Référent : Faculté des sciences d'Orsay

Thèse préparée dans l'unité de recherché **Service d'Études Mécaniques et Thermiques** (Université Paris-Saclay, CEA),
sous la direction de **Lionel ROSSI**, Directeur de recherche,
et le co-encadrement de **Valérie BISCAY**, Ingénieure de recherche

Thèse soutenue à Cadarache, le 9 Mai 2022, par

Naz TURANKÖK

Composition du Jury

Mickael BOURGOIN Directeur de recherche, CNRS / ENS de Lyon	Président
Laurent DAVID Professeur, Université de Poitiers	Rapporteur & Examinateur
Yassin HASSAN Professeur, Texas A&M University	Rapporteur & Examinateur
Henda DJERIDI Professeure, Grenoble INP	Examinatrice
Vincent FAUCHER Directeur de recherche, CEA Cadarche	Examinateur
Elisabeth LONGATTE Ingénieure de recherche, EDF / LMPS / ENS Paris-Saclay	Examinatrice
Lionel ROSSI Directeur de recherche, CEA Cadarche	Directeur de thèse

THÈSE DE DOCTORAT

NNT : 2022UPAST074

université PARIS-SACLAY
ÉCOLE DOCTORALE
Sciences mécaniques et énergétiques, matériaux et géosciences (SMEMAG)

Titre : Etude expérimentale de la dynamique couplée des forces et champs de pression et de vitesse en écoulements complexes et turbulents

Mots clés : fluctuation de pression, fluctuation de vitesse, turbulence, grille, PWR

La production d'énergie nucléaire contribue à la production d'électricité décarbonnée et à la réduction de l'utilisation des énergies fossiles. Les réacteurs les plus utilisés à échelle industrielle sont les réacteurs à eau pressurisée (REP).

La production d'énergie dans les REP commence dans le cœur du réacteur où les assemblages combustibles produisent de la chaleur (circuit primaire) qui est transformée en vapeur (circuit secondaire) pour produire de l'électricité via des turbines. Les assemblages combustibles sont formés de nombreux crayons. Des grilles d'espacement maintiennent les crayons ensemble. Elles assurent l'intégrité structurale des assemblages combustibles. En plus du support structurel, elles créent un espacement entre chaque crayon et génèrent un brassage dans l'écoulement. Sur chaque grille se trouvent différents éléments tels que des bossettes et des ressorts qui supportent les crayons. On peut également trouver des ailettes qui favorisent le mélange de l'écoulement.

Dans le cœur des réacteurs, le fretting est un phénomène dû à l'interaction entre le fluide et la structure. Avec le vieillissement des grilles, les vibrations conduisent au fretting par contacts entre les crayons et les éléments de grille. Le fretting grille-crayon est l'une des causes majeures de la dégradation de la couche externe des crayons de combustibles. Ceci est donc important pour la conception et l'exploitation des centrales nucléaires.

Pour étudier la physique derrière ce phénomène, il est nécessaire d'étudier les forces exercées sur les crayons par l'écoulement. Pour cette étude, une installation expérimentale nommée CALIFS 5x5 est utilisée au CEA, Cardarache, France. CALIFS est une boucle d'essais analytique basse pression équipée de 5x5 crayons. L'échelle de CALIFS est de 2,81 par rapport à un REP, ce qui génère une résolution spatiale plus élevée pour les mesures de l'écoulement. Les grilles de maintien analytiques sont simplifiées. Pour cette étude, deux configurations différentes de grille d'espacement sont utilisées : avec ou sans ailettes.

La caractérisation de l'écoulement turbulent est réalisée en mesurant la pression et la vitesse autour du crayon central. CALIFS a un accès optique sur trois côtés permettant des mesures optiques. Pour les mesures de vitesse, les technique PIV avec RIM et LDV sont utilisées. Avec ces mesures, les propriétés de vitesse de l'écoulement sont étudiées à la fois en tant que champ et point par point.

Pour les mesures de pression, des capteurs de pression piézorésistifs sont utilisés. Les mesures de pression sont effectuées à l'aide d'un capteur de pression et d'un dispositif multicapteur nouvellement développé. Avec le dispositif multicapteur, la pression est mesurée instantanément avec plusieurs points dans l'écoulement pour l'étude des événements de pression et de leur mouvement.

Pour compléter les mesures séparées, des mesures simultanées de pression et de PIV sont effectuées afin d'étudier le lien entre la pression et la vitesse.

Les événements périodiques sont représentés par des spectres de fluctuations de pression et de vitesse. L'origine de ces événements périodiques est illustrée à l'aide de mesures PIV. Ces événements périodiques sont liés à des tourbillons dans la zone en aval des bossettes. Ces allées tourbillonnaires sont caractérisées par leur nombre de Strouhal. La relation entre le nombre de Strouhal et le nombre de Reynolds (variant de 13200 à 108800) est caractérisée pour les deux configurations étudiée. La taille de ces tourbillons est quantifiée avec une échelle de longueur intégrale pour les fluctuations de vitesse et de pression montrant la cohérence des signaux de pression et vitesse. De plus, les fluctuations de pression mesurées sur le crayon s'avèrent être convectées par l'écoulement comme le démontre les mesures de pression multi-capteurs et les corrélations croisées entre les mesures simultanées de vitesse et de pression.

université PARIS-SACLAY
ÉCOLE DOCTORALE
Sciences mécaniques et énergétiques, matériaux et géosciences (SMEMAG)

Title : Experimental study of the coupled dynamics of forces and pressure and velocity fields in complex and turbulent flows

Keywords : pressure fluctuations, velocity fluctuations, turbulence, spacer grids, PWR

Nuclear energy production is one way to decrease the use of carbon fossils for the energy production. Pressurized Water Reactors (PWR) are most common type of reactor in commercial use for power production. The energy production in PWR starts from the reactor core where fuel assemblies produce the heat (primary circuit) that is transformed to vapour (secondary circuit) to produce electricity via turbines. The fuel assemblies are formed from many rods. Spacer grids held the fuel rods together. They maintain the structural integrity of the fuel assemblies. In addition to the structural support, they create spacing between each rod and generate mixing in the flow. On each mesh of spacer grids different elements are found such as dimples, springs (to support the fuel rods) and possibly mixing vanes enhance the mixing in the flow.

In Pressurized Water Reactors, grid-to-rod fretting is a phenomenon occurring due to fluid-structure interaction. With the aging of the grids, vibrations lead to fretting by contacts between the rods and the grid elements. Grid-to-rod fretting is one of the major reason for the degradation of the outer layer of the fuel rods and this then of importance for the conception and exploitation of nuclear power plants.

To investigate the physics behind this phenomena, it is necessary to study the forces exerted on the fuel rods by the flow. For this study an experimental rig named as CALIFS 5x5 is used in CEA, Cardarache, France. CALIFS is an analytical low-pressure experimental rig with 5x5 rod bundle. The scale of CALIFS is 2.81 compared to PWR which generates a higher spatial resolution for the flow measurements. The rod bundle are held with analytical spacer grids with simplified design. For the current study, two different configurations of spacer grid are used: With Mixing Vane (WMV) and No Mixing Vane (NMV).

The characterization of the turbulent flow is performed by measuring the pressure and velocity around the central rod. CALIFS has optical access (Perspex windows) on three sides permitting optical measurements. For velocity measurements Particle Image Velocimetry with Refractive Index Matching and Laser Doppler Velocimetry methods are used. With these measurements, velocity properties of the flow are investigated both as a field and as point by point.

For pressure measurements, piezoresistive pressure sensors are used. The pressure measurements are performed using single pressure sensors and a newly developed multi-sensor device. With the multisensor device, the pressure is measured instantaneously with multiple points in the flow for the investigation of the pressure events and their transport.

To complement separate pressure and velocity measurements, simultaneous pressure and PIV measurements are performed to investigate the coupling between pressure and velocity.

Periodic events are shown in spectra of pressure and velocity fluctuations. The origin of these periodic events is explored using PIV measurements. These periodic events are shown to be connected to eddies in the wake zone downstream the dimples. These eddy streets are characterized by their Strouhal number and a map is built for Reynolds number from 13200 to 108800. The size of these eddies are quantified with the integral length scale and are observed to be connected to the velocity fluctuations. The relation between the velocity and the pressure fluctuations are characterized by the periodic length scale. Moreover, pressure fluctuations measured on the rod are found to be convected by the mean flows, are as the identified eddies.

ACKNOWLEDGEMENT

I'd like to express my deepest thanks to my director of thesis Lionel ROSSI who improved my knowledge immensely, listened me and guide me throughout all my thesis. I would also like to thank to my supervisor Valerie BISCAY who was so helpful professionally and personnaly and also to Thibaud LOHEZ who patiently worked side by side with me and help me a lot during all my thesis. It was such an honour to work with this team during my thesis and I really consider myself very lucky to have this chance.

I am also very thankful to all the people in both laboratories LTHC and LETH. Everyone was so fun and helpful in a lot of aspect. It was a pleasure to be able to work with all of you. I would also like to thank to Guillaume RICCIARDI for his comments, contributions and support and also Fabrice FRANCOIS for his support and fun conversations.

Now I want to specially thank to my office friends Louise BERNADOU, Benjamin JOURDY and Lorenzo LONGO. I am so happy to be able to have such a good friendship with all of you, it make this period so much fun and easier. I will miss working with all of you. I would also like to thank the former PhD students for their friendship as Roberto CAPANNA, Chunhui DANG, Mathieu DARNAJOU, Mira CHITT, Ouardia AIT OUCHEGGOU and Samy MOKHTARI.

Beside the CEA, firstly I would like to thank to Maxime BENSOAM and his family. I am so grateful that you are in my life and thank you a lot for your endless support during all these year.

I am also grateful for all my friends who supported me all these years. I would like to thank specially to Oya Neva DEMIRKOL BINGUL, Yasemin TAŞCI and Can YILDIRIM.

I would also like to thank Prof. Sedat TARDU for introducing the turbulence and for his guidance.

Finally I would like to thank all my family for their support. Most importantly I would like to specially thank to my mom and my dad who I also like to dedicate this thesis. I am so lucky to be their daughter and enormously grateful for their endless support and love. Sizi çok seviyorum ve iyi ki varsınız.

RÉSUMÉ ÉTENDU

Cette section présente un résumé étendu en français du document suivant, rédigé en anglais.

- **Contexte Général**

La production d'énergie nucléaire contribue à la production d'électricité décarbonnée et à la réduction de l'utilisation des énergies fossiles. Les réacteurs les plus utilisés à échelle industrielle sont les réacteurs à eau pressurisée (REP).
Il y a deux circuits principaux dans un REP : le circuit primaire et le circuit secondaire. Le circuit primaire est composé du cœur du réacteur, du pressuriseur, de la pompe de refroidissement et du générateur de vapeur. Le cœur du réacteur est composée d'assemblages combustibles entre lesquels circule de l'eau. La fonction des assemblages combustibles est de générer de la chaleur grâce à la fission nucléaire. L'eau s'écoulant dans le cœur est utilisée pour transférer cette chaleur générée vers le circuit secondaire. Le circuit secondaire comprend une turbine, un alternateur et un condenseur. La génération d'énergie électrique se produit via la vapeur et les turbines, c'est-à-dire que l'énergie thermique se transforme en énergie cinétique dans ce circuit secondaire. Cette thèse se concentre sur un phénomène qui se produit à l'intérieur du cœur du réacteur REP.
L'écoulement entre dans le cœur du réacteur par la buse d'entrée d'eau froide et circule vers le bas du réacteur. Cet écoulement passe à travers les assemblages de combustibles où la chaleur est générée. Après cela l'écoulement va dans la boucle secondaire via la buse de sortie d'eau.
Un assemblage combustibles est composé d'un faisceau de 17x17 crayons. Ces crayons sont maintenus dans l'assemblage grâce à des grilles. Les grilles sont utilisées pour garantir le bon espacement entre chaque crayon et pour favoriser le mélange et le transfert de chaleur dans l'écoulement. Sur chaque grille se trouvent différents éléments tels que des bossettes et des ressorts qui supportent les crayons. On peut également trouver des ailettes qui favorisent le mélange de l'écoulement.
A l'intérieur du cœur du réacteur, l'écoulement peut atteindre jusqu'à 5 m/s. Les éléments de grille évitent une interaction directe entre la grille et les crayons mais avec ces vitesses élevées, les vibrations conduisent à des phénomèmes de fretting générés par des contacts répétés entre les crayons et les éléments de grille. Ce fretting grille-crayon est l'une des causes majeures de la dégradation de la gaine externe des crayons de combustibles. Il est donc important de prendre en compte ce phénomène pour la conception et l'exploitation des centrales nucléaires, la gaine étant la première barrière de confinement du point de vue de la sureté nucléaire.
Dans ce contexte, l'écoulement est étudié expérimentalement pour comprendre l'origine du phénomène qui conduit au fretting sur les crayons. Avec cette étude, il est prévu de créer les bases de données pour faire des simulations.
A l'intérieur du cœur d'un réacteur, l'état de fonctionnement est à haute température, à haute pression et des géométries complexes : plusieurs assemblages de crayons et grilles. Cette situation génère différents phénomènes hydrodynamiques et thermodynamiques dans le cœur de réacteur. Une installation expérimentale simplifiée a été conçue au CEA de Cadarache, afin d'isoler les phénomènes connectés à l'interaction entre les crayons et l'écoulement. Cette installation s'appelle CALIFS.

- **Boucle expérimentale**

CALIFS est une installation d'essais analytiques basse pression et basse température. La similitude de Reynolds est utilisée dans CALIFS pour représenter l'écoulement à l'intérieur du cœur du réacteur. Dans le cœur du réacteur, le nombre de Reynolds de l'écoulement peut atteindre 500000 ce qui est une propriété caractéristique de l'écoulement turbulent. Pour obtenir un écoulement turbulent dans CALIFS trois paramètres ont été utilisés : la vitesse, la viscosité cinématique et la longueur

caractéristique de la géométrie qui définissent le nombre de Reynolds. Le premier paramètre est la longueur caractéristique qui est liée à l'échelle de l'installation. CALIFS, échelle de 2.81 par rapport à un cœur de réacteur industriel, ce qui permet d'atteindre un nombre de Reynolds plus élevé. Pour atteindre une plage étendue de nombres de Reynolds, la vitesse et la température sont modifiées dans CALIFS. La vitesse maximale pouvant être atteinte est de 5 m/s, ce qui est identique à un cœur de réacteur. La plage de température de CALIFS est de 12°C à 55°C, ce qui affecte la viscosité cinématique. La plage de nombre de Reynolds pouvant être atteinte est de $12000 \leq Re_{Dh} \leq 250000$, suffisante pour représenter l'écoulement turbulent à l'intérieur de CALIFS.
L'écoulement arrive à l'intérieur du CALIFS depuis la chambre de stabilisation où les imperfections sur l'écoulement d'entrée sont réduites. L'écoulement passe ensuite dans la section d'essai, la chambre de stabilisation supérieure et atteint finalement un réservoir d'eau avec une surface libre. Toutes ces connexions sont équipées de joints élastomère qui atténuent les vibrations liées à l'installation.
La section d'essai CALIFS est équipée d'un faisceau de 5x5 crayons maintenus par des grilles en INOX. Ces grilles analytiques ont une conception simple pour reproduire les principales caractéristiques de l'écoulement. Elles ont été installées sur 4 niveaux et il existe deux conceptions différentes. L'une est "No Mixing Vane" (NMV) qui a des bossettes et des ressorts et l'autre est "With Mixing Vane" (WMV) qui a des ailettes en plus des bossettes et des ressorts. Pour ces deux configurations, les mesures sont effectuées en aval de la troisième grille. Ces mesures sont réalisées autour du crayon central pour améliorer la représentativité de l'écoulement dans l'assemblage combustible en diminuant l'effet de paroi. Pour définir l'échelle de longueur caractéristique de CALIFS, le diamètre hydraulique est calculé à 27.7 mm.
CALIFS a été construite en 2015 et une première mesure de pression et de vitesse a été effectuée avec les deux configurations pour un nombre de Reynolds de 66000. Dans les résultats, un pic de fréquence caractéristique est apparu sur les spectres de pression.
Le but de cette thèse est d'étudier :

- une gamme de nombre de Reynolds où ce phénomène peut être observé sur ces fluctuations
- l'existence du pic caractéristique sur les fluctuations de vitesse
- l'origine de ce pic de fréquence observé sur les fluctuations de pression
- le transport de ces fluctuations

L'idée de départ de cette thèse est la présence de tourbillons dans les assemblages combustibles. Les tourbillons sont une propriété caractéristique des écoulements turbulents et ils génèrent des fluctuations de pression lorsqu'ils sont transportés dans l'écoulement. Afin d'étudier l'existence de tourbillons et d'étudier la relation entre ces tourbillons et les fluctuations de vitesse et de pression, des informations spatiales et temporelles sur la pression et la vitesse sont obtenues en utilisant différentes techniques de mesure.

- **Techniques de mesures**

Les capteurs de pression piézorésistifs sont utilisés pour les mesures de pression. Ces mesures comprennent deux types de campagne : mesures en « mono-capteur » et mesures en « multi-capteur ». Pour la campagne « mono-capteur », un capteur a été installé sur le crayon central et les mesures sont réalisées autour du crayon à différentes distances qui fournissent l'information temporelle. Pour l'information spatiale un nouveau dispositif « multi-capteurs » a été installé sur le crayon et permet des mesures de pression simultanées avec de multiples capteurs pour différentes distances par rapport à la grille.
Pour les mesures de vitesse, les méthodes optiques de Laser Doppler Velocimetry (LDV) et Particle Imaging Velocimetry (PIV) sont réalisées. Ce sont deux méthodes non intrusives qui permettent de

mesurer la vitesse de l'écoulement. La LDV est une technique de mesure ponctuelle utile pour l'information temporelle.
La méthode PIV a été réalisée pour obtenir des informations supplémentaires sur la vitesse spatiale. Pour la PIV, il est important d'accéder partout dans le fluide avec une distorsion optique minimale, or les crayons dans CALIFS sont en INOX qui est un matériau opaque. Un accès optique étendu est donc obtenu grâce à la méthode RIM (Refractive Index Matching). Pour l'application de la RIM, les deux crayons en INOX devant le crayon central sont remplacés par des crayons transparents en éthylène-propylène fluoré (FEP).
Les mesures de PIV comprennent deux types de campagne : « High-speed PIV » avec un laser continu et « Low-speed PIV » avec un laser pulsé. La configuration « High-speed PIV » est utilisée pour un écoulement à faible vitesse pour lesquelles le déplacement des particules peut être détecté et conduire aux données résolues dans le temps de la vitesse. Pour des vitesses plus élevées, afin de capturer le déplacement des particules, la configuration « Low-speed PIV » est utilisée. Cette méthode consiste à prendre 2 images dans un court intervalle de temps suffisant pour détecter le déplacement des particules. Du fait de la différence de temps entre chaque impulsion du laser, seules les informations spatiales sont réalisables.
Deux types de particules ont été utilisés pour la PIV : les « Polydisperse PMMA Rhodamine B » et les « Monodisperse Vestosint 2070 + Sulforhodamine B ». Ces deux types de particules ont une densité proche de celle de l'eau. Leurs caractéristiques de diffusion de la lumière les rendent visibles avec la lumière du laser. Pour les traitements des données PIV, la même particule est détectée sur différentes images grâce à la méthode de cross-corrélation et le déplacement est déterminé en pixel par image, et grâce aux mesures réalisées pour les étalonnages converti en m/s.

- **Résultats**

Caractérisation globale de l'écoulement

Pour comprendre la pression autour du crayon central, les mesures sont effectuées à différentes distances de la grille. Pour ces mesures les deux configurations, NMV et WMV, sont utilisées avec un nombre de Reynolds qui est de 66000. Les résultats montrent que pour la configuration NMV, avec l'augmentation de la distance par rapport à la grille, les fluctuations deviennent quasi-homogènes. En revanche, pour la configuration WMV, même pour une distance de $y/D_h = 20$, la distribution de pression observée est plus hétérogène par rapport à la configuration NMV. Pour les deux configurations, les fluctuations maximales sont observées entre la bossette et le ressort. Avec l'augmentation de la distance par rapport à la grille, l'intensité de ces fluctuations diminue.
Le même comportement est observé pour des fluctuations de vitesse autour de crayon central.Dans les deux configurations, les fluctuations de vitesse maximales sont observées en aval de la bossette. Du fait de ces résultats, la PIV est effectuée en aval d'une bossette afin de visualiser et quantifier le champ de vitesse dans la zone où les fluctuations les plus élevées sont observées. Pour les deux configurations, des régions à forte et faible vitesse sont observées avec les couches de cisaillement qui sont visibles. Pour la configuration NMV, la couche de cisaillement est située de part et d'autre de la bossette et pour la configuration WMV, une forme "λ" de la couche de cisaillement est observée. Pour la configuration NMV, la zone où la vitesse est la plus élevée se trouve de part et d'autre de la bossette avec une zone de vitesse plus faible au centre de la zone de mesures. Pour la configuration WMV, les vitesses les plus élevées se trouvent à proximité de l'ailette.
Pour comprendre la direction de l'écoulement, les composantes de la vitesse sont étudiées. Pour NMV, l'écoulement se déplace vers le centre de la bossette. Pour WMV, l'écoulement suit la direction de l'ailette après $y/D_h = 0.5$. Par rapport à la configuration NMV, des composantes de valeurs négatives élevées sont observées dans la zone entre la grille et l'ailette. Ce mouvement de l'écoulement est lié aux « écoulements secondaires/secondary flows » du fait de la présence des ailettes.

Domaine des fréquences des fluctuations

Les résultats avec $Re_{Dh} = 66000$ montre l'existence du pic de fréquence à 69Hz pour les deux configurations pour la distance $y/D_h = 0.5$. Pour NMV, ce pic persiste avec l'augmentation de la distance par rapport à la grille, alors que pour WMV le pic commence à disparaître après $y/D_h = 5$. Pour trouver la gamme du nombre de Reynolds où ce phénomène peut être observé, les mesures sont effectuées avec différentes distances comprise en $y/D_h = 0.5$ et $y/D_h = 2$, avec différentes vitesses et différentes températures. Le pic de fréquence caractéristique est observé pour une large gamme de nombres de Reynolds.

Les données de LDV et PIV sont utilisées pour l'analyse du domaine des fréquences des fluctuations de vitesse. Le pic de fréquence caractéristique est observé avec les deux méthodes.

Pour illustrer les résultats, le nombre de Reynolds et le nombre de Strouhal sont utilisés. Le nombre de Reynolds représente l'écoulement et le nombre de Strouhal représente le phénomène qui est connecté au pic de fréquence caractéristique. Dans ces résultats, les nombre de Strouhal varient entre de 0.20 à 0.27 ce qui montre l'existence du phénomène pour les fluctuations de vitesse et les fluctuations de pression sur la gamme $12000 \leq Re_{Dh} \leq 108000$.

L'origine du pic de fréquence

Il s'agit de trouver une relation entre le pic de fréquence observé et les tourbillons. Les résultats de PIV sont utilisés pour cette étude.

La visualisation des structures est basée sur les lignes de courant dans l'image se déplaçant avec U_{flow}. Pour montrer le cœur des tourbillons en plus de la ligne de courant, la fonction « swirling » est calculée. Dans les deux configurations, les tourbillons sont observés sur la couche de cisaillement et ces structures persistent avec l'augmentation de la distance par rapport à la grille.

Pour le domaine de fréquences, les spectres sont étudiés à l'endroit où les tourbillons sont visibles et invisibles. D'après ces résultats, pour les deux configurations, le pic de fréquence caractéristique est observé dans la zone où les tourbillons transitent. Aucun pic de fréquence n'est observé en l'absence de tourbillons.

Pour la caractérisation de ces tourbillons, deux échelles de longueur différentes sont utilisées : l'échelle de longueur intégrale et échelle de longueur périodique. L'échelle de longueur intégrale est calculée avec la fonction d'autocorrélation de la fluctuation de vitesse qui représente la taille du tourbillon. L'échelle de longueur périodique représente la distance entre chaque tourbillon identifié. Avec les échelles calculées et la confirmation visuelle, les tourbillons sont liés aux fluctuations de vitesse et à l'origine du pic de fréquence caractéristique.

Transport des fluctuations

Pour l'étude du transport des fluctuations, des mesures simultanées sont effectuées avec la PIV et le dispositif multi-capteurs. Le dispositif multi-capteurs est installé à l'endroit où les tourbillons sont observés.

Pendant que ces tourbillons sont transportés en aval des bossettes, des fluctuations de pression sont générées par ces tourbillons. Cela conduit à des signatures similaires sur les signaux du capteur de pression. Étant donné que les tourbillons sont connectés aux fluctuations de vitesse, dans cette thèse, le transport des fluctuations est étudié de deux manières :

- Suivi d'événement capteur par capteur, via un dispositif multi-capteurs
- Suivi de la corrélation entre les fluctuations de pression et les tourbillons, via PIV et dispositif multi-capteurs

Le résultat des deux méthodes montre un comportement cohérent et que le transport des fluctuations est observé autour de la valeur U_{flow}.

CONTEXT

NOMENCLATURE

Acronyms

CEA	Commissariat à l'énergie atomique
CFD	Computational fluid dynamics
DNS	Direct numerical simulations
FEP	Fluorinated ethylene propylene
FIV	Flow induced vibrations
LDA	Laser doppler anemometry
LDV	Laser doppler velocimetry
LES	Large eddy simulations
MPS	Multi pressure sensor
NMV	No mixing vane
PIV	Particle image velocimetry
PMMA	Poly(methyl methacrylate)
PWR	Pressurized water reactor
RANS	Reynolds averaged numerical simulations
Re	Reynolds number
RI	Refractive index value
RIM	Refractive index matching
RMS	Root mean square
SPS	Single pressure sensor
St	Strouhal number
TKE	Turbulent kinetic energy
WMV	With mixing vane

Symbols

θ	Angle around the rod	$\bar{P}$	Mean pressure
P_{atm}	Atmospheric pressure	$\bar{U}$	Mean velocity
R_{xx}	Autocorrelation coefficient	τ^-	Negative time lag
$\langle\ \rangle$	Average over space	$\tau_{xx}, \tau_{yy}, \tau_{zz}$	Normal stresses
$\overline{}$	Average over time	τ^*	Normalized time shift
f	Characteristic frequency	ρ_p	Particle density
f_{peak}	Characteristic frequency peak	d_p	Particle diameter
U_c	Convection velocity	Pa	Pascal
R_{xy}	Cross-correlation coefficient	$\wp_{sq}$	Perimeter around the rod
℃	Degree celsius	L_p	Periodic length scale
ρ	Density	k	PIV image selection coefficient
D_{rod}	Diameter of rod	$\aleph_i$	PIV integral length scale

E^*	Dimensionless energy spectra
$\|U\|/U_{flow}$	Dimensionless instantaneous velocity magnitude
$\|\overline{U}\|/U_{flow}$	Dimensionless mean velocity
$\|U^{\Delta}\|/U_{flow}$	Dimensionless velocity field corrected according to U_{flow}
U'_{RMS}/U_{flow}	Dimensionless velocity fluctuation
ε	Dissipation rate
d	Distance
μ	Dynamic viscosity
π	Energy flux
f_{ext}	External forces
ρ_f	Fluid density
F	Force
D_g	Geometric diameter
g	Gravitational acceleration
Hz	Hertz
D_h	Hydraulic diameter
$U(u_x, u_y, u_z)$	Instantaneous local velocity
L_i	Integral length scale
$P_{swirl}, Q_{swirl},$	Invariants of velocity gradient tensor
ϑ	Kinematic viscosity
$E(k)$	Kinetic energy in spectral space
η	Kolmogrov length scale
f_{laser}	Double pulse laser frequency
$\aleph_L$	LDV integral length scale
f_{past}	LDV recording frequency
L	Length scale
m	Mass
P/D	Pitch to diameter ratio
pxl	Pixel
x, y, z	Position vector
τ^+	Positive time lag
P	Pressure
ΔP	Pressure drop
$\aleph_P$	Pressure integral length scale
K	Pressure loss coefficient
K_p	Pressure sensor calibration coefficient
$f_{recording}$	Recording frequency
τ_p	Relaxation time of particle
$f_{resample}$	Resampled frequency
U'_{RMS}	Root mean square of velocity fluctuation
τ_{limit}	Searching area for correlation
$\tau_{xy}, \tau_{xz}, \tau_{yx}, \tau_{yz},$	Shear stresses
σ	Standard deviation
S_{ij}	Strain-rate tensor
$f_{surface}$	Surface forces
S^*	Swirling strength
t	Time
τ	Time lag
u_t	Transport velocity of fluctuation
U'	Velocity fluctuation
U_{flow}	Velocity of flow
U_e	Velocity of pressure events
$\forall$	Volume
WS	Window size

CHAPTER 1
INTRODUCTION

1. INTRODUCTION

1.1 General context

Nuclear energy production is one of the way to decrease the use of carbon fossils for the energy production. According to (World Nuclear Association, 2021) in 2020, France generated 70.6% of the country's electricity from nuclear with 56 operable reactors. Pressurized Water Reactors (PWR) are most common type of reactor in commercial used for power production.

PWR has two major part as primary system and secondary system. The primary system consist of reactor core, pressurizer, reactor cooling pump and stream generator. The reactor core consists fuel assemblies and coolant flow. The function of the fuel assemblies is the generation of the heat with nuclear fission. The coolant flow is used to transfer this generated heat to the secondary system. The secondary system includes turbine, electric generator and condenser. The generation of electricity energy occurs via the steam and the turbines, i.e. the thermal energy conversion to kinetic energy in this secondary system. More details about PWRs are discussed in Chapter 2. The current study is focused on the primary system specifically the reactor core of the PWR.

Fuel assemblies consist of 17x17 rod bundle in general. These rod bundle are held by spacer grids which are used to maintain the spacing between each rod and enhance the mixing and the heat transfer in the flow. These spacer grids have different grid elements such as dimple and spring to support the rods and also mixing vanes to contribute to the mixing in the flow.

All these geometries contribute to the complex flow in the fuel assemblies. The velocity of the coolant flow inside the nuclear core can reach up to 5 m/s. This generates highly turbulent flow where the spacer grids and its elements contribute to this turbulent flow.

The relation between the structure, i.e. spacer grid, and fluid, i.e. coolant flow, generates the fluid-structure interaction. The highly turbulent flow induces vibration on the fuel assemblies. With the aging of the grid, the clamping mechanism that holds the rod bundle in the spacer grid, starts to lose its efficiency. This leads to enough space for the relative movement of the fuel rod towards the supporting grid elements. The contact between the grid elements and rods provoke fretting on the rods. This leads to a phenomenon called as Grid-to-rod fretting.

The degradation of the outer layer of the fuel rods can lead to damaged rods (Hu, 2018; International Atomic Energy Agency, 2010). This will cause nuclear fuel leakage where the solution for the damaged rods are changing the fuel assemblies, i.e. extra costs.

To improve the knowledge and modelling of this phenomena different experimental and numerical studies are conducted at CEA (Bhattacharjee, et al., 2017) (Moreno, et al., 2016) (Farges, et al., 2021) (Gauffre, et al., 2020).

The topic of the current thesis is to focus on the experimental part and the flow physics around a single rod amenable to provoke its vibration.

The flow in the fuel assemblies are simulated in the laboratories with different arrays, scales and fluids to study the phenomena.

Some different array measurements can be found as 3x3 array (Dominguez-Ontiveros & Hassan, 2014), 5x5 array (Qu, et al., 2019) and 4x1 array (Rehme, 1978). Different shape of arrays can be found as triangle arrays (Carajilescov & Todreas, 1976) or square arrays (Rowe, et al., 1974).

These studies characterize the turbulent flow with properties such as flow pulsation (Möller, 1991) (Rehme, 1987) and swirling motions (McClusky, et al., 2002), (Chang, et al., 2008). More examples of the experiments performed in fuel assemblies are discussed in Chapter 2.

Addition to the physical experiments in recent decades, with the increasing computing power and its availability, numerical analyses are started to become popular. These analyses include different methods such as Direct Numerical Simulation (DNS), Large Eddy Simulation (LES) and Computational Fluid Dynamics (CFD) with different approaches like Reynolds Averaged Navier-Stokes (RANS).

Even though the computational power is increased, one of the disadvantage of the numerical analysis is the computational costs. These costs depend on different parameters such as the resolution of the results, i.e. the scales of the flow, the mesh size for the computations and amount of grid points. (Nicoud, 2007)

For DNS method, the Navier-Stokes equations are solved which provides all flow details. Therefore huge amount of grid points are necessary with refined mesh size. This leads to need of high computational power, i.e. high computational cost. (Kraus, et al., 2021) is an example of DNS method for nuclear applications.

RANS method gives the statistical treatment on Navier-Stokes equation and the results provide average quantities. The resolution of the results don't include the small scales less, i.e. less mesh refinement is needed and the computational costs are lower than the other methods. (Bovati, et al., 2021) is an example of RANS method in nuclear application.

LES is an approach between these two methods. Instead of calculating all the scales, a low-pass filter is applied on the Navier-Stokes equation where the small scales are filtered and then modelled. (Bieder, et al., 2014) is an example of LES method in nuclear application.

Details about numerical analysis with other examples in nuclear application is discussed in Chapter 2.

The increase of the turbulence, i.e. increase of Reynolds number, leads to more scales in the flow. This increase the need to have more grid point and a refined mesh. Addition to the scales, the more complex geometries inserted in the flow, also increase the need of more grid point. All of these parameters leads to an increase of the computational cost.

CALIFS is an experimental rig that is designed to investigate the turbulent flows in 5x5 rod bundle. CALIFS has a simplified design to support the numerical analysis, i.e. decreasing the computational costs, e.g. (Gauffre, et al., 2020) (Farges, et al., 2021) and makes more comprehensible understanding to the flow by separating the flow phenomena.

CALIFS has the scale of 2.81 compared to PWR which generates a higher spatial resolution for the flow measurements. The rod bundle are held with analytical spacer grids with simplified design. In CALIFS, it is possible to install different grid configurations. For the current study two different configurations are used: With Mixing Vane (WMV) and No Mixing Vane (NMV) configuration. On NMV configuration, there is dimple and spring to support the rods. For WMV configuration there is mixing vanes in addition to dimple and spring. More details about CALIFS and the experimental rig is explained in Chapter 4.

The working conditions of CALIFS is different than PWR working conditions. For CALIFS the temperature range is between 12°C-55°C with low-pressure, whereas for PWR the temperature is around 325°C with high pressure, i.e. 155 bar.

To present the hydrodynamic similitude between PWR and CALIFS, the Reynolds number is selected. In PWR, the Reynolds number can reach up to 500000. The first experiments in CALIFS are performed at sufficiently high Reynolds number, i.e. 66000 (Moreno, et al., 2016) (Turankok, et al., 2020). The flow is fully turbulent within the rod bundle with the presence of the main features of the flow that is expected in PWR where the numerical analysis can be performed for comparison, i.e. (Gauffre, et al., 2020) (Farges, et al., 2021).

In the current thesis, the range of Reynolds number is extended to 13000-120000. This range provides experimental data with higher Reynolds number to confirm the results obtained at 66000. Additionally the experimental data with lower Reynolds number provides simplification of the comparison with numerical analysis by reducing the computational cost while improving the resolution of the numerical results. This range of Reynolds number is provided by changing the velocity and the temperature, i.e. the viscosity of the water.

For the investigation of the local forces applied on the rods and the characterization of the flow in CALIFS, velocity, pressure and their fluctuations are measured. With the quantification of the fluctuations, the aim is to explain the physics behind the turbulent flow in rod bundles. It is expected to contribute to the knowledge and explanations of the forces that leads to the excitation of the rods in the fuel assemblies.
For all the measurements, the measurement domain is selected around the central rod.

1.2 Measurements performed in CALIFS

For velocity measurements, Laser Doppler Velocimetry (LDV) and Particle Image Velocimetry (PIV) are performed.
LDV is also a non-intrusive method for the velocity measurements in a small volume for the selected point. For LDV measurements, two laser beams generate a fringe volume and each time a particle passes through the fringe it reflects its scattered light. This light is recorded by the photodetector which converts this information into signal. Different applications of LDV can be seen as (Xiong, et al., 2014) which is investigated turbulent flow by performing 3D LDV measurement. (Ikeda & Hoshi, 2006) is another example for LDV which is developed a "rod LDV". Fiber LDV probe is implemented on the inside of the rod which gives the opportunity to perform velocity measurements at different positions without disturbing the flow field. Other examples of LDV can be found in Chapter 5 where the implementation of LDV in CALIFS is going to be discussed in Chapter 5.
PIV is a non-intrusive way to quantify the fluid flow by adding particles and tracking their displacements (Tropea, et al., 2007). Compared to LDV, the flow is studied as a field instead of in a small volume. PIV consists of different measurement techniques such as 2D2C (planar), 2D3C (stereo), and 3D3C (tomo) PIV.
For planar PIV, the measurement domain is defined by a light-sheet which illuminates the particles in the flow. This illumination is supplied by a laser. The selected measurement domain is recorded as frame-by-frame by using high-speed camera with each pulse of the laser. The displacement of the particles within the selected two frame leads to the 2D velocity field. With planar PIV, the third-component of the velocity field is not measured, i.e. the particles moving in the width of the laser sheet.
Stereo and tomo PIV methods can be used to overcome this loss of the third component, i.e. out-of-plane motion, which is perpendicular to the measurement plane. These methods perform by using multiple cameras. Even though the advantage of tomographic PIV or stereo PIV, Planar PIV configurations are still widely being used where it is applicable, i.e. the third component of the flow has smaller effect compared to other two components.
For CALIFS velocity measurements, planar PIV is use due to low requirements of equipment and also less complicated applications compared to other PIV techniques.
Two different setting of planar PIV is used as High-speed PIV and Low-speed PIV for CALIFS experimental campaign. For High-speed PIV, continuous laser is used with high-speed camera. The advantage of this method is the time-resolved velocity information with the usage of continuous laser. The disadvantage of the High-speed PIV is the measurement range being limited with relatively low Reynolds number. With high Reynold number, i.e. high flow velocity, the high-speed camera starts to be not enough for capturing the displacement of the particles between each images.
To overcome this difficulty Low-speed PIV is used with pulsed laser and dual frame camera. Pulse lasers are using Q-switch device which stores and releases energy of the laser rapidly. It is possible to capture the high displacement of the particles by using this small time difference between pulses it. The advantage of this setting is the increase of the spatial information and performing measurements with higher Reynolds number whereas the disadvantage is the loss of temporal

information. By using this two methods of PIV, it is aimed to get the statistical information of the velocity field for a wide range of Reynolds number.
To perform PIV measurements, the access to the measurement domain is one of the most important step. CALIFS has optical access (Perspex windows) on three sides which gives opportunity to perform optical measurements. For CALIFS the main difficulty is to reach the measurement domain, i.e. central rod which is positioned behind two INOX rod.
For creating this visual access, the materials that creates an optical distortion needs to be removed or minimized. To be able to create a measurement domain with minimized optical distortion Refractive Index Matching (RIM) method is started to be used. (Wright, et al., 2017) Refractive index is the value which is related to the angle of incident and refracted ray of light. Each material and environment have its own refractive index value.
In literature different material selection for different environment can be found. (Zhu, et al., 2016) uses Poly Methyl Methacrylate (PMMA) particles used as index matching solid for 2,2'-thiodiethanol – phosphate-buffered saline – glycerol mixture to perform μPIV measurements where (Aziz & Wong, 2003) uses PMMA spheres with dibutyl phthalate as the matching liquid for PIV measurements. Another environment – material matching can be seen in turbomachines where sodium iodide (NaI) with deionized water used as liquid and acrylic material used for rotor and stator as matching solid (Uzol, et al., 2001).
A popular material for performing PIV measurements in water is Fluorinated ethylene propylene (FEP) due to its similar refractive index values, i.e. 1.33 for water at 20°C and 1.34 for FEP. Different purposed measurements with FEP can be found in literature such as for holographic PTV measurements (Satake, et al., 2015) or for velocity profile of jet flows (Amini & Hassan, 2009).
For the application of RIM in CALIFS, FEP is selected as the transparent material where the working fluid is water. Only the two rods are changed not to disturb the integrity of the rod bundles in CALIFS. By minimizing the difference of refractive index value for the environment and the material, it is possible to have the access to the measurement domain through the transparent material with low optical distortion.
For measurements, the camera and the laser are placed perpendicularly by performing calibration.
All the details about PIV and implementation of PIV to for the first time in CALIFS is discussed in Chapter 6.
Pressure represents the molecular activity in scalar form. To be able to measure the non-directional motions of pressure, it is necessary to use a device which is at rest relative to the flow. (Tropea, et al., 2007)
In CALIFS two different pressure measurements are performed as pressure drop measurements and pressure fluctuation measurements.
Pressure drop shows the energy loss in the flow due to the work that is done to overcome the friction. In fuel assemblies with the geometry change due to spacer grids, the area of the flow passing through becomes tighter. The increase in the coolant acceleration, generates energy losses as pressure drop. (Masterson, 2020) Therefore the pressure drop characterization is important to estimate the possible losses in the rod bundle.
For the pressure drop measurement, pressure taps are being widely used. Some examples can be given as the pressure drop measurements in microchannel as (Pfund, et al., 2000) and pipes as (Bordet, et al., 2018), (Martinez-Padilla, et al., 1997). Pressure drop measurements in the rod bundle can be found for different scales of fuel assembly, such as in a full-scale fuel assembly in liquid metal reactor (Choi, et al., 2003), in hexagonal arrangement (Rehme, 1972) or for wire-wrapped fuel assembly (Chun, et al., 2001).
In CALIFS, pressure drop measurements are performed with pressure taps that are mounted on the wall of the test section for different distances away from the spacer grid. The results are used for the

estimation of the friction velocity for different configuration of spacer grid and different Reynolds numbers.

Addition to the energy losses, the friction coefficient is used for the characterization of the flow via the smallest scale, i.e. Kolmogorov scale. In this range of scale, the mechanism is connected to the diffusion of momentum. The details about the scales are discussed in Chapter 3 and the pressure drop measurements and the results are explained in Chapter 7.

Depending on the application, different devices can be used to perform pressure fluctuations measurements such as microphones (Tsuji & Ishihara, 2003), piezoelectric transducers (Holbert, et al., 2004) (Berger, 1967) and piezoresistive transducers (Beresh, et al., 2011).

For the current study, piezoresistive sensors are used for pressure fluctuation measurements. Piezoresistive sensors have a silicone membrane and another metal membrane behind. These membranes are connected to the strain gauges. According to the mechanical load, the membrane deforms and transfer this deformation into resistance change by four active arm Wheatstone bridge which is then converted into voltage signal. Different applications using piezoresistive sensor can be found in literature as (Camussi, et al., 2008) and (Lofdahl, et al., 1994).

The advantage of piezoresistive sensors are the high-resolution measurements and the supposed durability of the sensor. To characterize the flow with pressure fluctuations, two main measurement campaigns are performed. The first measurements are performed under the experimental campaign for Reynolds number 66000 with single pressure sensor implemented on the central rod.

To investigate the transport of these pressure fluctuations a new multi-sensor device is designed. The multisensor device gives opportunity to install multiple pressure sensors with different distances from each other. With this device, the pressure measurements are performed instantaneously by multiple sensors. The measurements are performed for a different range of Reynolds number, i.e. $13000 < Re_{Dh} < 120000$.

The details about single and multisensor pressure measurements are going to be discussed in Chapter 7.

During both experimental campaign, different improvements are needed to increase the performance of the pressure sensors. For the physical support, a heat shrink tubes are applied around the sensors. To decrease the electrical noise, improvement are made in the data acquisition system. Additionally new precautions are applied in the measurement protocol.

The details about the problem solving regarding pressure measurements are discussed in Chapter 7.

To find out the physics behind the structures in the flow with respect to velocity and pressure fluctuation, simultaneous measurements are performed with PIV and pressure measurements. For PIV measurements, the High-speed PIV configuration is used which gives the time resolved information of the velocity fluctuations. For pressure measurements, multisensor device is used where all the sensors are included in the PIV measurement frame. The details of the measurements are going to be given in Chapter 8. In rod bundles the flow pulsation is a phenomena that has periodic characteristic. To investigate the correlation of these periodic events on both fluctuations, the cross-correlation method is used. The application of the cross-correlation method is going to be explained in Chapter 12.

In Chapter 9, the global evolution of the flow is studied with the pressure and velocity measurements. In the first part of the chapter, the pressure and velocity fluctuations are investigated around the central rod for $Re_{Dh} = 66000$ by using single pressure sensor and LDV, respectively. In the second part of the chapter, the characterization of the flow is extended for $13000 < Re_{Dh} < 120000$ and the velocity field is studied with PIV measurements.

In Chapter 10, these fluctuations are studied in frequency domain to find the signatures of the fluctuations. The energy spectra shows evidence of a periodic event. The source of these periodic events are investigated by the PIV method which gives the opportunity to visualize the flow.

As results of the visualization, the structures in the flow are represented in Chapter 11. To investigate the relation between the structures and the fluctuations, different length scales are calculated as integral length scale and periodic length scale.
For the evolution and transportation of these structures, simultaneous measurements are studied in Chapter 12. These studies include the instantaneous multisensor pressure measurements and the simultaneous PIV-pressure measurements. The combination of both measurements create a link between the flow and these structure in terms of fluid-structure interaction.
In the last chapter, the summary of the results are discussed with some perspectives for the future experiments.

CHAPTER 2
INDUSTRIAL CONTEXT

2. INDUSTRIAL CONTEXT

2.1 Pressurized Water Reactor

The Pressurized Water Reactor (PWR) is currently the most common type of nuclear reactor in commercial use for power production. Figure 1(a) shows the schematics of PWR.
PWR have two major part as the primary system and the secondary system. The primary system transfers the heat from the fuel assemblies to the steam generator, where the secondary system begins for the energy production.

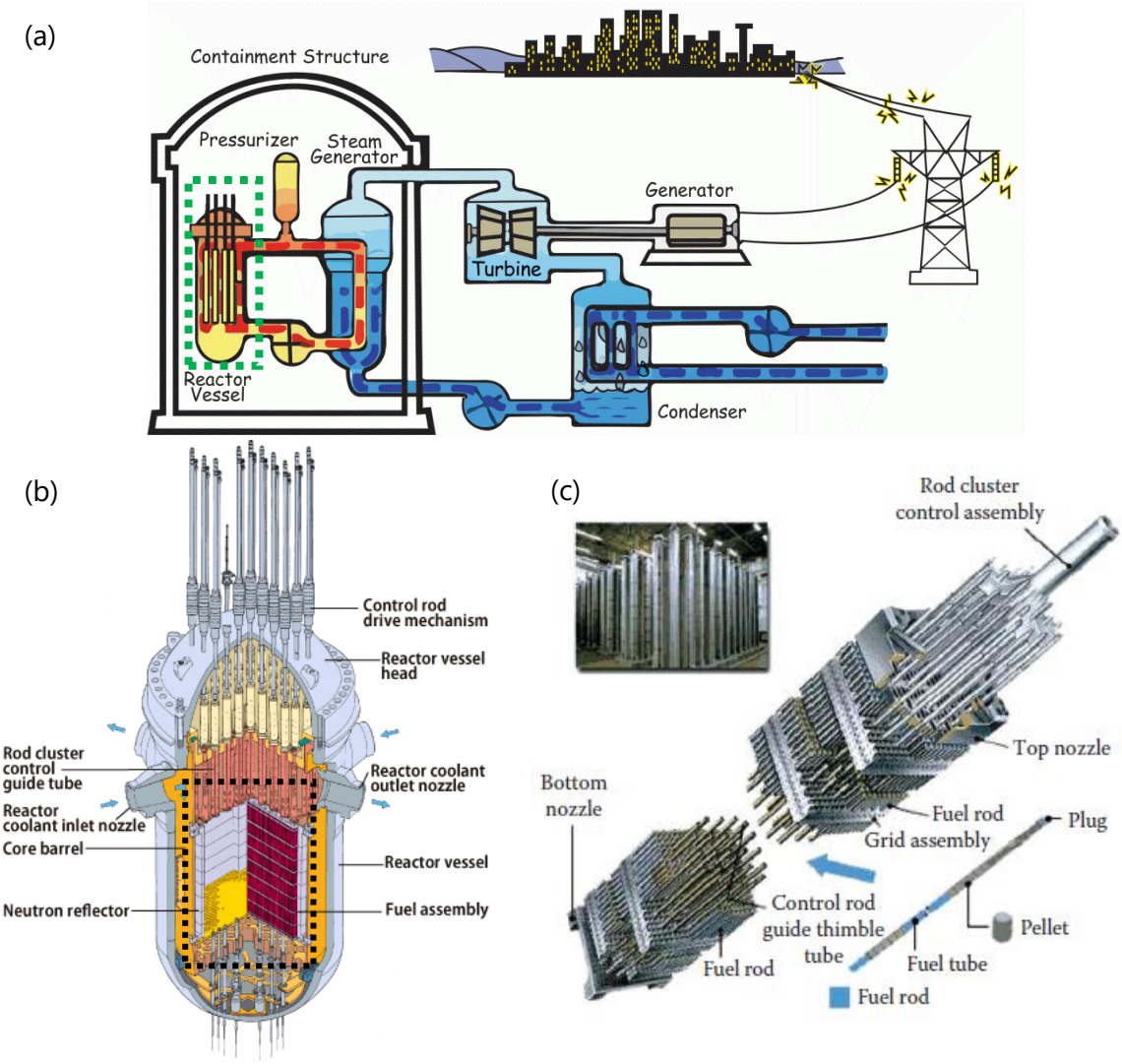

Figure 1: (a) Schematic of (a) pressurized water reactor (Breeze, 2014) the reactor pressure vessel is marked with green dotted line (b) reactor pressure vessel (Masterson, 2019) the reactor core is marked with black dotted line (c) one fuel assembly (Masterson, 2019)

2.1.1 Primary system

Primary system is used as the reactor coolant system. This system consists of a reactor core, a pressurizer, cooling loops which can be 2, 3 or 4 loops in total, with reactor cooling pump and steam

generator on each loop. The amount of the cooling loops connected to the reactor depends on the power output of the plant. (Hassan & Chaplin, 2010)
Inside the reactor core, the heat is generated by the fuel assemblies. This heat is transferred into the coolant flow. The pressurizer keeps the coolant, i.e. water, pressure up to 155 bar which allows the water to reach 325°C without boiling or creating a steam formation. (Breeze, 2014)

2.1.1.1 Reactor core and industrial turbulent flow

Figure 1(b) shows the schematics of the reactor pressure vessel. The reactor pressure vessel is around 12m-13m height. In Figure 1(b), the reactor core is marked with black dotted line inside the reactor pressure vessel.
The reactor core is around 4.2m height with 3.3m diameter. The reactor core contains around 175-225 fuel assemblies depending on the design where these assemblies can be arranged as square and/or rectangular arrays.
The core of the reactor is filled with coolant. The coolant enters to the reactor pressure vessel from inlet nozzle and goes through downwards of the vessel. The entrance of the coolant flow to the reactor core happens from below. The flow is distributed between the individual fuel assemblies where the velocity inside the fuel assembly at about 5 m/s. The Reynolds number of this coolant flow in the fuel assembly vary between 100 000 and 600 000. (Masterson, 2020)
The reactors open lattice structure permits mixing of the flow in the core.

2.1.1.2 Fuel assemblies and fuel rods

Figure 1(c) shows the schematics of one fuel assembly. The fuel assemblies consist individual fuel rods which can vary between 30-300 rods depending on the size/design of the reactor. The diameter of the fuel rods are 9.5mm. The pitch of the fuel rods in a PWR fuel assembly is about 12.6 mm so that the Pitch-to-diameter ratio (P/D) is 1.32.
Inside each rod, uranium dioxide (UO_2) ceramic pellets is placed as nuclear fuel where the nuclear chain reaction occurs. The generated heat is the product of this chain reaction. Around these pellets, Zircaloy is used as cladding which absorbs the neutrons.

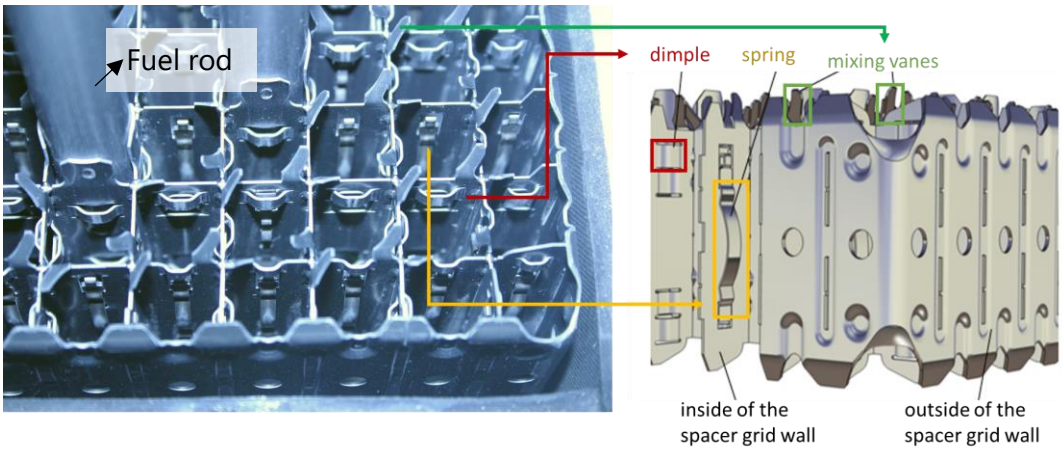

Figure 2: (a) Photo of the spacer gids with grid elements (b)Schematics of spacer grids with grid elements

These fuel rods are typically arranged as 17x17 arrays, i.e. rod bundles.
The rod bundles are held by spacer grids. Figure 2(a) shows a photo of the spacer grids with two fuel rods as an example.
The main purpose of the spacer grids are to maintain the structural integrity of the fuel assemblies. (Masterson, 2020) In addition to the structural support, it creates spacing between each rod and

generate mixing in the flow. On each mesh of spacer grid, different grid elements are found as shown in Figure 2(b). Dimples and springs support the fuel rods and prevent the fuel rods to get in contact with the spacer grids. Depending on the design, some spacer grids can have mixing vanes at the outlet of the grid. The mixing vanes enhance the mixing within an assembly and between adjacent fuel assemblies by promoting secondary flows, such as transverse and possibly swirling around rods flows.

2.1.2 Secondary system

As explained in Chapter 2.1.1.2, the heat is generated inside the fuel assemblies and transferred into the coolant water flow. The pumps carry this heated water into steam generator which is the link between the primary loop and the secondary loop. In the steam generator, the heat from the heated and pressurized water is transferred to a secondary coolant water. This heat converts the secondary coolant water into steam. This steam follows the secondary system.
The secondary system includes turbine, electric generator and condenser. (Green & Hetsroni, 1995) The steam first goes through the turbine and the turbine converts this thermal energy to kinetic (rotation) energy. Afterwards the generator converts this kinetic energy into electric energy. The steam that is leaving the turbine condenses in a condenser. This process is maintained at a vacuum using either vacuum pumps or air ejectors. Cooling of the steam is provided by external cool water sources that is pumped and circulate in the condenser.
As the last step the water, which is condensed from steam, is pumped back to the steam generator for reuse. (Hassan & Chaplin, 2010)

2.2 Grid-to-Rod Fretting

Inside the reactor core, there are different source of Flow Induced Vibrations (FIVs) such as operating conditions or extreme accident conditions. (Ferrari, et al., 2020) With regular operating conditions, i.e. the high Reynolds number and spacer grids, the coolant flow becomes turbulent. This turbulence is one of the source of the FIV that is observed as the interaction between the coolant flow and the rod bundles.
Inside the reactor core, one end of the fuel rods have a clamping mechanism which keeps the fuel rods in a defined position. The induced vibrations leads to a relative movement of the fuel rod towards the supporting grid elements, i.e. dimple and/or spring.
This interaction leads to a wear on the rod, i.e. fretting. This fretting can be observed in the contact part of the rods cladding with the grid elements.
With the aging during the reactor cycles, the clamping mechanisms start to decrease in efficiency which leads to decrease of the clamping force on the fuel rod. This leads to the creep or relaxation of the fuel rods while having contact with grid elements. As a result the wear increases on the outer part of the fuel rods.
This phenomena, i.e. Grid-to-Rod fretting, is one of the leading causes for nuclear fuel leakage. The solution of this kind of damage is changing the fuel rods which leads to extra costs.
To understand the phenomena, it is necessary to investigate the forces applied on the fuel rods.

2.3 Experimental Studies for Flow in Rod Bundle

To study the phenomena that is connected to the forces in the flow, it is important to characterize the flow in terms of velocity and pressure. For these measurements that is performed in the lab, the rod bundle is often simplified according to the features sought for in a particular investigation. Different studies can be found in literature for flow in fuel assemblies with different measurement techniques, different rod bundle settings and different grid systems.

In (Rowe, et al., 1974) the turbulent crossflow mixing is investigated for a mixture of 2x3 rod bundle with 1x3 half diameter of rod bundle without any grid. The measurements are performed with 2D LDV measurements. In the results periodic behaviour on correlation functions are observed for certain regions on the flow.
Similar behaviour observed in (Hooper & Rehme, 1984) where the measurements are performed with hot wire for the 1x4 rod bundle and 2x3 rod bundle without any grid. The aim of the measurement is the investigation of mean velocity components, wall-shear stress variation, axial pressure distribution and Reynolds stresses. In the results large scale semi-periodic structures are observed. These structures are observed to develop by the axial turbulent-velocity component.
Another study is made by (Moller, 1991) that is focused on the periodicity of the flow. The measurements are performed 1x4 rod bundle without any grid with air as a fluid. For the experiments, hot wires are used for velocity and the microphones are used for the pressure measurements. In the results, a quasi-periodic behaviour, i.e. flow pulsation, is observed across the gaps of the rod bundle. The importance of these quasi-deterministic structures is described as the mass exchange between the subchannels of the rod bundle.
Another two measurements without grid can be seen in (Rehme, 1978) and (Rehme, 1987). These measurements are performed with 1x4 rod bundle by using hot wire. The velocity components and kinetic energy of turbulence is investigated. It is observed that the turbulent velocity component is generated by parallel-channel instability.
In addition to square and rectangle arrays, the studies can be found for different configurations, i.e. triangular, hexagonal.
In (Carajilescov & Todreas, 1976), the measurements are performed with Laser Doppler Anemometry (LDA) for triangular rod bundle without any grid. The aim of the study is to measure the velocity field to perform heat transfer calculations. In the study axial velocity, turbulent kinetic energy and Reynolds stresses are investigated.
As shown in Chapter 2.1.1.2, in real fuel assemblies these rod bundles are held by spacer grids. To show the effect of the spacer grids, (Rehme & Trippe, 1980) is performed the measurements with and without spacer grids using 19 rods in hexagonal array. The measurements are performed with pitot tubes. In the results vortex shedding is observed downstream the spacer pins.
To decrease the effect of the boundary, i.e. wall of the measurement setup, 5x5 rod bundles are minimum requirement for measurements.
(Yang & Chung, 1998) is performed LDV measurement to investigate the velocity fluctuations and turbulent intensity for 5x5 rod bundle with mixing vane spacer grid . The results show high fluctuation close to the grid and decay of the turbulent intensity with the increased distance from the grid.
For the experiments performed by (Ikeda & Hoshi, 2006), a new developed LDV rod is used in 5x5 rod bundle with mixing vanes spacer grid. The rod gives the opportunity to perform LDV with different positions without disturbing the flow. The results show decrease of mean crossflow velocity and turbulence with the increased distance from the grid.
These measurements are compared with PIV measurements of (McClusky, et al., 2003). The results show similar trends where the differences are attributed to the uncertainty of the rod positions and high velocity gradient near the surface of the rod.
To have the optical access within the rod bundle, RIM method is a method to decrease the optical distortion in the flow while performing PIV. (Dominguez-Ontiveros & Hassan, 2009) is an example of RIM method applied for PIV measurements. In this study the rod bundle are held with mixing vane spacer grid. The velocity field and the vorticity is investigated. With the mixing vanes, due to stretching in the flow, the vorticity is observed to be suppressed. As another effect of mixing vanes, large scale unsteadiness is observed.

(McClusky, et al., 2002) is performed the experiments with split vane type of spacer grid. The lateral and axial velocity measurements are performed. The type of the large-scale structures are investigated, i.e. wing tip vortex, swirling flow in the pipe and Lamb-Oseen vortex. The results show that the velocity and the circulation data is fit with Lamb-Oseen vortex.
(Qu, et al., 2019 (a)), (Qu, et al., 2019 (b)) and (Xiong, et al., 2020) are other PIV measurements that are performed downstream the split-type mixing vane. In both measurements, the cross-flow pattern is observed to determine with the mixing vanes and rod bundle structure.
(Chang, et al., 2014) is performed the experiments with two types of spacer grid, i.e. split-type and swirl-type of spacer grid. The measurements are performed with 2D-LDA method. In the study, velocity fluctuations are investigated and turbulence intensity, vorticity maps are derived from the velocity measurements.
(Lee, et al., 2020) is investigated the cross flow with spacer grid using PIV. As a result, a mixing coefficient is defined to estimate the performance of rods and to be used as a parameter in numerical studies.

2.4 Numerical Analysis for Flow in Rod Bundle

Computational fluid dynamics (CFD) is a way of finding a numerical description of the flow of interest by using mathematical equations. These equations are expressed the fluid flows that follow conservation of mass, energy and Newton's second law.
With the decrease of the relative costs due to the computational power, CFD becomes a popular tool that compliment both pure experiments and pure theory (Wendt, 2009).
The advantage of the CFD is that in some cases it can provide excellent control and characterization of boundary conditions. Additionally it can reach to all flow field where can be challenging to reach with physical experiments (Kraus, et al., 2021).
The disadvantage of CFD is that it can't reproduce physics that are not properly included in the formulation of the problem. The flow inside nuclear core is highly turbulent. Most of the CFD solutions, i.e. except Direct Numerical Simulation (DNS), of turbulent flows contain turbulence models. These models are an approximation of the real physics and depends on empirical data (Wendt, 2009). Therefore it is necessary to validate the numerical analysis with physical experiments to find best model and simulation that can represent the phenomena observed in the reactor core.
CFD includes different approaches depending on the desired resolution of the results. The resolution of the result is connected to the modelled scales of the flow, i.e. from large scales to Kolmogorov scales. These scales are determined by the grid while the accuracy of these scales is determined by the numerical method (Moin & Mahesh, 1998). The costs of the CFD computations are depending on the Reynolds number, i.e. the increased Reynolds number leads to higher turbulence which increases the range of scales in the flow.
In DNS, the full Navier-Stokes equations are solved directly with a very fine mesh. This removes the need of empirical model while resolving all the scales of the turbulent flow (Kraus, et al., 2021) which gives a key advantage compared to other CFD methods. The downside of this method is the high computational cost compared to other numerical methods.
Different example of DNS can be found in nuclear application. (Kraus, et al., 2021) is performed DNS with 5x5 rod bundle without the spacer grids. Velocity behaviour, Reynolds stresses and Turbulent Kinetic Energy is discussed in various areas of computational domain. Flow structures are investigated and vortex street is observed between the rods and the outer wall. (Sergeenko, et al., 2019) is another example of DNS in hexagonal rod bundle which shows the capability of predicting the thermo-hydraulics of the flow.
The most basis of CFD computation is Reynolds Averaged Navier-Stokes (RANS) approach. This method is used where the main interest is the steady-state fluid flow where the instantaneous flow

and the fluctuations are not simulated. Instead only the averaged quantities are solved while the turbulent motion is modelled by a turbulence model. (Zhiyin, 2015)
(Cinosi, et al., 2014) and (Wiltschko, et al., 2021) are examples of RANS simulations with spacer grids in rod bundles. Both studies include different turbulent models results and their comparison. (Cinosi, et al., 2014) also includes the mesh refinement comparisons.
Large Eddy Simulation (LES) is an alternative method between RANS and DNS. In LES the large scales of turbulent flow are calculated which are the structures of the flow that contain the most of the turbulent kinetic energy. The small scale motions which are computed in DNS, are modelled by sub-grid scale (SGS) in LES method.
The CFD with LES is highly performed method in rod bundle. (Ju, et al., 2020) is investigated the mixing of the flow in 3x3 rod bundle. In the results quasi periodic flow properties are observed. (Bieder, et al., 2014) is performed LES computations on the wake of the 5x5 rod bundle mixing vane. In the results swirling structures are observed which is imposed by mixing vanes. (Kraus, et al., 2021) is another example of LES computation in 5x5 rod bundle which includes comparison with DNS calculations.

2.5 CALIFS Analytical Experiments

CALIFS experiments are the part of "FULL ASSEMBLY" project in CEA. The project includes different scales of experiments to investigate the behaviour of the fuel assembly and the interaction of the flow. The project is funded by EDF, Framatome and CEA.
CALIFS is a water experimental analytical rig dedicated to the study of turbulent flows within rods bundle and create a database for numerical analysis. The aim of the CALIFS analytical experiments are the investigation of the forces exerted on the central rod with the different design of spacer grid. CALIFS is a 5x5 rod bundle where two types of analytical spacer grids are used as NMV and WMV. In both of the grids, dimples and springs are supporting the rods.
CALIFS has the scale of 2.81 compared to PWR. The higher scale gives the opportunity to zoom in the phenomena downstream the spacer grid. The pressure and the temperature are low compared to real reactor conditions in PWR. Therefore to represent the similitude with PWR, the Reynolds number is used. The Reynolds number range is achieved by changing the velocity and the temperature of the flow. The details of CALIFS is discussed in Chapter 4.
The first measurement campaign performed in CALIFS is to investigate the forces at $Re_{Dh} = 66000$ with NMV configuration by using pressure sensor (Moreno, et al., 2016). To compare the configuration, the measurements are performed with WMV configuration for the same Reynolds number value, i.e. $Re_{Dh} = 66000$ (Moreno, et al., 2019). In the results frequency peak is observed in both configuration for the measurement domain close to the spacer grid.
The details of these measurement campaigns are discussed in Chapter 7 and the results are discussed in Chapter 9 and Chapter 10.
As mentioned in Chapter 2.4, the higher Reynolds numbers lead to increased computational costs. One of the aim of CALIFS is to find the range of Reynolds number that the related phenomena can be observed. By finding the range, it is aimed to support CFD calculations with low Reynolds number. With this aim, the first CFD calculation that is performed in CALIFS 5x5 is (Gauffre, et al., 2020) (Farges, et al., 2021). Computations give very satisfactory results for the pressure drop, the mean velocity, and the Reynolds stresses at different locations. From the results some differences is observed compared to the experimental results performed in CALIFS, i.e. failure of reproduction of the pressure fluctuations for increased distances from the grids and some missing persisting structures which are related to the frequency peak.
To support the future CFD calculations, the CALIFS measurements are performed for wide range of Reynolds number, i.e. $13000 - 120000$ which is the aim of the current manuscript. These

measurements include PIV measurements with RIM method, LDV measurements and pressure measurement with new designed multisensor device. These methods are discussed in Chapter 5, 6 and 7, respectively.

CHAPTER 3
PHYSICAL CONTEXT

3. PHYSICAL CONTEXT

3.1 Fundamental aspects of turbulent flows

Turbulence is a fundamental aspect of fluid mechanics. This means turbulent flows need to satisfy the conservation of mass and momentum.

The conservation of mass is shown in Eq.(1) where m is the mass, ρ is the density and ∀ is the volume.

$$m = \rho \forall \tag{1}$$

The differential equation of mass conservation leads to the continuity equation. The continuity equation shows the conservation of mass throughout the volume of fluid (Tardu, 2014). Eq.(2) is the continuity equation in Eulerian form where $\boldsymbol{U}(u, v, w)$ is the 3 dimensional instantaneous local velocity vector in the direction of $\boldsymbol{x}(x, y, z)$, i.e. the position vector.

$$\frac{\partial \rho}{\partial t} + \frac{\partial \rho \boldsymbol{U}}{\partial \boldsymbol{x}} = 0 \tag{2}$$

In incompressible fluids, the total derivative of density is zero, i.e. $\rho = cte$ which means a selected fluid elements density does not change with the time. This leads to reduction of Eq.(2) to Eq.(3).

$$\frac{\partial \boldsymbol{U}}{\partial \boldsymbol{x}} = 0 \; or \; \nabla . \boldsymbol{U} = 0 \tag{3}$$

Eq.(4) shows the Newton's second law where $\boldsymbol{F}$ is the force applied on a body and $\boldsymbol{a}$ is the acceleration of the body. According to the Newton's second law, for the conservation of momentum, the rate of change of momentum of a body needs to be equal to the force applied.

$$\boldsymbol{F} = m\boldsymbol{a} \tag{4}$$

These forces separates into two groups as long-range forces and short-range forces.

The long-range forces act on the entire fluid element equally and named as volume/body/external forces. These forces show slow variation with the distance of the selected fluid element. Some of the examples for these forces can be given as gravity, electromagnetic forces and fictitious forces such as centrifugal force.

The short-range forces have molecular origins. These forces decreases extremely rapidly with the increase of the distance from the selected fluid element. The effect of these forces can be found only when the distance is in order of molecules of the selected fluid element.

The contribution of the molecular forces are not included in equation of fluids. On the other hand, when these molecular forces act on the fluid elements, it causes a reaction on the boundary of the fluid element. Therefore these forces are determined by the surface area of the fluid element (Batchelor, 1967) and are named as surface/internal forces.

The presence of these surface forces give arise to stresses. There are two types of stresses as normal stresses and shear stresses. Normal stresses act along the normal to the surface area, i.e. perpendicular to the surface. The shear stresses act along the place of the surface area, i.e. parallel to the surface area.

In a moving fluid, two type of surface forces are found as pressure forces and viscous forces. The pressure forces acts normal to the surface of the fluid element, i.e. normal stresses as τ_{xx}, τ_{yy} and τ_{zz}.

The viscous forces act on both stresses as normal and shear stresses, i.e. normal stresses as τ_{xx}, τ_{yy}, τ_{zz} and additional shear stresses as $\tau_{xy}, \tau_{xz}, \tau_{yx}, \tau_{yz}, \tau_{zx}$ and τ_{zy}.

Eq.(5) shows the connection between the stresses and the rate of deformation according to Newton's law of viscosity. S_{ij} is the strain-rate tensor and for Newtonian fluids $\mu = \rho\vartheta$.

$$\tau_{ij} = \rho\vartheta\left(\frac{\partial u_i}{\partial x_j} + \frac{\partial u_j}{\partial x_i}\right) = 2\rho\vartheta S_{ij} \tag{5}$$

Eq.(6) shows the net viscous force applied on rectangular fluid element from ith direction.

$$f_i = \frac{\partial \tau_{ji}}{\partial x_j}\forall \tag{6}$$

The sum of the surface forces apply on a fluid element therefore the sum of the pressure forces and the viscous forces which can be written as Eq.(7) and with the substituting the Eq.(5) to Eq. (7) leads to the final form of the surface forces acts on the fluid element as Eq.(8). (Davidson, 2004)

$$f_{surface} = -\boldsymbol{\nabla}P + \frac{\partial \tau_{ji}}{\partial x_j} \tag{7}$$

$$f_{surface} = -\boldsymbol{\nabla}P + \rho\vartheta\frac{\partial}{\partial x_j}\left(\frac{\partial u_j}{\partial x_i} + \frac{\partial u_i}{\partial x_j}\right) = -\boldsymbol{\nabla}P + \mu\left(\frac{\partial^2 u_i}{\partial x_j^2}\right) \tag{8}$$

The implementation of the conservation of mass, continuity and law of viscosity i.e. Eq.(1), Eq.(3) and Eq.(5) respectively, to conservation of momentum, i.e. Eq.(4), leads to the Navier stokes equation. Eq. (9) is the Navier-stokes Equation for Newtonian incompressible fluid with constant viscosity.

$$\rho\left[\frac{\partial \boldsymbol{U}}{\partial t} + (\boldsymbol{U}\cdot\boldsymbol{\nabla})\boldsymbol{U}\right] = -\boldsymbol{\nabla}P + \mu\nabla^2\boldsymbol{U} + \rho f_{ext} \tag{9}$$

The right-hand side shows the total forces applied on a fluid element, i.e. surface and volume forces. $\boldsymbol{\nabla}P$ shows the pressure forces, $\mu\nabla^2\boldsymbol{U}$ shows the viscous forces and f_{ext} is any external force like gravity, i.e. volume/body forces.

On left-hand side, the first term ρ, density, is the mass and the second term is the $\frac{\partial \boldsymbol{U}}{\partial t} + (\boldsymbol{U}\cdot\boldsymbol{\nabla})\boldsymbol{U}$ is the acceleration term.

In acceleration tem, $\frac{\partial \boldsymbol{U}}{\partial t}$ is the unsteady component and $(\boldsymbol{U}\cdot\boldsymbol{\nabla})\boldsymbol{U}$ is the convective component.

Navier-Stokes is a complex equation. Even though turbulent flows have common characteristics, the existence of a unique solution of Navier-Stokes equation is not mathematically proven.

To be able to study turbulent flows, one of the tool is using the scales which is relevant to the specific for the studied case, i.e. dimensional analysis.

Table 1 shows the scaling parameters used for the process of creating non-dimensional Navier-Stokes equation.

Scaling parameter	Description
L	Characteristic length
U	Characteristic velocity
f	Characteristic frequency/time
ρU^2	Pressure scale
g	Gravitational acceleration

Table 1: Scaling parameters used for non-dimensional process

By using scaling parameters, the dimensionless variables can be defined as Eq.(10).

$$t^* = \frac{t}{L/U} \qquad \boldsymbol{x}^* = \frac{\boldsymbol{x}}{L} \qquad \boldsymbol{U}^* = \frac{\boldsymbol{U}}{U}$$
$$P^* = \frac{P}{\rho U^2} \qquad \boldsymbol{\nabla}^* = L\boldsymbol{\nabla} \qquad g^* = \frac{U^2}{L} g \tag{10}$$

Eq.(11) shows Navier-Stokes equation, i.e. Eq. (9) with the introduced dimensionless variables.

$$\frac{U^2}{L}\frac{\partial \boldsymbol{U}^*}{\partial t^*} + \frac{U^2}{L}(\boldsymbol{U}^*\boldsymbol{\nabla}^*)\boldsymbol{U}^* = -\frac{U^2}{L}\boldsymbol{\nabla}^* P^* + \frac{U\mu}{\rho L^2}\boldsymbol{\nabla}^{*2}\boldsymbol{U}^* + \frac{U^2}{L} g^* \tag{11}$$

By organizing and cancellation of the terms, the Eq.(11) takes the form as Eq.(12).

$$\frac{\partial \boldsymbol{U}^*}{\partial t} + (\boldsymbol{U}^*\boldsymbol{\nabla}^*)\boldsymbol{U}^* = -\boldsymbol{\nabla}^* P^* + \left[\frac{\mu}{\rho U L}\right]\boldsymbol{\nabla}^{*2}\boldsymbol{U}^* + g^* \tag{12}$$

This leads to Navier-Stokes equation with dimensionless numbers as Eq.(13) where Re is the Reynolds number.

$$\frac{\partial \boldsymbol{U}^*}{\partial t} + (\boldsymbol{U}^*\boldsymbol{\nabla}^*)\boldsymbol{U}^* = -\boldsymbol{\nabla}^* P^* + \left[\frac{1}{Re}\right]\boldsymbol{\nabla}^{*2}\boldsymbol{U}^* + g^* \tag{13}$$

In 1883, O. Reynolds characterized the flow according to the internal motion of the fluid (Reynolds, 1883). One of these motion is that the elements of fluids following the lines of motion, i.e. laminar flow. The second motion includes the elements that follow sinuous paths, i.e. eddies. The flow where this second motion with eddies can be observed is turbulent flows.

According to (Reynolds, 1883) experiments, the birth of these eddies are observed to depend on a definite value of a dimensionless number which is named after him as Reynolds number.

Reynolds number is the ratio of inertial forces to viscous forces. Inertial forces are connected to momentum of the fluid, i.e. Eq.(4), and it is balanced by the friction forces, i.e. Eq.(6). The inertial forces promote turbulent flow while the viscous forces promote the laminar flow. The dimensional analysis of Reynolds number can be shown as Eq.(14) where F_i is the inertial forces and F_v is the viscous forces. (Topea, et al., 2007).

$$Re = \left|\frac{F_i}{F_v}\right| = \frac{mU^2}{L}\frac{1}{\tau L^2} = \frac{\rho L^3 U^2}{L^3 \mu\, U/L} = \frac{\rho * U * L}{\mu} = \frac{\mathrm{U_{flow}} * D}{\vartheta} \tag{14}$$

In Eq.(14), D is the geometric length scale and $\mathrm{U_{flow}}$ represents the mean flow passing through this geometry where ϑ represents the viscosity.

Reynolds number represents the flow which is related to geometry, velocity and temperature, via the viscosity term, of the flow. In cases where $Re > 2000$, i.e. for flow in pipes, the flow is observed to have transition from laminar flow to turbulent flow (Davidson, 2004). The higher Reynolds number leads to higher intensity of turbulence where the transitional flow becomes fully turbulent flow. Turbulent flows are the natural state of most fluids (Davidson, 2004).

Turbulence arises from instabilities occuring on originally laminar flows (Tennekes & Lumley, 1972). Even though turbulence doesn't have certain accepted definition, it is represented with its own characteristic properties as flow.

Turbulence is a complex, disordered and unsteady flow which means the flow by itself evolves in time and space. Turbulent flows have the irregularity/random motions. The diffusivity of turbulence creates a mixing process in the flow while increasing the rates of momentum, heat and mass transfer. (Tennekes & Lumley, 1972).
The product become unpredictable with rapid irregular fluctuations of velocity in both space and time. (Tritton, 1988)
The velocity fluctuations consist of a random collection of eddies. Turbulent eddies are the filaments of vorticity in the flow which is associated with velocity field. These eddies show the evolution of a field of turbulence. The vorticities are stretched and twisted by the velocity field. These vorticities evolve and interact with the flow by their own inducted velocity field. Addition to the interaction with velocity field, when an eddy evolves in spacer at one location, it generates pressure waves which are distributed in the flow. This leads to interaction of eddies with each other (Davidson, 2004).
These eddies vary from large scales to small scales which is one of the properties of turbulent flows, i.e. multiscale properties. Figure 3 shows examples of different scales in the flow.

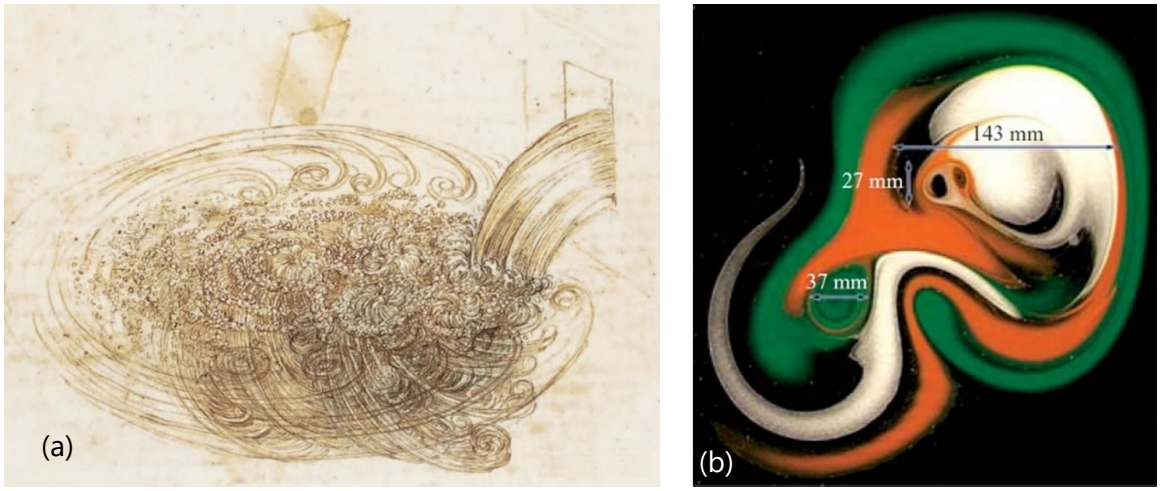

Figure 3: (a) A sketch of a turbulent flow by Leonardo da Vinci (b) a laminar projection of a multi-scale flow (Rossi, et al., 2006)

The largest scale of the flow is defined as integral length scale and the smallest scale is represented by Kolmogorov scale. The variation of these length scales are associated with a mechanism called turbulent cascade.
The largest eddies are created by the instabilities of the mean flow. Within these eddies they are subject to inertial instabilities which lead them to rapidly break-up/evolve into smaller eddies. While this evolution is happening, these large scales are passing their energy into smaller scales. This continual energy is led by the inertial forces where in high Reynolds number the viscous forces become negligible. Although at the smallest scale, the Reynolds number based on this scale of eddy becomes so small which leads to viscous forces to become dominant. At this level of the cascade, the dissipation starts and the whole energy left is swept by viscosity. (Davidson, 2004)
In shear flows, the mean velocity is predominantly one dimensional in nature (Davidson, 2004). The energy of the large scaled eddies have to be maintained by the shear flow where the mechanism of turbulent cascade are continuously leading larger scales to lose their energy to smaller scales. The most powerful large scaled eddies are the one who can absorb the energy from the shear flow most efficiently. It is observed that this effectiveness of the eddies are higher where the principle axis of these eddies are roughly aligned with the mean strain rate. The energy transfer mechanism of eddies

are associated with vortex shedding. The eddies are being strained by the shear and conservation of momentum leads to the energy transfer (Tennekes & Lumley, 1972).
Turbulent kinetic energy budget shows the energy transfer mechanism as Eq. (15) which is obtained from Navier-Stokes equation. (Tennekes & Lumley, 1972)

$$U_j \frac{\partial}{\partial x_j}\left(\frac{1}{2}\overline{u_i u_i}\right) = -\frac{\partial}{\partial x_j}\left(\frac{1}{\rho}\overline{u_j p} + \frac{1}{2}\overline{u_i u_i u_j} - 2\nu\overline{u_i s_{ij}}\right) - \overline{u_i u_j} S_{ij} - 2\nu\overline{s_{ij} s_{ij}} \tag{15}$$

In Eq.(15), the mean kinetic energy is shown as $\frac{1}{2}\overline{u_i u_i}$. The S_{ij} and s_{ij} term shows the mean and fluctuating rate of strain and they are defined as Eq.(16), respectively.

$$S_{ij} = \frac{1}{2}\left(\frac{\partial U_i}{\partial x_j} + \frac{\partial U_j}{\partial x_i}\right)$$
$$s_{ij} = \frac{1}{2}\left(\frac{\partial u_i}{\partial x_j} + \frac{\partial u_j}{\partial x_i}\right) \tag{16}$$

The term $-\overline{u_i u_j} S_{ij}$ is the turbulent energy production term. The turbulence stresses, i.e. Reynolds stresses, perform deformation work and kinetic energy benefits from this work. On the other hand $-2\nu\overline{s_{ij} s_{ij}}$ term is the dissipation term. This shows the viscous stresses perform deformation work against the fluctuating strain rate. This is the loss of the kinetic energy in the system.
The rest of the terms are represents the transport part of the mechanism. The parts are related with pressure work, transport by Reynolds stresses and transport by viscous stresses. This part is responsible for the redistribution of the energy inside the system. (Tennekes & Lumley, 1972)
The transport of the mean flow energy to fluctuations are performed by the turbulent eddies. These turbulent eddies are continually creating with the distortion in the flow. The produced eddies wrinkle, stretch and intensify the turbulent vortices. As the end result of these changes on the eddies, the mean flow energy is transferred into fluctuations, i.e. $\bar{u}$ to u'. The deformation of work shows the tendency for mean shear layer to stretch and intensify the vorticity which leads to increase of the turbulent energy. (Davidson, 2004)
Turbulence kinetic energy, TKE, is the kinetic energy calculated with turbulent fluctuating velocities as shown in Eq.(17).

$$TKE = \frac{1}{2}(\overline{u'^2} + \overline{v'^2} + \overline{w'^2}) \tag{17}$$

As a summary, the mean flow supply the energy to the large turbulent scales and with the turbulent cascade the flux of energy transferred to the small scales. This can be shown as Eq. (18) where G is kinetic energy to the cascade, π is the flux down to cascade and ε is the dissipation at small scales. (Davidson, 2004)

$$G = \pi = \varepsilon \tag{18}$$

Each length scale have their own time scale and characteristic property. Small scales in turbulence have a very short time scales which tend to make them statistically independent of the mean flow. This also means that the most of the transportation of energy, i.e. turbulent kinetic energy, is happening by the large in the flow.

The typical large scales are imposed by the flow geometry. For the pipe the diameter of a pipe or for channels the depth of the channel is used as the representative geometry length scale (Shen, et al., 2002). In fuel assemblies, this geometry is defined with hydraulic diameter, D_h.
Eq.(19) shows the general formula for the calculation of hydraulic diameter.

$$D_h = 4 * \frac{cross\ sectional\ area}{wetted\ perimeter} \tag{19}$$

The size of the large scales in the flow is represented with integral length scale, l. The integral length scale in the flow can be estimated by the autocorrelation function of the velocity fluctuations. The autocorrelation is a measure of the memory of the flow (Shen, et al., 2002). Eq. (20) shows the autocorrelation function. τ is the time delay between selected signal where the selected signal is x(t) (Bendat & Piersol, 1993)

$$R_{xx}(\tau) = \lim_{T\to\infty} \frac{1}{T} \int_0^T x(t)x(t+\tau)dt \tag{20}$$

It is assumed that these large eddies lose the most of the kinetic energy $k = \frac{1}{2}u^2$ around one turnover time. Eddy turnover time is the time taken for a hypothesized turbulent eddy to perform one complete $360°$ rotation. This time scale(t_l) represents the typical time for a structure of size (l) to undergo a significant distortion due to relative motion of its components (l/u). The structure volume will be squeezed with (t_l) while the energy is going to be transferred from bigger scales to smaller scales.
Therefore, in about one turnover time a finite fraction of the kinetic energy carried by the moving fluid is transferred by nonlinear interactions to scales sufficiently small for viscosity to be able to remove it into heat. This energy flux is shown in Eq.(21). (Davidson, 2004)

$$\pi \sim \frac{u_l^2}{t_l} = \frac{u_l^2}{\frac{l}{u_l}} = \frac{u_l^3}{l} \tag{21}$$

The small-scale motion depends on the rate at which it is supplied with energy by the large-scale motion and on the kinematic viscosity. This rate which named as dissipation range, corresponds to small length scales and at such scales kinetic energy of fluid motion is converted to thermal energy. The dissipation rate per unit mass (ε) represents the changes in the energy of the fluid. The contributions to this term is coming from the rate of working of the net viscous force acting on the fluid element and the mechanical energy change of the fluid. Therefore, the parameters governing this small-scale motion include at least the dissipation rate per unit mass ε $(m^2 sec^{-3})$ and the viscosity v $(m^2 sec^{-1})$. With these parameters the length, time and characteristic velocity scales are shown in Eq. (22), respectively.

$$\eta = \left(\frac{\vartheta^3}{\varepsilon}\right)^{1/4}, \tau = \left(\frac{\vartheta}{\varepsilon}\right)^{1/2}, v = (\vartheta\varepsilon)^{1/4} \tag{22}$$

This leads to the Reynolds number that is formed for small scales as $Re = \frac{\eta v}{\vartheta} = 1$. This illustrates the dominant viscosity in small-scale motion and that the viscous dissipation adjusts itself to energy supply by adjusting length scales.

In Eq.(18), the relation between the turbulent energy enters the system and the dissipation is discussed. By using this relation the energy flux will be dissipated from larger eddies to smaller eddies can be found as Eq.(23) .

$$\pi \sim \varepsilon$$
$$\frac{u_l^3}{l} \sim \vartheta \left(\frac{v^2}{\eta^2}\right) \tag{23}$$

The relation of the scales and the Reynolds number can be found by substituting energy cascade into scales for small-scales as in Eq.(24).

$$\frac{\eta}{l} = Re^{-3/4} \tag{24}$$

The kinetic energy distributed across different eddy sizes can be estimated in frequency domain by using wave number, k. $E(k)$ represents the kinetic energy distribution in spectral space which can be shown as Eq.(25). (Davidson, 2004)

$$\frac{1}{2}\overline{u'^2} = \int_0^\infty E(k)dk \tag{25}$$

The connection between the energy spectra and the eddies is summarized in Figure 4. In the production of the turbulence area, two length scales are related as hydraulic diameter and integral length scales. The energy of these scales transferred into smaller scales which is shown as inertial subrange. In the end of the cascade, the Kolmogorov length scale is reached with the dissipation area. (Davidson, 2004)

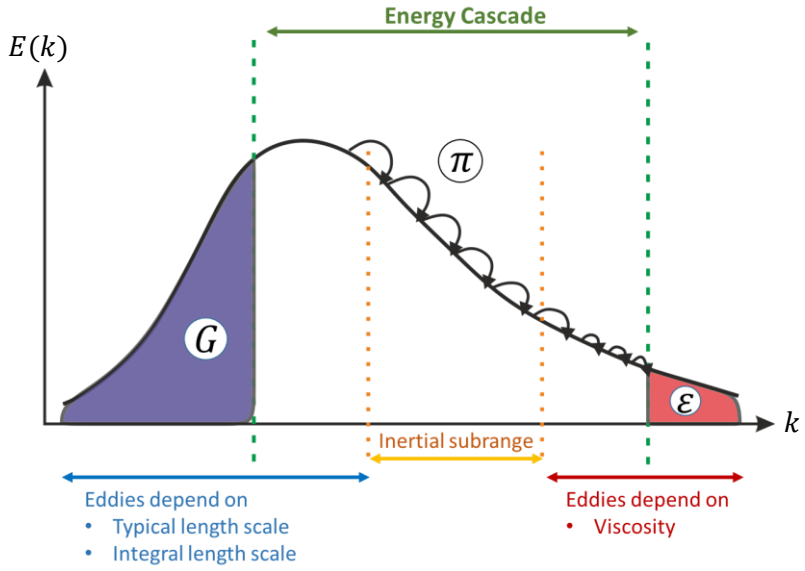

Figure 4: Schematics representation of energy cascade (Davidson, 2004)

From Figure 4 it can be also seen that the large scales have low frequencies where the small scales have high frequencies. In the inertial subrange, according to Kolmogorov's Second Similarity Hypothesis, the statistical properties have a uniform form. This leads to the Kolmogorov's five-thirds law and can be shown in terms of the energy spectrum as Eq. (26). (Davidson, 2004)

$$E(k) = \alpha \varepsilon^{2/3} k^{-5/3} \tag{26}$$

(Saddoughi & Veeravalli, 1994) shows an example of different types of turbulent flows following the five-thirds law.

These different types of turbulent flows includes canonical flows. Some examples of the canonical flows include wall bounded (Tardu, 2014), boundary layer (Schroder, et al., 2008), mixing layer (Dimotakis & Brown, 1976), pipe (Hultmark, et al., 2012), channel (Liu, et al., 2001), cavity (Ozalp, et al., 2010), wake (Lee & Lee, 2008) and jet flows (Abramovich, 1963). All of these flows, follow all the properties of turbulence.

These canonical flows are the basic turbulent flows where more complex turbulent flows can be observed with their own unique characteristics.

The flows in rod bundle have inhomogeneous cross section which can be observed with different local conditions of turbulence and the presence of localized-effects characteristics of external flows. These effects can include the oscillating pattern of vortices in the rod bundles. (Kraus, et al., 2021). Many examples of this phenomena where the oscillating patterns are observed is discussed in Chapter 2.

To characterize the vortex shedding mechanism in rod bundle, Strouhal number, St, is used which can be seen in Eq.(27).

$$St = \frac{f * D}{U_{flow}} \tag{27}$$

In Eq.(27), f represents the shedding frequency of the oscillating patterns and D is the dominant geometry that generates this phenomena. In Navier-Stokes equation, i.e. Eq.(13), this term is represented by the unsteady component of velocity, i.e. $\partial \vec{U}^* / \partial t$.

3.2 Statistical description of flow

3.2.1 Mean flow properties

The directions are indicated as x, y and z.

The velocity vector is noted by $\boldsymbol{U}$ which has three components, i.e. u_x, u_y and u_z.

For the measurements performed in CALIFS only two dimensions are measured as u_y and u_z. u_y is the velocity component on the direction of the flow, U_{flow}, i.e. vertical component.

The velocity magnitude of the 2D field, u, is given by Eq.(28).

$$\|\boldsymbol{U}\| = \sqrt{u_y^2 + u_z^2} \tag{28}$$

3.2.2 Fluctuations and their intensities

The fluctuation component of velocity and pressure, i.e. $\boldsymbol{U}'$and $\boldsymbol{P}'$, at any position can be found by Reynolds decomposition. The instantaneous velocity/pressure is a composition of the mean part and the fluctuation part. (Tennekes & Lumley, 1972) The Reynolds decomposition for fluctuation is defined as Eq.(29) where $\boldsymbol{U}$ and $\boldsymbol{P}$ represent instantaneous velocity and pressure, $\overline{\boldsymbol{U}}$ and $\overline{\boldsymbol{P}}$ represents mean velocity and mean pressure.

$$\begin{aligned} \boldsymbol{U}' &= \boldsymbol{U} - \overline{\boldsymbol{U}} \\ \boldsymbol{P}' &= \boldsymbol{P} - \overline{\boldsymbol{P}} \end{aligned} \tag{29}$$

The local root mean square of the velocity fluctuations is defined as Eq.(30) where each components fluctuation is calculated separately as $\boldsymbol{u}'_y$ and $\boldsymbol{u}'_z$.

$$\boldsymbol{U}'_{RMS} = \sqrt{\overline{\boldsymbol{u}'^2_y + \boldsymbol{u}'^2_z}} \tag{30}$$

The root mean square of the velocity fluctuations represents the intensity of the turbulence.

3.2.3 Structure quantification in the flow

As mentioned earlier, in turbulent flows there are many different size of structures.
For the identification of structure, different methods and criteria can be found in the literature. These methods can be separated in four main parts as, Eulerian non-local, Eulerian local region-type, Eulerian local line-type and Lagrangian vortex identification.
The Eulerian local region-type has advantages such as parallelized computation and instantaneous respond to an evolving unsteady flow. (Epps, 9 - 13 January 2017) Under this category different sub-methods can be found such as $|\omega|$ vorticity magnitude (Saffman, 1993), Q criterion in 2D (Okubo, 1970) (Weiss, 1991) (Rossi, et al., 2012) (Rossi & Doorly, 2013) (Zang, et al., 2013), Δ criterion (Chong, et al., 1990) and Swirling strength criterion (Zhou, et al., 1999) (Berdahl & Thompson, 1993) can be given as some examples.
In this manuscript, Swirling Strength criterion (Lambda-Ci) (Zhou, et al., 1999) is used. For the calculation of this method first velocity gradient tensor is calculated as Eq.(31).

$$D_{ij} = \frac{\partial u_i}{\partial x_j} = \begin{bmatrix} \frac{\partial u}{\partial x} & \frac{\partial u}{\partial y} & \frac{\partial u}{\partial z} \\ \frac{\partial v}{\partial x} & \frac{\partial v}{\partial y} & \frac{\partial v}{\partial z} \\ \frac{\partial w}{\partial x} & \frac{\partial w}{\partial y} & \frac{\partial w}{\partial z} \end{bmatrix} \tag{31}$$

The Swirling Strength correspond to the imaginary part of the complex eigenvalues of velocity gradient and the characteristic equation of velocity gradient, D_c, is defined as Eq.(32) where P_{swirl} , Q_{swirl} and R_{swirl} are the first, second and third invariants of velocity gradient tensor, respectively. (Lindner, et al., 2020)

$$\lambda^3 + \mathrm{P_{swirl}}\lambda^2 + \mathrm{Q_{swirl}}\lambda + \mathrm{R_{swirl}} = 0$$

where,

$$P_{swirl} = -\left(\frac{du}{dx} + \frac{dv}{dy} + \frac{dw}{dz}\right) \tag{32}$$

$$Q_{swirl} = \frac{du}{dx}\frac{dv}{dy} + \frac{dw}{dz}\frac{du}{dx} + \frac{dw}{dz}\frac{du}{dx} - \frac{du}{dy}\frac{dv}{dx} - \frac{du}{dz}\frac{dw}{dx} - \frac{dv}{dz}\frac{dw}{dy}$$

$$R_{swirl} = \det(D_{ij}) = \frac{du}{dx}\left(\frac{dv}{dz}\frac{dw}{dy} - \frac{dv}{dy}\frac{dw}{dz}\right) + \frac{du}{dy}\left(\frac{dv}{dx}\frac{dw}{dz} - \frac{dw}{dx}\frac{dv}{dz}\right) + \frac{du}{dz}\left(\frac{dw}{dx}\frac{dv}{dy} - \frac{dv}{dx}\frac{dw}{dy}\right)$$

To solve the characteristic equation P_{swirl} is taken as 0 for incompressible flow and since the measurements performed in 2D, the z component of velocity and displacement is discarded, i.e. $dw/dz = 0$.

To find the Swirling Strength, Δ criterion is used as calculated in Eq.(33) where the discriminant of Δ> 0 shows the core of the vortex.

$$\Delta = \left(\frac{Q}{3}\right)^3 + \left(\frac{R}{2}\right)^2 \tag{33}$$

The result tensor has one real eigenvalue and a conjugate pair of imaginary eigenvalues when the discriminant is positive. The imaginary part of λ_{ci} of the complex pair of eigenvalue represents the Swirling strength and any value that is greater than 0 shows a vortex. (Lindner, et al., 2020)

$$\beta = \left|\sqrt{|\Delta|} - \frac{D_c}{2}\right| + \left|\sqrt{|\Delta|} + \frac{D_c}{2}\right| \qquad \lambda_{ci} = \frac{\sqrt{3}}{2}\beta \tag{34}$$

CHAPTER 4
EXPERIMENTAL SETUP

4. EXPERIMENTAL SETUP

4.1 MERCURE 400

MERCURE 400 is a water experimental facility supplying different rigs dedicated to the study of turbulent flows within rod bundles. The temperature and the flow rate of the loop can be fully controlled.

4.1.1 General description and geometries

Figure 5 shows the schematics of the experimental loop MERCURE 400. The route of the flow starts from below tranquilization chamber, passes through the test section, upper tranquilization chamber and the free surface water tank, respectively.

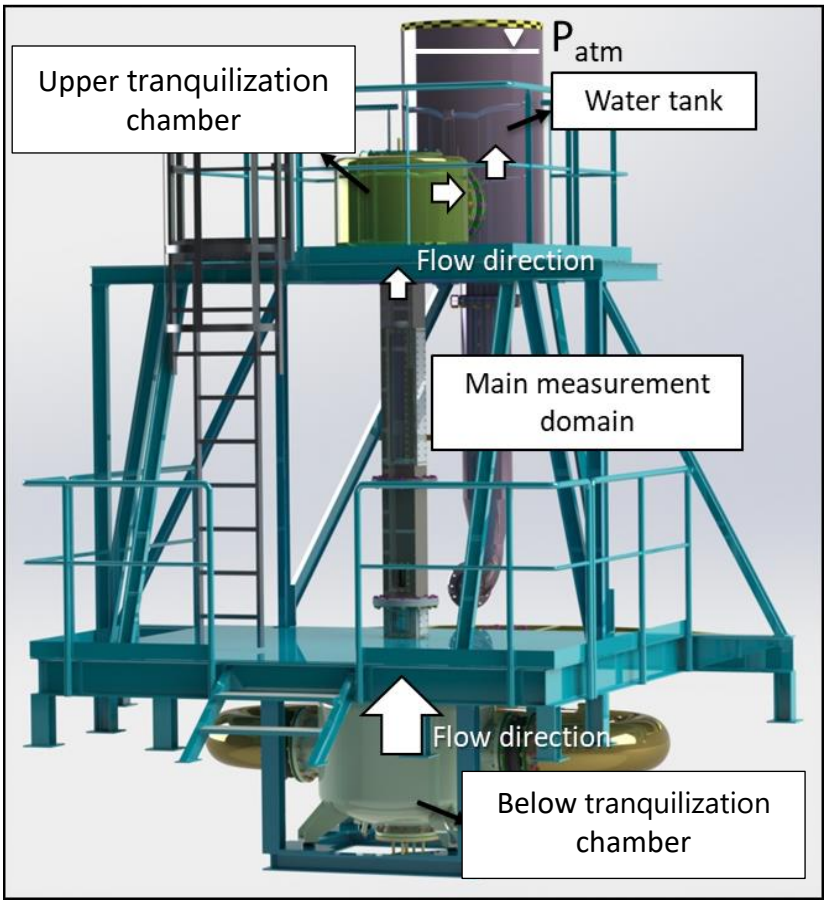

Figure 5: 3D schematics of MERCURE 400

The below and upper plenum are used as the tranquilization chamber for the inlet and the outlet of the test section.

The aim of the below tranquilization chamber is filtering the effects coming from the different geometric singularities of the loop before passing through the test section. Below tranquilization chamber has a diameter of 1200mm with an average height of 900mm. This creates a large difference between the diameter of the below tranquilization chamber and the test section, i.e. 184mmx184mm. This difference in diameter stabilizes the flow since the flow intensity reduces passing through the upstream the test section.

The below tranquilization chamber has an upper rounded shape where the diameters of top and bottom side of the plenum contract from 1200 mm to 270 mm with a height 270 mm. A conical convergent is placed in between the top of the below tranquilization chamber and the test section to further reduce the flow cross section from 270 mm to 184 mm with a height of 50 mm.
The upper tranquilization chamber is being used to reduce the upstream effect of the sudden change of direction in the flow and the regulation of the flow at the outlet of the hydraulic channel.
The test section of MERCURE 400, i.e. CALIFS, can be seen in between the upper and the below tranquilization chamber.

4.1.2 Temperature range

The working range of MERCURE 400 is from 10°C to 55°C which is regulated with a 90kW heat exchanger. The temperature is measured in the below tranquilization chamber with a Pt probe off accuracy ±0.1°C.
Figure 6(a) shows the temperature measurements for different experiments. Figure 6(b) shows the flow temperature fluctuations. The standard deviation is found around 0.25°C.

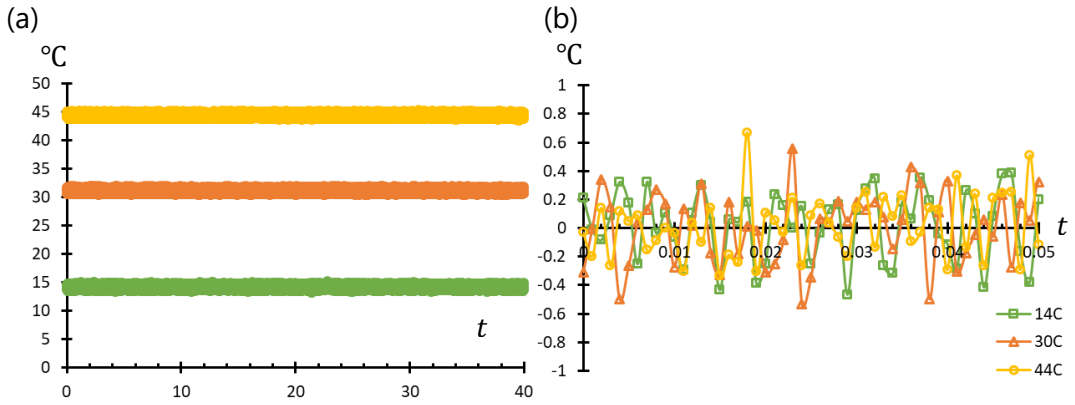

Figure 6: (a) Flow temperature and (b) temperature fluctuations during the measurements for 15℃, 30℃, 45℃

4.1.3 Velocity range

The flow rate inside the MERCURE 400 can be reach up to 400 m3/h which gives the maximum velocity as 5m/s. The flow rate is measured with a 8800D ROSEMOUNT vortex flow meter before the entrance of the test section. The accuracy of the flowrate measurements are ±0.5%.
The flow rate can be controlled via a pump with a variator. The model of the pump is Ingersoll-Dresser CNX 200-150-400. The brand of the variator is SCHNEIDER ELECTRIC Altivar 61 W/E5. For recirculation of the flow, two way can be used in the loop i.e. with bypass and without bypass. Bypass mode creates an extra passage to the flow and supply a slower flow inside the loop.

4.1.4 Pressure range

MERCURE 400 is a low pressurized rig. The loop has a free surface tank which is open to atmospheric pressure.
The loop is equipped with 3051 ROSEMOUNT pressure transducer for static pressure measurements. These pressure transducers are used in their 10–100% range which ensures ± 0.65% accuracy.

4.1.5 Vibration reduction

All of the installation is equipped with rubber and shock mounts for filtering the vibration and pressure fluctuations coming from the pump.

4.1.6 Quality of water

Demineralized water is used inside the loop. The quality of water is also important for the optical measurements, i.e. PIV. To ensure there is no extra particles in the flow, an extra filtration is applied in loop of MERCURE400 before the measurements. After the filtration, this filter is removed. Figure 7(a) shows the position of the filter. Figure 7(b) shows an example result of the filtration.

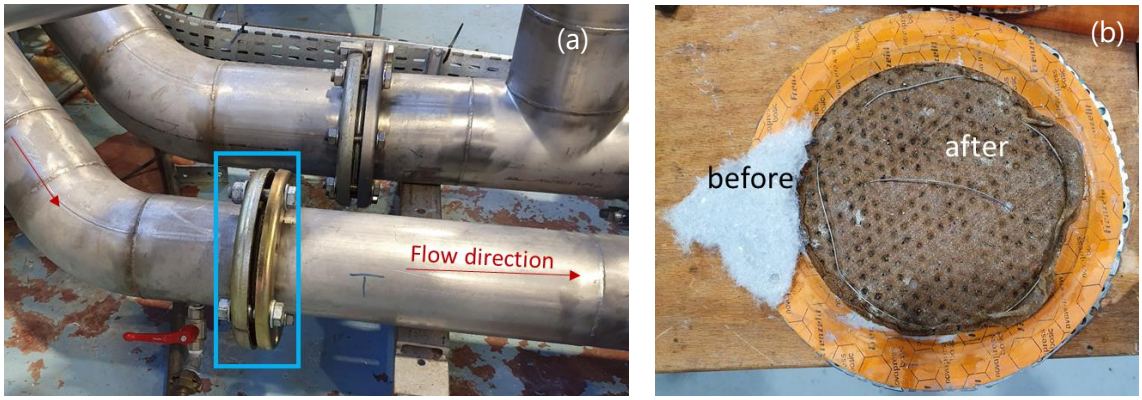

Figure 7: MERCURE 400 filter application (a) the filter position marked as blue rectangle (b) filter used inside MERCURE 400

4.2 CALIFS 5X5

CALIFS 5X5 is the test section that is mounted on MERCURE 400. CALIFS consists a 5x5 rod bundle maintained with analytical spacer-grids. Figure 8(a) shows the photo of CALIFS.

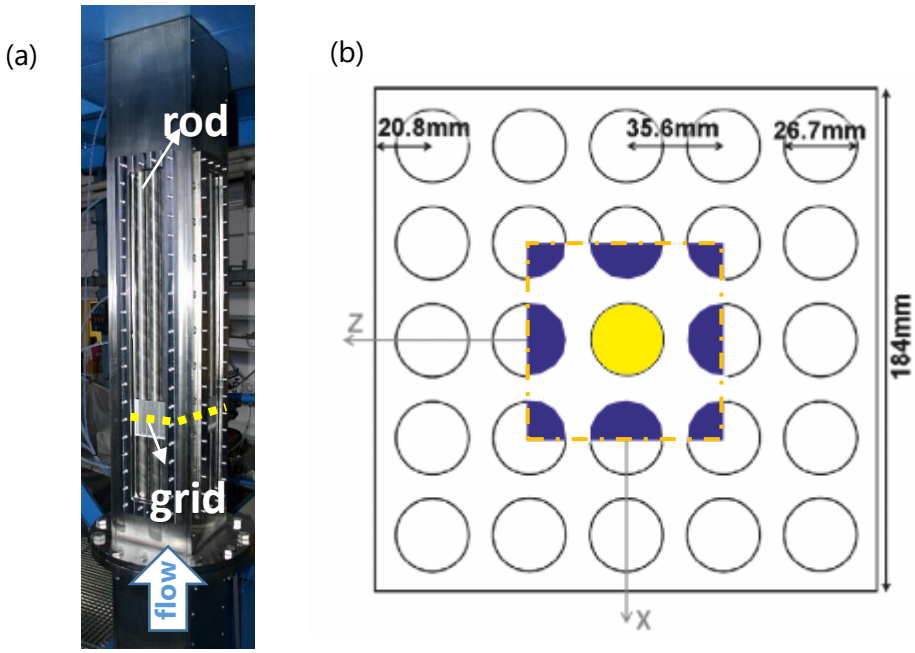

Figure 8: (a) Photo of test section of CALIFS (b) Top view of the rod bundles where yellow circle represents the selected rod and the blue part represents zone minimized from the wall effect

The test section has optical access (Perspex windows) on three sides. The length of the test section is about 2.5m. The flow cross section is a square of 184mm side. Inside the test section, 5x5 rods bundle is installed using identical INOX rods with a diameter (D_{rod}) of 26.7mm. Scale of the rod bundles are found according to ratio of diameter of rods in CALIFS to diameter of real diameter of rods, i.e. 9.5mm (Masterson, 2019). Compared to PWR, the scale of the rods bundle is 2.81, i.e. the diameter of the rods is 2.81 time larger than the PWR fuel rods. The higher scale of the CALIFS facilitate measurements with a higher spatial resolution.

Figure 8(b) shows the top view of CALIFS. The shortest distance is the gap between two rods which is 8.9mm and the Pitch-to-diameter ratio (P/D) is 1.33. The hydraulic diameter, D_h, of CALIFS is 27.7mm. The geometric diameter calculated as $D_g = 1.21D_h$. The yellow circle in Figure 8(b) shows central rod. Around this rod a 3x3 zone is created where the effect of the boundaries are minimized. Therefor the flow around the central rod is representative of the flow in larger arrays.

Inside CALIFS, there is four analytical spacer-grids to maintain the rod bundle. Figure 9(a) shows the positions of these grids which are numbered from 1 to 4. These analytical spacer grids are up-scaled spacer-grids. This design is aimed to reproduce key features of fuel assemblies' grids with a simplified geometry for manufacturing and numerical simulations.

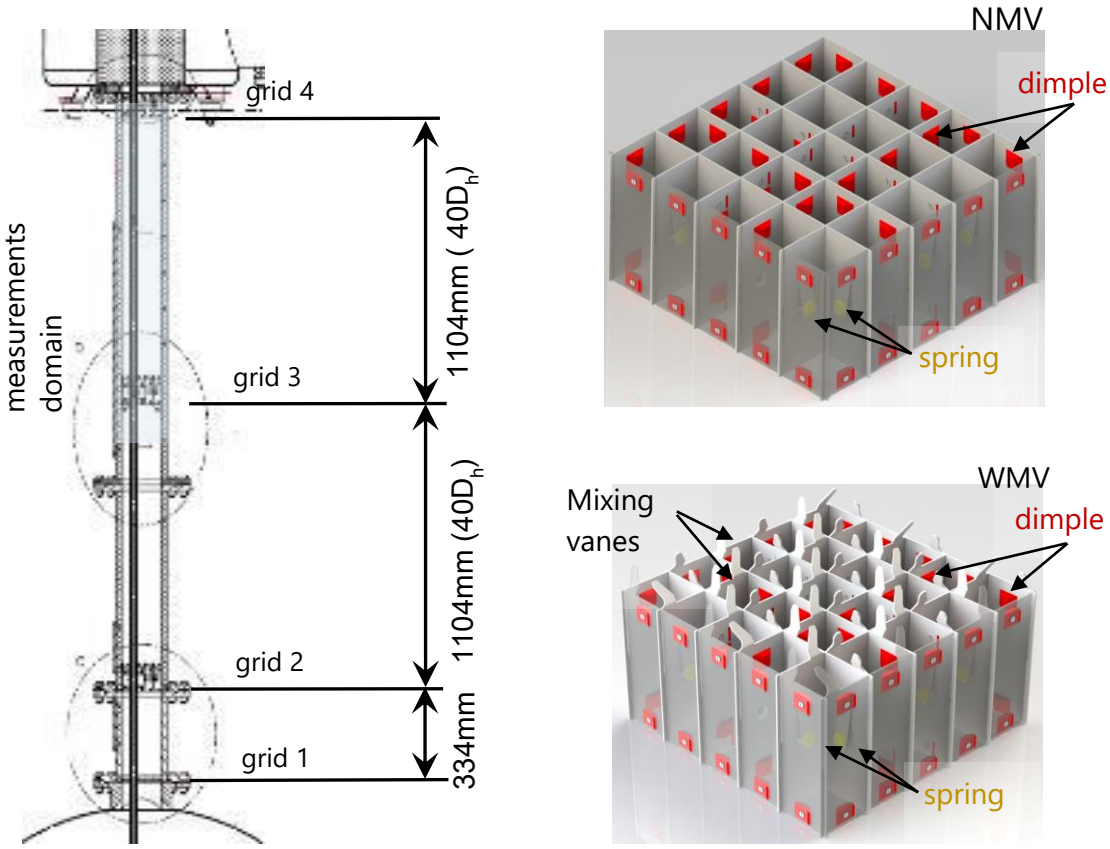

Figure 9: (a)Schematics of test section (b) schematics of grids without mixing vane (NMV) and with mixing vane (WMV)

Different designs of spacer grids can be installed in CALIFS. Figure 9(b) gives the schematics of two analytical grids that are used inside CALIFS as No Mixing Vanes (NMV) and With Mixing Vanes (WMV).

The first and the last level spacer-grids, i.e. $grid_1$ and $grid_4$, are with NMV configuration to maintain the rods and the extremity of the test section. For the second and third level spacer-grids, i.e. $grid_2$ and $grid_3$, NMV or WMV configurations can be installed depending on the study.
Both of the grids are made with 1.2mm thick plates of stainless steel 304L. The height of the plates is 93mm high and 183.6 mm long. They are assembled perpendicularly to design a mesh with 25 cells. Within each cell, the rods are sustained radially using dimples and springs-blades.
Figure 10 shows the details of the dimples and springs. The dimples are made of TEFLON and the dimensions are given in Figure 10(b). The springs-blades are made with 1 mm thick blades of stainless steel 301 T4. For WMV configuration, in addition to dimple and springs, mixing vanes are being used. The mixing vanes have the same material as the grids.

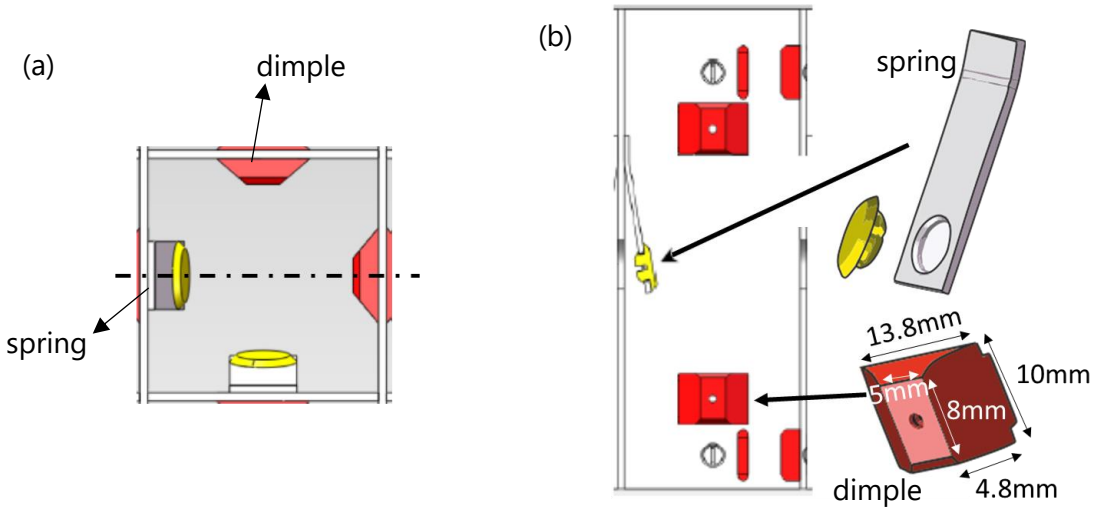

Figure 10: Schematics of dimple and spring (a) top view from one mesh of grid (b) cross-section of Figure 10(a)

To study the effect of the grids and the effects from the rod bundle, the distances are chosen sufficiently long to get the damping of the turbulent wake of the grids (usually observed within $20D_h$). The distance between $grid_2 - grid_3$ and $grid_3 - grid_4$, i.e. $40D_h$, is also sufficiently coherent with the spacing of spacer-grids in PWR, e.g. about $50D_h$ (Masterson, 2019).
The measurements are performed downstream the $grid_3$. Downstream the $grid_3$, the flow has seen one iteration while going through $grid_1 - grid_2$ and its wake before entering the measurement domain. This removes any imperfection might be caused from the tranquilization chamber in the first iteration.

CHAPTER 5
PARTICLE IMAGE VELOCIMETRY

5. PARTICLE IMAGE VELOCIMETRY

5.1 Principles of PIV

Particle Image Velocimetry (PIV) is a non-intrusive measurement technique that captures velocity information of flow fields by using camera, tracer particles and laser.

Different types of PIV can be performed depending on the experimental setup, the equipment, i.e. camera and laser, and the investigated quantities of flow. The types of PIV measurement are 2D2C (planar), 2D3C (stereo), and 3D3C (tomo) PIV. For CALIFS, planar PIV is performed with one laser and one camera.

Figure 11(a) shows the typical planar PIV setup. To measure the velocity field, firstly small tracer particles are added in the flow. After the addition of particles, the selected measurement domain is illuminated with a laser sheet. To isolate the measurement domain, the experimental setup is placed in a dark environment. The dark environment isolates the main light source as laser and avoid other external light sources interfere with the measurement domain. By this step, only the particles that are passing through the laser sheet are became visible.

As the final step, the positions of visible particles are recorded with a camera in intervals of time.

Figure 11(b) shows the processing procedure of the PIV measurements. In the end of the PIV, a series of images are obtained as the results of the measurements.

For the processing of these images, the PIV recording is divided into small subareas called interrogation areas. The detection of the particles are performed by using statistical methods like autocorrelation and cross-correlation. These methods are performed based on the luminosity level of the particle in the interrogation area between two images, i.e. t and $t + dt$. When the same particle is found in both image, the displacement of the particle is measured as pixel between two images. The local flow velocity is then calculated with the time information between the images, dt and the displacement of the particle.

This process of interrogation is repeated for all the areas of the PIV recording and the local velocity is calculated for each subpart of the interrogation areas. As a result of the PIV measurements, these subparts of velocity information generates the velocity field.

This interrogation method gives the opportunity to record images of large parts of the flow field and extract the necessary information out of small areas. (Raffel, et al., 2007)

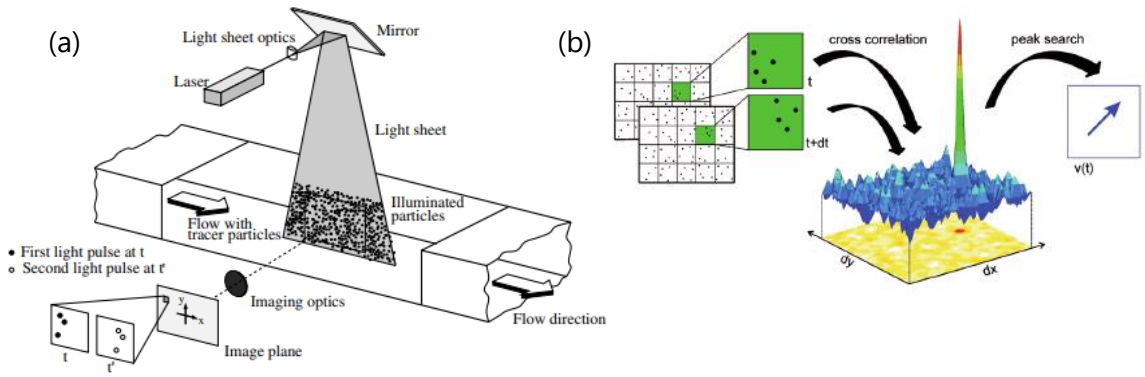

Figure 11: (a)Typical PIV setup (b) processing the PIV data with correlation. (Raffel, et al., 2007)

5.2 Technical factors of PIV

For PIV measurement there are important technical factors needs to taken into account for high quality of results.

5.2.1 Particle selection

PIV is a measuring technique of the flow velocity indirectly by tracing a group of particles inside the fluid. For optimal results of PIV measurement, properties of particles, the distribution of these particles in the fluid and the amount of the particles per image is important.
Different types of particles can be used depending on the fluid and the application. Table 2 shows a summary of the particles according to their type, i.e. solid, liquid or gas particles, with their mean diameter.

Type	Material	Mean diameter in µm
Solid	Fluorescent particles	0.3-100
	Polyamide particles	20-100
	Aluminium flakes	2-7
	Hollow glass spheres	10-100
Liquid	Granules for synthetic coatings	10-500
Gaseous	Different oils	50-500
	Oxygen bubbles	50-1000

Table 2: Types of particles

- **Light scattering properties of particles**

Particles used for PIV measurements have light scattering behaviour. The scattered light power effects the particle image intensity and contrast of the PIV recording. During the light scattering, the light is not blocked by the particle, instead it is being spread in all the direction from the particle. The appearances and origins of light scattering can be various and dependent on the diameter of the medium as well as the wavelength of the incident light beam.
The light scattering behaviours can be classified as general by three major categories such as, Rayleigh scattering, Mie scattering and Tyndall scattering, depending on the ratio of wavelength of light source to the radius of particle. Rayleigh scattering can be characterized where the radius of the particle is 10 times smaller than the wavelength of the medium and Tyndall scattering can be characterized by an almost constant scattering. For Tyndall scattering the radius of the particle is 100 larger than the wavelength which makes the scattering become independent of the wavelength. (He, et al., 2009)
Mie scattering occurs between these two types which is the interest of the PIV measurements. Mie scattering is the function of multiple aspects of environment and the particle. The elements of the function is;

- The ratio of refractive index of the particle and the medium
- The particle size and shape
- Observation angle
- Polarization

Mie theory can be applied to find the intensity of the scatter, , by using Eq.(35). The intensity of the scatter is the ratio between the diameter of the spherical particle, d_p, and the incident light λ.

$$q = \frac{\pi d_p}{\lambda} \tag{35}$$

Figure 12 shows an example behaviour of Mie scattering with two different size of glass particle in the water. The light is coming through the x-axis. The circles represents the intensity of the scatter on the log scale.
In both cases the intensity of the light scatter is increasing from forward to backward scattering with the local maximum as 0° and 180°. It can be also seen that the size of the particle creates different pattern of scatter since the larger size of the particle creates small regions where the intensity is high and low because of the light scatters start to interfere with each other.

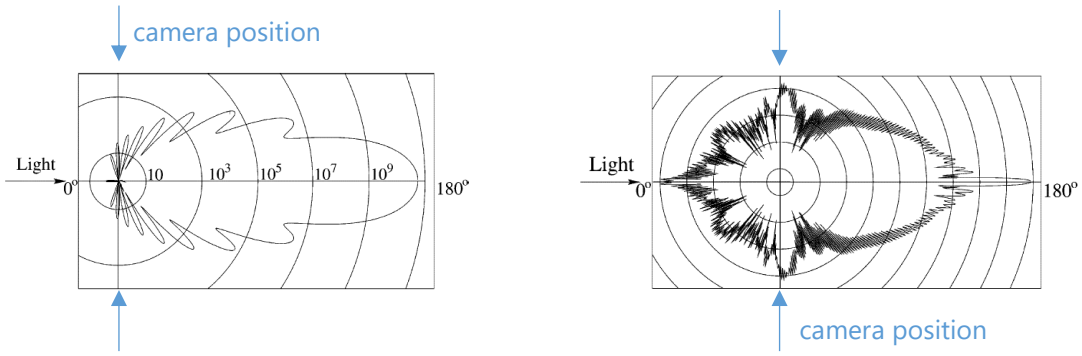

Figure 12: Light scattering with 1 µm glass and 10 µm glass particle in water (Raffel, et al., 2007). The optimum camera positions are marked with blue arrows

The intensity of light scatter can be adjust by the laser, camera and their position. To increase the intensity, right laser power setting needs to be selected. In addition to the laser, extra filter lenses can be added to camera for filtering the light of the laser.
For higher quality PIV measurements, the higher intensity of the light scatter is better. From Figure 12, it can be seen that this point is at 180° where due to limited depth of field, it is not practical to position the laser and the camera in the same line. To have an optimal intensity of light scattering, the recordings are generally performed with 90° from the laser.
Addition to position of camera and laser, the amount of the particles is an important parameter for the light scattering. With a proper amount of particles seeded in the fluid, the recording lens catches the scattering light directly from these particles. In case of high amount of particles, this situation will lead multi-scattering. This means in addition to the direct scattering light, the recording lenses will also catch the light scattered from more than one particle.

- **Density and size properties of particles**

The type of the particles can be selected according to its density and size.
The density of the particle can be selected according to the density of the flow. The primary errors are coming from when the particle has a mismatched density with the fluid because of the influence of gravitational forces. This force yields to an acceleration effect and a time lag between the particle and the fluid flow.
Gravitationally induced velocity depends on the diameter of particle, dynamic viscosity of the fluid and the density difference between the fluid and the particle. In case of a mismatched situation, this gravitationally induced velocity follows an exponential law and if the fluid acceleration is not a constant this leads to complicated equations for particle motion.

The mismatched density can be solved by changing the size of the particle but it is important to have the right balance. The selection of particles can be done according to the relaxation time of the particle. The particles relaxation time, τ_p, can be estimated according to Eq.(36), where ρ_p and ρ_f are respectively the density of the particle and the fluid, $d_p$is the particle diameter. (Tropea, et al., 2007)

$$\tau_p = \frac{\rho_p}{\rho_f}\frac{d_p^2}{18\nu} \tag{36}$$

The relaxation time should be smaller than the recording frequency of the PIV measurements to capture the displacement since it is assumed that the right particles will move with the flow.
For the size of the particle it is important to have a smaller particle size than the measurement size, i.e. interrogation subarea of the PIV results.
Each particle will have some advantages and disadvantages. Smaller size of particles will give a better performance for the tracking of the particle whereas the light scattering behaviour of the particles decreases with the size. On the other hand the large size of particles create the risk of the loss of information in critical areas such as vortex cores, shear layer and boundary layers.
Another method to increase the light scattering behaviour is to increase the density of the particles in the flow. The disadvantage of this method is that it will increase the background noise. With increased light scattering, the luminosity of all the measurement domain will increase. This will lead to the decrease of the contrast between the particles and the background and lower tracking of the particles. For PIV measurements, homogenous distribution of medium amount of particles are observed to give the optimal result. (Raffel, et al., 2007)
For the current study, fluorescent particles are used as tracer particles where the details are going to be discussed in Chapter 5.4.4.

5.2.2 PIV recording method and material selection

There are different pulse and frame code that can be applied for PIV measurements such as single pulse, double pulse and multiple pulse for laser and single frame and multi frame for camera. (Adrian, 1991) In CALIFS two different recording methods are High-speed PIV, i.e. time resolved PIV/multi-frame single pulse, and Low-speed PIV, i.e. dual frame PIV/multi-frame double pulse.
Figure 13 shows the schematics of High-speed PIV and Low-speed PIV, respectively as Figure 13(a) and Figure 13(b).

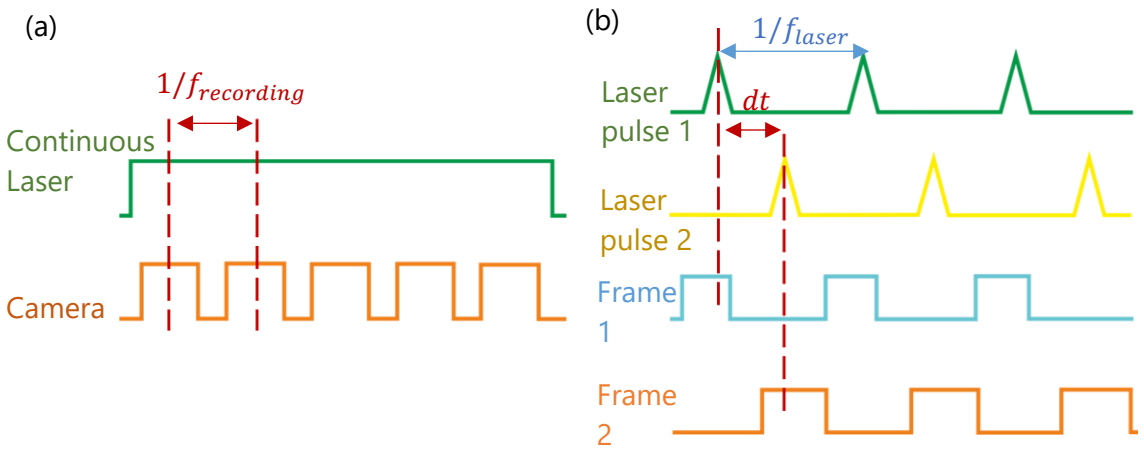

Figure 13: Schematics of (a)High-speed PIV (b)Low-speed PIV

Duration between these pulses, i.e. $f_{recording}$ for High-speed PIV and dt for Low-speed PIV, depends on the displacement of the particles. The time separation between the pulses determines the maximum and the minimum displacement that can be measured. The delay between two pulses has to be long enough to capture displacement on the particles and it has to be short enough to avoid the particles leaving the light sheet between subsequent illuminations. The duration of the light pulses to illuminate the particles has to be short enough to freeze the motion to avoid the effect of blurred images. For image qualities, it is important to configure the right parameters such as frame rates and size of sampling volume.

Frame rate can be single frame which includes several pulses are superimposed on a record or multiple frame where it refers to cinematic film or sequences of video-image frames. Size of sampling volume is connected to the pixels contained in a frame size. (Adrian, 1991)

For High-speed PIV, the frame rate and the frame size are two main parameters that needs to be balanced to have the optimum temporal and spatial resolution of the results. These two parameters have inverse relation. With lower frame size, i.e. reducing the field of view, higher frequency rates can be achieved which lead to higher temporal resolution. Even though higher temporal resolution is important, this situation leads to loss of some information such as velocity measurements of the order of the Kolmogorov scale. (Keane, et al., 1995)

Due to the limitations, the High-speed PIV measurements can be performed with lower flow velocities.

To achieve higher velocity flow measurements, Low-speed PIV measurements are being used. With Low-speed PIV, it is possible to capture the displacement of the particles with very low dt values. Another advantage of the Low-speed PIV is that the size of the frame doesn't depend on the frame rate therefor the measurements can be performed with high spatial resolution.

Even though large spatial resolution of Low-speed PIV is an advantage, this also creates low temporal resolution due to technological restrictions, i.e. limited $1/f_{laser}$ values that depends on the laser properties. (Raffel, et al., 2007)

Additional to the frame rate and frame size, the power of the laser is an important parameter. The optimal power necessary for illumination of the particles depends on the size of the particles. As mentioned earlier, large particles scatter much more light than the small particles so lower peak power of the laser is needed. Increasing the image intensity by using proper particles are more effective and economical than using high power lasers.

5.2.3 Adjustment of Refractive Index Matching

To perform PIV measurements, the optical access to the measurement domain is necessary. In the case where the optical access is blocked by opaque materials, these materials can be changed with transparent materials. By selecting the materials which have closely matching refractive index (RI) values, the errors that are due to optical distortions can be decreased. This technique called refractive-index matching (RIM) (Wright, et al., 2017).

Refractive index, n, can be defined as the ratio of velocity of the electromagnetic wave in vacuum shown as c, to the phase velocity of the same wave in the selected transparent material, shown as v in Eq.(37). (Palik, 1998)

$$n = \frac{c}{v} \tag{37}$$

Every material has its own refractive index value which is also related to the angles (θ) of the incident (i) and refracted (r) rays. The ratio of these angles is a constant for any given pair of media. By using the Snell's law, the angles of incident and refraction can be found as Eq.(38) (Batsanov, et al., 2016)

$$n = \frac{sin(\theta_i)}{sin(\theta_r)} \tag{38}$$

For the light to pass from a medium with higher RI to that with lower RI, if θ_i exceeds the critical angle, θ_c (corresponding to $\sin\theta_r = 1$), the light will be fully reflected back into the high-RI medium. One of the determination way of the refractive index value of a sample, is using a reference prism with precisely known (high) RI and the critical angle. Refractive index values of sample can be calculated by using the known values of prism and the Eq.(39). (Batsanov, et al., 2016)

$$\theta_c \rightarrow sin\theta_r = 1 \rightarrow sin\theta_r = \left(\frac{n_i}{n_r}\right) sin\theta_i \tag{39}$$

There are different techniques than critical angle method to measure the refractive indices of optical materials such as prism method, interferometric technique, immersion method or optical homogeneity. (Batsanov, et al., 2016)

For PIV measurements, it is important to have undisturbed or fully known optical paths of the measurement domain. During the measurements, the optical distortions happen due to the refraction and/or reflection of the light at the interface of two media due to directional change in the light path. This change of path depends on the angle of incidence and the optical speeds in the two transmission media. (Wright, et al., 2017) It had been observed that larger change in the light path occurs due to materials with a different refractive index values. This causes the light bending at the interface of the materials causing distortion or hidden areas. (Dominguez-Ontiveros & Hassan, 2009) For the materials where the light travels from high RI value to low RI, the fully reflected light creates the areas which are optically inaccessible beyond the critical angle. By adapting the Eq.(39) for two different medium, the critical angle can be found as Eq.(40) where $n_1$and $n_2$represents the high and low RI material, respectively. (Wright, et al., 2017)

$$\theta_c = arcsin\left(\frac{n_2}{n_1}\right) \tag{40}$$

There are important points for the selection of the refractive index matched materials for both liquids and solids. Since the change in the material will affect the RI value, the materials should be stable and unreactive to experiments conditions. The liquids should not give any damage to solid materials and both liquids and solids have to stay strong to light sources/lasers. For safety, it is important to have low-toxicity and low-flammability materials. For example the safety of the solid materials decrease greatly after the refractive index value larger than 1.580 (Wright, et al., 2017). For high quality results, the materials should be transparent at all experimental wavelengths. In addition to optical clarity and accuracy, the contact angle of the interaction between solid and liquid is important parameter for the measurements. This angle represents the surface energy between the fluid and the solid phases and it is dependent to the behaviour of the material. Lastly, the low-cost and accessibility should be also considered for the selection of the material.

For the index matching, the first option is to select a liquid/solid according to the solid/liquid material, respectively. Another option is to create a liquid mixture according to the selected solid material. In case of usage of a mixture, density and RI index of mixture can be found with mixing rules shown in the Eq.(41). In these equations, n represents RI, p represents mass fraction, φ represents volume fraction and ρ represents density. (Tasic, et al., 1992) These rules can only applied when there is no volume change during mixing.

Mixing rules

- Lorentz-Lorenz Equation: $\frac{n_{12}^2-1}{(n_{12}^2+2)\rho_{12}} = \left(\frac{n_1^2-1}{n_1^2+2}\right)\frac{p_1}{\rho_1} + \left(\frac{n_2^2-1}{n_2^2+2}\right)\frac{p_2}{\rho_2}$
- Wiener Equation: $\frac{n_{12}^2-n_1^2}{n_{12}^2+2n_1^2} = \varphi_2 \frac{n_2^2-n_1^2}{n_2^2+2n_1^2}$
- Heller Equation: $\frac{n_{12}-n_1}{n_1} = \frac{3}{2}\left(\frac{m^2-1}{m^2+2}\right)\varphi_2,\ m = \frac{n_2}{n_1}$ (41)
- Dale-Gladstone Equation: $n_{12} - 1 = \frac{n_1-1}{\rho_1}p_1 + \frac{n_2-1}{\rho_2}p_2$
- Arago-Biot Equation: $n_{12} = \varphi_1 n_1 + \varphi_2 n_2$
- Lichtenecker Equation: $\ln n_{12} = \varphi_1 \ln n_1 + \varphi_2 \ln n_2$
- Newton Equation: $n_{12}^2 = \varphi_1 n_1^2 + \varphi_2 n_2^2$

The results of these equations can be different from each other and depending on the condition different equations can be used for prediction. The study which was using benzene-cyclohexane, acetone-benzene, and acetone-cyclohexane cases, it has been observed that the Lorentz-Lorenz mixing rule gives the least standard deviation between experimental results and expected results (Tasic, et al., 1992). Another study where 2,2'-thiodiethanol – phosphate-buffered saline – glycerol used as a mixture, Arago-Biot Equation selected as mixing rule. (Zhu, et al., 2016)
Many experiments are performed with different materials for Refractive index method can be found in literature such as (Zhu, et al., 2016) (Aziz & Wong, 2003).
For PIV measurements one of the common material that can be used is FEP. FEP is a hydrophobic fluoropolymer with a RI of 1.338 and has good chemical resistance. FEP isn't fully transparent but translucent at optical wavelengths and by having FEP with thin wall, the quality of the images observed to be efficient. For the RIM methods, FEP used with water because of the close RI value as 1.333 at 20°C. (Bertocchi, et al., 2018)
Different measurements with FEP can be found in literature. The measurement of turbulent flow in rods bundle of smaller size is performed by using FEP rod bundle (Dominguez-Ontiveros & Hassan, 2009) (Qu, et al., 2019) (Conner, et al., 2012) (Hosokawa, et al., 2012).

5.2.4 Calibration

Calibration procedure is necessary to position the camera and laser. In Chapter 5.2.1, the optimal position for the camera and the laser is discussed and according to the scattering properties of the particles, the angle is given as 90° (in possible cases).
The calibration process is performed with calibration grids. The camera is placed accordingly to see the calibration grid clearly and the laser is placed parallel to the calibration plane.
The PIV measurements give the displacement of the particles as pixel. To be able to convert the pixel information to mm, "a pixel to mm" constant is necessary. This conversion constant can be calculated from the grid line on the calibration grid.
The calibration implementation for CALIFS is discussed in Chapter 5.4.1.

5.2.5 Literature review of PIV measurements

Different types PIV measurements for a wide range of applications can be found in the literature.
One of the "old-time method" had been performed by (Sridhar & Katz, 1995) to find the forces applied on a microscopic bubble. For this, triple-exposure imaging, i.e single frame multiple pulse, is applied by one camera so each particle is being exposed three times, i.e. three displacement per particle.
Another method approach is applied by (Jakobsen, et al., 1997) by four-CDD-camera arrangement for fast-time sequences of fluid-flow velocity fields. (Elsinga, et al., 2006) is another example for

Tomographic PIV with four camera setting. The measurements are successfully performed for ring vortex flow and wake flow. (David, et al., 2012) is characterized the tip of the vortex and the leading edge vortex around a flapping wing with Tomographic scanning PIV technique.
(Ganapathisubramani, et al., 2007) is an example for time-resolved stereo PIV where the turbulent shear flows are investigated for the jet flows.
Even though the developments on tomographic PIV or stereo PIV, Planar PIV configurations are still widely being used due to low requirements of equipment and also less complicated applications compared to other PIV techniques.
Many examples can be found in literature regarding the applications of Planar PIV. (Panda, et al., 2017) is one of the examples that is performed for the measurement of vorticities. Another example can be given as (Bigillon, et al., 2006) who applied Planar PIV to investigate the turbulence characteristics of open-channel flow. (Kurtulus, et al., 2007) is performed time-resolved planar PIV for the measurement of wake flow.
PIV is also a popular method for the investigation of flow in rod bundle. Several examples can be given as (Qu, et al., 2019), (Dominguez-Ontiveros & Hassan, 2009), (Lee, et al., 2020) (McClusky, et al., 2002).

5.3 Refractive Index Matching in CALIFS 5x5

The rods inside CALIFS are made from INOX which is an opaque material. For this cause, RIM method is implemented on CALIFS.
For application of RIM, two opaque rods are selected which are creating a barrier for the measurement domain, i.e. central rod. The schematics of the replaced rods can be seen in the Figure 14.

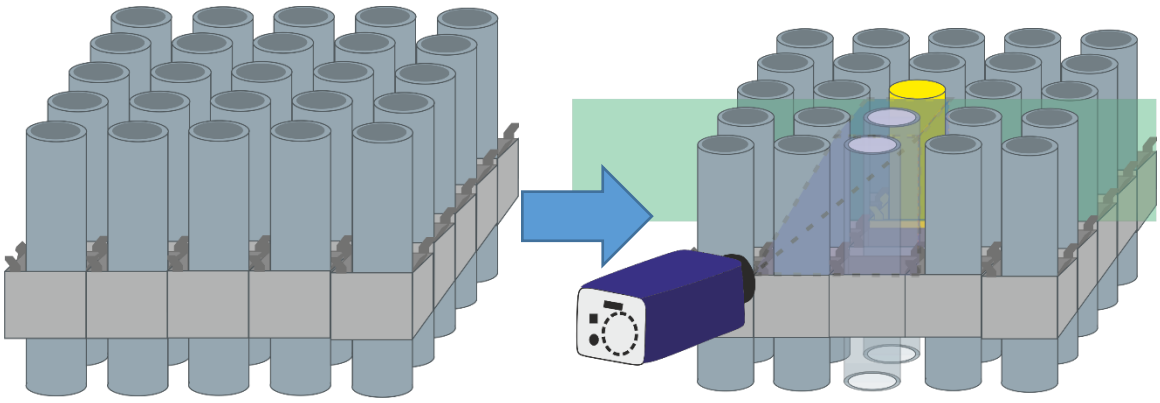

Figure 14: Schematics of RIM application in CALIFS 5x5

In CALIFS experiments, large volumes of fluid is needed to be used. Water is selected as fluid due to its availability, non-toxic and non-corrosive properties.
For solid material, several tests are performed with different materials. Figure 15 shows the preliminary tests, in air (RI: 1.0003) and water (RI: 1.34) for three materials as Fluorinated ethylene propylene (FEP) (RI: 1.34), Perfluoroalkoxy alkanes (PFA) (RI: 1.34) and Plexiglas (RI: 1.5).
Figure 15(a) shows the optical distortion on the mesh due to the difference of RI between the air and the materials. Figure 15(b) shows that with the minimized RI difference between the water and the materials, the optical distortion is minimized on the mesh. Compared to FEP and FPA, Plexiglas still has a difference of RI with water and the effect can be seen on the border of the material. In Figure 15(b), the mesh can be seen clearly with FEP or PFA where the FEP rod is more translucent than the PFA. As a result, FEP is selected for the material to use in CALIFS.

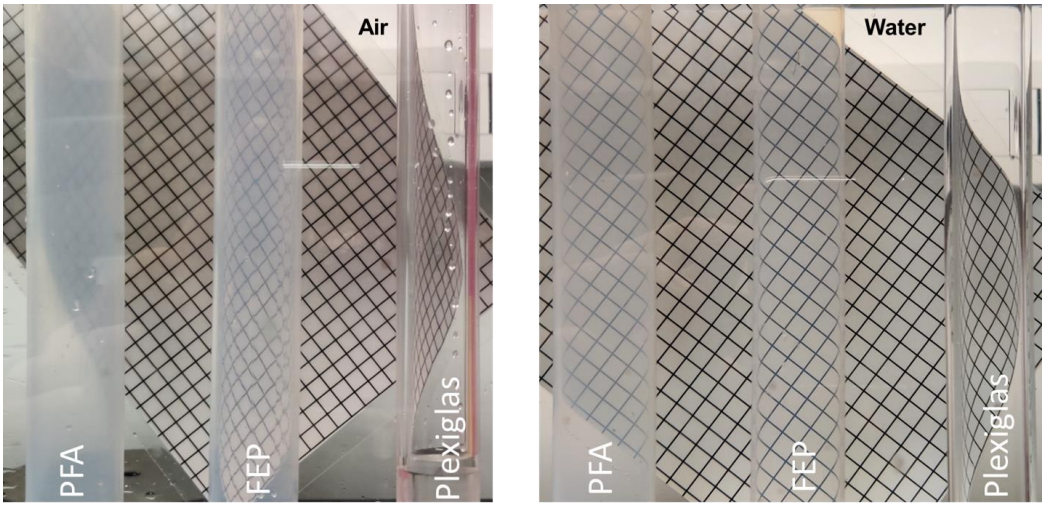

Figure 15: Materials as PFA, FEP and Plexiglas inside the air and water

For the implementation of the rods in CALIFS, two different FEP application is performed. During the first PIV measurements, the selected two INOX rods are modified with FEP parts (75cm length). The upper and lower parts of these rods are left as INOX to ensure the rigidity. During the following experimental campaigns with the high temperatures of the flow, i.e. 55°C, the connection between FEP and the INOX rods are observed to be damaged. To overcome this damage, the modified rods are replaced with 2.5m FEP rods. To ensure the rigidity of experimental setup, the other rods left as INOX as the previous FEP application. The results of PIV are checked for both FEP applications and no difference is observed on the results. In both FEP configurations to diminish the refraction, the FEP parts are filled with water.

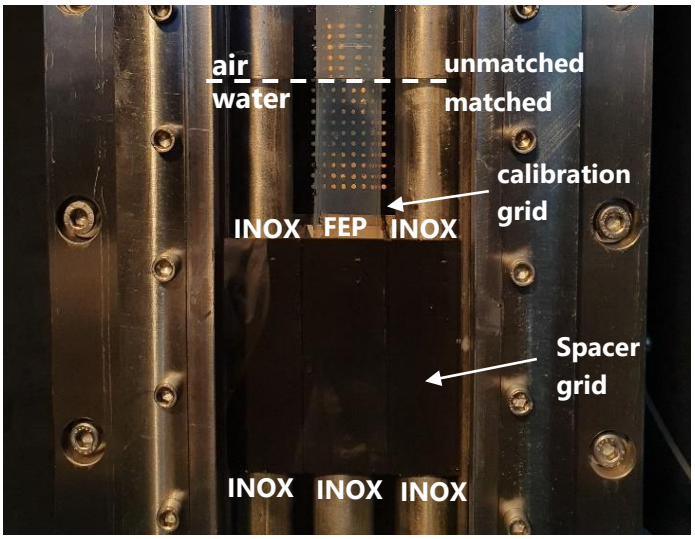

Figure 16: RIM application on CALIFS with modified FEP rods

Figure 16 shows the RIM application with the modified FEP rods. To present the effect of this method the test section is partially filled so water and air. To generate a mesh, a calibration grid is used where the details of the grid is discussed in Chapter 5.4.1. By using "white" LED lighting, the optical visibility of the calibration grid is controlled. From the photo the calibration grid can be seen through two FEP rods clearly visible where the setup is filled with water. For the air part of the setup the optical distortion of the grid can be observed.

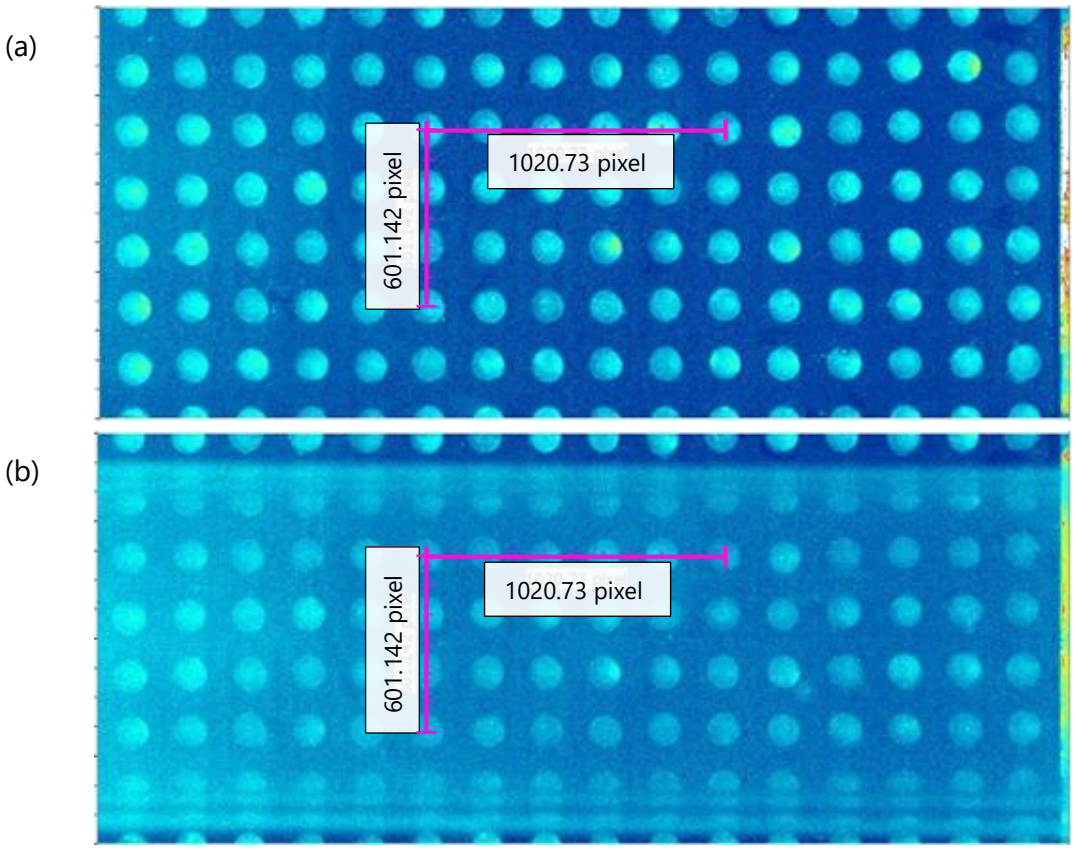

Figure 17: Calibration grid (a) without FEP rods (b) with FEP rods

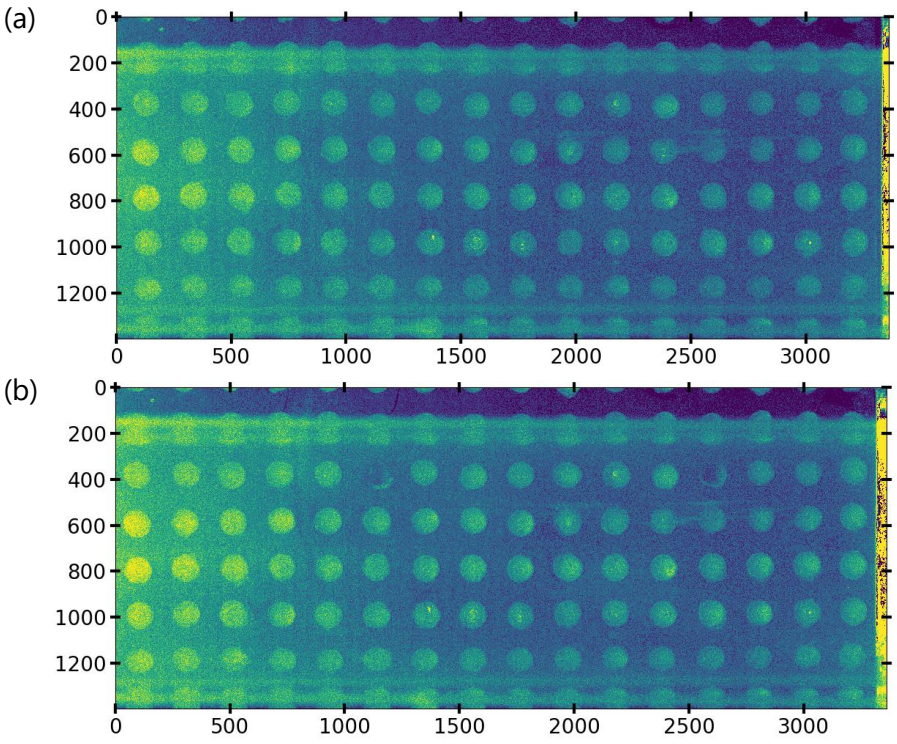

Figure 18: Temperature effect on FEP rods where flow temperature is (a) at 13°C (b) at 55°C

To ensure the FEP rods aren't creating an optical distortion, the calibration grid is used with and without the FEP rods. Figure 17 shows the result for both cases. The middle point of the buttons on the calibration grid are used to calculate any distortion. No pixel difference between the positions of the buttons are observed on the images. This shows there is no optical distortion due to the FEP rod. The PIV measurements are performed with different temperatures. One of the parameters regarding the RI value, is the temperature of the water. The RI is observed to decrease with the increasing temperature. (Waxler & Weir, 1963) To see the amount of optical distortion due to the temperature difference on CALIFS, tests are performed with calibration grid for different temperature, i.e. 13°C, 20.5°C, 26°C, 30°C, 35.5°C, 40°C, 46.5°C, 50°C and 55°C. Figure 18 shows the results for 13°C and 55°C where no optical distortion observed due to temperature change between 13°C-55°C.

5.4 Implementation of PIV in CALIFS 5x5

5.4.1 Calibration Procedure

For the placement of the camera and the laser, calibration procedure is performed with calibration grid. To perform the calibration, two different type of calibration grid are used.
Figure 19(a) shows the first calibration grid build by the 3D printer with a fluorescent compound added to the cartridge. This permits an easier setup using the fluorescence while keeping full safety classes for the laser. The calibration procedure is successfully performed with the first grid where CALIFS is filled with water. During performing the calibration the pump of MERCURE 400 is stopped. During the experiments dedicated to investigate of the temperature effect on the optical quality, the pump is used to reach the desired temperature of the flow where during the calibration procedure this pump is stopped. To stabilize the calibration grid in the flow, the INOX rod is used as a weight. After several days of measurement, some deformations are observed on the calibration grid due to the extra weight.

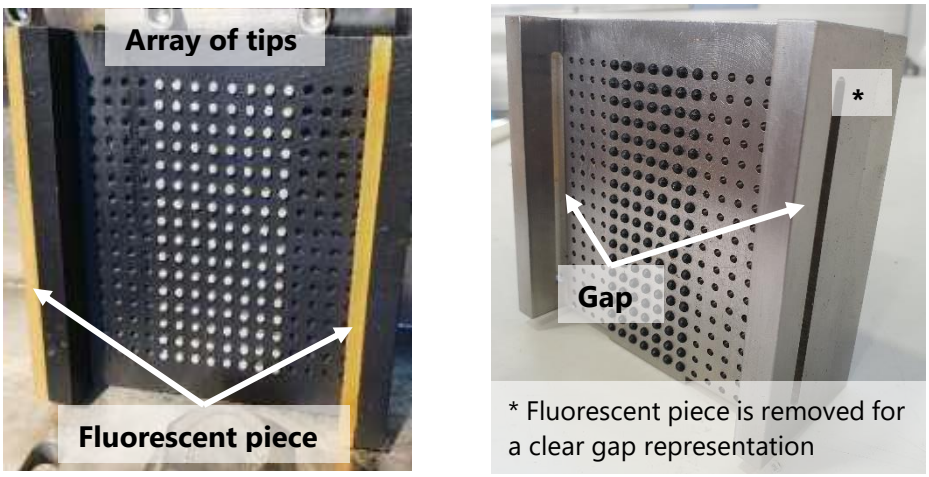

Figure 19: Calibration grids (a) 3D printed (b) Inox

Figure 19(b) shows the calibration grid with INOX which is designed to create more durable calibration grid.
The calibration grids have two rectangular gaps on the side with a fluorescent rectangular piece. This piece is used to position and set the thickness of the laser light sheet. In addition to gaps, a rectangular array, i.e 8x16, of 5mm spaced cylinders with 1mm height is placed on the centre of the calibration grid. These tips are used for a finer adjustment instead of performing calibration with just the gap alone. Additionally the camera is positioned according to these tips.

To perform the calibration procedure, the central rod is removed and placed with the calibration grid. The fluorescent/non-fluorescent tips are positioned at 2mm from the wall of the central rod with an accuracy of ±0.1mm.
Figure 20 shows calibration result for two different configurations, i.e. NMV and WMV configuration. In the figure, orange border shows the measurement domain selected. The measurement domain is selected according to the geometry and the defaults which are due to the borders of the transparent rods.

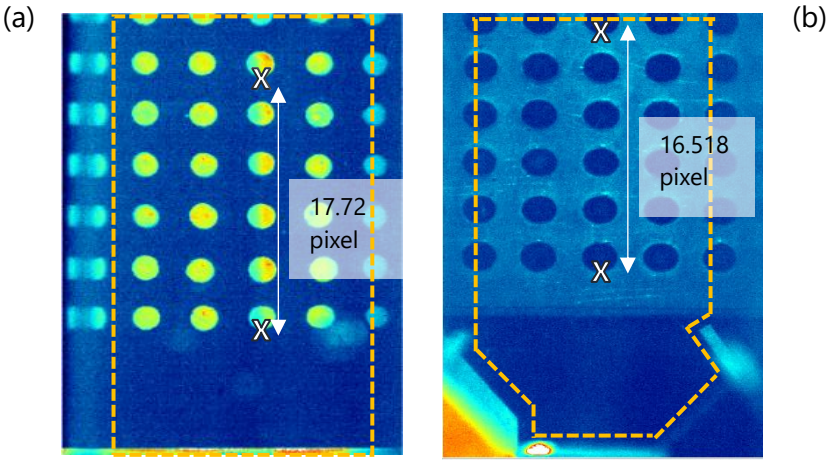

Figure 20: Calibration frame for (a) NMV configuration and (b) WMV configuration

In addition to adjustment of the position of the camera and the laser, the calibration grid also gives the opportunity to calculate the spatial resolution for the calculation of the conversion coefficient from pixel to mm. For the conversion coefficient two of the aligned tips are selected. To achieve the most accurate conversion coefficient, the distance between selected tips are maximized. After the selection of the tips, the coefficient is calculated according to known pixel and mm distance between the tips.
For NMV case, i.e. Figure 20(a), the distance between two "X" is found as 768 pixel which gives the conversion coefficient as 17.72pxl/mm. For WMV configuration, the spatial resolution on Figure 20(b) is found as 16.518 pixel/mm.

5.4.2 Materials and Data Acquisition System for PIV

For the configuration of PIV, two different setup is used, i.e. High-speed PIV and Low-speed PIV. The selection of the method depends on the limitation of the camera and lasers where it is not possible to capture the displacement of particles with High-speed PIV system as mentioned earlier in the Section 5.2.
For the data acquisition of the PIV measurements, LaVision Software DAVIS (version 10.0.5.52200 and version 10.1.2.65556) is used with PTU-X hardware.
PTU-X is a Programmable Timing Unit which creates the connection between the laser, camera and LaVision recording software, i.e. DAVIS (LaVision GmbH, n.d.).

5.4.2.1 High-Speed PIV configuration

- **Recording method:**

For recording the PIV frames, Phantom Miro Lab110, 1280pix x 800pix at 1690Hz, 12bit is used as a high-speed camera. For the laser the 532nm Nd:YAG continuous laser is used which gives the opportunity to perform time resolved PIV.

- **Data acquisition system and recording parameters:**

The PIV recording settings include camera opening, image rate i.e. recording frequency and the field of recording. These settings are selected accordingly for the best condition of the detection of the particles.
The main way to define the recording frequency is the shape of the particles. It is necessary to prevent the presence of elongated particle in the frames. This is achieved by using high recording frequencies. To be able to increase the recording frequencies, the field of the recording can be decreased.
This two settings create the limitation for our measurements. In one case of NMV configuration PIV measurements, the recording frequency is achieved as 5044Hz with field of recording as 768x512pixel. The limit for the U_{flow} is found as 0.9m/s.
The setting of the camera opening depends on the contrast between the particles and the background. This contrast is also depending on the amount of particle injected in the flow. The more particle added will increase the light scattering coming from the particle. This will decrease the contrast between the particles and the background. To change the contrast, the camera opening setting can be used. The higher the camera opening value means higher luminosity.
All of the parameters regarding the recording parameters can be found as tables in Chapter 5.4.6.

5.4.2.2 Low-Speed PIV configuration

- **Recording method:**

For recording the PIV frames, LaVision Imager SX 9M, 3360pix x 2712pix at 18frame/s, 8/12bit is used as dual frame camera. For laser 532nm Nd:YAG pulse laser (200mJ, 15Hz) is used. The displacement of particles are measured by using the pulses of the laser with small time difference, i.e. 60µsec-200µsec.
To be able to minimize the time difference, pulse lasers are using Q-switch device. This device gives the opportunity to store and release the energy rapidly. With the closure of the Q-switch, the laser starts to store the energy by not releasing the photons in the laser cavity. When the maximum power is accumulated, i.e. each 15Hz for Nd:YAG, the gate that hold the photons is opened. This process will lead to a pulse with high energy. According to the time difference defined, i.e. dt, the second pulse will be generated as the same way by using the second cavity of the laser. Even though this gives a high spatial information for high velocities, due to the limitation between each pair of pulses the temporal information is lost.

- **Data acquisition system and recording parameters:**

For Low-speed PIV configuration, the main parameters are the lasers power and the reference time between lasers pulses. Like in High-speed PIV, these parameters are selected according to the best condition for the results.
The power of the lasers effect the light scattering of the particles and the reflections coming from the background. With the increased power due to the illumination of the background, the contrast between the particles and the background starts to decrease. After a certain limit, this will result as low detection of particles and increased errors on the results. After finding the ideal power, the reference time can be selected according to the maximum displacement of the particles. To be in a certain level of uncertainty range, this limit selected as 20 pixel. Before performing the measurements, a reference time is tested for each velocity and the measurements are performed according to the selected reference time information.
All of the parameters regarding the recording parameters can be found as tables in Chapter 5.4.6.

5.4.3 PIV Processing Methods

The displacement is calculated by Davis Version 10.0.5.52200 and version 10.1.2.65556.
For both PIV configuration, an extra mask is applied on the border of the recording. This mask eliminates the uncertainties which will arrive due to the optical distortion connected to the corners of the FEP rods. In case of WMV configuration, this mask is also applied on the mixing vanes. The examples for NMV and WMV masking can be seen in Figure 21.

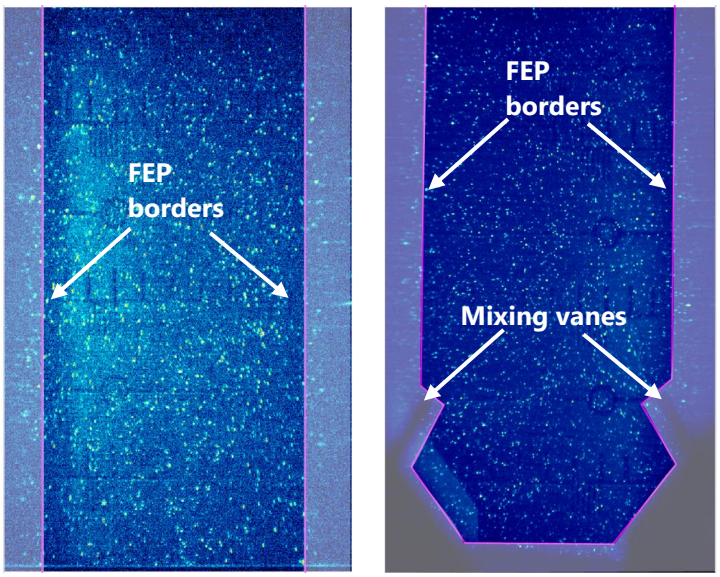

Figure 21: Mask application for NMV and WMV configuration

5.4.3.1 High-speed PIV processing

As mentioned earlier, High-speed PIV recording measure the position of particles according to the recording frequency, $f_{recording}$, i.e. the time difference between each frame defined as $1/f_{recording}$.
The first step of the processing is selection of the frames where the displacement of the particles are going to be searched. The frame coefficient, i.e. k coefficient, represents the sequence of images that is going to be selected. For example, if k is 3, the correlation calculation is performed between the images (n) and (n+3) and the displacement of the particles are calculated between these selected images.
The selection of k coefficient, depends on the velocity of the flow and the measured maximum displacement of the particle. In situation of low flow rate, this value should be big enough to select two frames where the particle will be displaced enough and for high flow rate this value should be selected where the particle can be found on the next selected frame.
For the experiments performed on CALIFS, the maximum displacement is selected around 12-16 pixel and the k coefficient is selected 2-4 depending on the flow rate.
For the calculation of displacement of particles, 2 step of correlation window is used. The initial window size is selected as 64x64 pixel square windows with 50% overlap and then 16x16 pixel square windows with 50% overlap.
The final correlation windows size is 16 pixel, i.e. 0.032Dh and the mesh step of the PIV grid is 0.016Dh.
After the displacement calculation, for High-speed PIV an extra 2nd order polynomial time series filter over 5 time-steps is applied, i.e. smoothing frequencies above 1kHz. The processing is finished by applying a 3x3 spatial smoothing (mobile average) on the filtered data.
In the end of the process, position (x-y) and the velocity components (u_y and u_z) is found.

5.4.3.2 Low-speed PIV processing

Different than High-speed PIV, the time difference between the frames, i.e. dt, is selected while performing the recording. This step generates an automatic pairs of frames for the processing of the Low-speed PIV recording, i.e. no additional step is needed such as selection of k coefficient.
For the calculation of displacement of particles, 2 step of correlation window is used. The initial window size is selected as 64x64 pixel square windows with 50% overlap and then 16x16 pixel square windows with 50% overlap. The final correlation windows size is 16 pixel, i.e. 0.009Dh and the mesh step of the PIV grid is 0.0042Dh.
After the displacement calculation, 3x3 spatial smoothing (mobile average) is applied. No time filter is used since with Low-speed PIV the temporal resolution is lost.
In the end of the process, position (x-y) and the velocity components (u_y and u_z) is found.

5.4.4 Particle selection

The measurements in CALIFS are performed with florescent particles.
The fluorescent firstly absorb the energy from the light source as laser. Because of the absorption, the excitation of some of the electrons in the fluorescent substance, resulting certain electrons raised temporarily to higher orbits. As the excited electrons return to normal positions, the emission of energy happens in the form of photons (light). The emitted (fluoresced) energy nearly always has longer wavelengths and lower frequencies than the absorbed energy because some energy is lost in the process (Stokes' law). (Wilson, et al., 1986) This different absorption and emission spectrum of the fluorescent molecules creates an opportunity to increase the quality of the results by reducing the effect of undesired reflections with filters. (Pedocchi, et al., 2008)
For performing PIV measurements, two different fluorescent particles are used.
The first PIV measurement is performed with polydisperse PMMA-Rhodamine B-Particles. The size of the particles are in range of 1-20µ (mean diameter 10 µ) and the density is 1.18g/cm3.
After the first PIV campaign, the water inside the loop is observed to be contaminated with some metal particles due to external sources. With the laser sheet, an extra reflection is observed from these metal particles which end up with inaccurate PIV results. For the solution, the water inside the loop filtered. The application is shown in Chapter 4.1.6.
After the filtration of the water, monodisperse Vestosint 2070 + Sulforhodamine B particles are decided to be used. The diameter of particles are 10µ with density of 1.19(g/cm3). With the monodisperse particles, it is observed that the detection of displacement of these particles are decreased compared to polydisperse option.
To have an optimal solution, two type of particle is mixed which increased the amount of particles in the flow with 10 µ diameter. In addition to the monodisperse particles, the different size of particles increase the detection of displacement of particles on the PIV processing.
The reaction time of the particle is calculated according to the Eq. (36).
The importance of the response time is, it has to be sufficiently smaller than the duration between the frames of PIV recording. Table 3 shows the calculation of the response time for different particle diameter.

Parameters		High-speed PIV				Low-speed PIV		
Recording frequency (Hz)		5044	5044	3982	3982	15		
k coefficient		2	2	2	2	No k coefficient		
Temperature (°C)		12	55	12	55	12	12	55
Time difference between each frame (µsec)		594.77	594.77	502.26	502.26	500.00	55.00	60.00
	Particle diameter							
Response time(µsec)	1µm	0.05	0.13	0.05	0.13	0.05	0.05	0.13
	20µm	21.23	52.04	21.23	52.04	21.23	21.23	52.04
	10µm (average)	5.31	13.01	5.31	13.01	5.31	5.31	13.01

Table 3: Response time of particles

5.4.5 PIV uncertainties

5.4.5.1 Uncertainties related measurements

The measurements errors and uncertainties combine different aspects, e.g. systematic errors and residual errors.

Systematic errors are mainly the errors that can be reduced or removed by the application of different statistical methods, i.e. improving processing methods. The residual errors are related to measurement uncertainties and can not be reduced or removed with different approaches. The total error related to these groups can be defined as the sum of measurement bias and the random errors. The causes of the measurement bias is connected to the under/over estimation of the displacement vector where the random errors are related to the measurement uncertainties.

Different parameters are contributes to this total errors can be summarized as (Raffel, et al., 2007) :

- Particle diameter in pixel
- Particle displacement between selected frames
- Out-of-plane motion
- Effect of background
- Effect of displacement gradients

For the estimation of these errors, in the current study, the actual PIV recording is used.

In the calculation of uncertainties the effect of the projection, gradient effect and the numerical effects are included.

For the effect of the projection, i.e. the displacement of the particle in laser sheet is introduced by the angle between the camera and the frame. This value is calculated as 0.045 pixel.

For the gradient effect, the "Measurement uncertainty as a function of displacement gradient" plot is used from (Raffel, et al., 2007). This effect is estimated about 0.1 pixel including the both NMV and WMV configuration.

For the numerical effect typical 0.05 pixel is used.

This leads to the σ_{error} about 0.12 pixel. According to the typical maximum displacement the uncertainties are estimated about 3%.

5.4.5.2 Energy filtering of PIV measurements

In Chapter 3, the large scale structures are defined as the responsible of the transportation of momentum, produce and dissipate the turbulent kinetic energy. While processing PIV, the energy of the fluctuations is filtered from scales smaller than the correlation windows, noted as WS.
The relation with the velocity fluctuations and the energy spectra is shown in Eq.(42). (Davidson, 2004)

$$u'_{RMS}{}^2 = \int_0^\infty E(k)dk \tag{42}$$

$E(k)dk$ shows the contribution from all eddies with wave numbers, i.e. k. This relation shows how the energy is distributed across different length scales. By using this relation with length scales, it is possible to estimate the energy that is not represented in the PIV results where the small scales are filtered.
Figure 22 shows the energy spectra taken from PIV measurements in order to show the different energy regions. These regions are marked as A, B, C and D and their separation is selected according to the related length scales.

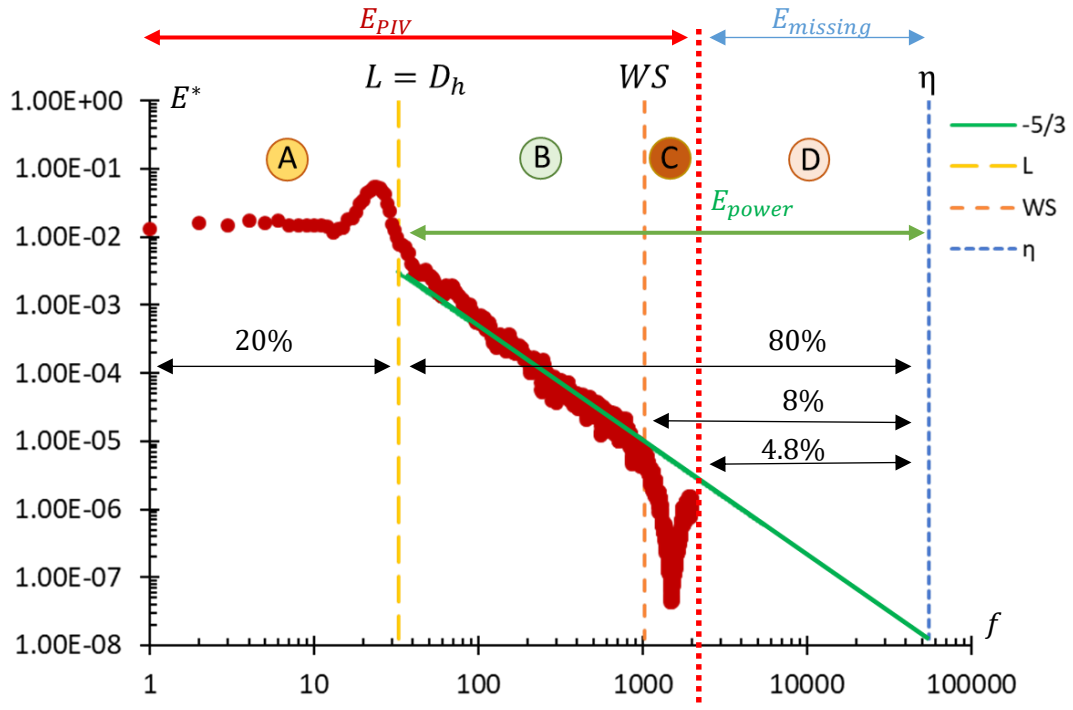

Figure 22: Schematics of energy regions

E_{PIV} shows the sum of the regions A, B and C which corresponds to the energy captured by the PIV measurements.
The region A corresponds to the large scales with high energy levels. The end of this region is selected according to the hydraulic diameter, i.e. reference large scale.
The region B, C and D follow the $-5/3$ power law and the sum of these regions correspond to the E_{power}.
The region B includes the structures larger than the WS which are not subjected to the filtering due to the window selection of PIV.

The region C captures the area between the WS and the cut-off frequency of PIV measurements. The energy of the structures in this region is partially captured, i.e. the PIV processing does not filter the results with 100%.
The region D shows the energy that is not measured with PIV. This region starts from the cut-off frequency which depends on the maximum recording frequency of the PIV measurements. The end of this region is related to the Kolmogorov scale, η.
The region C and D leads to the underestimation of the u'_{RMS}.
Each energy term is calculated according to the related length scales as shown in Eq.(43). In the equation L is defined as the large scale in the flow, i.e. hydraulic diameter and η is the Kolmogorov scale.

$$E_{power} = \int_{\frac{1}{L}}^{\frac{1}{\eta}} k^{-5/3} dk = -\frac{1}{2/3}\left[k^{-2/3}\right]_{1/L}^{1/\eta}$$
$$E_B = \int_{\frac{1}{L}}^{\frac{1}{WS}} k^{-5/3} dk = -\frac{1}{2/3}\left[k^{-2/3}\right]_{1/L}^{1/WS} \quad (43)$$

The Kolmogorov scale is estimated by using the relation between Reynolds number and the largest scale of the flow, i.e. $\eta = L * Re^{-3/4}$. To quantify the region where the ${u'_{RMS}}^2$ is representative, the ratio of E_B/E_{power} is calculated as Eq.(44) which is simplified for large Reynolds numbers.

$$\frac{E_B}{E_{power}} = \frac{\left(\frac{WS}{L}\right)^{2/3} - 1}{Re^{-1/2} - 1} \cong 1 - \left(\frac{WS}{L}\right)^{2/3} \quad (44)$$

With this approximation, while supposing no energy measured beyond WS, PIV measures only 90% of the energy present in the power law domain, i.e. E_B.
With more precision, the energy present in E_A for scales larger than D_h is about 20% of the E_{total}. This demonstrates that PIV measures 92%, i.e. $20 + 0.9 * 80$, of the energy.
The energy measured in the domain filtered by the size of the correlation windows for PIV measurements is about %3.
This means the ${u'_{RMS}}^2$ is underestimated about 6% which should be considered in case of numerical simulations.
This demonstrates that the window size for processing PIV, WS, needs to be much smaller than the reference length scale, L, to be able to measure u'_{RMS} with minimum loss of energy.

5.4.6 Technical details of experimental campaigns: Tables

The PIV measurements are performed for different velocities, temperatures and distances. The measurements are separated according to the PIV technique that is used, i.e. High-speed PIV and Low-speed PIV. Each section has different table according to Single-PIV measurements and PIV+Pressure Simultaneous measurements. The PIV+Pressure Simultaneous measurements are discussed in detail at Chapter 8.

5.4.6.1 High-Speed PIV

In Table 4 the general parameters of PIV measurements are given. The rest of the tables are showing the flow parameters with more detailed PIV parameters.

PIV Properties	Recording rate	Recording length	Particle diameter	Processing Method
NMV - Single PIV	5088Hz	25727 image	1-20μm	Square window 50% overlap initial:64x64 final:16x16
	Exposure time	Duration	Particle name	
	195.60μsec	5sec	Rhodamine B-labeled Poly particles	
	Recording rate	Recording length	Particle diameter	Processing Method
WMV - Single PIV	4000Hz	24809 image	1-20μm	Square window 50% overlap initial:64x64 final:16x16
	Exposure time	Duration	Particle name	
	203.35μsec	6.202sec	monodisperse Vestosint 2070 + Sulforhodamine B particles+Rhodamin	
	Recording rate	Recording length	Particle diameter	Processing Method
NMV - PIV+Pressure	3982Hz	20040 image	1-20μm	Square window 50% overlap initial:64x64 final:16x16
	Exposure time	Duration	Particle name	
	150.49μsec	5.032sec	monodisperse Vestosint 2070 + Sulforhodamine B	
	Recording rate	Recording length	Particle diameter	Processing Method
WMV - PIV+Pressure	4907Hz	24809 image	1-20μm	Square window 50% overlap initial:64x64 final:16x16
	Exposure time	Duration	Particle name	
	202.85μsec	5.055sec	monodisperse Vestosint 2070 + Sulforhodamine B	

Table 4: PIV Properties for "Single PIV measurements" and " PIV+Pressure simultaneous measurements"

Single High-speed PIV Measurement							
Configuration	Domain	Temperature (°C)					
NMV	y/Dh= 0 - 1.4	20	U_{flow}	Re_{Dh}	multi-frame buffer coefficient	Maximum displacement	Pixel to mm
			0.5	13818	3	12pxl	17.72pxl/mm
			0.55	15200	3	12pxl	
			0.6	16582	3	12pxl	
			0.7	19345	3	12pxl	
Configuration	Domain	Temperature (°C)					
WMV	y/Dh= 0 - 1.4	20	U_{flow}	Re_{Dh}	multi-frame buffer coefficient	Maximum displacement	Pixel to mm
			0.5	13818	3	8pxl	16.518pxl/mm
			0.6	16582	3	8pxl	
			0.7	19345	2	8pxl	
			0.8	22109	2	8pxl	

Table 5: "Single PIV measurements" details for NMV and WMV configuration

PIV+Pressure High-speed PIV Simultaneous Measurement										
Configuration	**Domain**	**Temperature (°C)**	**U_{flow} (m/s)**	**Re_{Dh}**	**Sensor Type**	**Angle**	**Pxl to mm**	**multi-frame buffer coefficient**	**Maximum Displacement**	**Duration of sensor recording (sec)**
NMV	y/Dh=0-1.4	12°C	0.5	11209	0.6bar	20°	18.77pxl/mm	3	13-16pxl	80
			0.6	13451				3		
			0.7	15693				2		
			0.8	17935				2		
			0.9	20177				2		
	y/Dh=0-1.4	20°C	0.5	13818	0.6bar	20°	18.77pxl/mm	3		80
			0.6	16582				3		
			0.7	19345				2		
			0.8	22109				2		
			0.9	24872				2		
	y/Dh=0-1.4	37°C	0.5	19876	0.6bar	20°	18.77pxl/mm	3		80
			0.6	23851				3		
			0.7	27826				2		
			0.8	31801				2		
			0.9	35776				2		
	y/Dh=0-1.4	46°C	0.5	23370	0.6bar	20°	18.77pxl/mm	3		80
			0.6	28044				3		
			0.7	32718				2		
			0.8	37392				2		
			0.9	42067				2		
	y/Dh=0-1.4	12°C	0.5	11209	0.6bar	-20°	18.77pxl/mm	3		40
			0.6	13451				3		
			0.7	15693				2		
			0.8	17935				2		
			0.9	20177				2		
	y/Dh=0-1.4	32°C	0.5	17302	0.6bar	20°	18.77pxl/mm	3		40
			0.6	20763				3		
			0.7	24223				2		
			0.8	27684				2		
			0.9	31144				2		
	y/Dh=3-4.4	15°C	0.5	12167	0.6bar	20°	18.86pxl/mm	4	17-18pxl	40
			0.6	14600				4		
			0.7	17033				3		
			0.8	19466				3		
			0.9	21900				3		
	y/Dh=0-1.4	15°C	0.5	12167	0.35bar	20°	18.77pxl/mm	3	13-16pxl	40
			0.6	14600				3		
			0.7	17033				2		
			0.8	19466				2		
			0.9	21900				2		
	y/Dh=2-3.4	25°C	0.5	15532	0.35bar	20°	16.45pxl/mm	3	11-15pxl	40
			0.6	18638				3		
			0.7	21744				3		
			0.8	24851				3		
			0.9	27957				3		

Table 6: "PIV+Pressure" simultaneous measurements details for NMV configuration using High-speed PIV

PIV+Pressure High-speed PIV Simultaneous Measurement										
Configuration	**Domain**	**Temperature (°C)**	**U_{flow} (m/s)**	**Re_{Dh}**	**Sensor Type**	**Angle**	**Pxl to mm**	**multi-frame buffer coefficient**	**Maximum Displacement**	**Duration of sensor recording (sec)**
WMV	y/Dh=0-1.4	12°C	0.5	11209	0.35bar	20°	16.51pxl/mm	3	9-12pxl	40
			0.6	13451				3		
			0.7	15693				3		
			0.8	17935				2		
			0.9	20177				2		
	y/Dh=0-1.4	12°C	0.5	11209	0.35bar	0°	16.51pxl/mm	3		40
			0.6	13451				3		
			0.7	15693				3		
			0.8	17935				2		
			0.9	20177				2		
	y/Dh=1.5-3	12°C	0.5	11209	0.35bar	20°	16.35pxl/mm	4	13-14pxl	40
			0.6	13451				4		
			0.7	15693				3		
			0.8	17935				3		
			0.9	20177				3		
	y/Dh=1.5-3	12°C	0.5	11209	0.35bar	0°	16.35pxl/mm	4		40
			0.6	13451				4		
			0.7	15693				3		
			0.8	17935				3		
			0.9	20177				3		
	y/Dh=3-4.4	12°C	0.5	11209	0.35bar	20°	16.42pxl/mm	4	9-12pxl	40
			0.6	13451				4		
			0.7	15693				3		
			0.8	17935				3		
			0.9	20177				3		
	y/Dh=3-4.4	12°C	0.5	11209	0.35bar	20°	16.35pxl/mm	3		40
			0.6	13451				3		
			0.7	15693				3		
			0.8	17935				3		
			0.9	20177				3		

Table 7: "PIV+Pressure" simultaneous measurements details for WMV configuration using High-speed PIV

5.4.6.2 Low-Speed PIV

The details of Low-speed PIV measurement parameters are given as in the side of the tables. Even the Low-speed PIV measurements are performed for domain $y/D_h = 3-5$, the results didn't included in the manuscript due to measurement errors, i.e. low level of particle, camera issues.

Single Low-speed PIV Measurement										
Configuration	**Domain**	**Temperature (°C)**	**U_{flow}**	**Re_{Dh}**	**dt(µsec)**	**Maximum Displacement**	**Laser 1**	**Laser 2**	**Camera opening**	**Properties**
NMV	y/Dh=0-2.21	12	0.5	11209	280	14	100%	50%	70µsec	**Trigger Rate**
			0.6	13451	250	14	100%	50%	70µsec	14.59Hz
			0.8	17935	200	15	100%	50%	70µsec	**Duration**
			1	22419	150	14	100%	50%	70µsec	342.746sec
			2.4	53805	65	14-15	90%	90%	70µsec	**Recording length**
		20	0.6	16582	200	12	50%	50%	42µsec	5000 image
			0.8	22109	200	14	50%	50%	42µsec	**Pixel to mm**
			1	27636	140	13-14	90%	90%	70µsec	54.67pxl/mm
			1	28652	140	13-14	80%	80%	70µsec	**Particle name**
			1.2	33163	100	12	50%	50%	42µsec	Rhodamine B-labeled
			1.8	49745	70	12	50%	50%	42µsec	Poly particles
			2.4	66327	70	16	50%	50%	42µsec	**Particle diameter**
			2.8	77381	62	14	90%	90%	70µsec	1-20µm
		55	0.6	32511	240	14	80%	80%	70µsec	**Processing Method**
			0.75	40639	190	14	80%	80%	70µsec	Square window 50%
			1	54185	140	14	80%	80%	70µsec	overlap initial:64x64
			1.2	65022	120	13	80%	80%	70µsec	final:16x16
			1.4	75859	95	13	75%	75%	70µsec	
			1.6	86696	90	13	75%	75%	70µsec	
			1.8	97533	80	13	75%	75%	70µsec	
			2	108370	70	13	75%	75%	70µsec	
			2.2	119207	65	13	75%	75%	70µsec	
			2.4	130044	65	14	75%	75%	70µsec	
			2.8	151718	60	14-15	75%	75%	70µsec	
	y/Dh=3-5.21	12	0.5	11209	500	14	80%	100%	70µsec	**Trigger Rate**
			0.6	13451	430	14	80%	100%	70µsec	15Hz
			1	22419	250	13-14	80%	100%	70µsec	**Duration**
		20	0.6	16582	400	14	80%	100%	70µsec	309.33sec
			1	27636	250	13-14	80%	100%	70µsec	**Recording length**
			1.2	33163	200	14	80%	100%	70µsec	5000 image
			1.45	40072	180	14	80%	100%	70µsec	**Pixel to mm**
			1.8	49745	150	14	80%	100%	70µsec	40.45pxl/mm
			2.4	66327	110	13	80%	100%	70µsec	**Particle name**
		55	0.75	40639	350	13-14	80%	100%	70µsec	Rhodamine B-labeled
			1	54185	250	13-14	80%	100%	70µsec	Poly particles
			1.4	75859	185	13-14	80%	100%	70µsec	**Particle diameter**
			1.6	86696	165	13-14	80%	100%	70µsec	1-20µm
			1.8	97533	150	13-14	80%	100%	70µsec	**Processing Method**
			2	108370	148	14-15	80%	100%	70µsec	Square window 50%
			2.2	119207	130	13-14	80%	100%	70µsec	overlap initial:64x64
			2.4	130044	110	13-14	80%	100%	70µsec	final:16x16
			2.8	151718	95	13-14	80%	100%	70µsec	

Table 8: "Single PIV measurements" details for NMV configuration using Low-speed PIV

PIV+Pressure Low-speed PIV Simultaneous Measurement													
Configuration	**Domain**	**Temperature (°C)**	**U_{flow}**	**Re_{Dh}**	**dt(µsec)**	**Sensor Type**	**Angle**	**Pxl to mm**	**Maximum Displacement**	**Laser 1**	**Laser 2**	**Camera opening**	**Properties**
WMV	y/Dh=0-2.21	20°C	0.8	22109	200	0.35 bar	20°	69.97 pxl/mm	20-21pxl	55%	63%	42µsec	**Sensor Recording info**
			1	27636	140					55%	63%	42µsec	
			1.3	35927	100					55%	63%	42µsec	40sec; 10kHz
			1.6	44218	90					55%	63%	42µsec	**Trigger Rate**
			1.9	52508	80					55%	63%	42µsec	9Hz
			2.2	60799	65					55%	63%	42µsec	**Duration**
			2.4	66000	60					64%	80%	42µsec	4.62min
			2.5	69090	60					55%	63%	42µsec	**Recording length**
		40°C	0.8	33626	200					98%	100%	42µsec	2500 image
			1	42033	140					98%	100%	42µsec	**Particle name**
			1.3	54643	100					98%	100%	42µsec	monodisperse
			1.6	67253	90					98%	100%	42µsec	Vestosint 2070 +
			1.9	79863	80					98%	100%	42µsec	Sulforhodamine B
			2.2	92472	65					98%	100%	42µsec	particles+Rhodamin
			2.5	105082	60					98%	100%	42µsec	e B-labeled Poly
			2.8	117692	55					98%	100%	42µsec	particles
	y/Dh=3-5.21	20°C	0.8	22109	200			67.93 pxl/mm	10-11pxl	100%	80%	52µsec	**Particle diameter**
			1	27636	140					100%	80%	52µsec	1-20µm
			1.3	35927	100					100%	80%	52µsec	**Processing Method**
			1.6	44218	90					100%	80%	52µsec	
			1.9	52508	80					100%	80%	52µsec	Square window
			2.2	60799	65					100%	80%	52µsec	50% overlap
			2.4	66000	60					100%	80%	52µsec	initial:64x64
			2.5	69090	60					100%	80%	52µsec	final:16x16
			2.8	77381	55					100%	80%	52µsec	

Table 9 : "PIV+Pressure" simultaneous measurements details for WMV configuration using Low-speed PIV

CHAPTER 6
LASER DOPPLER VELOCIMETRY

6. LASER DOPPLER VELOCIMETRY

LDV is used for point-wise velocity measurements in a volume. The results are non-intrusive, sensitive to direction, have high spatial and temporal resolution, and high accuracy.
The schematics of the performed LDV measurement can be seen in the Figure 23. The system consist of;

- Laser
- Transmitting optics: beam splitter and focusing lens
- Receiving optics: focusing lens, an interference filter and photodetector
- Signal conditioner

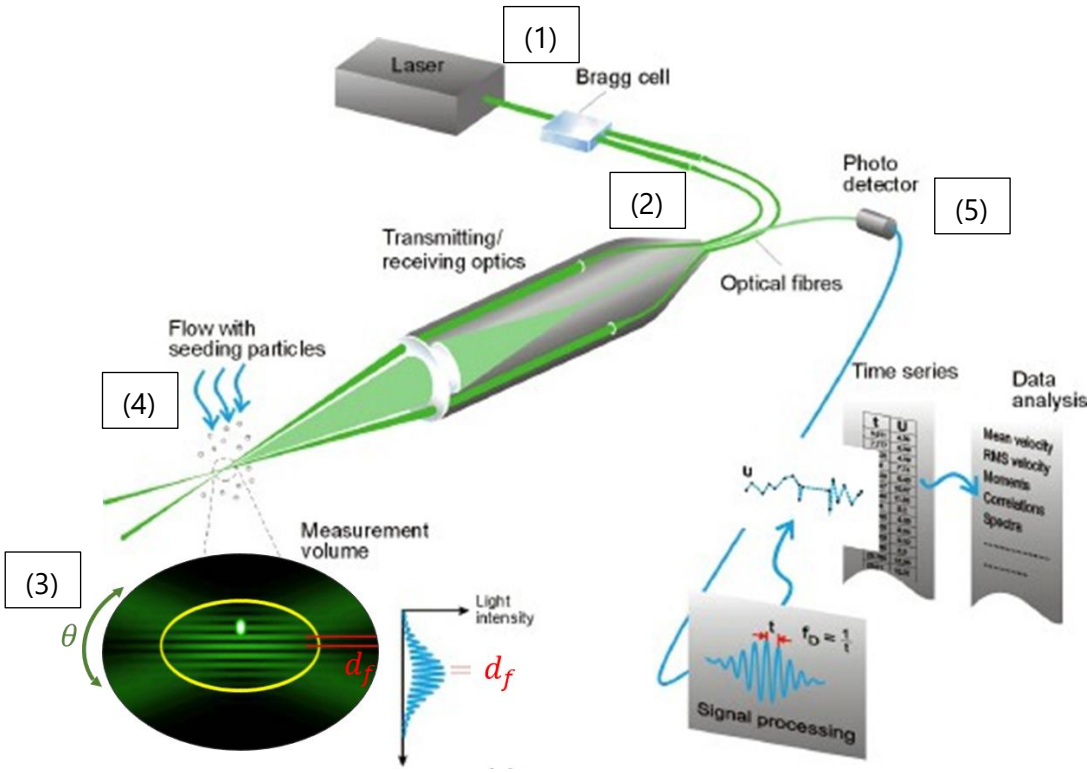

Figure 23: Schematics of LDV measuremens [implemented from DANTEC DYNAMICS]

The measurement steps are marked in Figure 23 according to the processing order.

1. The laser sends a continuous beam to the Bragg cell. This cell is used as a beam splitter. The sent beam divided into two beams with the same intensity but with different frequencies, i.e. f_0 and f_{shift}.
2. By using optical fibers, these beams are sent to probe. Inside the probe, two beams are focused by a lens to intersect in the probe volume.
3. Due to the interference between two laser beams with different frequencies, a fringe pattern is produced. This fringe pattern is the parallel planes of high light intensity. The distance of two parallel plane in fringe pattern, d_f, can be found by Eq.(45) where λ is the laser wavelength and θ is the angle between the two beams.

$$d_f = \frac{\lambda}{2\,sin\left(\frac{\theta}{2}\right)} \tag{45}$$

4. The seeded particles in the flow scatters the light while moving through the measurement volume. The scattered light contains the Doppler frequency, f_D, which is proportional to the velocity component perpendicular to the fringe pattern.
5. This scattered light is collected by a receiver lens and focused on a photo-detector. The velocity information is calculated as Eq.(46).

$$u = \frac{d_f}{1/f_D} \tag{46}$$

The signal generation depends on the parameters of LDV system such as beam diameter, focused beam diameter, beam angle, focal length of optics, fringe spacing and fringe number. The signal generation and the trajectory of the particle influence both the low-frequency and modulated portion of the signal. The ratio of these frequencies are defined as signal-to-noise ratio and the low level of this ratio leads to undetected information. Amplitude of the signal which depends on the particle size, is another effect on this ratio. The smaller particles will result a lower signal amplitude and a low signal-to-noise ratio even though the particles will follow the flow fluctuation more accurately. For the data processing of the LDV measurements, the irregularity of the sampling time and the short-term rate of random particle arrivals should be considered since this might lead to biased results. (Tropea, et al., 2007)
Different methods for LDV can be found in the literature for flow measurements. (Rowe, et al., 1974) is studied turbulent velocity by the performing measurements by two component LDV system. (Carajilescov & Todreas, 1976) and (Bartzis & Todreas, 1979) are performed LDV measurements with the triangular array of bare rod bundles for the investigation of turbulence modelling. (Xiong, et al., 2014) is investigated turbulent flow by performing 3D LDV measurement. (Ikeda & Hoshi, 2006) is performed the measurements with a "rod LDV" contains fiber LDV probe inside the rod which gives the opportunity to perform velocity measurements at different positions without disturbing the flow field.

6.1 Implementation of LDV in CALIFS 5x5

Two experimental campaign is performed for LDV measurements in CALIFS, i.e. LDV-2015 and LDV-2019. Both of the experiments are performed by Thibaud LOHEZ and Fabienne BAZIN. Figure 24 shows the LDV setup on CALIFS.

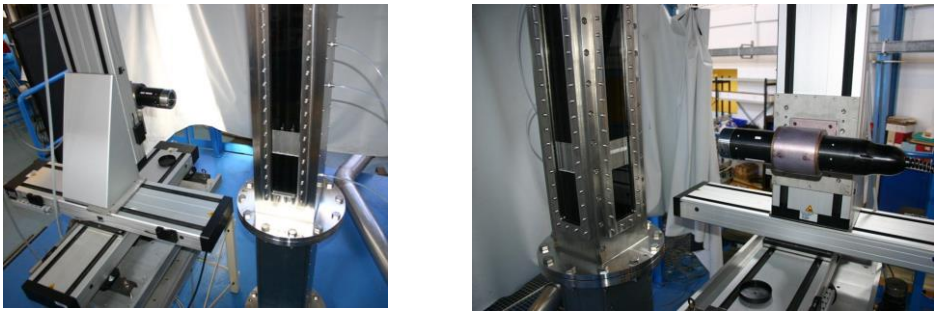

Figure 24 : LDV setup on CALIFS 5x5

For the LDV measurements no RIM method is performed, i.e. the measurements performed with 5x5 INOX rod bundle.

6.1.1 LDV-2015 campaign

LDV measurements are performed around the rod in a square segment. Figure 25 shows the measurement points of the LDV results. The central square shows the perimeter, $\wp_{sq}$, and the measurement lines can be seen for each side of the central square.

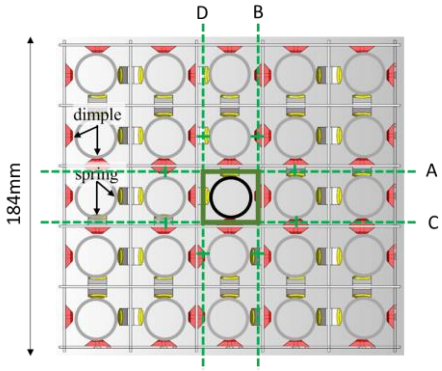

Figure 25: Measurement points for LDV-2015 campaign

The measurements start from 1.33mm away from wall of the CALIFS. The measurements are repeated each 1.33mm up to 175.5mm. Beyond this position, the measurements are observed to be disturb by the reflection of the laser light.
The largest length of the measurement volume is about 0.94 mm.
The particles used for LDV measurements are selected as 4µm NYLON beads of density 1.02g/cm3.
The LDV statistics rely on 10 000 valid events for each measurements points. The durations of recordings vary from 4 s to 30 s. The uncertainty on the position of the measurement volume is about ± 0.5 mm whilst the displacement uncertainty is of the order of 0.01 mm. (Turankok, et al., 2020)
The measurements are performed for both NMV and WMV configuration. The Reynolds number is selected as 66000 for $20°C$.
The measurements are repeated for different longitudinal positions from the grid, i.e. $y/D_h = 1, 2, 3, 4, 5$ and 10.

6.1.2 LDV-2019 campaign

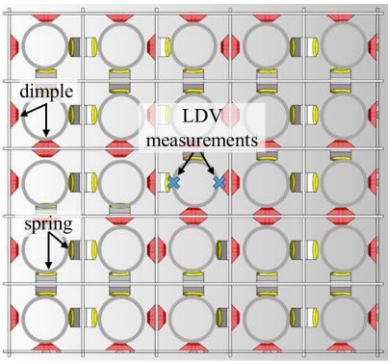

Figure 26: Measurement points for LDV-2019 campaign

Figure 26 shows the measurement points for LDV-2019 campaign.

In LDV-2015 campaign, even though information about velocity fluctuation are obtained, the valid events for each measured points are observed to be not enough for spectral analysis. Due to this reason, LDV measurements are repeated with higher frequency rates for the points of interest, i.e. downstream the dimple and the spring.
With LDV-2019 campaign, 190 000 valid events for each measured points is found which corresponds on average the crossing rate of the particles as 1800Hz.
LDV-2019 measurements are performed for the Reynolds number range from 13 400 to 53 600 for flow temperature of 12°C. The flow velocity, U_{flow}, ranges from 0.6m/s to 2.4m/s.
The grid configuration is selected as WMV configuration. The LDV measurements are performed at 1mm from the central rod. The measurements are repeated for different longitudinal positions from the grid, i.e. $y/D_h = 1, 2, 3, 4, 5$ and 10.

6.2 LDV processing

6.2.1 Mean velocity calculation

The mean velocity field is calculated for each velocity points according to Eq.(47) where u_n represents velocity magnitude per selected point and N represents the total points, i.e. duration of the signal. For each component, $\bar{u}$ is calculated separately as $\overline{u_y}$ and $\overline{u_z}$.

$$\bar{u} = \frac{\sum u_n}{N} \tag{47}$$

6.2.2 Spectral analysis

The sampling of the data taken by LDV depends on the particle passing through the measurement volume. Since these particles are not regularly distributed in the flow, the particles arrival time to the measurement volume is irregular. As a result the sample time of the flow velocity doesn't have a regular time sampling, i.e. the time between each sampled data is different. To be able to process the velocity data, a reconstruction of the sampled signal is needed.
Different reconstruction methods can be found in literature such as Direct Method, Correlation Method, Slotting Technique and Hold-and-Sample Method. (Tummers & Passchier, 1998) For the current case Hold-and-Sample method is used for the reconstruction of the signal. (Tropea, et al., 2007; Herrin & Dutton, 1993) The crossing rate of the particles is 1800Hz which gives enough points to perform the Hold-and-sample method. With the resampled data, the recording frequency is updated as 7500Hz.
For Hold-and-sample method, the velocity information is taken from the current sample until the next particle arrives to the measurement volume. This leads to rectangular shape of signal. After completing the continuous rectangular signal, reconstructed signal is created according to the resampling frequency.
The algorithm can be shown as Eq.(48).

$$\begin{aligned} u_{cont}^{SH}(t) &= u_{particle}(t_i), for\ t_i \le t < t_{i+1} \\ u_{resample}^{SH} &= u_{cont}^{SH}(i\Delta t), for\ i = 0, \dots, N_{R-1} \end{aligned} \tag{48}$$

In the algorithm, t_i shows the time information of the particle which sampled randomly and u_{cont}^{SH} represents the continuous rectangular signal. Δt represents the resampling time step where N_{past} represents total number of sample with the recorded frequency as f_{past}. The resampled frequency value can be found as below.

$$f_{resample} = \frac{N_{past}}{Recording\ duration}, \Delta t = \frac{1}{f_{resample}} \tag{49}$$

Figure 27 shows an example of resampling process.

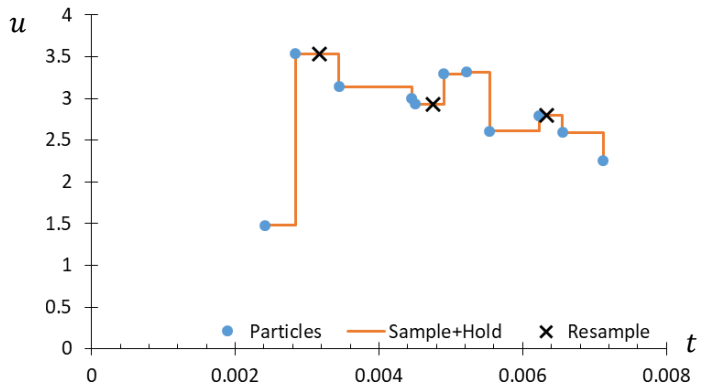

Figure 27 : Resampling process of LDV data

For the processing of the velocity fluctuations, resampled velocity signal is used. Energy spectra are computed over the resample data using 3s duration windows spaced by 1s, i.e. 66% overlap. A mobile average over 7 points (1Hz window) is applied to the spectra. Power spectra are normalised by the total energy.

To ensure the results don't effect with a bias on spectra, the resampling method is also repeated for Slotting technique.

Figure 28 shows a comparison of methods, i.e. slotting method and sample and hold method. Figure 28(a) shows the velocity fluctuations calculated from resampled velocity signal. Figure 28(b) shows the normalized energy spectra. On spectra after 200Hz, a difference in slope is started to observed where the investigated phenomena is focused on the frequency peak. For both method the frequency peak is observed on the same value.

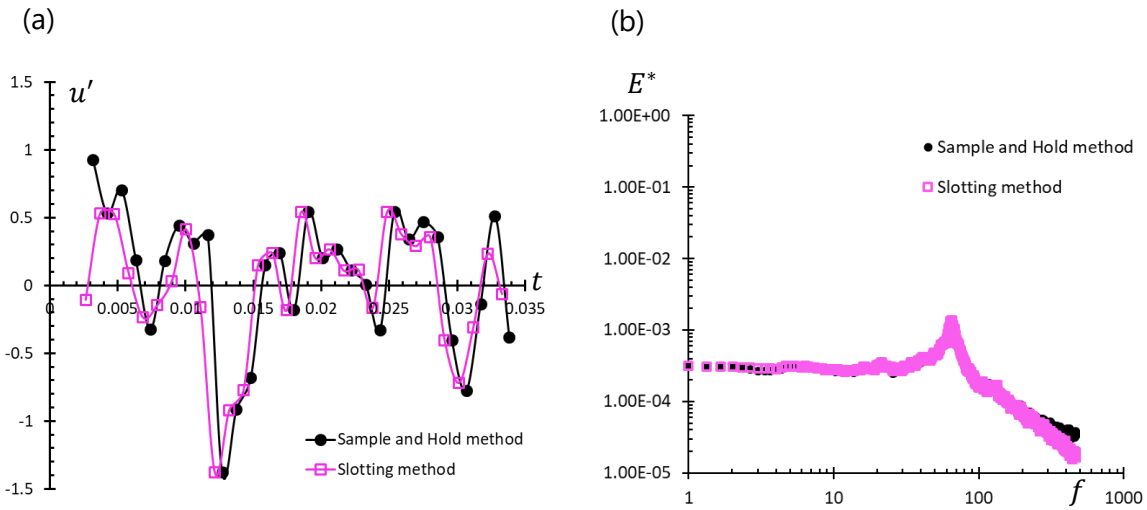

Figure 28: Comparison of LDV processing methods (a) resampled velocity fluctuations (b) normalized energy spectra

CHAPTER 7
PRESSURE MEASUREMENTS

7. PRESSURE MEASUREMENTS

7.1 Pressure and pressure drop measurements

In flows when a geometry change occurs, the pressure rises or fall in response to this area change. This geometry difference leads to sudden pressure changes in the flow. This effect can be quantified with an empirical loss coefficient K. (Masterson, 2020)

$$\Delta P = \frac{1}{2} K \rho u^2 \tag{50}$$

Eq.(50) show the relation between the pressure drop ΔP, where u is the velocity and ρ is density.
In fuel assemblies this geometry change can be observed with the spacer grids, wire-wrap spacers and orifice plates. When the coolant come across with the spacer grids, the area becomes tighter. This leads to increase in coolant acceleration around the spacer grid which creates a pressure drop, i.e. energy loss. Therefor it is important to characterize the losses in the fuel assembly connected to the spacer grids. The total losses connected to spacer grids are the sum of the losses connected to pressure drop, a frictional loss factor due the presence of grid itself and the rod friction for the region where the rods are covered with spacer grids. (Masterson, 2020)
In literature several application with different scaled fuel assembly can be found. (Choi, et al., 2003) is performed pressure drop in a full-scale fuel assembly in liquid metal reactor. (Rehme & Trippe, 1980), is investigated the effect of the spacer grids on the pressure drop results. Pressure drop measurements with different arrangement can be found as (Rehme, 1972; Chang, et al., 2014; Chen, et al., 2018) for hexagonal arrangement, (Chun, et al., 2001) for wire-wrapped fuel assembly and (Bastos & Carajilescov, 2000) for 4x4 rod bundles.
For the pressure drop measurements in 5x5 rod bundles on CALIFS, pressure taps is used with WMV configuration. Figure 29 shows the pressure taps and the pressure sensors which are placed next to the experimental setup CALIFS. The brand of the sensors are ROSEMOUNT- 3051.
There is two type of measurement channel used for pressure drop measurements which are “dPf” and “dPg”. “dPf” represents slow frequency data acquisition where the pressure results are smaller than 62mbar and “dPg” represents fast frequency data acquisition where the pressure results are smaller than 620mbar.

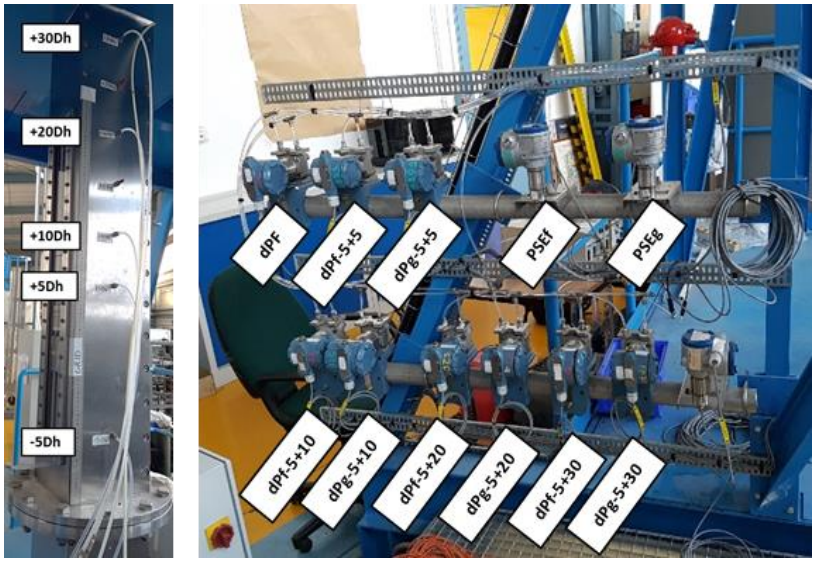

Figure 29: CALIFS pressure drop setup

The measurements are saved by both of the channel. After 62mbar the "dPf" results become saturated, i.e. the measured voltage stabilize at 5Volt. For this reason, for the pressure drop measurements higher than 62mbar, the "dPg" channel is used.
The pressure drop measurements are performed between -5Dh and +30Dh, -5Dh and +20Dh, -5Dh and +10Dh, -5Dh and +5Dh. The measurements repeated for temperatures are 16°C, 18°C, 20°C, 25°C and 37°C with the velocity range from 0.33m/s to 3.22m/s. Re_{Dh} varies from 10000 to 80000.
Figure 30 shows the total loss coefficient for the grid with mixing vanes as:

- For -5Dh and +30Dh $K_{WMV} = 15.90Re_{D_h}^{-0.17}$ with dispersion ±2%
- For -5Dh and +20Dh $K_{WMV} = 13.48Re_{D_h}^{-0.17}$ with dispersion ±2%
- For -5Dh and +10Dh $K_{WMV} = 10.79Re_{D_h}^{-0.15}$ with dispersion ±2%
- For -5Dh and +5Dh $K_{WMV} = 8.97Re_{D_h}^{-0.14}$ with dispersion ±1%

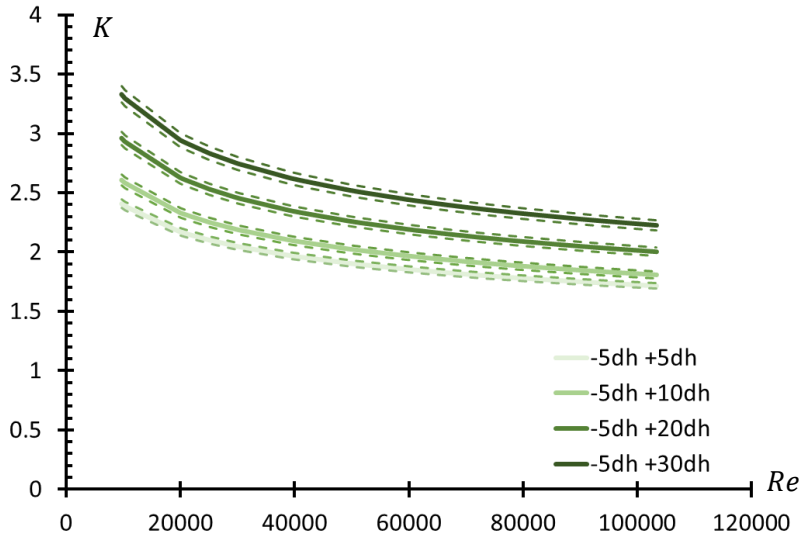

Figure 30: Loss coefficient due to spacer grid for WMV configuration

The pipes connected to pressure sensors have the water with ambient temperature. In the calculation of the pressure drop, the temperature difference between the ambient temperature and the flow temperature isn't taken into account which can be the source of the dispersion.
By using the pressure drop measurement, the Kolmogorov scale, η, of the flow can be estimated by Eq.(51).

$$\begin{aligned} \tau &= \Delta P D_h / 4L \\ u^* &= \sqrt{\tau/\rho} \\ \eta &= \nu/u^* \end{aligned} \tag{51}$$

The friction velocity noted as u^*, and the friction noted as τ. The friction velocity can be estimated by the pressure drop ΔP over a length L of the rods bundle. By using the u^* and the kinematic viscosity, ν, in Figure 31 the Kolmogorov map is built according to the Reynolds number. The relation found as $\eta/D_h = 4.25Re_{D_h}^{-0.86}$ with dispersion ±5%.

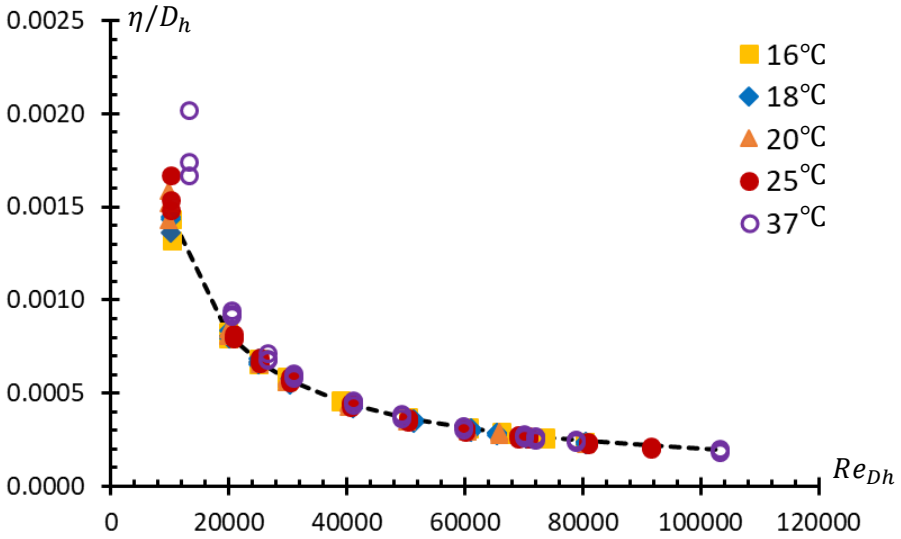

Figure 31: Kolmogorov length scale for different Reynolds numbers

7.2 Pressure fluctuations measurement

7.2.1 Measurement principle of piezoresistive sensors

Measurement principle of the piezoresistive sensors is based on mechanical load deforming the sensor structure. In silicon sensors the deformation is transduced into a resistance change and this change is converted to a voltage signal using a measurement circuit. Typically for circuits, which are attached to the metal diaphragm, the transducers are using fully active four semiconductor strain gauges.

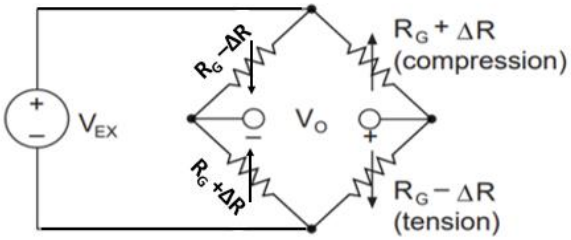

Figure 32: Illustration of Wheastone bridge with fully active 4

These gauges were employed, two at the diaphragm center and two at the edge, allowing configuration into a four active arm Wheatsone bridge with a silicone membrane on top of the metal diaphragm. (Doll & Pruitt, 2013) The principle of the fully active four arm can be found in the Figure 32. V_{EX} represents the voltage applied to the bridge, V_O represents the output voltage that is measured, R_G represents the strain gauge and ΔR respresents the difference of resistance applied on the strain.

The change in resistance is proportional to the stress which is proportional to the pressure difference applied between the pressure sensor and its inner membrane. This measurement which is recorded as voltage can be converted to pressure by using the Eq.(52).

$$\frac{V_{out}}{V_{EX}} \sim K_p * P_{flow} \tag{52}$$

P_{flow} is pressure and K_p is the pressure coefficient that depends on the transducer, amplifiers and the temperature. For the determination of K_p calibration procedure is performed.

7.2.2 Calibration of pressure sensors

To determine the coefficient K_p , the calibration of the sensors are performed in two different method as static and dynamic calibration.
For static calibration, the pressure measurements are performed with flow at rest where the distance between the sensors and the water level is varying.
For dynamic calibration, the calibration measurements are performed with minimum flow rate of CALIFS and the sensors heights are changed with a manual mechanism.

7.2.2.1 Static Calibration

Eq. (53) shows the equation that is used for determining the calibration coefficient with static calibration. K_p is the calibration coefficient, $\vartheta = V_{out}/V_{EX}$ is the measured voltage, ϑ_{ref} is the voltage for a given height of water level, i.e. sensor is installed as the same level of water.
CALIFS has free surface tank therefore the difference of $P - P_{ref}$ is defined by the height difference, i.e. $h = P/\rho g$, of the sensor level and the water level.

$$P - P_{ref} = K_p(\vartheta - \vartheta_{ref}) \tag{53}$$

After finding the ϑ_{ref} value, different voltage values are measured for different water level by increasing the water amount in the test section while the sensor stays at the same height. Figure 33 shows an example calibration curve for different sensors by using the multisensor device. The slope of each curve gives the calibration coefficient K_p for each sensor where the signals recorded simultaneously.

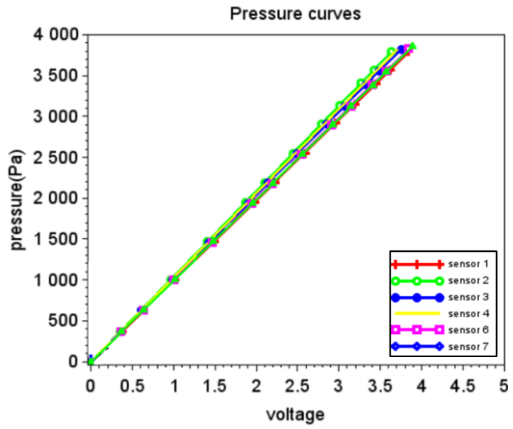

Calibration coefficient	
sensor 1	986.52
sensor 2	1043.92
sensor 3	1019.36
sensor 4	1030.33
sensor 6	995.91
sensor 7	992.34

Figure 33: Example of calibration curves for different sensor with calibration coefficient K_p

During the static calibration, the stability problem is observed on the measured voltage values. This variation is connected to various effects such as variations on temperature of the flow, small variations on voltage source and environmental noises. To decrease this effect, dynamic calibrations are performed.

7.2.2.2 Dynamic Calibration

Dynamic calibration is performed with the flow where the sensors height is changed by using a manual mechanism from the top of CALIFS.
The velocity of the flow is selected as minimum as possible, i.e. $\sim 0.3 m/s$, by using the bypass function of the pump. The distance of the measurement points are selected accordingly to minimize the pressure drop in CALIFS.

$$P - P_{ref} = K_p\left(\vartheta - \vartheta_{ref}\right) + \Delta P \tag{54}$$

Eq. (54) shows the calibration equation including the pressure drop, ΔP, parameter due to the movement of the sensor in the flow. The calculation of the ΔP is discussed in Chapter 7.1.
Figure 34 shows an example result of dynamic calibration where the velocity is $0.28 m/s$ for temperature 33°C.

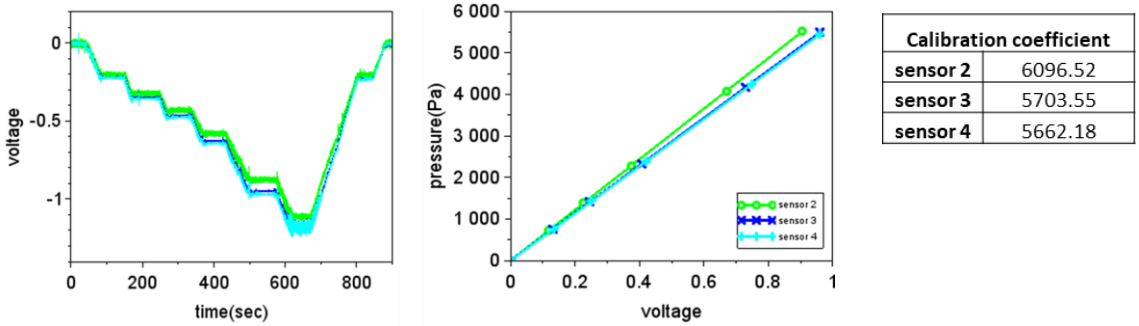

Calibration coefficient	
sensor 2	6096.52
sensor 3	5703.55
sensor 4	5662.18

Figure 34: Example of dynamic calibration curves for different sensor with calibration coefficient $\boldsymbol{K_p}$

7.2.3 Pressure measurement campaigns

Figure 35 shows schematics of the evolutions and modifications that are performed on the pressure measurement devices.

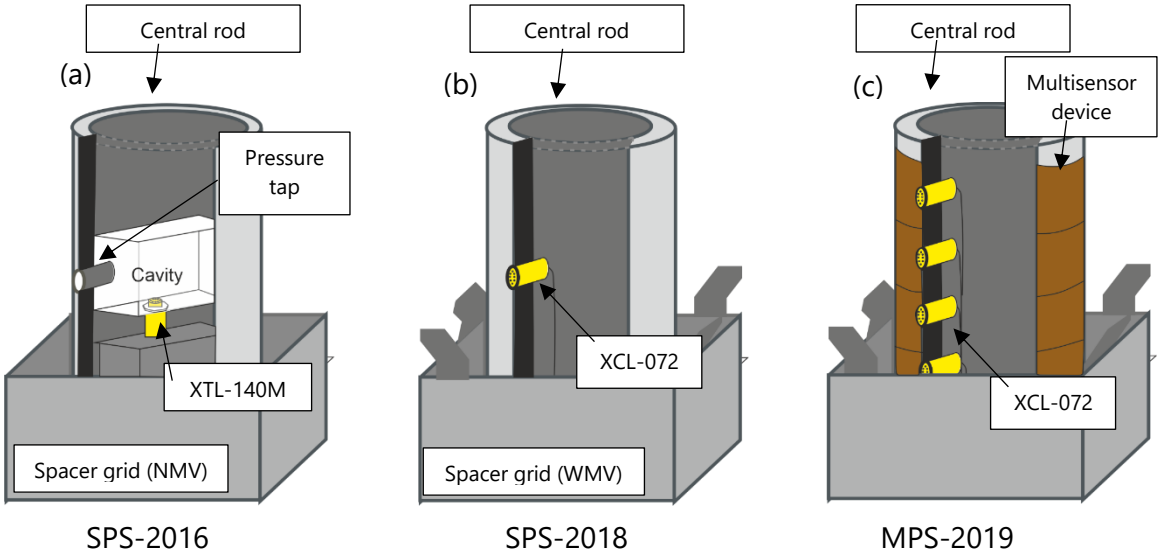

Figure 35: Modifications performed on pressure measurement techniques

The chronological order of the measurements are performed with pressure sensors are given as below.

1. SPS-2016: The measurements are performed with piezoresistive sensor KULITE XTL-140M for NMV configuration. Schematic is shown in Figure 35(a)
2. SPS-2018: The sensor is switched for more sensible type of model which is KULITE XCL-072 for WMV configuration. Schematic is shown in Figure 35(b).
3. MPS-2019/2020/2021: A new multi-sensor device is developed which permits for the installation of multiple sensors. Measurements performed for both NMV and WMV. Schematic is shown in Figure 35(c).

Data sheets of sensors can be found in Appendix.

7.2.4 Single pressure sensor measurements in CALIFS 5x5

To investigate the pressure around the central rod, single pressure sensor measurements are performed in CALIFS 5x5. These measurements are performed by Fabrice MORENO, Thibaud LOHEZ and Fabienne BAZIN during the years 2016-2018.

Single sensor pressure measurements are performed in two measurement campaign as SPS-2016 and SPS-2018.

7.2.4.1 SPS-2016 measurement configuration

Figure 36 shows the detailed schematics of SPS-2016 campaign. The central rod is modified with a cavity within the rod. This cavity is connected to the flow with a 2 mm diameter hole pressure tap on the surface of the rod. The sensor is mounted on the cavity. To be able to measure the pressure without any perturbation, the cavity is filled with a mixture of alcohol and deaerated water. The uncertainties are connected to calibration and the transfer function is found around 10%. (Moreno, et al., 2016) The measurements are performed for the NMV configuration.

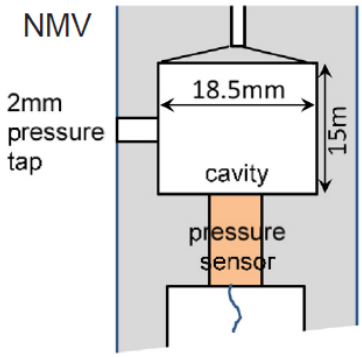

Figure 36: SPS-2016 configuration with NMV configuration

7.2.4.2 SPS-2018 measurement configuration

For SPS-2018 campaign new sensor is selected as KULITE XCL-072 with working limit 0.6 BarG, and a diameter of 1.9 mm. For the installation of the sensor new modifications are performed on the rod. Instead of measuring pressure from the cavity, the sensor directly installed inside the rod where the surface of the sensor is flushed to the flow. The measurements are performed for WMV configuration where the detailed schematics can be seen in Figure 37. The uncertainties of the pressure sensors are 4 Pa or 8% whichever is the higher.

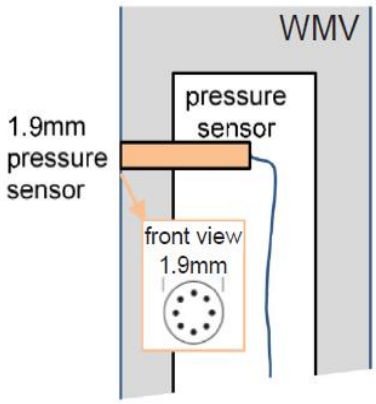

Figure 37: SPS-2018 configuration with WMV configuration

7.2.4.3 Data acquisition system

The pressure sensors are connected to the signal conditioner amplifier. The amplifier are used to supply DC voltage to the sensors and receive the output signal from sensors as voltage. The output signal is then sent to filter and by data acquisition system the filtered signal is transferred to the computer. Table 10 shows the materials that is used for the data acquisition of the pressure signals.

Power Supplier	Convergie CLES 30-3
Signal Conditioning Amplifier	VISHAY 2210B
Filter	KEMO BenchMaster 8
Bus	National Instruments NI PXI-1036 with NI PXI-6225

Table 10: Data acquisition system for years 2016-2019

For the recording of the signal, a software developed by CEA, i.e. TRIDENT is used.
Figure 38 shows the experimental platform used for the measurements.

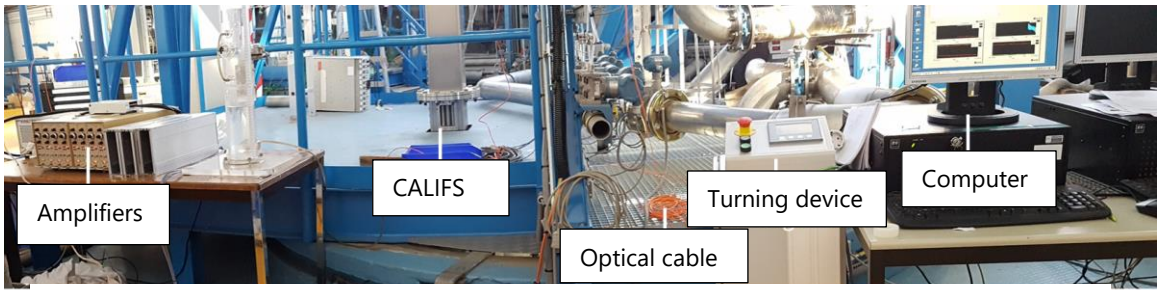

Figure 38: Recording devices for SPS-2016 and SPS-2018

Each local pressure measurement is performed during 20 s at 1600 Hz using a 400 Hz low pass analogue filter which filters the 500 Hz (low level) noise issued from the electrical regulation of the rotation speed of the pump.

7.2.5 Multisensor device pressure measurements in CALIFS 5x5

7.2.5.1 Description of multisensor device

To be able to investigate the transport of pressure fluctuations a new multi-sensor device is developed which can be seen in Figure 39.

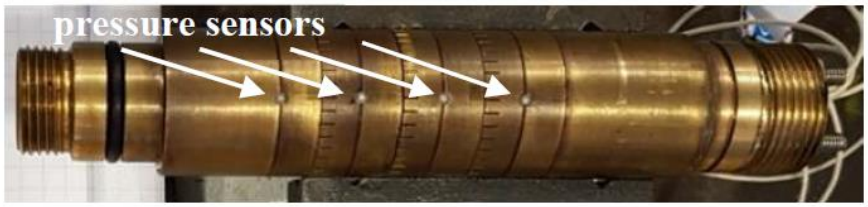

Figure 39: Multisensor device

Its modular design allows adapting distances and angles between measurements points. The device has eight modules, which gives opportunity to install up to eight sensor with different distances and also different angles. (Turankok, et al., 2021)
The sensors for multisensor device are selected as Kulite-XLC 072. The diameter of the sensors are 1.9mm which is 44 times smaller than rods perimeter. The RMS of the measured noise level is observed to be around 1Pa-2Pa. All effects included, the uncertainties are obtained from pressure measurements are about 4 Pa or 8% whichever is the higher.
The details of measurement campaign can be found in Table 11.

Campaign name	Sensor type	Sensor amount	Configuration	Purpose
MPS-2019	0.35 bar	8	WMV	The reproduction of data from SPS-2016 and SPS-2018
MPS-2020	0.35 bar	4	WMV	Investigation of transport of pressure fluctuations
MPS-2021-1	0.6 bar	4	NMV	Investigation of transport of pressure fluctuations
MPS-2021-2	0.6 bar 0.35 bar	4	NMV	Simultaneous measurements with PIV
MPS-2021-3	0.35 bar	4	WMV	Simultaneous measurements with PIV

Table 11: Details of multisensor pressure measurements campaign

7.2.5.2 Data acquisition system and improvements of equipment

For MPS-2019, same data acquisition system is used as SPS-2016 and SPS-2018. To improve the autonomy of the recording system, the rest of the measurements are performed with a new data acquisition system.

Figure 40 shows the improved data acquisition system and Table 12 shows the materials that is used for the data acquisition of the MPS-2020 to MPS-2021.

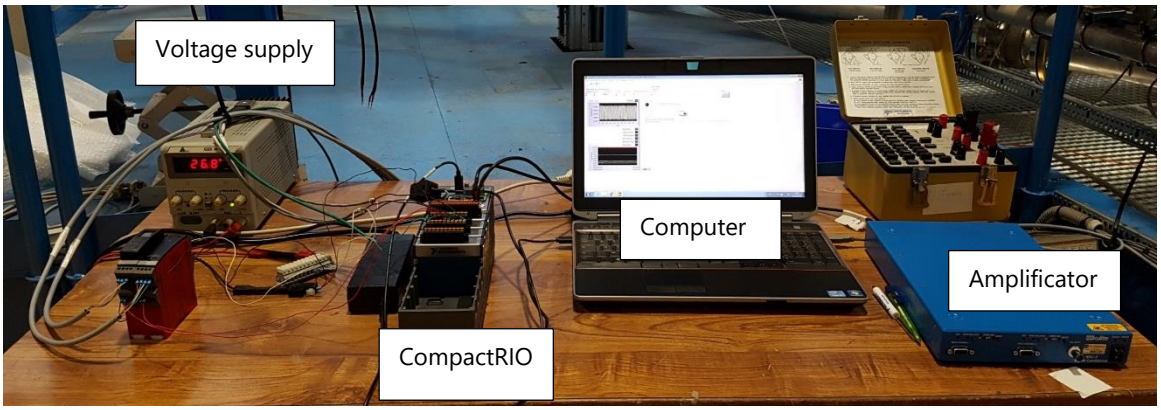

Figure 40: Improved Data Acquisition System

The amplifiers are switched with newer version to increase the measurement quality.
The PXI bus is switched with CompactRIO systems which provide sensor-specific conditioned I/O and an integrated software toolchain.

Power Supplier	Convergie CLES 30-3
Signal Conditioner	Kulite KSC-2
Data acquisition system	CompactRIO
Modules for CompactRIO	NI9202, NI9203, NI9263

Table 12: Data acquisition system for years 2020-2021

For the data acquisition, a new LABVIEW code is developed.
For all MPS campaigns, each local pressure measurement is performed at least for 40 s at 10kHz using a 1kHz low pass filter.

7.2.6 Pressure fluctuation processing

7.2.6.1 Energy spectra of pressure fluctuations

Energy spectra are computed using 3sec duration windows spaced by 1sec. A mobile average over 11 points (1Hz window) is applied to the spectra. Power spectra are normalised by the total energy.

7.2.6.2 Cross-correlation between pressure sensors

To search the signature of the pressure fluctuations sensor by sensor, cross-correlation method is used. The cross-correlation equation is shown as Eq.(55) where τ is the time delay (Bendat & Piersol, 1993).

$$Rxy(\tau) = \lim_{T\to\infty} \frac{1}{T} \int_0^T \{x(t) - \mu_x\}\{y(t) - \mu_y\} dt \tag{55}$$

For the application of cross- correlation, the normalized pressure fluctuations are used. Small size of correlation windows are applied on the selected pressure fluctuations, i.e. selected pressure sensors. The selection for the size of the windows are explain in detail in Chapter 12.

Figure 41 shows the schematics of the cross-correlation process between selected two sensors, i.e. $sensor_{0Dh}$ and $sensor_{0.5Dh}$ which is selected as an example.

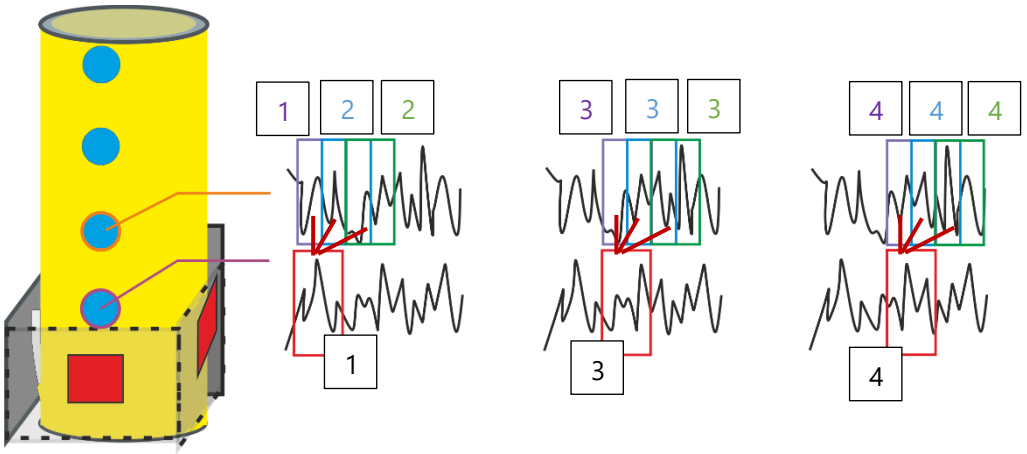

Figure 41: Cross-correlation schematics between selected two sensors

The flow direction is from $sensor_{0Dh}$ to $sensor_{1.5Dh}$ therefore it is expected to see the signature of the fluctuations in the $sensor_{0Dh}$ first.

1. The correlation process starts from the first window of $sensor_{0Dh}$ and first window of $sensor_{0.5Dh}$. The Eq.(55) is applied for these selected windows and the correlation coefficient is calculated.
2. The window for the $sensor_{0.5Dh}$ is moved point by point and the correlation coefficient is calculated until the selected time range.
3. The window of $sensor_{0Dh}$ is moved one point and the second step repeated again.
4. The third step is repeated point by point for $sensor_{0Dh}$ until the end of measurement

7.2.7 Challenges with pressure sensors

The reason for the change of the sensor type between the MPS measurements are the challenges connected to the sensors. Figure 42 shows some examples occurred during the measurements.
While performing the MPS-2019 measurements, the pressure isn't controlled in the test section which leads to exceeding the working range of the pressure sensors with velocities higher than 2.8 m/s. It is observed that with the damage, the sensors keep working for a certain duration and stop working afterwards the membrane is totally destroyed. This leads to water leakage inside the sensors which ends up as the oxidation that can be seen with orange colour in Figure 42(a) and Figure 42(b).
During the MPS-2020, to avoid the exceeding the working range of the sensors, the pressure levels are measured below and above the spacer grids during the measurements and the velocity range is selected according to the limits. Even respecting the working range, the sensors are observed to be broken after 2 weeks of use.
For MPS-2021-1, to perform measurements with higher durability, sensors are switched to the one with 0.6BarG working limit. To increase the life duration of the sensors, extra heat shrink tube is applied around the sensors. This heat shrink tube on a sensor can be seen on Figure 42(c) where the sensor is broken due to several electricity cut occurred during the measurements.
With the heat shrink tube application, the life duration of the sensor is observed to increase. Even though the 0.6BarG sensors are also observed to be more durable, with the increase durability, the sensitivity of the sensor is observed to be decreased.

As the final method for pressure measurements, i.e. MPS-2021-2 and MPS-2021-3, 0.35BarG pressure sensors are used with heat shrink tube. The results show increased durability of the sensors with high sensibility.

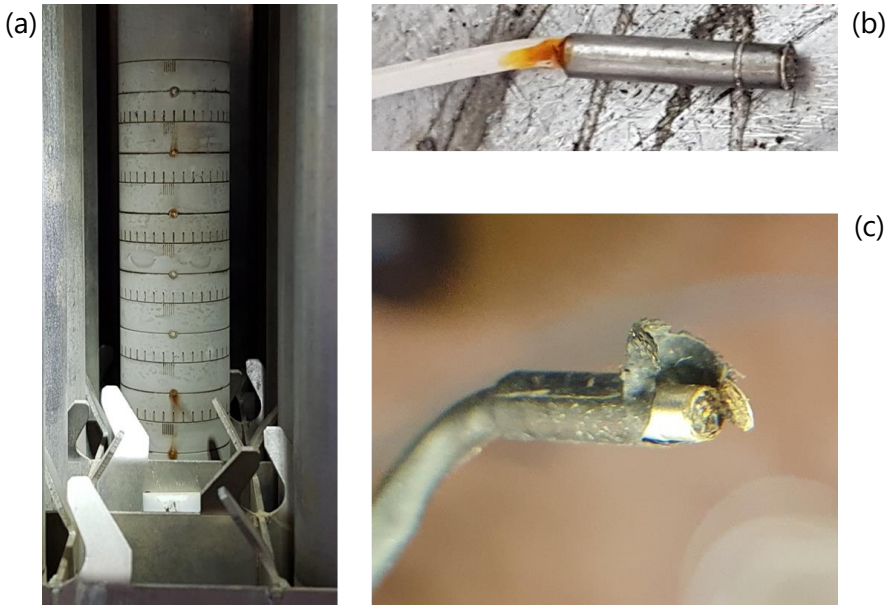

Figure 42 : Broken sensors from (a) MPS-2019 (b) MPS-2020 (c) MPS-2021-2

CHAPTER 8
SIMULTANEOUS MEASUREMENTS IN CALIFS 5X5

8. SIMULTANEOUS MEASUREMENTS IN CALIFS 5X5

The aim of the simultaneous measurement is to investigate the coupling between the velocity and pressure fluctuation in a transportation of fluctuation frame. To be able capture both of the fluctuations together simultaneous measurements are performed with multi-sensor pressure device and PIV measurements.

8.1 Configuration

Figure 43 shows schematics the configuration of the simultaneous measurement. For the pressure measurements four pressure sensor is used, i.e. KULITE-072 piezoresistive, with $0.5D_h$ intervals for grid level, i.e. $0D_h$ to $1.5D_h$.
The pressure sensors are positioned according to be included in the PIV frame. The angular position of the sensors are selected according to the previous pressure and PIV measurement results as 20° for NMV configuration and 0° for WMV configuration. The details of the angular position selection is discussed in Chapter 12.

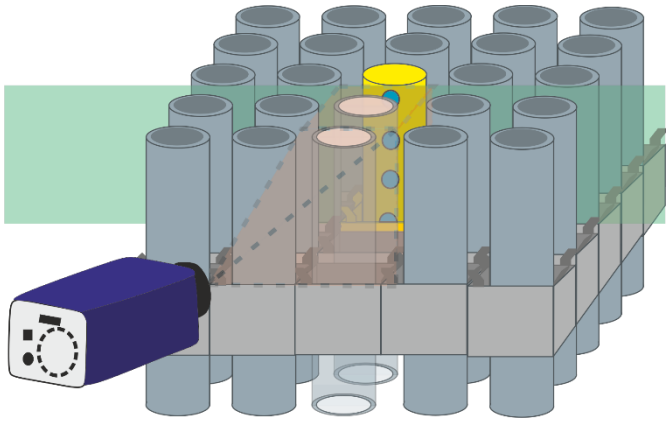

Figure 43: Schematics of simultaneous measurement configuration. The pressure sensors are marked with blue circles

The multi-sensor device is made from brass and the sensors are INOX which leads to reflection with the use of laser. To decrease this reflection, the sensors are painted with black permanent marker while ensuring no decrease on the sensitivity of the sensors.
For RIM application in single PIV measurements, 75cm long partial transparent rods are used. For simultaneous measurements the RIM application is updated with 2.5m new transparent rods to increase the overall strength of the FEP rods.
Comparison between two sets of pressure results is performed to ensure no additional effect is observed due to two FEP rods in INOX rod bundle. The pressure measurements that is performed with INOX rods and with the new two FEP rods shows no difference on pressure fluctuation results.

8.2 Data acquisition system for simultaneous measurements

For the recording of the simultaneous measurements, in-house LABVIEW code is developed and connected with DAVIS software by PTU-X hardware.
Figure 44 shows the algorithm of the measurements on the LabVIEW code. For the measurements, the selected velocities are given to LabVIEW as a list. After the recording starts, the voltage values

are sent to the pump according to the selected velocity, i.e. with POD function in LabVIEW. After the desired velocity is achieved, the algorithm pause for 1min to wait for the flowrate is stabilized.
The measurements start with pressure sensor recording. A trigger is sent from LABVIEW to PTU-X 10 sec after the pressure recording is started. After 10 sec another trigger is sent from PTU-X to PIV camera. During this process, the laser is rested on so no additional trigger is needed between the PTU-X and the laser. The recording of the PIV measurements are finished around 5sec where the pressure sensors are still recording. After the given "duration of time for recording" is completed, the sensors are stopped recording.
Before passing to the new velocity, the loop is paused for 10min for the saving the PIV data to the hard-disk.
The total measurement time per one Reynolds number is around 12min. To ensure the simultaneousness of pressure measurements and PIV measurements, time information of recordings is registered by LABVIEW.

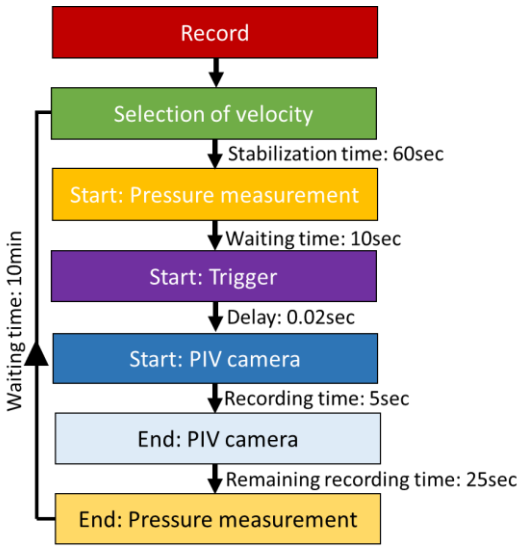

Figure 44: Schematics of the recording algorithm

Figure 45 shows the schematics of the signal map for voltage versus time. The V values shows the activation and 0 values shows deactivation of the measurement equipment.

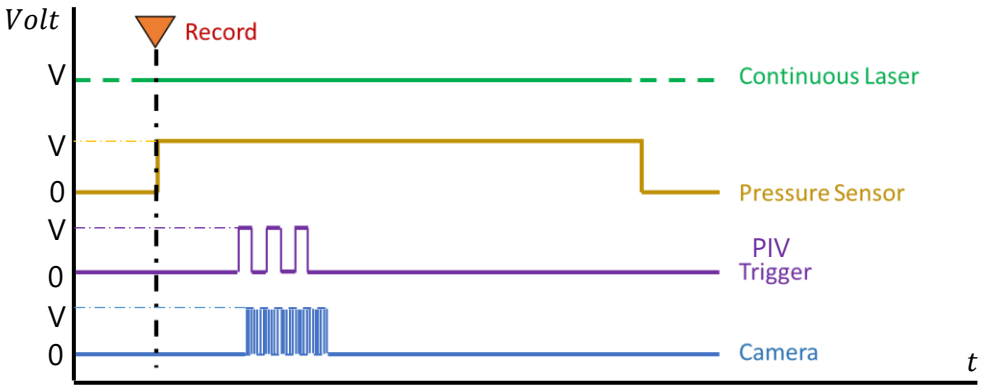

Figure 45: Signal map voltage versus time. V values represents the active recording

8.3 Simultaneous measurements processing

For the velocity-pressure correlation, cross-correlation method is performed with the velocity data that is obtained by the High-speed PIV and the pressure data that is obtained from the multi-sensor device. To be able to apply this method, two signal with the same length is necessary. Since the velocity measurements are performed with lower sampling frequency than pressure measurements, i.e. 10kHz, an additional mobile averaged pressure signal is resampled by 2^{nd} order interpolation. (Chapra & Canale, 2009)

The cross-correlation method between the velocity and pressure is performed as Chapter 7.2.6.2 with Eq.(55).

Figure 46 shows the schematics of the simultaneous measurements cross-correlation between one pressure sensor and the one position of PIV. Different than Chapter 7.2.6.2, the correlation signals are selected as selected sensor and velocity fluctuation from PIV results.

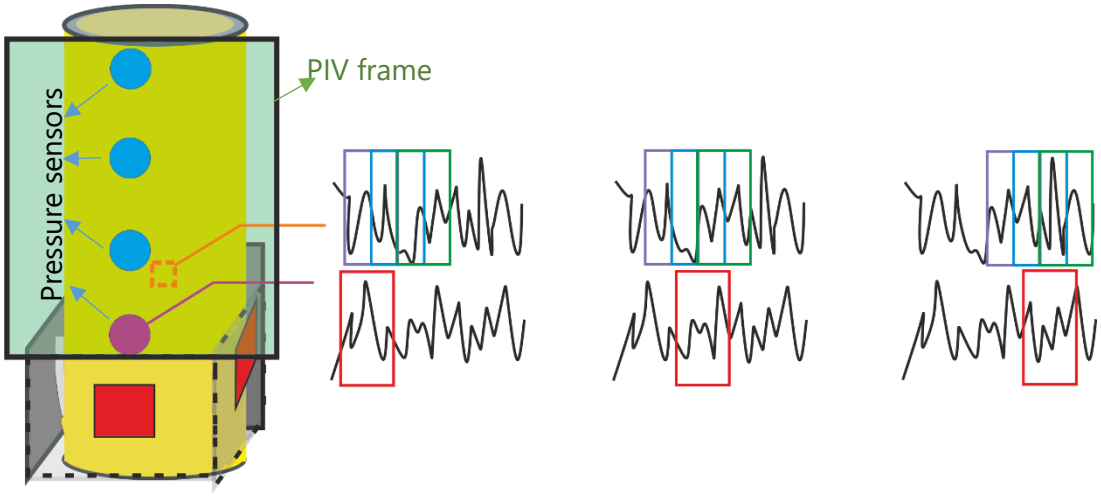

Figure 46: Schematics of cross-correlation between selected pixel on PIV frame and the selected sensor

After performing the cross-correlation for one position of the PIV, the process is repeated for the selected other positions and the other sensors.

The details of the processing and the results are discussed in Chapter 12.

CHAPTER 9
GLOBAL CHARACTERIZATION OF THE FLOW

9. GLOBAL CHARACTERIZATION OF THE FLOW

Grid-to-rod phenomena is connected to the fluid-structure interaction. To understand the excitation of the rods which generates this interaction, it is important to quantify the velocity and pressure along with their fluctuations.

To characterize the flow, a series of measurements are performed as;

- LDV velocity measurements
- Single sensor pressure measurements
- Multisensor pressure measurements
- PIV with RIM velocity measurements

As mentioned in the Chapter 2, the measurement domain is selected as central rod to measure the flow that is representative in larger arrays by decreasing the effect of the wall.

The first measurements are performed with $Re_{Dh} = 66000$, i.e. $U_{flow} = 2.4\ m/s$ and the temperature 20°C, by using LDV and single pressure measurements. This permit to have a similitude of hydrodynamic conditions of PWR where the Reynolds number is sufficient to generate the mean structures of turbulent flow. The measurements are performed for both NMV and WMV spacer grids which give an opportunity to explore the effects of spacer grid design.

According to these measurements, a new measurement region is selected as downstream the dimple. The measurements are performed with PIV and multisensor pressure device for a broad range of Reynolds number, i.e. 13000 to 120000. This permits to create a database while exploring the limits of the phenomena investigated.

All the measurements are repeated for different distances from the spacer grid.

9.1 Velocity and pressure fluctuations around the rod at Reynolds number 66000

For the exploration of the velocity profiles, LDV-2015 measurements are performed around the rod in a square segment. Figure 47 shows the measurement points of the LDV-2015. The central square shows the perimeter, $\wp_{sq}$, and the measurement lines are $2D_h$ for each side of the central square. Each measurement line is designated with a letter as;

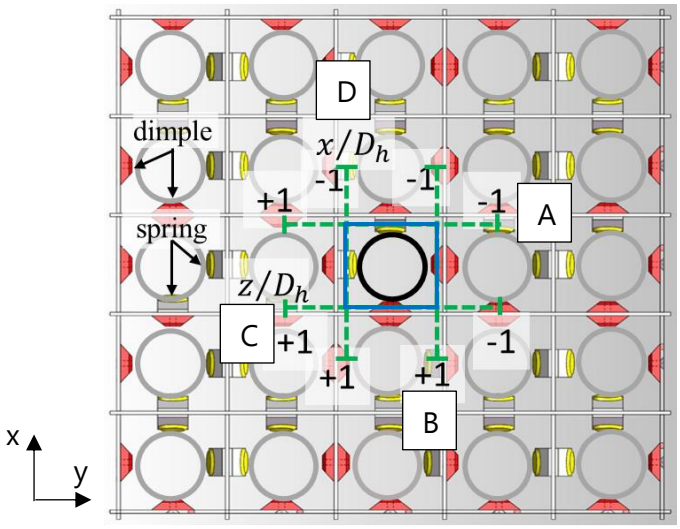

Figure 47: LDV measurement domain. Blue square shows measurement perimeter and green parts show the measurement lines

- A: $x/D_h = -0.53$
- B: $z/D_h = -0.53$
- C: $x/D_h = +0.53$
- D: $z/D_h = +0.53$

Figure 48 shows the dimensionless mean velocity, $\bar{u}/U_{flow}$, profiles around the central rod for the four lines of measurements A, B, C and D. Each graphics give the velocity profiles for different distances from the grid, i.e. $y/D_h = 2, 3, 4, 5, 10, 15$. The left column shows the results for NMV configuration and the right column show the WMV configuration.

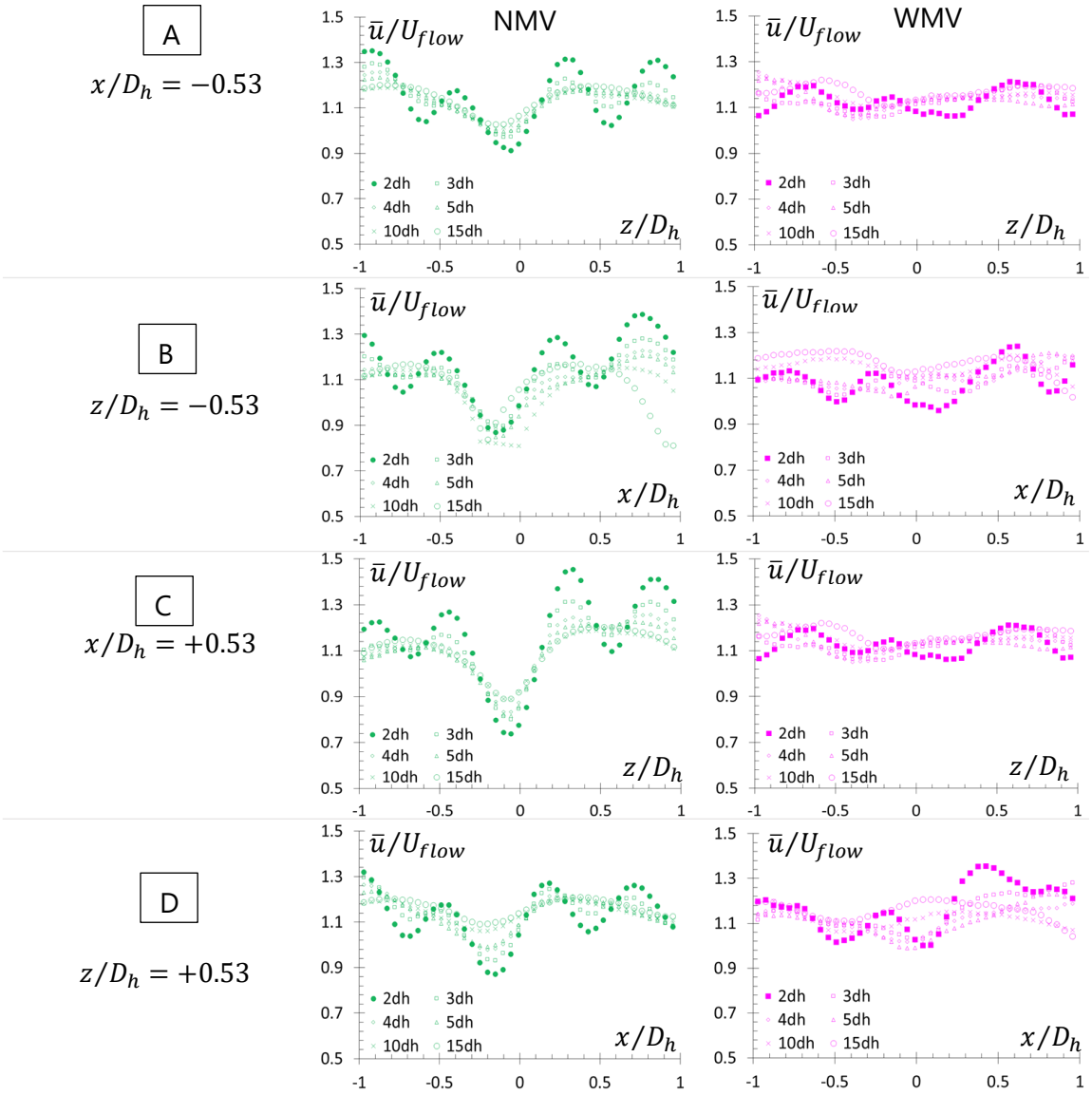

Figure 48: Dimensionless mean velocity profiles $\bar{u}/U_{flow}$ from LDV-2015 measurements

The oscillations are observed to be higher for NMV configuration compared to WMV configuration. In both configuration these oscillations are observed to decrease with the increased distance from the grid.

The oscillations are defined as the percentage of the local maximum of $\bar{u}/U_{flow}$ to the local minimum of $\bar{u}/U_{flow}$.

The average oscillations is found around 38% at $y/D_h = 2$ for NMV configuration. This value is decreased to 20% with the increased distance, i.e. $y/D_h = 15$.

For WMV at $y/D_h = 2$, this percentage is found around 22% and at $y/D_h = 15$ this value is observed to decrease to 16%.

In both configuration the maximum percentage of $\bar{u}/U_{flow}$ oscillation is observed at $y/D_h = 2$ for the position "C" which corresponds to the position of the dimple. For NMV the difference between the local minimum and the local maximum is found 49% and for WMV this value is decreased to 29%.

Figure 49 shows the main trends of the mean velocity per position and RMS values of velocity fluctuations per position for both NMV and WMV configuration. Position B and C shows the dimples and Position A and D shows the springs.

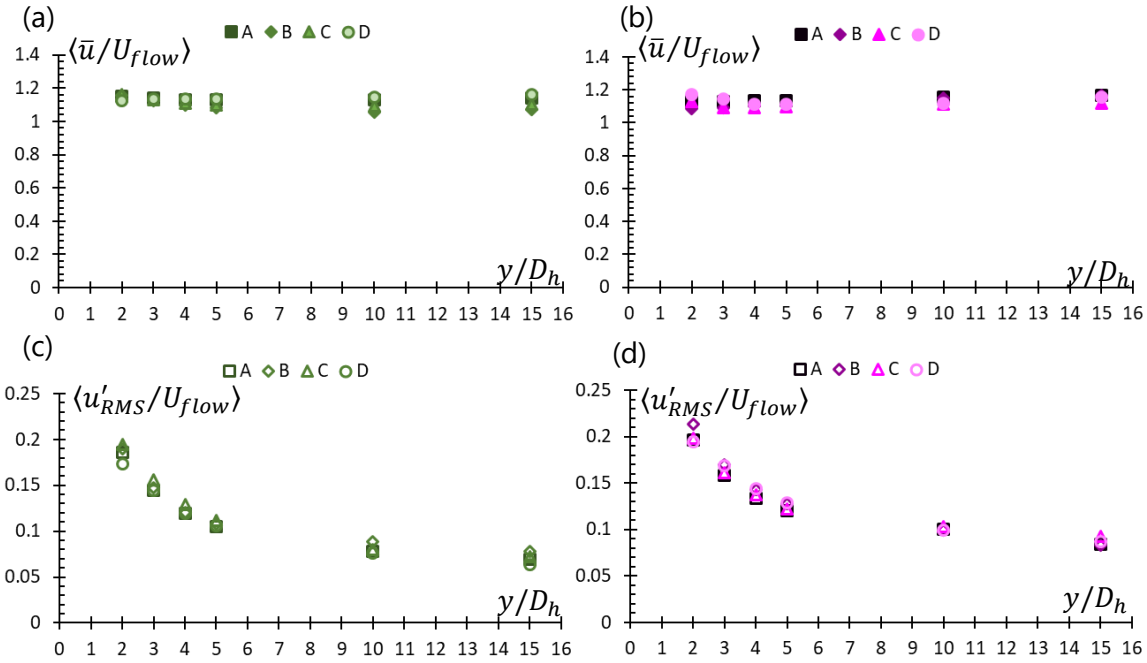

Figure 49: The mean profiles (a) $\langle \bar{u}/U_{flow} \rangle$ for NMV configuration (b) $\langle \bar{u}/U_{flow} \rangle$ for WMV configuration (c)) $\langle u'_{RMS}/U_{flow} \rangle$ for NMV configuration (d) $\langle u'_{RMS}/U_{flow} \rangle$ for WMV configuration

For both configuration, the average $\langle \bar{u}/U_{flow} \rangle_{A,B,C,D}$ including all the distances is found 1.12 ± 0.01. In both configuration, the highest $\langle \bar{u}/U_{flow} \rangle$ is observed around 1.16. Depending on the distance, this value is observed on both downstream the dimple and the spring.

The $\langle u'_{RMS}/U_{flow} \rangle$ profile is similar for both configuration. In both configuration the highest velocity fluctuations are observed downstream the dimples.

- For NMV configuration, the highest $\langle u'_{RMS}/U_{flow} \rangle$ is about 0.19 for $\langle u'_{RMS}/U_{flow} \rangle_B$ and $\langle u'_{RMS}/U_{flow} \rangle_C$. The difference compared to $\langle u'_{RMS}/U_{flow} \rangle_D$ and $\langle u'_{RMS}/U_{flow} \rangle_A$, i.e. springs, are found as 9% and 4.5%, respectively.
- For WMV configuration, the highest $\langle u'_{RMS}/U_{flow} \rangle$ is found at $\langle u'_{RMS}/U_{flow} \rangle_B$ with 0.21. The difference compared to $\langle u'_{RMS}/U_{flow} \rangle_D$ and $\langle u'_{RMS}/U_{flow} \rangle_A$, i.e. springs, are found as 9.8% and 1.6%, respectively.

To extract a value akin to a characteristic distribution around the rod, the average of u'_{RMS} are calculated around the measurement perimeter, i.e. $\langle u'_{RMS} \rangle_{sq}/U_{flow}$. The results are shown in Figure 50.

A decrease in the fluctuations is detected with the increased distance from the grid. For NMV, the average of velocity fluctuations are decreasing from 0.19 to 0.08 and for WMV the decrease is from 0.20 to 0.09. The trend with power law approximation is found as;

- NMV: $0.24\left(\frac{y}{D_h}\right)^{-0.46}$
- WMV: $0.25\left(\frac{y}{D_h}\right)^{-0.38}$

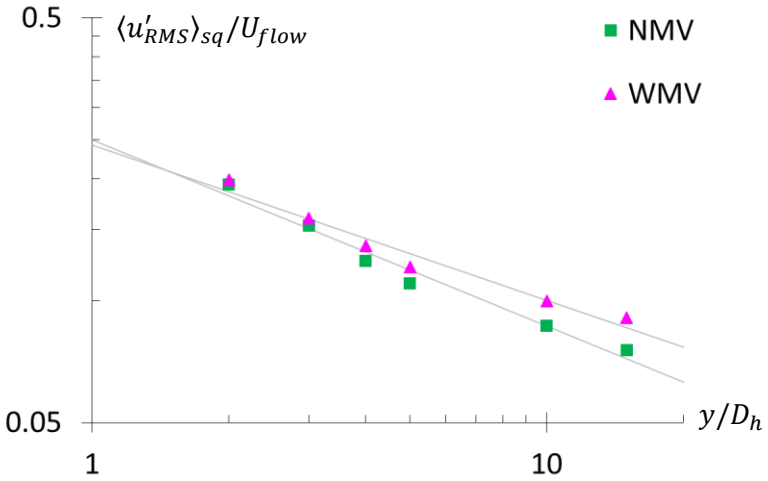

Figure 50: $\overline{u'_{RMS_{sq}}}/U_{flow}$ versus y/Dh for NMV and WMV

To explore the pressure fluctuations in rod bundle, the distribution of the pressure is measured around the central rod. In SPS-2016 and SPS-2018, the pressure measurements are performed for every 8° with different distances away from the spacer grid, i.e $0.5D_h, 1D_h, 2D_h, 3D_h, 4D_h, 5D_h, 10D_h$ and $20D_h$. Re_{Dh} is selected as 66000. The details of the configuration is explained in Chapter 7.

Figure 51 represents the azimuthal distributions of RMS pressure fluctuations, P'_{RMS}, around the rod. For all the distances, the pressure fluctuations are observed to be higher for the WMV configuration. For $0.5 \leq y/D_h \leq 5$, the difference between two configuration is increased from 11% to 56% and stabilize around 57% for the rest of the distances, i.e. $5 \leq y/D_h \leq 20$.

The effect of the grid elements are detected with the increasing distance.

- For the distances $0.5 \leq y/D_h \leq 2$, the area between dimple and spring have higher fluctuations. For both configuration this value is calculated 42% and 23% higher than the $\langle P'_{RMS}\rangle_{0.5D_h}$ and $\langle P'_{RMS}\rangle_{2D_h}$, respectively.
- For NMV configuration, the lowest fluctuations are in the region between two springs at $0.5 \leq y/D_h \leq 1$. At $y/D_h = 0.5$, the maximum fluctuations are 14% lower than the $\langle P'_{RMS}\rangle_{0.5D_h}$. At $/D_h = 1$, this value is calculated as 6% higher than $\langle P'_{RMS}\rangle_{1D_h}$. For the distances $2 \leq y/D_h \leq 20$, the lowest zone for NMV configuration is between two dimples. The difference between the average fluctuations are calculated as 1%.
- For WMV configuration, for the distance $0.5 \leq y/D_h \leq 4$ the lowest fluctuations are between two springs. At $y/D_h = 0.5$, the maximum fluctuations are 20% lower than the $\langle P'_{RMS}\rangle_{0.5D_h}$. At $y/D_h = 4$, this value is calculated as 8% higher than $\langle P'_{RMS}\rangle_{4D_h}$. After $y/D_h > 4$, the minimum fluctuation zone is switched between the grid elements. At $y/D_h = 5$, the minimum fluctuation zone is between dimple and spring. For $10 \leq y/D_h \leq 15$, it is between two springs with 9% and 2.5% higher than the average

$\langle P'_{RMS} \rangle$, respectively. At $y/D_h = 20$ it is observed between two dimples around the average $\langle P'_{RMS} \rangle_{20D_h}$.

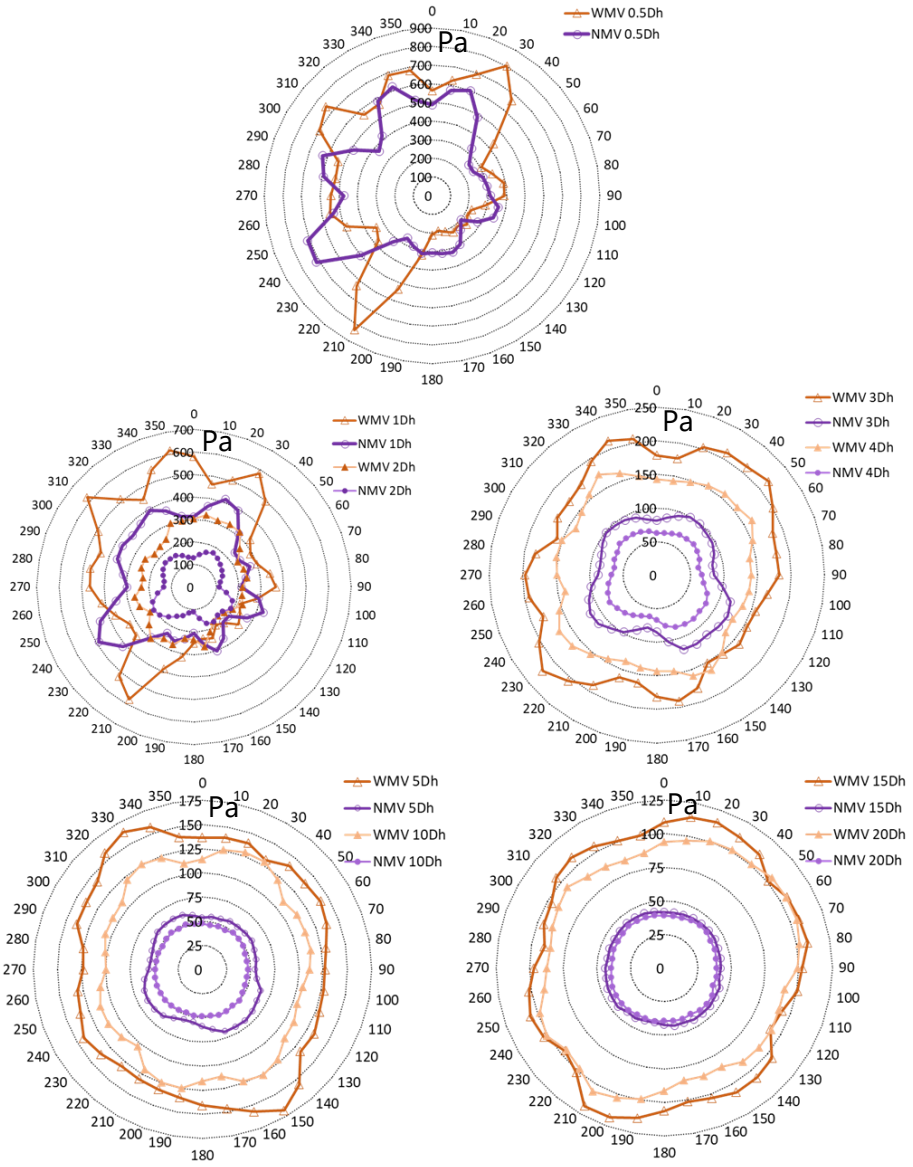

Figure 51 : Azimuthal distributions of the RMS pressure fluctuations around the rod for NMV and WMV configuration at $Re_{Dh} = 66000$

For both configurations, the pressure distributions are observed to be strongly non-homogenous for $y/D_h \leq 2$. For $y/D_h = 0.5$, the $\langle P'_{RMS} \rangle_{0.5Dh}$ is found as 468Pa and 414Pa where $\langle \sigma \rangle_{0.5Dh}$ is found as 144Pa and 192Pa for NMV and WMV, respectively. At $y/D_h = 2$, the $\langle \sigma \rangle_{2Dh}$is found as 41Pa and 23Pa, respectively. For WMV configuration with the increasing distance, $\langle \sigma \rangle$ values go down until 6Pa. For NMV configuration $y/D_h \geq 10$, $\langle \sigma \rangle_{10Dh}$ become 1 or smaller, i.e. pressure distribution becomes quasi-homogenous.

Figure 52 shows the global trend of P'_{RMS} downstream the grids. To quantify the trend, the average of P'_{RMS} is taken around the rod, i.e. $\langle P'_{RMS} \rangle_{\theta}$. From the result, for both configuration a decrease is observed with the increased distance away from the grid. For NMV, the average of P'_{RMS}, are decreasing from 400 Pa to 20 Pa and for WMV the decrease is observed from 460 Pa to 40 Pa.

The trends are approximated to power law as follows:

- NMV: $240.65\left(\frac{y}{D_h}\right)^{-0.68}$
- WMV: $334.99\left(\frac{y}{D_h}\right)^{-0.46}$

The negative power of $\left(\frac{y}{D_h}\right)$ shows a lower rate of change in the decrease of the intensity of pressure fluctuations which shows that the fluctuations persist farther with WMV configuration.

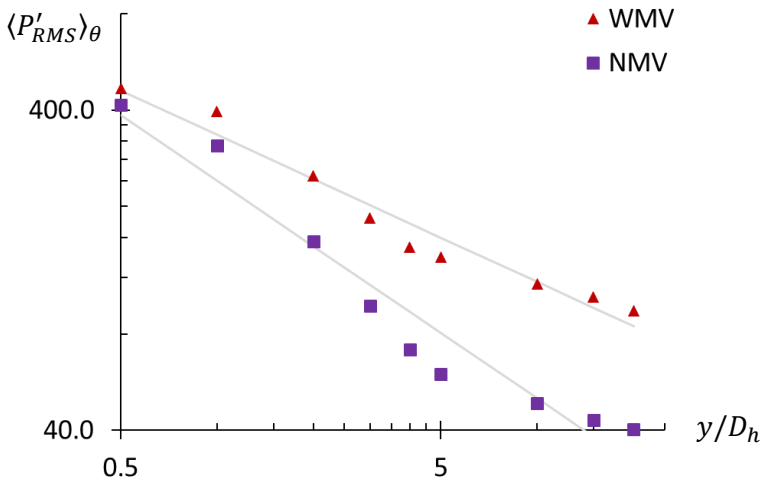

Figure 52 : Azimuthal average of the rms of the pressure fluctuations for NMV and WMV configuration at $Re_{Dh} = 66000$

Figure 53 shows the ratio of pressure fluctuations to velocity fluctuations, i.e. $\langle P'_{RMS}\rangle_\theta / \frac{1}{2}\rho\langle {u'_{RMS}}^2\rangle_{sq}$. For both configuration, the an increase is observed which shows the pressure fluctuations are decreasing slower compared to the velocity fluctuation, i.e. pressure fluctuations are persisting farther.

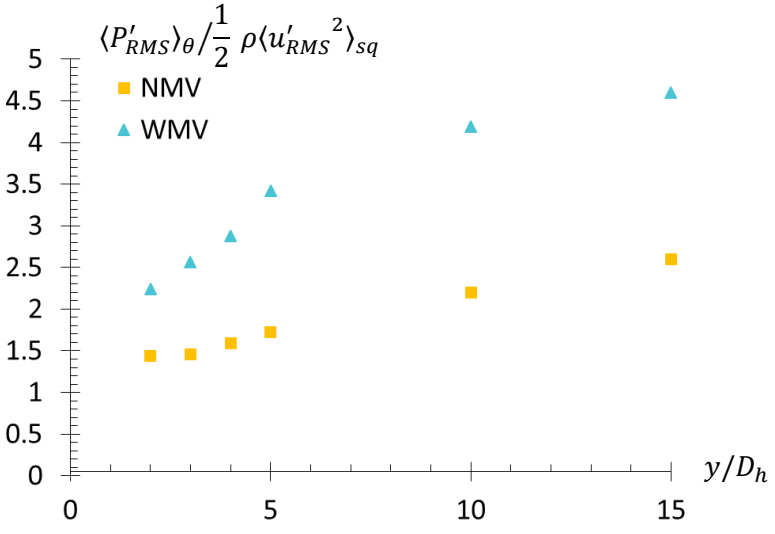

Figure 53: $\langle P'_{RMS}\rangle_\theta / \frac{1}{2}\rho\langle {u'_{RMS}}^2\rangle_{sq}$ for NMV and WMV with increasing distance from the grid

9.2 Velocity field downstream dimples

PIV measurements are performed to investigate the velocity field and its fluctuations. According to LDV-2015, for both configurations the maximum velocity oscillations and the maximum velocity fluctuations are observed at position "C", i.e. downstream the dimple. The SPS-2016 and SPS-2018 measurements also show coherent results where the maximum pressure fluctuations are observed in the corners between the spring and dimple.

Figure 54 shows an illustration of the selected measurement domain downstream the dimples. The domain is selected according to the optical access of CALIFS where the maximum fluctuations can also be included in the measurement field.

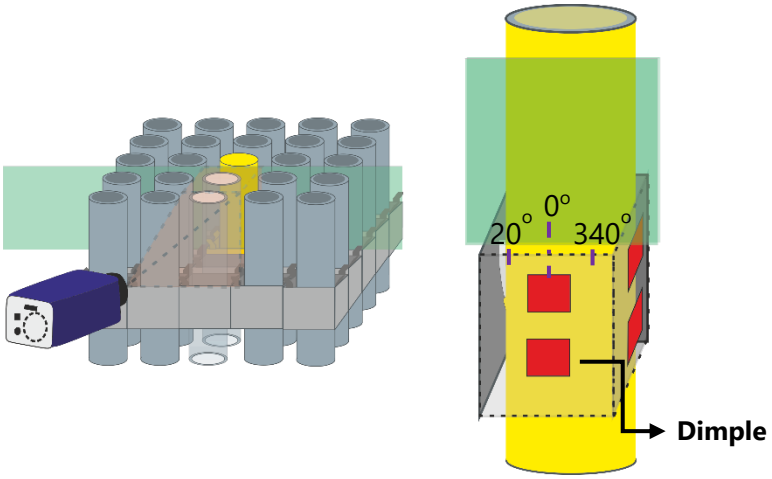

Figure 54: Illustration of the measurement domain

The measurements are performed for both configurations as NMV and WMV. The Reynolds number of the flow is varied from 11200 to 151700 by using different velocities and different temperatures. The measurements are repeated for different distances away from the spacer grid.

Two different PIV setups, i.e. camera and laser, are used for the High-speed PIV and Low-speed PIV. For high-speed PIV measurements, the limit of the mean flow is set to 0.9m/s. This limit is selected according to capture the maximum measurable displacement with the highest frequency which is permitting to have enough light, i.e. contrast of frame. The details about the limitations are discussed in Chapter 6.

9.2.1 Details of measurement domain and comparison of configurations

To illustrate the PIV measurement domain, the result from $Re_{Dh} = 20100$ is assembled with different distances from the grid. For both configuration the camera is positioned at 3 different distance. For NMV configuration, the placement of the frame is started from $y/D_h = 0, 2$ and 3 and for WMV this placement is from $y/D_h = 0, 1.5$ and 3.

Figure 55 shows an assembly of different PIV results to show the development of the flow downstream the grid. This gives opportunity to present the results over a wider distance downstream the grid.

Figure 55(a) and Figure 55(b) shows the $\|\overline{U}\|/U_{flow}$ for NMV and WMV, respectively. For NMV, relatively lower velocities in the frame are observed downstream the dimple. These velocities are illustrated with yellow colour. On both side of the dimple higher velocities are detected with red colour. With the increasing distance from the grid, the velocities are spotted to be more homogenous, i.e. the colour of the velocity field is with one tone of red. For WMV, the highest velocities are noticed with the direction of the mixing vane on left-hand side. Lower velocities are mainly observed on the other side of the frame. With the increasing distance from the grid, darker

tone of red is detected on the right-hand side of the frame, i.e. the velocity field seems heterogeneous compared to NMV configuration.
For NMV, the shear layers can be seen on the both side on the dimple. For WMV configuration the shear layer is observed with "λ" shape close to the grid. With the increasing distance this shear layer is noticed with the direction of the mixing vane.

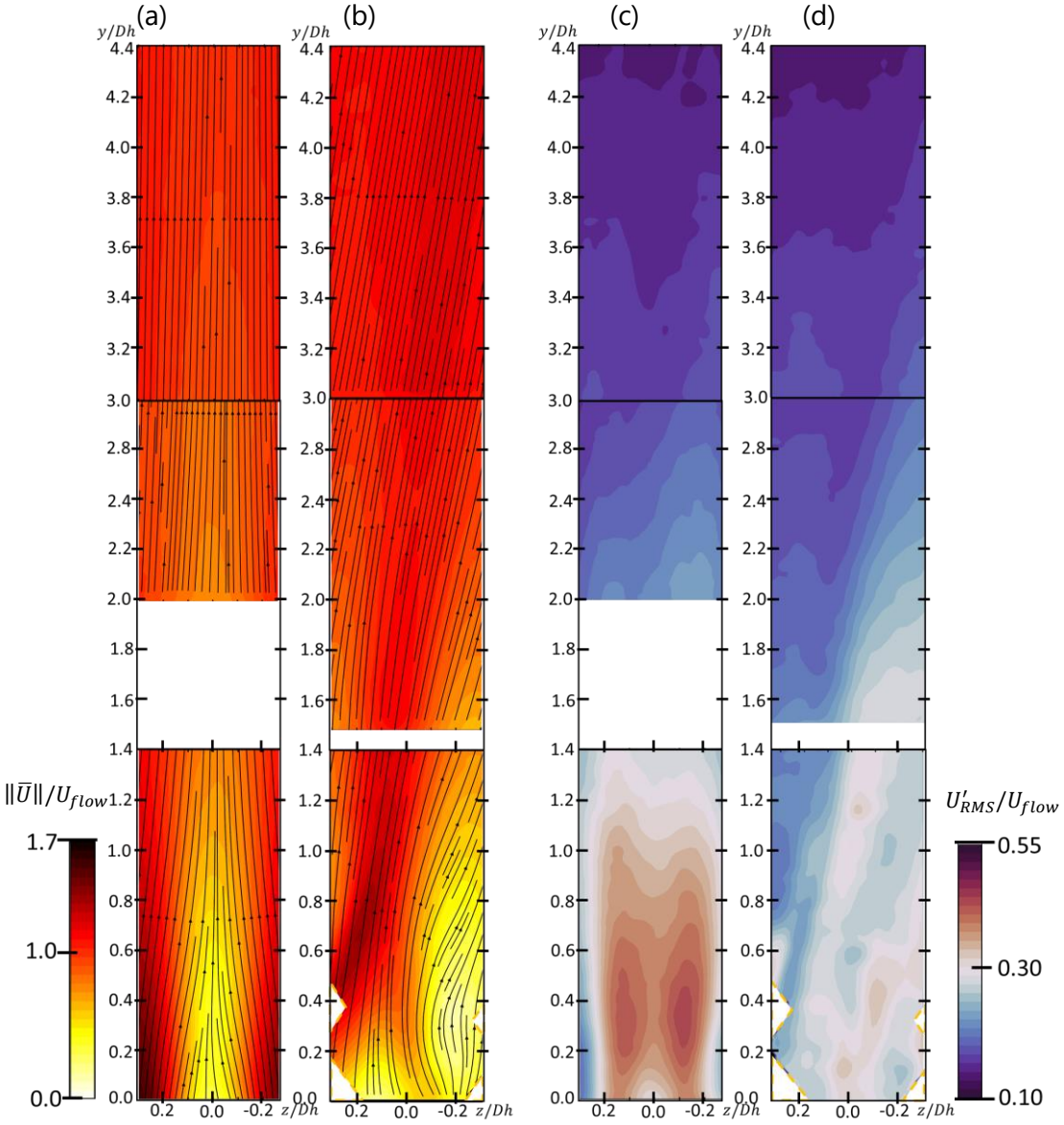

Figure 55: Comparison of (a) $\|\bar{U}\|/U_{flow}$ and (b) U'_{RMS}/U_{flow} for NMV and WMV configuration at $Re_{Dh} = 20100$

Figure 55(c) and Figure 55(d) shows the U'_{RMS}/U_{flow} for NMV and WMV configuration, respectively. For NMV, the highest fluctuations are spotted on both side of the dimple within the shear layers. These high fluctuations are close to the grid and with the increasing distance the intensity of the fluctuations are decreased. For WMV, the velocity fluctuations are observed with lower intensity compared to NMV configuration. Different than NMV, these fluctuations are ubiquitous in the frame with the direction of the mixing vane. Compared to NMV, for WMV the fluctuations are observed to lose their intensity slower for higher distances from the grid in the direction of mixing vane.
The detailed description of the velocity field is discussed in the following sections.

9.2.2 Velocity fields for configuration No Mixing Vane

Figure 56 shows the instantaneous velocity field, $\|\boldsymbol{U}\|/U_{flow}$, for NMV configuration at the exit of the spacer grid. The streamlines are plotted using the velocity components u and v in the frame reference of the laboratory.

In the figure, four results with different Reynolds number are presented as $Re_{Dh} = 11200, 15600, 66000, 151200$. For $Re_{Dh} = 11200, 15600$, the length of the measurement domain is $1.4D_h$ and for $Re_{Dh} = 66000, 151200$ the length of the measurement domain is $2.2D_h$.

The differences in the measurements domains are due to the different cameras. The dual frame camera used for Low-speed PIV has higher spatial resolution compared to high-speed camera which leads to larger measurement domain.

Different velocity regions are detected on the instantaneous velocity field. The low velocity region is where the instantaneous velocity is slower than the mean flow, i.e. $\|U\|/U_{flow} < 1$ and the high velocity region where the instantaneous velocity is faster than the mean flow, i.e. $\|U\|/U_{flow} > 1$. These low and high velocity region is presented as blue and red and marked as "H" and "L" on the figures, respectively. $\|U\|/U_{flow} = 1$ delimits the high and low velocity region with white colour.

In Figure 56, the low velocity region can be seen downstream the dimple. The high velocity region is observed on both side of this low velocity region. The maximum $\|U\|/U_{flow}$ is around 2 and the minimum $\|U\|/U_{flow}$ is at 0. Shear layers are in-between regions of high and low velocities, i.e. $0.8 \leq \|U\|/U_{flow} \leq 1.1$. The behaviour of the flow is about the same for the broad range of Reynolds number, i.e.$11200 \leq Re_{Dh} \leq 152000$.

The redistribution of the velocity field can be observed with the increased distance away from the spacer grid. This redistribution can be seen more clearly on Figure 56c and Figure 56d, with the increased measurement domain, i.e. after $y/D_h > 1.75$ the velocity field is around $0.8 \leq \|U\|/U_{flow} \leq 1.1$.

The mean velocity fields for $0 \leq y/D_h \leq 1.4$ with NMV configurations are presented in Figure 57. The results show a clear view of the shear layers with presence of high and low velocity regions close to the spacer grid. The streamlines show the direction of the flow. The flow is mainly on vertical direction, i.e. $y - direction$. The "L" region is observed, i.e. $0 \leq \|\overline{U}\|/U_{flow} \leq 0.8$ on the $-0.1 \leq z/D_h \leq 0.1$. The secondary flow can be spot where the flow is going from "H" to "L".

Figure 58 show the instantaneous velocity field, $\|U\|/U_{flow}$, for NMV configuration with $3D_h$ away from the spacer grid. The redistribution of the velocity field can be noticed with the increased distance away from the grid. The velocity field is observed to be more homogenous around the mean flow, i.e. $0.71 \leq \|U\|/U_{flow} \leq 1.5$. The difference between $\left(\|U\|/U_{flow}\right)_{max}$ and $\left(\|U\|/U_{flow}\right)_{min}$ is 49% and 55%, respectively for $Re_{Dh} = 11200$ and 15600. This difference is 96% for the measurement domain $0 \leq y/D_h \leq 1.4$.

Figure 59 shows the mean velocity field for $3 \leq y/D_h \leq 4.4$. The results are in coherence with the instantaneous velocity field. It can be seen that the velocity field is more homogenous, i.e. the velocity difference between the high velocity region and the low velocity region is decreased. Compared to $0 \leq y/D_h \leq 1.4$, the streamlines are observed to be more straight and vertical.

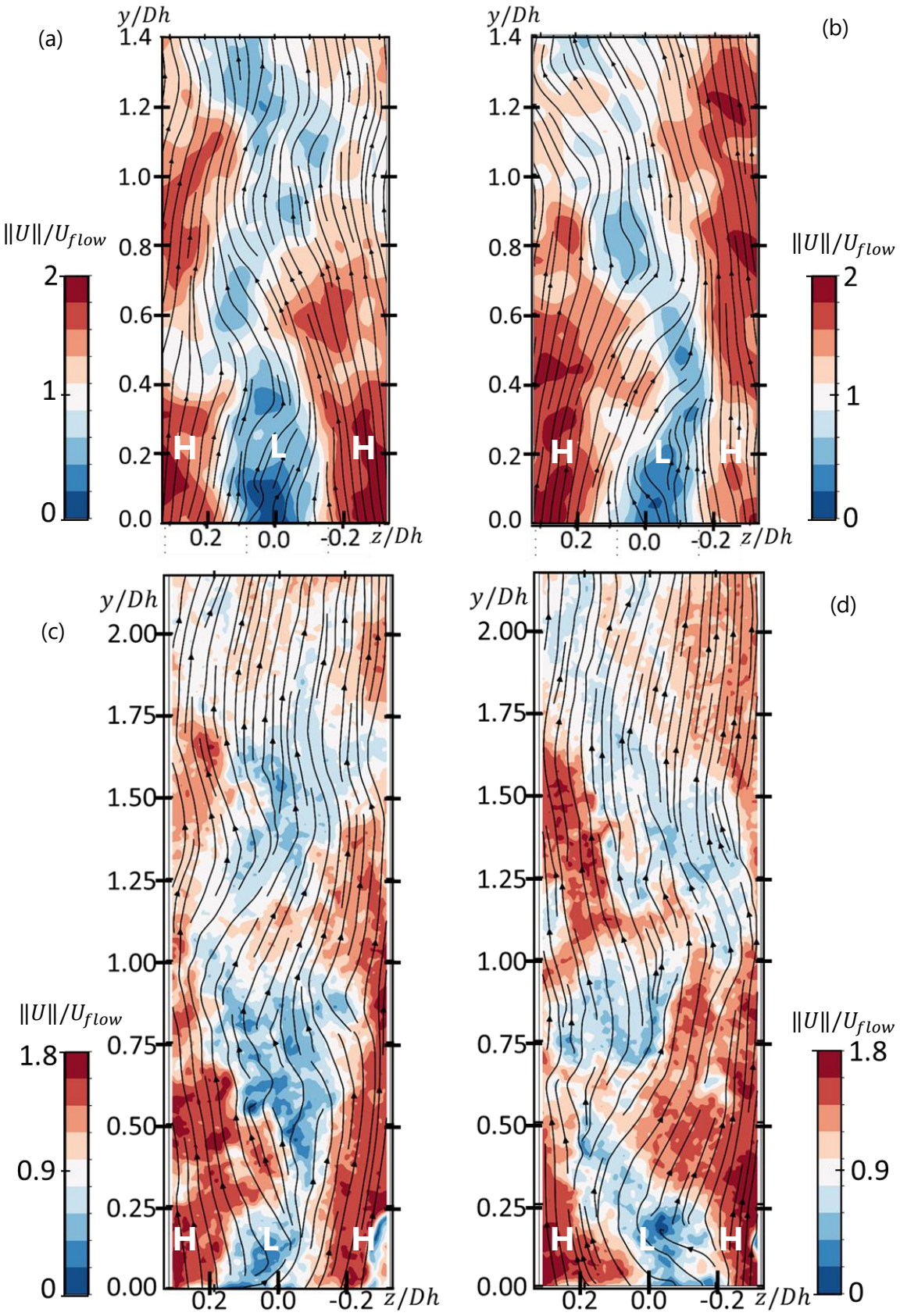

Figure 56: Instantaneous velocity field for NMV at measurement domain $0 \leq y/D_h \leq 1.4$ for $Re_{Dh} = (a)11200, (b)15600$ and at $0 \leq y/D_h \leq 2.2$ for $Re_{Dh} = (c)66000, (d)151200$

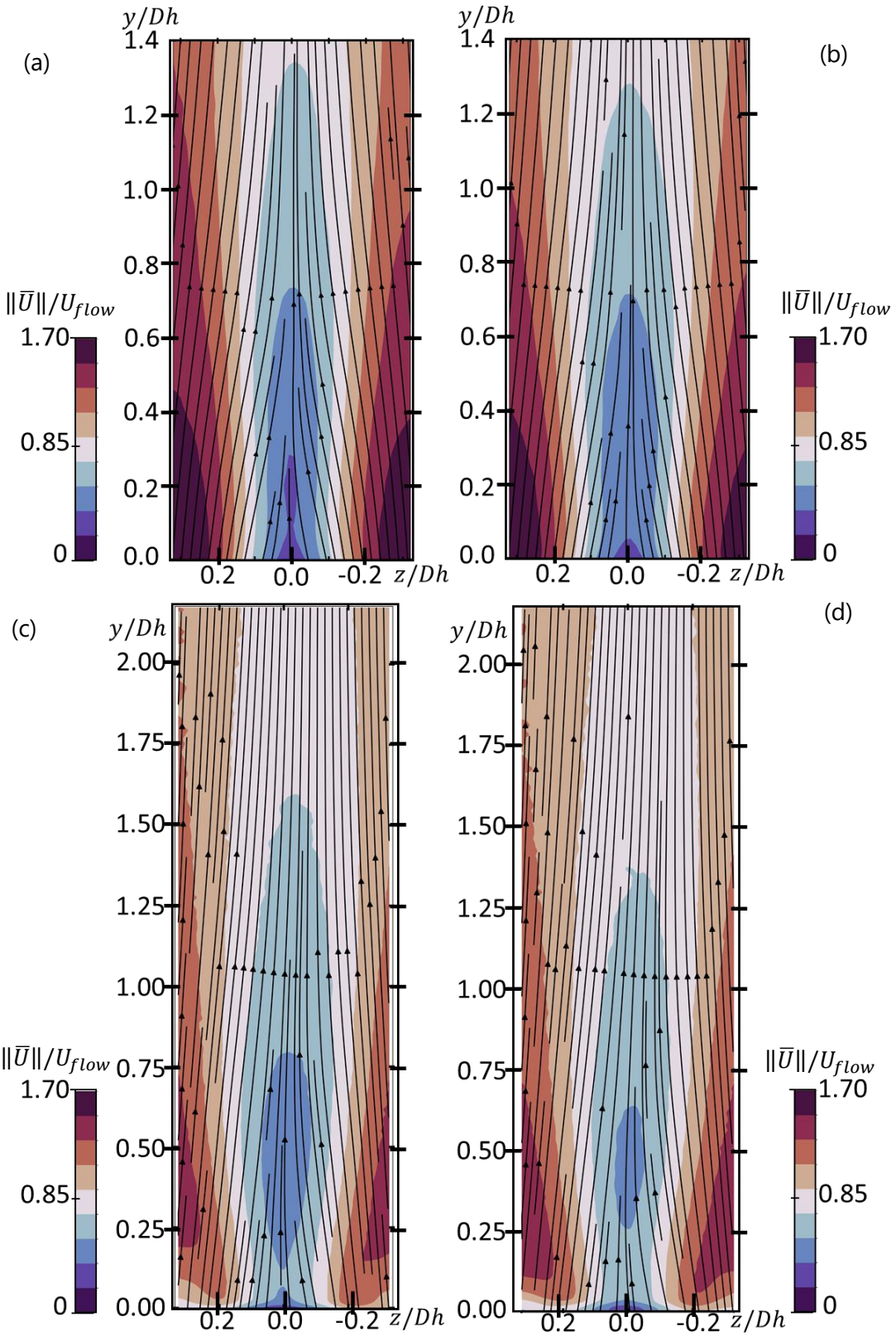

Figure 57: Mean velocity field for NMV at measurement domain $0 \leq y/D_h \leq 1.4$ for $Re_{Dh} = (a)11200,\ (b)15600$ and at $0 \leq y/D_h \leq 2.2$ for $Re_{Dh} = (c)66000,\ (d)151200$

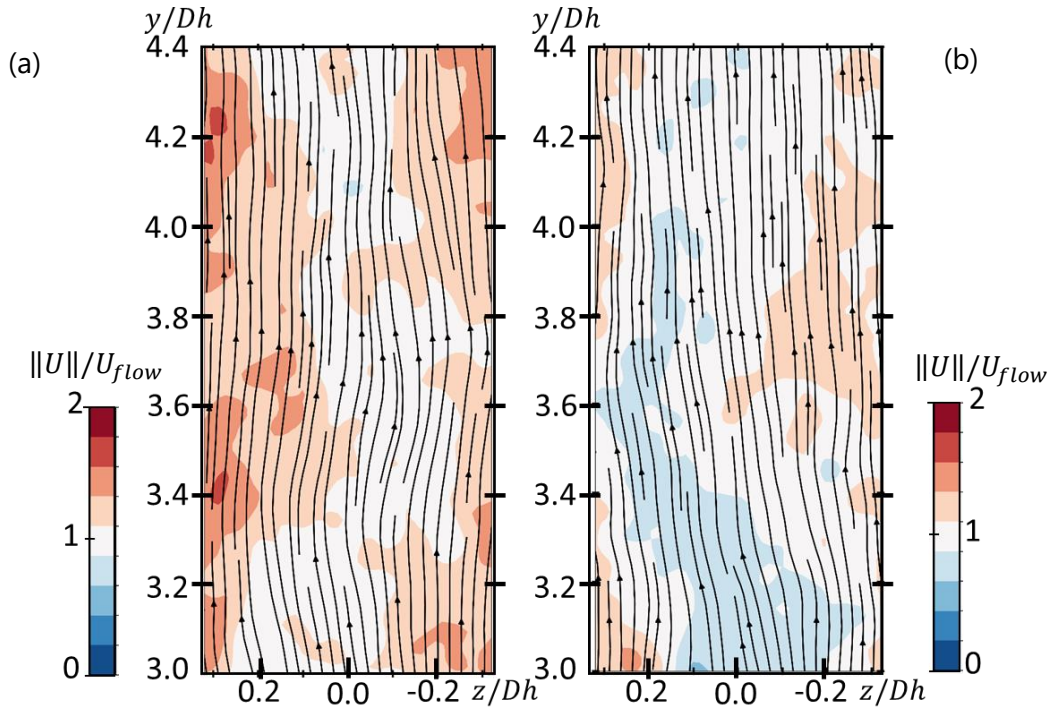

Figure 58: Instantaneous velocity field for NMV at measurement domain $3 \leq y/D_h \leq 4.4$ for $Re_{Dh} = (a)11200$ and $(b)15600$

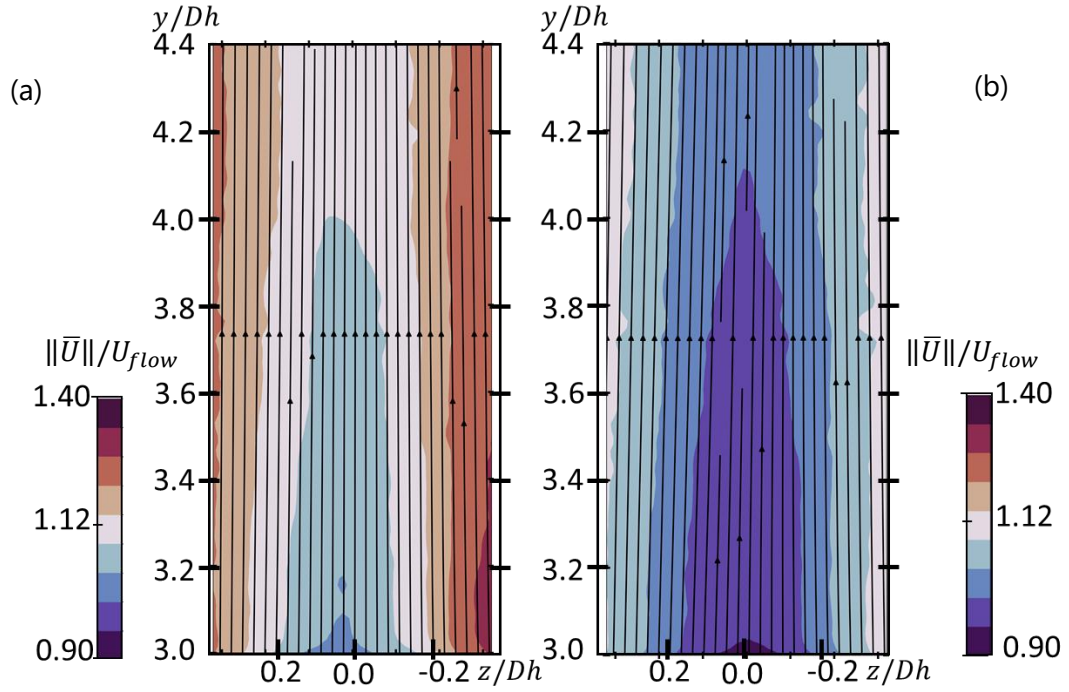

Figure 59: Mean velocity field for NMV at measurement domain $3 \leq y/D_h \leq 4.4$ for $Re_{Dh} = (a)11200$ and $(b)15600$

9.2.3 Velocity profiles for configuration No Mixing Vane

To study the further details of the velocity distribution, the velocity profiles are plotted for each component of the flow according to the distances away from the grid.

Figure 60 shows the profiles of dimensionless mean velocity field $\|\bar{U}\|/U_{flow}$ for $Re_{Dh} = 20100$. The redistribution of the velocity is noticed with the increased distance away from the grid.

- Between $0 \leq y/D_h \leq 1.4$, the low velocity region is detected downstream the dimple as $0.4 \leq \|\bar{U}\|/U_{flow} \leq 0.8$. The difference between the low and the high velocity region is decreased with the increasing distance from the grid.
- For $y/D_h \geq 3$, the velocity profile is close to be homogenous, i.e. $0.9 \leq \|\bar{U}\|/U_{flow} \leq 1.1$.

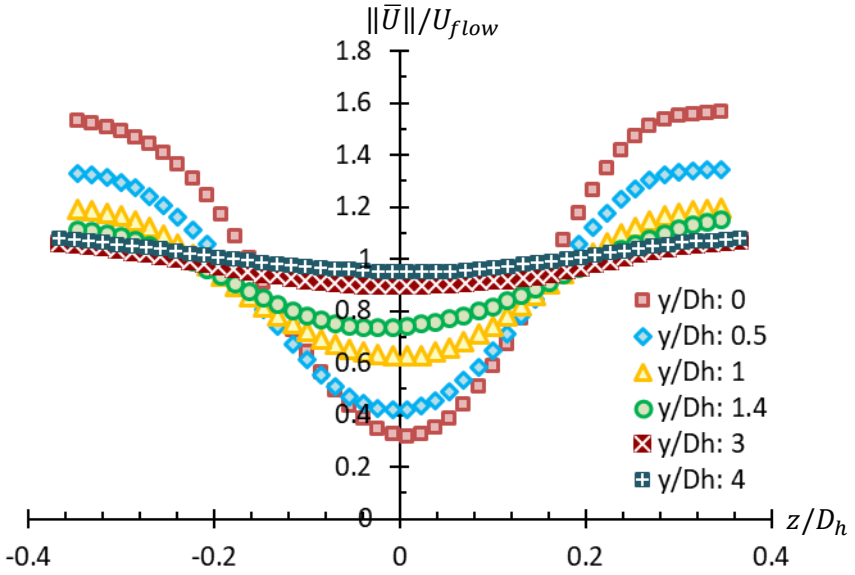

Figure 60: Velocity profiles of $\|\bar{U}\|/U_{flow}$ of $Re_{Dh} = 20100$ for NMV with different distances

The variation of the amplitude of $\|\bar{U}\|/U_{flow}$ is 80% for the $y/D_h = 0$ and decreases to 11% at $y/D_h = 4.4$. This variation, $\Delta\|\bar{U}\|/U_{flow}$ is observed to decrease exponentially with the distance from the grid as:

- $\Delta\|\bar{U}\|/U_{flow} \sim 77.31e^{-0.47\left(\frac{y}{D_h}\right)}$

Figure 61 shows the profiles of dimensionless velocity field component, u_y/U_{flow} and u_z/U_{flow} for $Re_{Dh} = 20100$. Figure 61(a) shows that the main component of the velocity field is the vertical component u_y, i.e. in direction of the mean flow. The result shows similar profile as the mean velocity profile.

Figure 61(b) shows the horizontal component u_z with the increased distance from the grid. The result shows a trend to symmetry on the profile. For $0 \leq z/D_h \leq 0.4$ the velocity shows positive values and for $-0.4 \leq z/D_h \leq 0$ this component becomes negative values. This kind of profile can be also observed in turbulent shear flow. (Dey, et al., 2018)

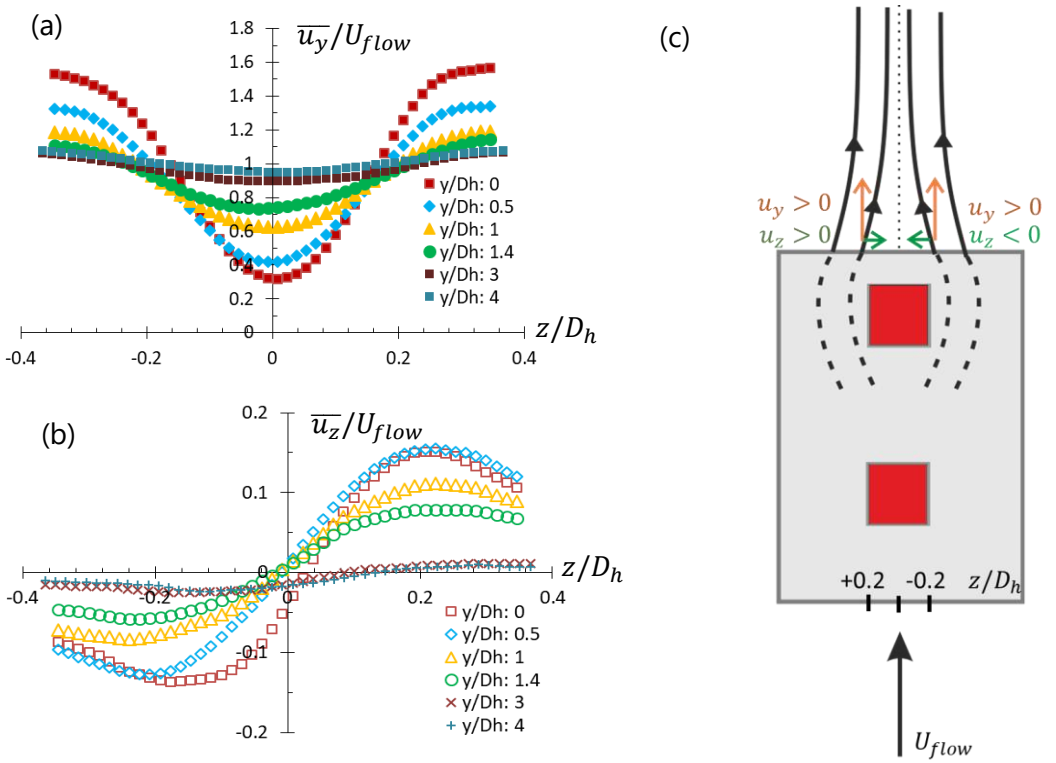

Figure 61: Velocity profiles of (a) u_y/U_{flow} (b) u_z/U_{flow} of $Re_{Dh} = 20100$ for NMV with different distances (c) schematics of the flow

From the result, on the centre of the dimple the zero-crossing can be observed from $0.5D_h$ to $1.4D_h$. This process is shown in the schematics of the flow as Figure 61(c).

The negative values of u_z/U_{flow}, shows that the flow moving towards the $0 \leq z/D_h \leq 0.4$, i.e. from right to left hand side. The positive values of u_z/U_{flow} shows the flow moving towards the $-0.4 \leq z/D_h \leq 0$, i.e. from left to right hand side. The intensity of the u_z/U_{flow} values are similar on both side, i.e. the difference in maximum value of $|u_z/U_{flow}|$ is 9%. This small difference leads the flow that is coming from the both side of the dimple towards the centre of the dimple, i.e. filling the zone behind the dimple.

With the increased distance, i.e. $y/D_h = 3$, u_z component is losing its intensity, i.e. $-0.02 \leq u_z/U_{flow} \leq 0.01$. This also shows coherent behaviour with the u_y component where the velocity field is start to get homogenous, i.e. standard deviation of u_y/U_{flow} is decreasing from 0.45 to 0.059 for $y/D_h = 0$ and 3, respectively.

Figure 62, Figure 63 and Figure 64 show velocity profiles for different Reynolds number i.e. $Re_{Dh} = 11200, 13500, 15600, 66000$ and 151200. Each profile is plotted for different distances as $y/D_h = 0, 0.5, 1$ and 1.4 as (a), (b), (c) and (d), respectively. All of the profiles show coherent behaviour with Figure 61.

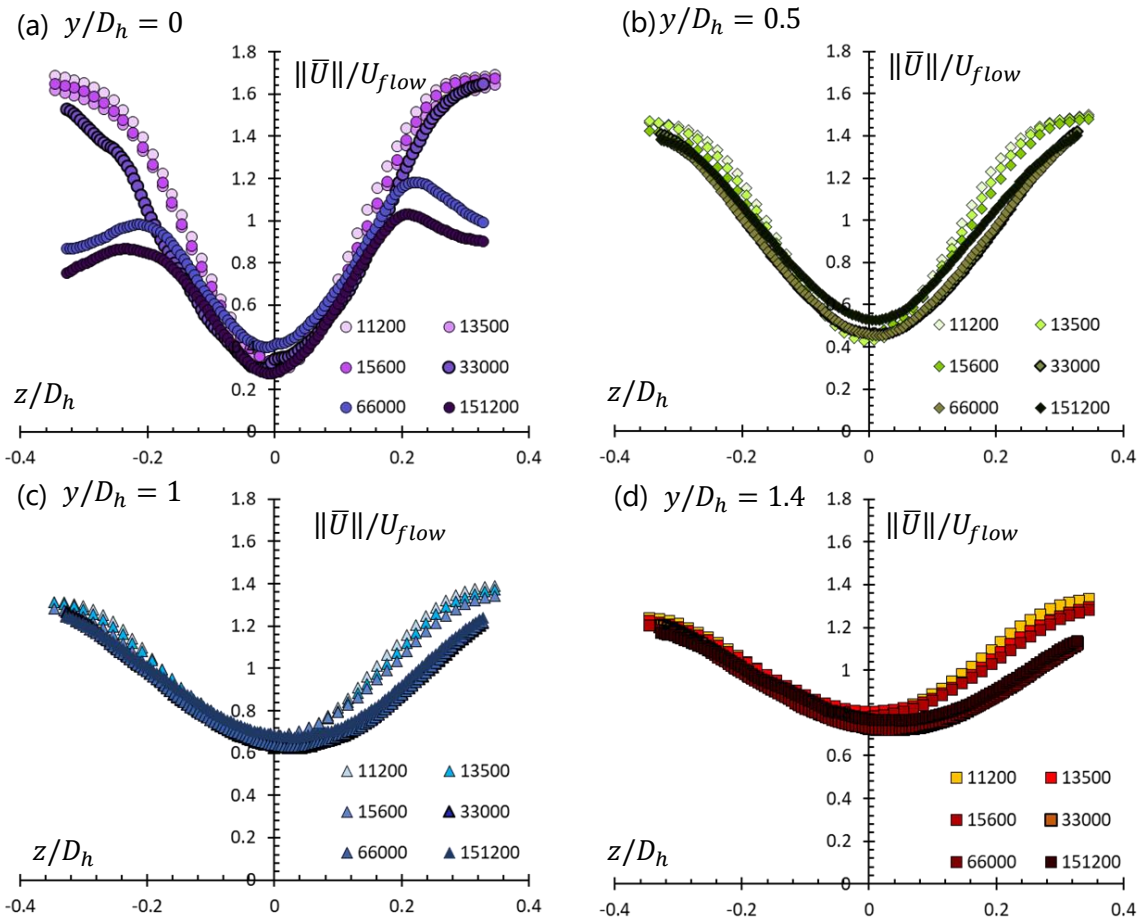

Figure 62: NMV configuration velocity profiles of $\|\overline{U}\|/U_{flow}$ of $Re_{Dh} = 11200, 15600, 33000, 66000, 151200$ for $y/D_h = (a)0, (b)0.5, (c)1$ and $(d)1.4$

Figure 62 shows the dimensionless temporal average of the velocity profiles, i.e. $\|\overline{U}\|/U_{flow}$. For all Reynolds numbers with the increase of the distance from grid, the flow starts to get more homogenous, i.e. the average standard deviation for $y/D_h = 0$ is 0.38 and for $y/D_h = 1.4$ this value is decreased to 0.15.

Figure 63 and Figure 64 shows the $\overline{u_y}/U_{flow}$ and the $\overline{u_z}/U_{flow}$ profiles, respectively.

- The results show that the main component of the flow is u_y where the profiles are matching with the $\|\overline{U}\|/U_{flow}$. As observed in Figure 62, with the increasing distance from the grid, the u_y component becomes more uniform.
- The $\overline{u_z}$ component shows the same "close to be symmetrical" behaviour as seen in Figure 61. The standard deviation of $\overline{u_z}/U_{flow}$ is decreasing with the increased distance from the grid, i.e. from 0.13 to 0.05 for $y/D_h = 0$ and 1.4 respectively.
- For $y/D_h = 0$, all of the Reynolds number shows same intensity for both side of the dimple with the zero-crossing in the centre. For $y/D_h \geq 0.5$, with the increase of Reynolds number, this zero-crossing point is observed to move towards to $0 \leq z/D_h \leq 0.4$ side. This also shows coherent behaviour where the streamlines shows slight tilt towards $0 \leq z/D_h \leq 0.4$ in Figure 57(c) and Figure 57(d) for $y/D_h = 0$ and Figure 59 for $y/D_h = 3$.

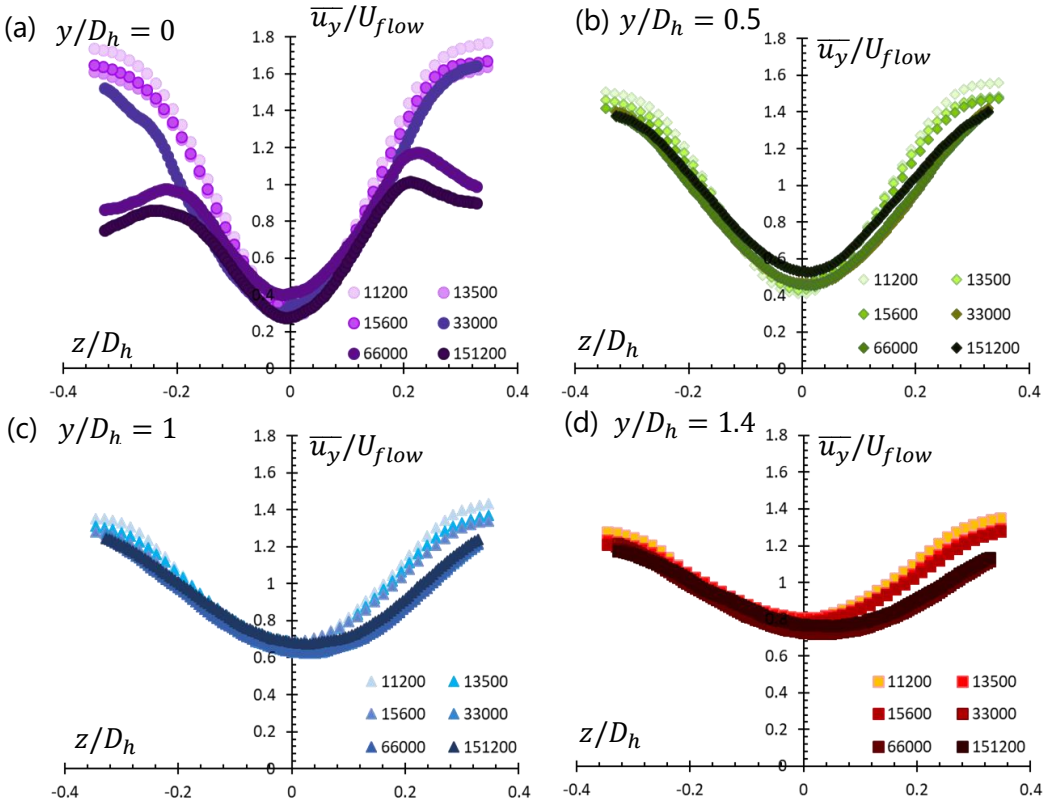

Figure 63: NMV configuration velocity profiles of $\overline{u_y}/U_{flow}$ of $Re_{Dh} = 11200, 15600, 33000, 66000, 151200$ for $y/D_h =$ (a)0, (b)0.5, (c)1 and (d)1.4

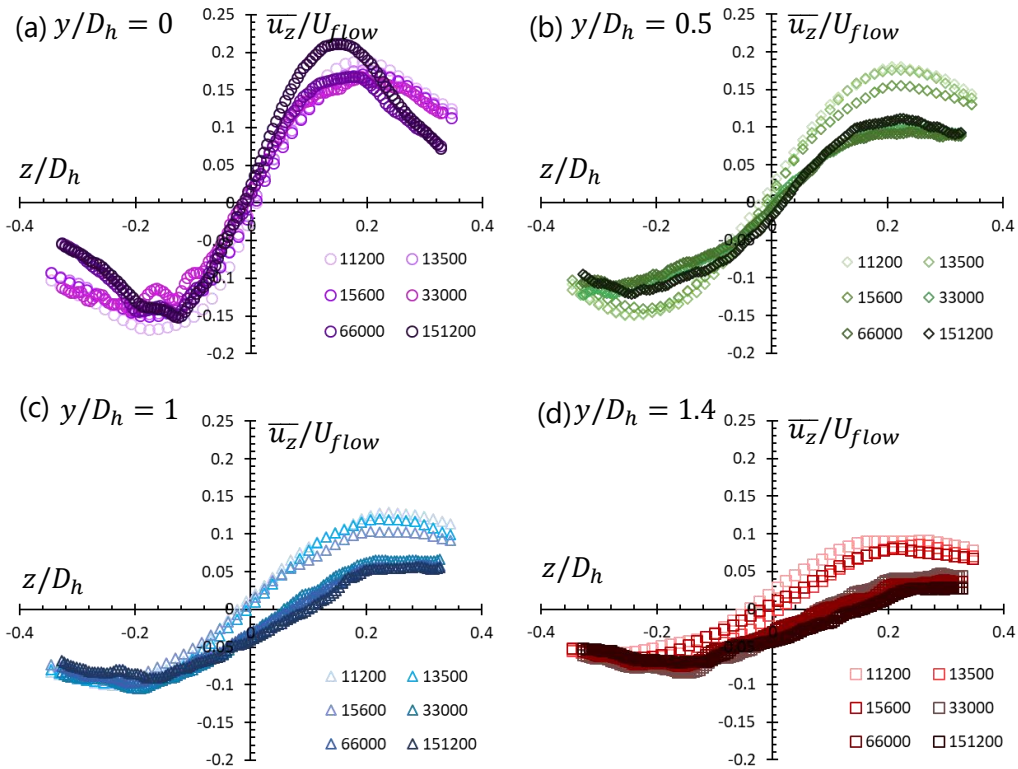

Figure 64: NMV configuration velocity profiles of $\overline{u_z}/U_{flow}$ of $Re_{Dh} = 11200, 15600, 33000, 66000, 151200$ for $y/D_h =$ (a)0, (b)0.5, (c)1 and (d)1.4

9.2.4 Velocity fluctuations for configuration No Mixing Vane

To study the velocity fluctuations, U'_{RMS}/U_{flow} is calculated. Figure 65(a) and Figure 65(b) shows the U'_{RMS}/U_{flow} field and profile, respectively for $Re_{Dh} = 20100$.

From the results of Figure 65(a), velocity fluctuations are observed to be more intense, i.e. $0.39 \leq U'_{RMS}/U_{flow} \leq 0.44$, within the shear layers, i.e. $z/D_h = +1.6$ and -1.6.

Close to the grid, i.e. $y/D_h = 0$, a "M" shape is observed. With the increase of the distance, i.e. until $y/D_h = 0.3$, the maxima of the "M" shape intensity is observed to increase from 0.40 to 0.44.

The intensity of the fluctuations are observed to be maximum on both sides of the dimple around $y/D_h = 0.3$. With more distance, i.e. around after $y/D_h = 1$, it is noticed that the two shear layers have merged and the intensity of velocity fluctuations are started to decrease from 0.4 to 0.3.

Figure 65(b) shows the change of intensity of the velocity fluctuations for different distances, i.e. $0 \leq y/D_h \leq 4.9$. The quantification of the decrease in U'_{RMS}/U_{flow} is plotted for these distances in Figure 65(c) for different z/D_h as $0.16, 0$ and -0.16. As observed in the U'_{RMS}/U_{flow} field and profiles, an initial increase in intensity of U'_{RMS}/U_{flow} from 0.3 to 0.4 can be seen between the range $0 \leq y/D_h \leq 0.5$ for all z/D_h profiles . After this increase, an exponential decrease is detected on the U'_{RMS}. The intensity of the fluctuations are higher on $z/D_h = 0.2$.

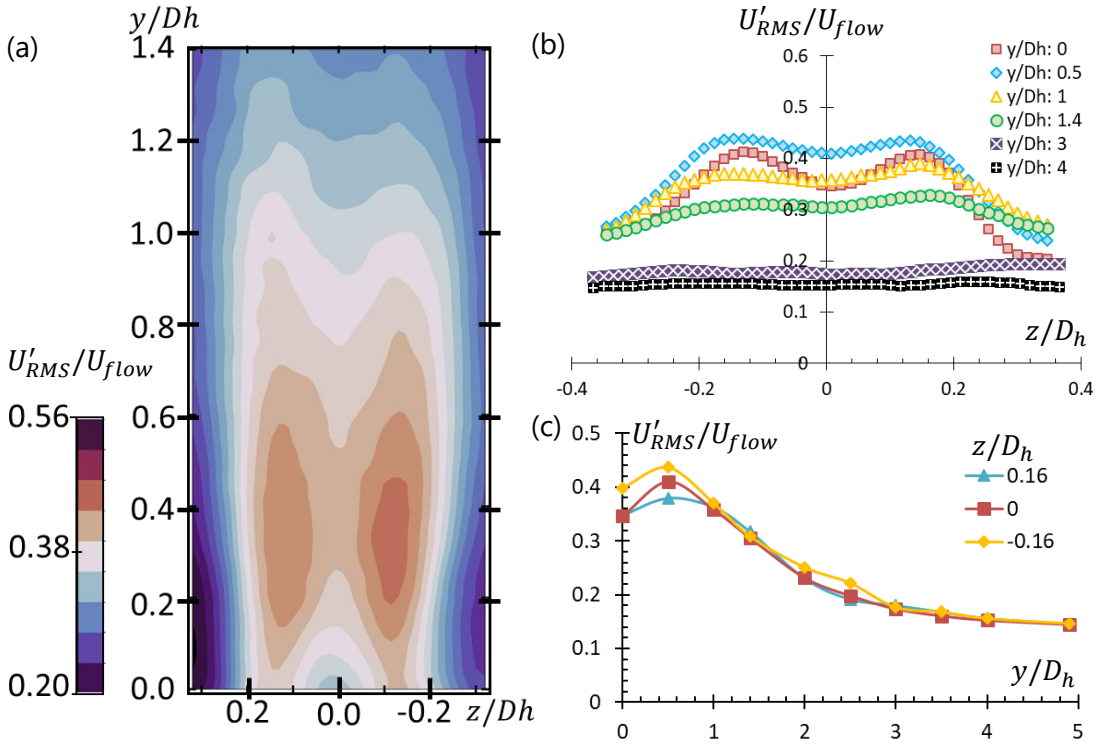

Figure 65: (a) U'_{RMS}/U_{flow} field at $y/D_h = 0$ and (b) U'_{RMS}/U_{flow} profile with different distances of Re=20100 for NMV (c) Intensity of U'_{RMS}/U_{flow} for different z/D_h profiles

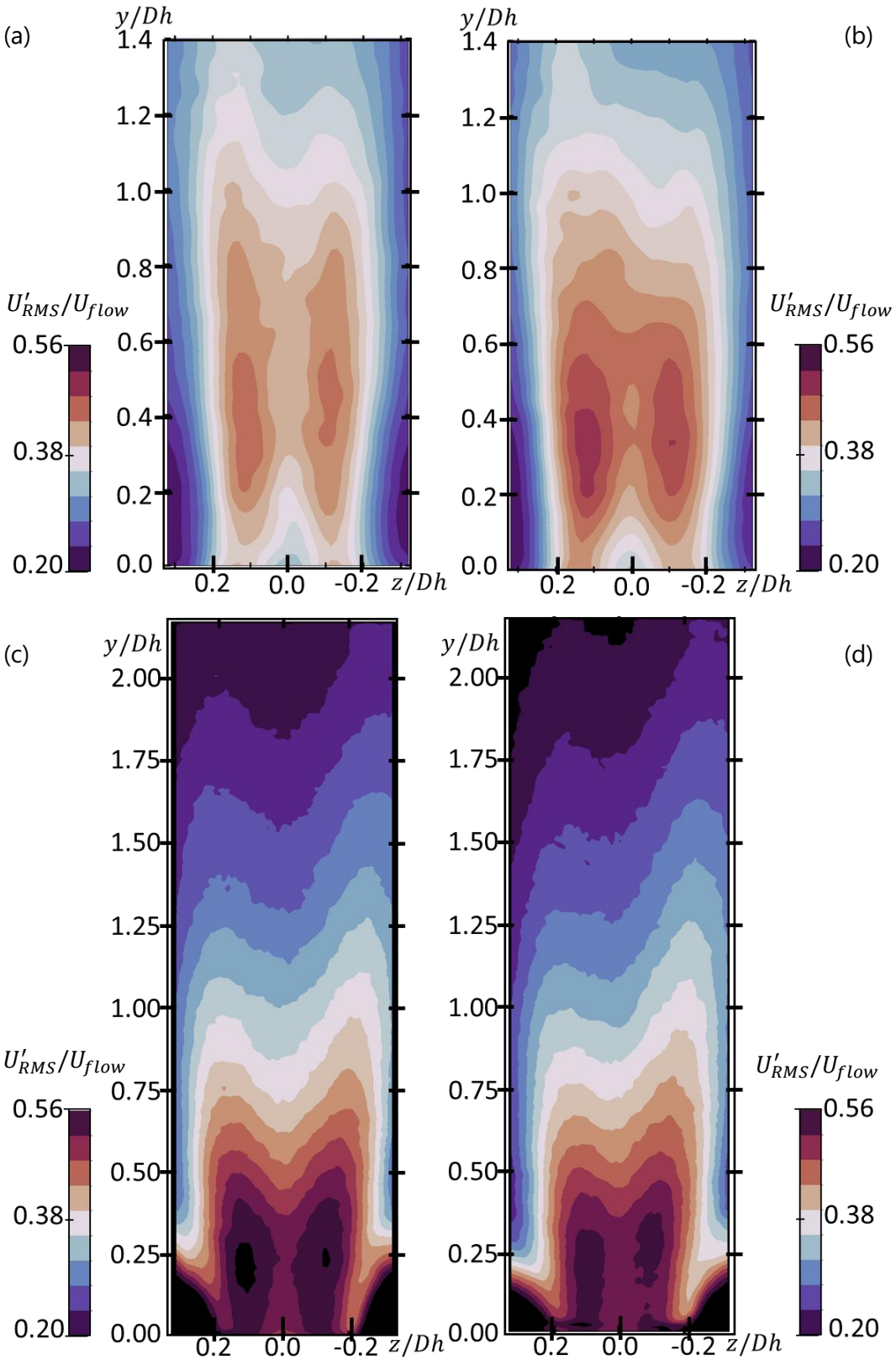

Figure 66: U'_{RMS}/U_{flow} field for NMV at $0 \leq y/D_h \leq 1.4$ for $Re_{Dh} = (a)11200, (b)15600$ and at $0 \leq y/D_h \leq 2.2$ for $Re_{Dh} = (c)66000, (d)151200$

The U'_{RMS}/U_{flow} field is plotted for different Reynolds number as $Re_{Dh} = 11200, 15600, 66000$ and 151200 in Figure 66. The results show high velocity fluctuations on both side of the dimple. It is observed that with the increase of the Reynolds number, the intensity of the velocity fluctuations are also increased. For $Re_{Dh} = 151200$ the maximum U'_{RMS}/U_{flow} is 0.56 at $y/D_h = 0$ and this value decreases to 0.40 for $Re_{Dh} = 11800$, i.e. 28% decrease. For the distance $y/D_h = 1.4$, the difference of U'_{RMS}/U_{flow} between $Re_{Dh} = 11800$ and 151200 becomes %11.

Figure 67 shows the U'_{RMS}/U_{flow} profiles for different Reynolds number, i.e. $Re_{Dh} = 11200, 13500, 15600, 33000, 66000$ and 151200. Each profile is plotted for different distances as $y/D_h = 0, 0.5, 1$ and 1.4 as (a), (b), (c) and (d), respectively.

The plots show the same behaviour as Figure 65 for all the Reynolds number. The fluctuations have high intensities close to spacer grid, i.e. $0 \leq y/D_h \leq 0.3$, and with the increased distance the intensity of fluctuations are decreasing.

At $y/D_h = 0$, the profile shows higher intensity of fluctuations with the increase of the Reynolds number. This difference of intensity is decreasing with the increase of the distance away from the grid for $Re_{Dh} = 11200, 13500, 15600$. At $y/D_h \geq 0.5$, the intensities of the fluctuations are observed as the same level. After $y/D_h = 0.5$, the intensity of fluctuations are decreasing where the velocity fluctuations are slightly higher on one side of the dimple, i.e. $0 \leq z/D_h \leq 0.3$ with the increasing distance.

The variation of the fluctuation intensity is found as 18% for $Re_{Dh} = 11200$ and 41% for $Re_{Dh} = 151200$ for the distance between $0.5 \leq y/D_h \leq 1.4$.

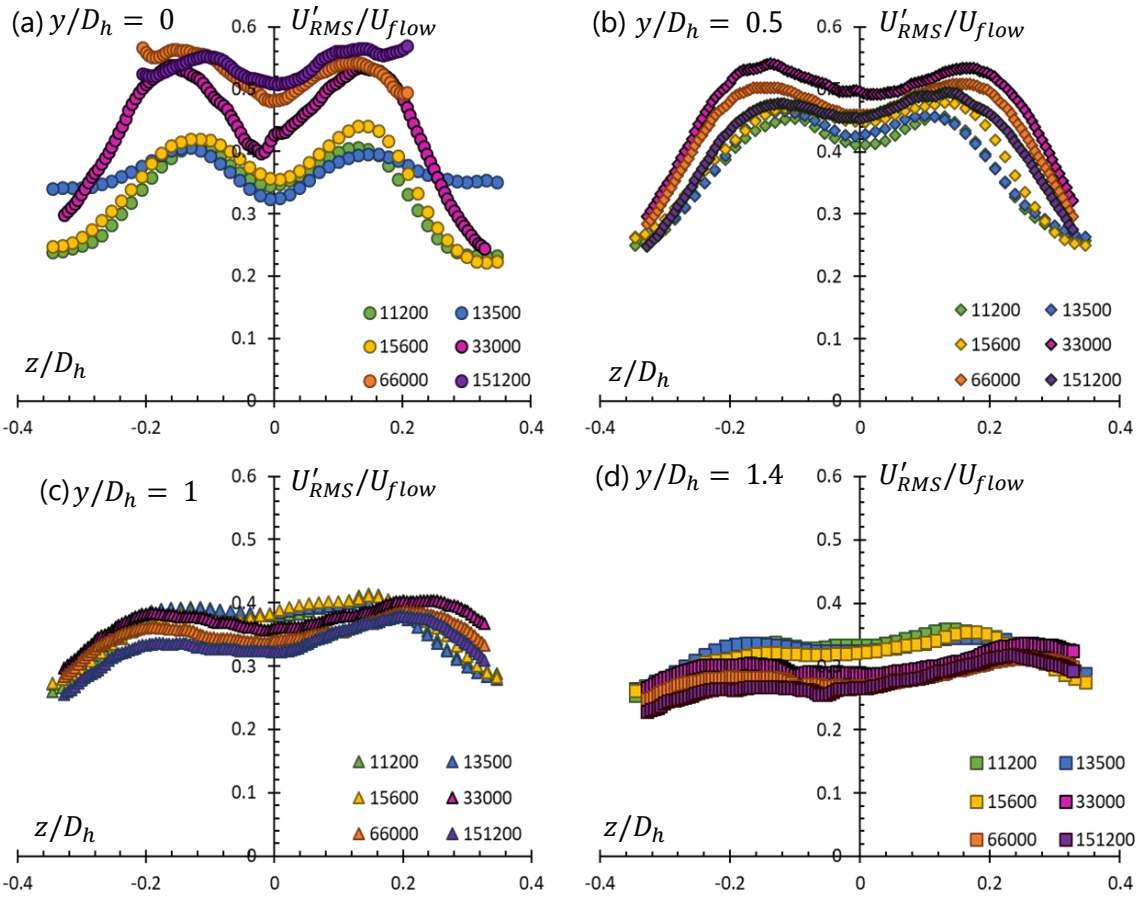

Figure 67: NMV configuration U'_{RMS}/U_{flow} profiles of $Re_{Dh} = 11200, 15600, 33000, 66000, 151200$ for $y/D_h =$ (a)0, (b)0.5, (c)1 and (d)1.4

Figure 68 shows U'_{RMS}/U_{flow} field at $3 \leq y/D_h \leq 4.4$ for $Re_{Dh} = 11200$ and 15600. The results shows maximum intensity of the velocity fluctuations is about 0.24 on $0 \leq z/D_h \leq 0.3$ side of the dimple. This result is in coherence with Figure 67(d) where the intensity of the fluctuations are observed higher on one side of the dimple. For lower Reynolds number, i.e. $Re_{Dh} = 11200$, the fluctuations are more intense farther from the grid.

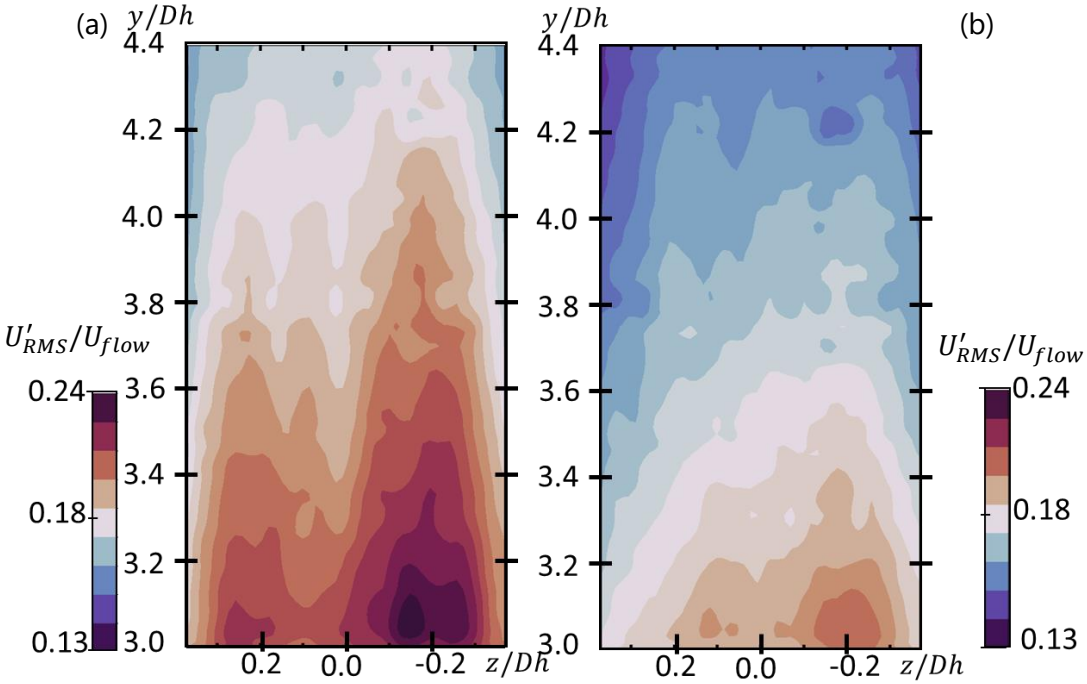

Figure 68: U'_{RMS}/U_{flow} field for NMV at measurement domain $3 \leq y/D_h \leq 4.4$ for $Re_{Dh} = (a)11200$ and $(b)15600$

9.2.5 Velocity field for configuration With Mixing Vane

Figure 69(a) shows the position of the laser sheet with the mixing vane. The mixing vanes that are visible on the measurement domain are marked with yellow. The mixing vane is directed towards the central rod is marked as "L" and the mixing vane of the front mesh is marked as "R". The orientation of the mixing vanes and the position of the dimples can also be seen in the Figure 69(b).

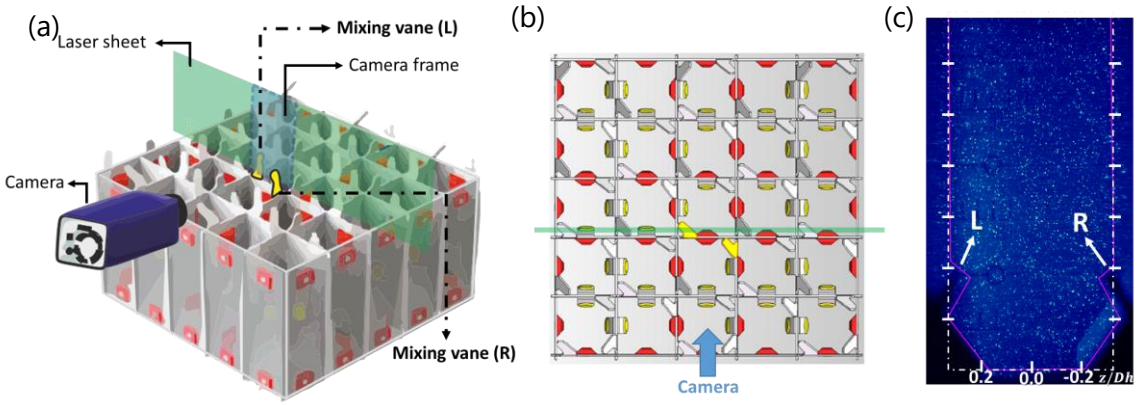

Figure 69: Position of mixing vane for PIV measurements (a) 3d schematic (b) top view of spacer grid (c) recording frame

Figure 69(c) shows the camera frame with the visible mixing vanes. The mixing vanes are marked with pink line. The mixing vanes can be seen on the left and right hand side are labelled with "L" and "R". The mixing vane "R" is positioned in front of the central mesh.

Figure 70 shows the instantaneous velocity field, $\|U\|/U_{flow}$, for WMV configuration at the exit of the grid. The streamlines are plotted using the velocity components u_y and u_z in the frame reference of the laboratory. The mixing vanes are marked with orange dashed line.

In the figures four different Reynolds number are presented. For $Re_{Dh} = 11200, 15600$, the length of the measurement domain is $0 \leq y/D_h \leq 1.4$ and for $Re_{Dh} = 60500, 104900$ the length of the measurement domain is $0 \leq y/D_h \leq 1.6$.

On instantaneous velocity field, similarly to the NMV configuration, different velocity regions are observed with low and high velocity regions. These low and high velocity regions are presented as blue and red, respectively.

In Figure 70, the high and low velocity regions are appeared as on different sides.

- The high velocity region is observed for $0 \leq z/D_h \leq 0.3$. The highest velocity region can be seen on the end of the mixing vane.
- Between $-0.1 \leq z/D_h \leq 0$ a second high velocity region is observed.
- The overall shape of the high velocity region resembles "λ" shape.
- The low velocity region is detected for the side $-0.3 \leq z/D_h \leq 0$.

This behaviour of the flow is about the same for the broad range of Reynolds number, i.e.11209 - 117550.

With the increasing distance from the spacer grid, the velocity field remains more heterogeneous compared to NMV configuration. The high velocity region persists with the distance away from the grid.

Figure 71 shows the mean velocity field $\|\bar{U}\|/U_{flow}$ at the exit of the grid. The results show a clear view of different velocity regions and the shear layers. The clear shape "λ" is observed for high velocity region. With the increasing Reynolds number, the intensity of this high velocity region is decreased. For all the Reynolds number, the "legs" of λ is noticed to merge around $y/D_h = 0.3$. Between the "legs" of λ, low velocity region is detected.

Compared to NMV configuration, for the WMV configuration presents a change of direction on the shear layer between these high and low velocity regions.

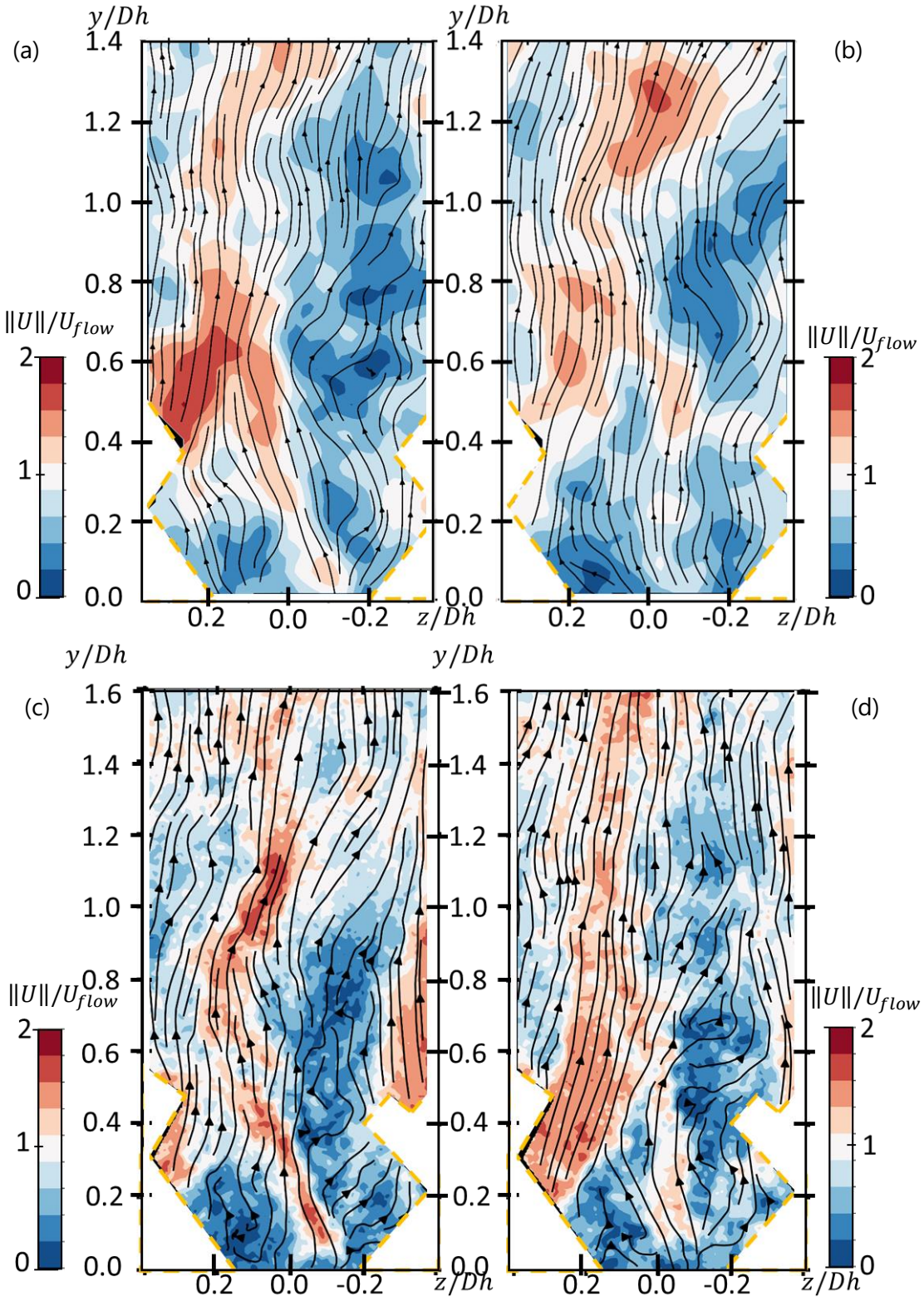

Figure 70: Instananeous velocity field for WMV at measurement domain $0 \leq y/D_h \leq 1.4$ for $Re_{Dh} = (a)11200,\ (b)15600$ and at $0 \leq y/D_h \leq 1.6$ for $Re_{Dh} = (c)\ 60500, (d)104900$

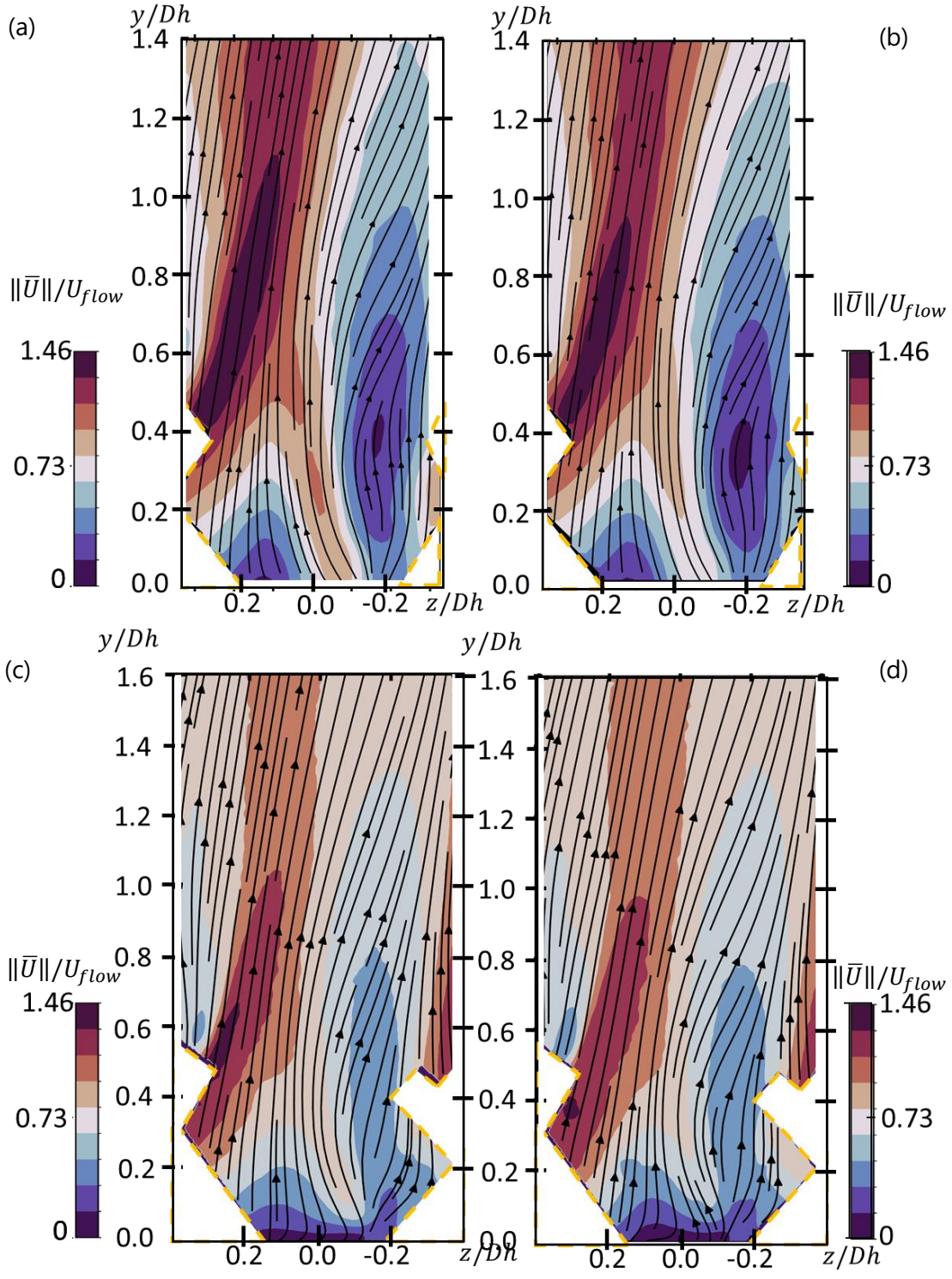

Figure 71: Mean velocity field for WMV at measurement domain $0 \leq y/D_h \leq 1.4$ for $Re_{Dh} = (a)11200,\ (b)15600$ and at $0 \leq y/D_h \leq 1.6$ for $Re_{Dh} = (c)\ 60500, (d)104900$

Figure 72 shows the instantaneous velocity field, $\|U\|/U_{flow}$, for WMV configuration from $y/D_h \geq 3$ away from the spacer grid. The velocity field is more homogenous. $\|U\|/U_{flow}$ is in the range of 0.8-1.2.

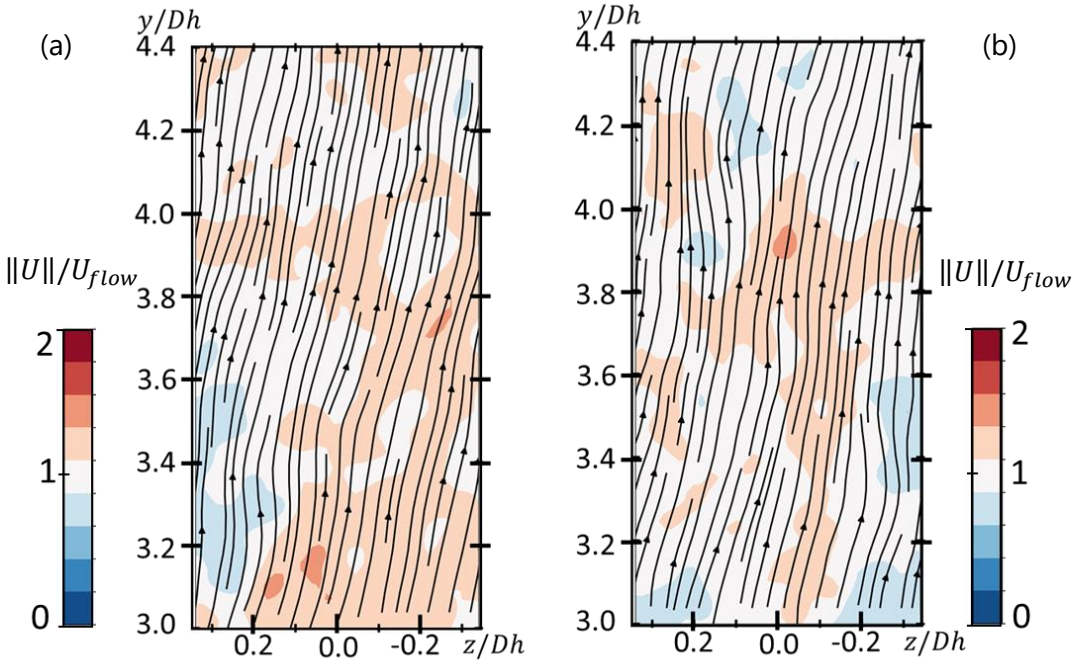

Figure 72: Instananeous velocity field for WMV at measurement domain $3 \leq y/D_h \leq 4.4$ for $Re_{Dh} = (a)11200,\ (b)15600$

Figure 73 shows the mean velocity field of $3 \leq y/D_h \leq 4.4$ for $Re_{Dh} = 11200, 15600$. The figures are plotted according to average minimum and maximum value of the results, i.e. $\|\bar{U}\|/U_{flow}$ ~$0.96 - 1.16$.

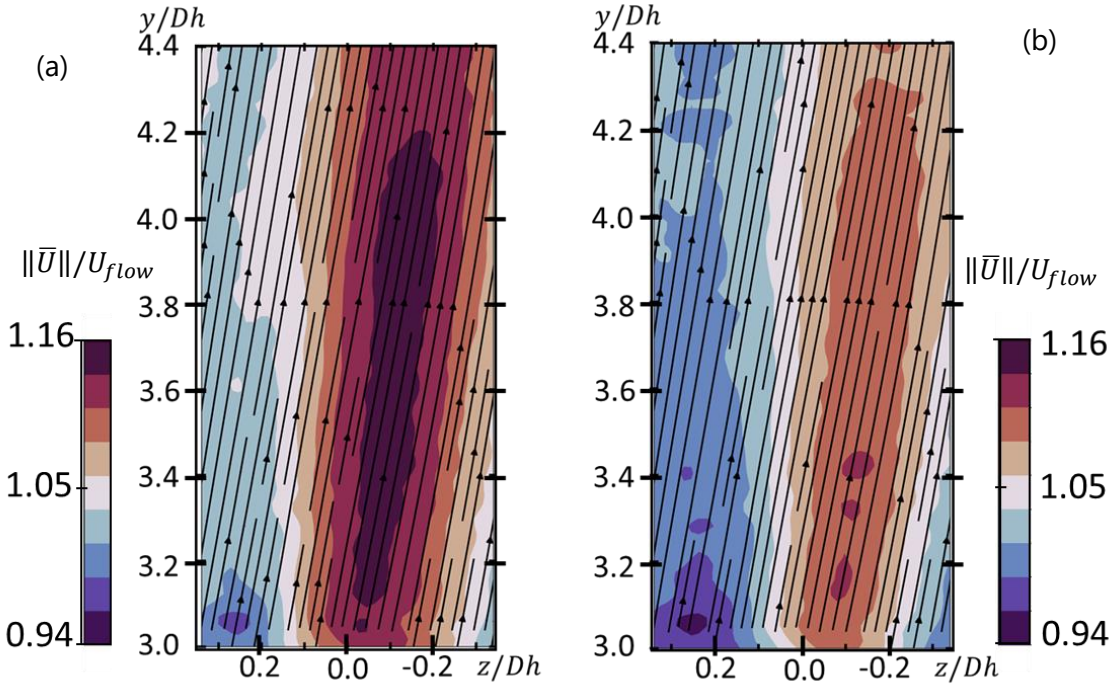

Figure 73: Mean velocity field for WMV at measurement domain $3 \leq y/D_h \leq 4.4$ for $Re_{Dh} = (a)11200,\ (b)15600$

The signature of the λ that is spotted for $0 \leq y/D_h \leq 1.4$, continues for $3 \leq y/D_h \leq 4.4$. This continuation can be seen as relatively higher velocity region, i.e. $1 \leq \|\overline{U}\|/U_{flow} \leq 1.16$, around $-0.2 \leq z/D_h \leq 0$.

9.2.6 Velocity profiles for configuration With Mixing Vane

To confirm the trends of the velocity distribution, the velocity profiles are plotted for each component of the flow according to the distances away from the grid.

9.2.6.1 Velocity profile at $y/D_h = 0$ for configuration WMV

Figure 74 shows the velocity profile of $\|\overline{U}\|/U_{flow}$ at $y/D_h = 0$ for $Re_{Dh} = 20100$. The results includes different PIV methods, i.e. High-speed PIV and Low-speed PIV, and different processing coefficient for High-speed PIV, i.e. k=1, k=2 and k=3. The k coefficient shows the reorganization of the frames. Time between each frame is represented as $t_{frame} = k * 1/f_{recording}$. This shows with the increasing k, the displacement of the particle is increasing.
In Figure 74, k=1 and k=2 shows similar profiles. The difference between the $\|\overline{U}\|/U_{flow}$ is found 13% in average.
For both k=1 and k=2, an increase on the $\|\overline{U}\|/U_{flow}$ can be seen around $z/D_h = 0.1$.

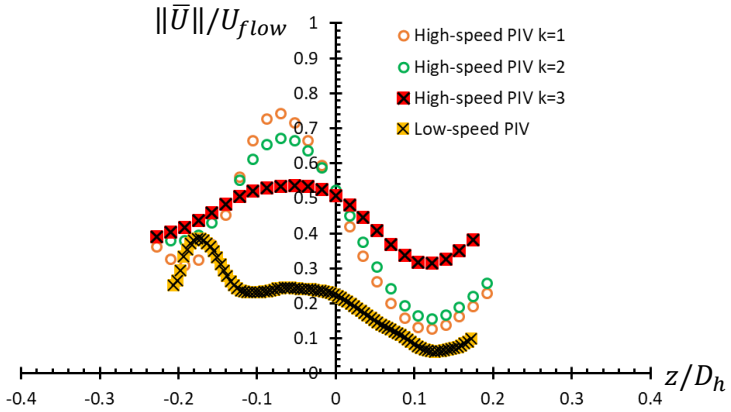

Figure 74: Velocity profile of $\|\overline{U}\|/U_{flow}$ of $Re_{Dh} = 20100$ for WMV configuration at $y/D_h = 0$

For High-speed PIV with k=3 and Low-speed PIV measurements, the $\|\overline{U}\|/U_{flow}$ profile is observed to have similar behaviour for $-0.1 \leq z/D_h \leq 0.2$. Although the profiles are similar, the values of $\|\overline{U}\|/U_{flow}$ are lower in comparison with k=1 and k=2.
In (Matozinhos, et al., 2021), at the tip of the mixing vanes the velocity contours shows two opposing secondary flows which follows the orientation of the mixing vanes. The components of the secondary flows are u_x and u_z.
The inconsistency of these results might be connected to high intensity of u_x component which is not measured with planar PIV. With lower time difference between the frames, i.e. k=1 and k=2, the displacement of the particles are able to captured with 3% pixel of uncertainties according to maximum displacement. For k=3 and Low-speed PIV, it can be seen that the particles pass through the laser sheet faster than the recording frequencies which leads to out of frame effect.
Although k=1 and k=2 give a representative profile of the flow, the mean flow, $\|\overline{U}\|$, is observed always lower than the U_{flow} where the maximum value is found around $\|\overline{U}\|/U_{flow} \sim 0.78$.
To understand the reason of difference between the results, the maximum displacement values are investigated. Table 13 shows the maximum displacement in the measurement domain and the mean displacement value for the selected $0 \leq y/D_h \leq 0.1$ region.

Measurement and processing method	Max. Displacement [pxl]	Mean displacement [pxl] at $y/D_h = 0 - 0.1$
High-speed PIV (k=1)	3.59	1.3
High-speed PIV (k=2)	7.30	2.5
High-speed PIV (k=3)	11.58	3.4
Low-speed PIV	15	3.7

Table 13: Pixel displacement information for $Re_{Dh} = 20100$

The displacement information shows 20% difference for mean displacement values for $0 \leq y/D_h \leq 0.1$ region between different processing coefficient of k. This increase of mean displacement value can lead to loss of position of the particles. The difference between k=3 and Low-speed PIV shows 8% difference on the mean displacement results which is an expected result since the profiles are observed to be similar.

Figure 75 shows the correlation windows of the High-speed PIV with k=2 for different positions.

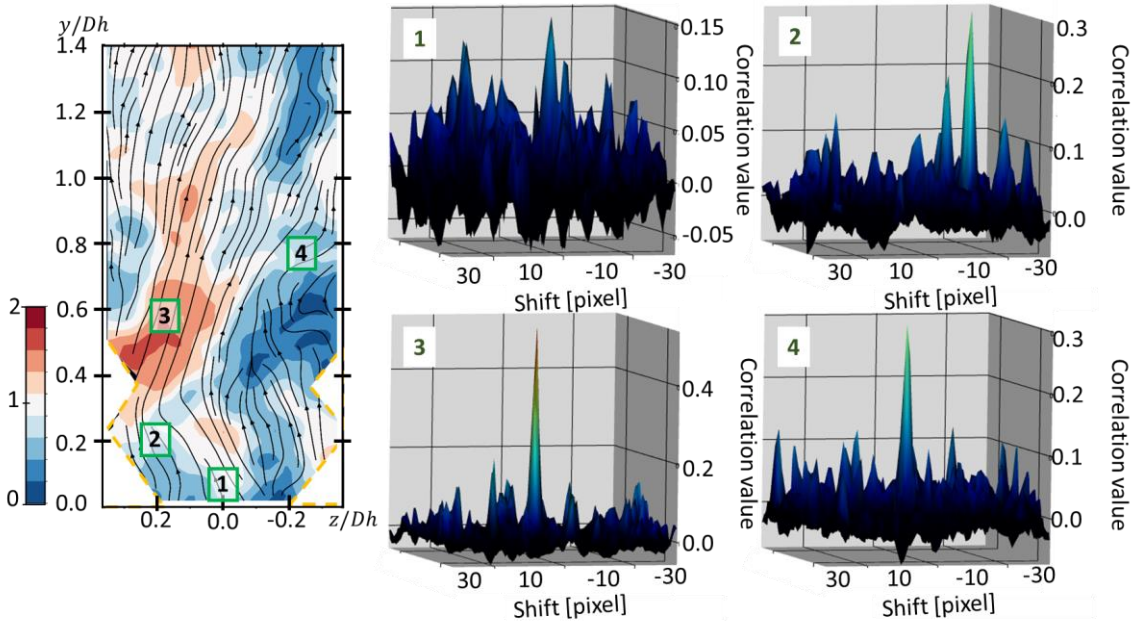

Figure 75: Correlation window of High-speed PIV measurements with k=2 for $Re_{Dh} = 20100$

From the results, it is seen that for region $0 \leq y/D_h \leq 0.1$, the correlation values are low and no clear peak can be observed. Around $y/D_h = 0.2$, i.e. position 2, the peaks are observed to be visible. The ratio between the first peak and the second peak (Xue, et al., 2013) is found 1.5. After the mixing vanes, i.e. position 3-4, each correlation window has one clear peak with low noise ratio.

Figure 76 shows the correlation window results for k=3 and Low-speed PIV as (a) and (b), respectively. For Figure 76(a), at both position 1 and 2, the measurements have a noisy results. In Figure 76(b), high noise levels are detected at position 1. For both k=3 and Low-speed PIV, the ratio between the first peak and the second peak is found 62% lower compared to k=2 for $0 \leq y/D_h \leq 0.1$, i.e. position 1.

For the increased distance from the grid, i.e. position 2, with Low-speed PIV measurements, the correlation results are observed with one clear peak.

Due to the inconsistent and low correlation at $y/D_h = 0$, the profile at this point is not included with profiles for other distances.

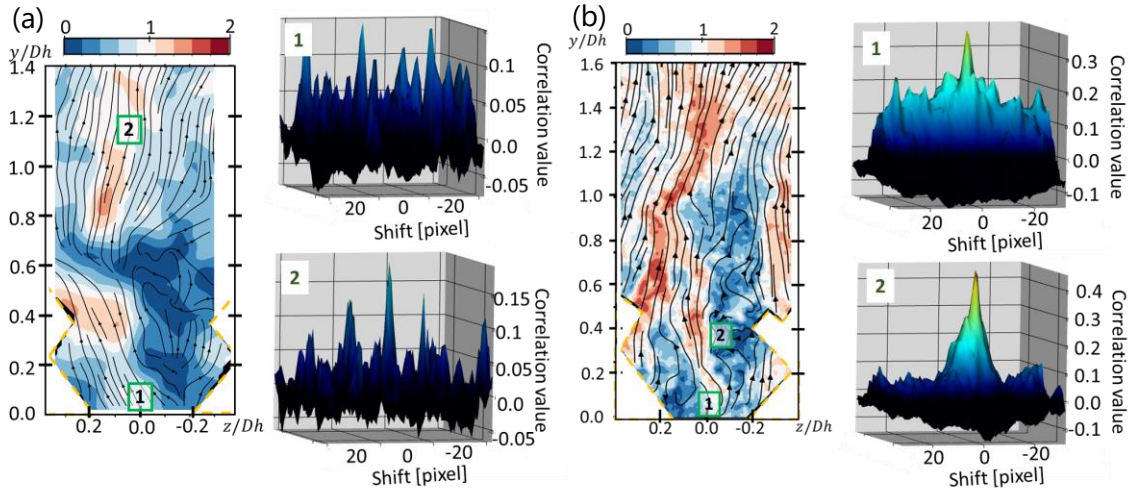

Figure 76: Correlation window of (a)High-speed PIV measurements with k=3 (b)Low-speed PIV for $Re_{Dh} = 20100$

9.2.6.2 Velocity profiles for different distances for configuration WMV

Figure 77 shows the profiles of dimensionless mean velocity field $Re_{Dh} = 20125$ for distances $y/D_h = 0.2, 0.5, 1, 1.4, 3$ and 4.

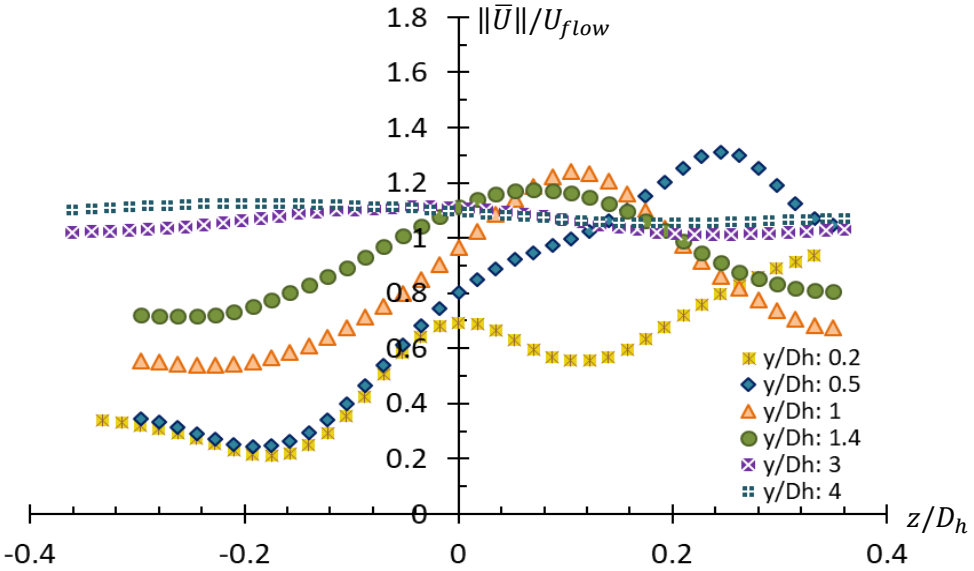

Figure 77: Velocity profiles of $\|\bar{U}\|/U_{flow}$ of $Re_{Dh} = 20100$ for WMV with different distances

For $y/D_h = 0.2$, an asymmetrical "W" shape is observed on profile. Two local minima of $\|\bar{U}\|/U_{flow}$, are about 0.21 and 0.55 , respectively at $z/D_h = -0.17$ and 0.12. Three local maxima of $\|\bar{U}\|/U_{flow}$, are 0.33 , 0.69 and 0.93 at $z/D_h = -0.34$, 0 and 0.34, respectively.
For $y/D_h > 0.2$, the profiles have a wave shape with one local maximum and minimum. In Table 14 the details of local maximum, i.e. $\left[\|\bar{U}\|/U_{flow}\right]_{max}$, local minimum, i.e. $\left[\|\bar{U}\|/U_{flow}\right]_{min}$ are given. This table includes the related positions with the amplitude of the wave shape.

y/D_h	$[\|\bar{U}\|/U_{flow}]_{max}$	z/D_h	$[\|\bar{U}\|/U_{flow}]_{min}$	z/D_h	Amplitude
0.5	1.31	0.24	0.24	-0.19	1.07
1	1.23	0.10	0.53	-0.24	0.70
1.4	1.17	0.06	0.71	-0.26	0.46
3	1.11	-0.02	1.01	0.24	0.10
4	1.13	-0.15	1.05	0.20	0.08

Table 14: Local maximum, local minimum and the amplitude of the $\|U\|/U_{flow}$ profile for $Re_{Dh} = 20100$ with WMV configuration

The local maximum positions at $y/D_h = 0.5$ corresponds to the tip of the mixing vane (L). Increasing of velocity is in agreement with mass conservation where the cross-sectional area is decreasing due to the mixing vanes. The difference between the maximum and the minimum velocity is the highest for the measurement domain, i.e. the amplitude is 1.07. The local minimum at $z/D_h = -0.19$ shows that no disturbance occurs on the flow in the measurement domain due to the neighbour mixing vane (R).

After mixing vane, i.e. $y/D_h > 0.5$, the maximum local velocity is observed to shifted towards the neighbour mixing vane (R) with decreasing difference between maximum and minimum local velocity.

The trend of the wave amplitude for $\|\bar{U}\|/U_{flow}$ between $0.5 \leq y/D_h \leq 4$ is approximated to logarithmic function:

- $-0.475 \ln\left(\frac{y}{D_h}\right) + 0.67$

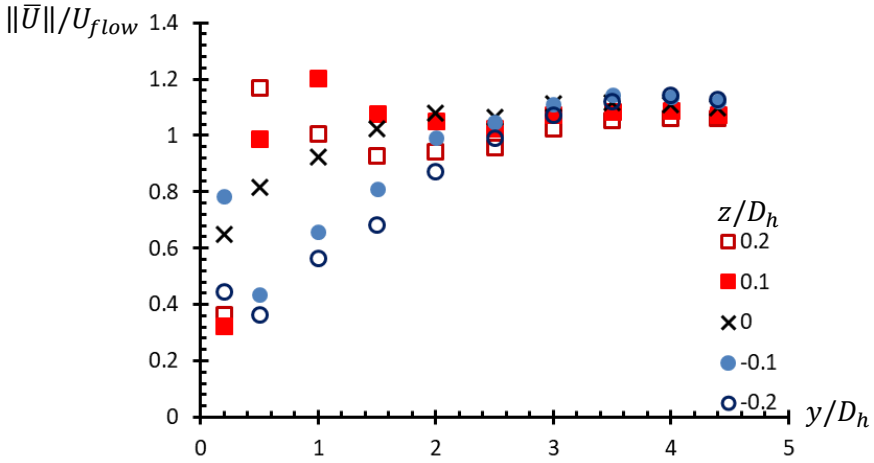

Figure 78: $\|\bar{U}\|/U_{flow}$ profile for increasing distance from grid with $z/D_h = 0.2, 0.1, 0, -0.1$ and -0.2

Figure 78 shows the $\|\bar{U}\|/U_{flow}$ profile for increasing distance from the spacer grid. The graph includes different z/D_h values.

The results complements the velocity profiles. The flow has high variations of $\|\bar{U}\|/U_{flow}$ between $0.2 \leq y/D_h \leq 2.5$. For $2.5 < y/D_h \leq 4.4$, the velocity starts to stabilize around $\|\bar{U}\|/U_{flow} = 1.1$.

Figure 79(a) and Figure 79(b) show the u_y and u_z components of the velocity, respectively. Figure 79(c) is the schematics of the flow built according to Figure 79(a) and Figure 79(b).

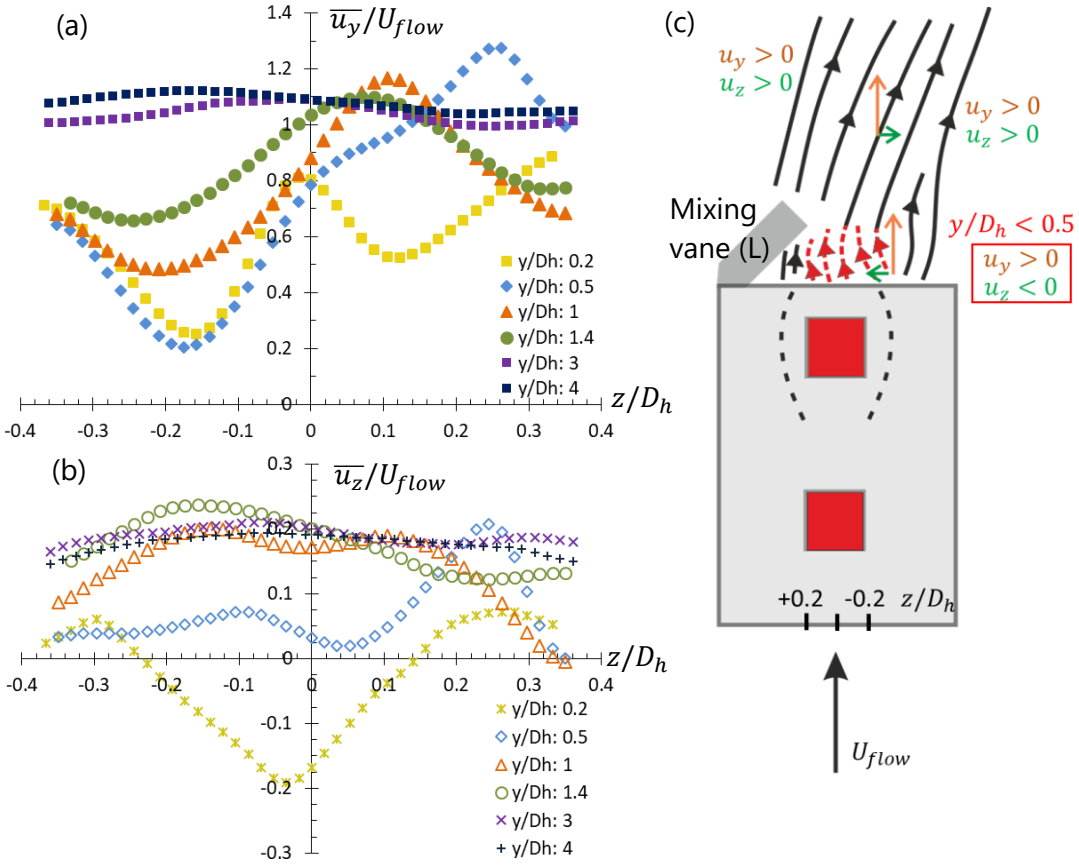

Figure 79 : Velocity profiles of (a) $\overline{u_y}/U_{flow}$ (b) $\overline{u_z}/U_{flow}$ of $Re_{Dh} = 20100$ for WMV with different distances (c) schematics of flow

Figure 79(a) shows profile of the vertical component u_y, i.e. in the direction of the mean flow.

- The dominant component is u_y component. Compared to u_z component at $y/D_h = 0.2$, $\overline{u_z}/U_{flow}$ is 18% of $\overline{u_y}/U_{flow}$. This ratio is decreased to 6.4% at $y/D_h = 4.4$.
- For $y/D_h = 0.2$, the u_y/U_{flow} is 90% of $\|\overline{U}\|/U_{flow}$. This ratio is increased to 98% with the distance at $y/D_h = 4.4$.
- For $y/D_h = 0.2$, the $\overline{u_z}/U_{flow}$ is negative downstream the dimple. The zero crossing of the velocity profile is on $z/D_h = -0.22$ and $z/D_h = +0.18$, i.e. sides of the dimple.

One of the possible source of this negative high intensity u_z component can be a secondary flow. The results support the discussion in Chapter 9.2.6.1 regarding the effect of the secondary flow. In (Matozinhos, et al., 2021) and (Xiong, et al., 2020), secondary flows are observed with higher intensities close to the mixing vane. With the increasing distance from the mixing vanes, the intensity of these secondary flows are observed to decrease. This is consistent with the current result where with the increasing distance the 3D effect is decreasing, i.e. $\overline{u_z}/U_{flow}$ is becoming positive.

- For $y/D_h = 0.5$, the u_z component becomes positive. A strong contribution from the u_z component is detected at the tip of the mixing vane i.e. $\sim z/D_h = +0.2$. This is in coherence with the $\|\overline{U}\|/U_{flow}$ where the maximum velocity is observed in this region
- With $y/D_h > 0.5$, the intensity of the $\overline{u_z}/U_{flow}$ is about 0.2 downstream the dimple.

Figure 79(c) shows the schematics of the flow for WMV configuration.

In Chapter 9.2.2 for NMV configuration, the flow fills the space downstream the dimple and the high velocity region is observed on both sides of low velocity region, i.e. $-0.2 \leq z/D_h \leq 0.2$.

For WMV configuration, the profiles shows different behaviour.

- Between $0 \leq y/D_h < 0.5$, $\overline{u_z}/U_{flow}$ is negative due to the possible high intensity secondary flow. The result of this is shown with red arrows in Figure 79(c) where the flow is moving towards the mixing vane (L).
- For $-0.2 \leq z/D_h \leq 0$, the intensity of $\overline{u_z}/U_{flow}$ is about 62% higher compared to the NMV configuration.
- For $/D_h \geq 0.5$, with positive u_y and u_z components, the flow is observed to move with the direction of the mixing vane.

Figure 80 shows the dimensionless mean velocity profiles, i.e. $\|\bar{U}\|/U_{flow}$ for different Reynolds number as $Re_{Dh} = 11200, 13400, 15600, 27500, 60500$ and 104900.

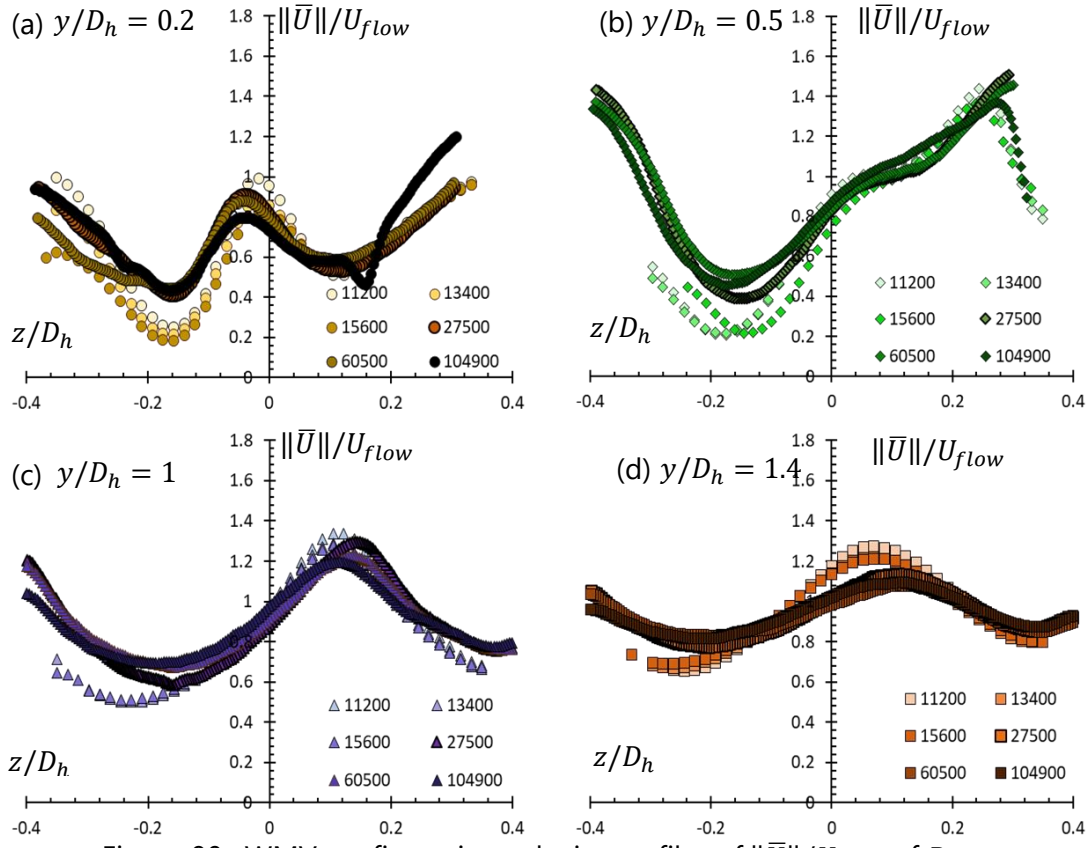

Figure 80 : WMV configuration velocity profiles of $\|\bar{U}\|/U_{flow}$ of $Re_{Dh} = 11200, 13400, 15600, 27500, 60500, 104900$ for $y/D_h =$ (a)0.2, (b)0.5 (c)1 and (d)1.4

- For $y/D_h = 0.2$, all the Reynolds number show similar "W" profile shape. At $z/D_h = 0$, $\langle\|\bar{U}\|/U_{flow}\rangle_{Re_{Dh}}$ is 0.82 ± 0.07. The maximum $\|\bar{U}\|/U_{flow}$ is at $z/D_h = 0.3$, i.e. the mixing vane (L) side, where the $\langle\|\bar{U}\|/U_{flow}\rangle_{Re_{Dh}}$ is 1.00 ± 0.09. The maximum $\|\bar{U}\|/U_{flow}$ is found as 1.2 for $Re_{Dh} = 104900$, i.e. 17% higher compared to $Re_{Dh} = 11200$. The variation between the minimum and maximum of $\|\bar{U}\|/U_{flow}$ is $67\% \pm 11\%$.
- For $y/D_h \geq 0.5$, all the profiles have a wave shape.
- At $y/D_h = 0.5$, the maximum velocity is observed at the tip of the mixing vane (L), i.e. $z/D_h = 0.3$ with the average value of 1.41 ± 0.06. While moving towards the centre,

$\|\bar{U}\|/U_{flow}$ are started to decrease and reach to the minimum at $-0.11 \leq z/D_h \leq -0.15$. The variation between the minimum and maximum of $\|\bar{U}\|/U_{flow}$ is $76\% \pm 9\%$. The minimum velocity of $\langle\|\bar{U}\|/U_{flow}\rangle_{Re_{Dh}}$ is 0.33 ± 0.13.

- For $y/D_h = 1$, maximum value of $\langle\|\bar{U}\|/U_{flow}\rangle_{Re_{Dh}}$ is 1.27 ± 0.05 where the minimum $\langle\|\bar{U}\|/U_{flow}\rangle_{Re_{Dh}}$ is 0.57 ± 0.08. The variation between the minimum and maximum of $\|\bar{U}\|/U_{flow}$ is $54\% \pm 8\%$.
- For $y/D_h = 1.4$, the maximum $\langle\|\bar{U}\|/U_{flow}\rangle_{Re_{Dh}}$ is 1.16 ± 0.07 and the $\langle\|\bar{U}\|/U_{flow}\rangle_{Re_{Dh}}$ is 0.73 ± 0.07. The variation between the minimum and maximum of $\|\bar{U}\|/U_{flow}$ is $36\% \pm 10\%$.

Figure 81 and Figure 82 shows the $\overline{u_y}/U_{flow}$ component and the $\overline{u_z}/U_{flow}$ component profiles, respectively.

- The $\overline{u_y}/U_{flow}$ profile shows similar results with $\|\bar{U}\|/U_{flow}$ since the u_y is the dominant component. For $y/D_h = 0.2$, $\overline{u_y}/U_{flow}$ is $89\% \pm 2\%$ of the $\|\bar{U}\|/U_{flow}$. For $y/D_h = 1.4$ this ratio becomes $94\% \pm 0.3\%$. The $\overline{u_y}/U_{flow}$ profile shows similar results with $\|\bar{U}\|/U_{flow}$.
- At $y/D_h = 0.2$, for the region $-0.12 \leq z/D_h \leq 0.12$, the $\overline{u_z}/U_{flow}$ is showing negative values for all the Reynolds number. For $y/D_h \geq 0.5$, $\overline{u_z}/U_{flow}$ values are observed to be positive.
- For $y/D_h \leq 0.5$, the difference between the local maximum and the minimum of $\overline{u_z}/U_{flow}$ tends to increase with the increasing Reynolds number. For $y/D_h > 0.5$, this trend is observed to change. The difference between the local maximum and the minimum starts to decrease with the increasing Reynolds number. It can be due to the increase of the intensity of secondary flows with the increasing Reynolds number close to the grid. With the increasing distance, these secondary flows start to lose their intensity.
- For $y/D_h = 1$, $\langle\overline{u_z}/U_{flow}\rangle_{Re_{Dh}}$ is observed about 0.16 ± 0.02 and for $y/D_h = 1.4$ this average is became 0.18 ± 0.01.
- Compared to NMV configuration, between $0.5 \leq y/D_h \leq 1.4$ the local maximum values of $\overline{u_z}/U_{flow}$ is 17% to 23% higher, respectively, in average of all Reynolds numbers.

For all the Reynolds number and all the distances, the $\overline{u_z}$ component is observed more dominant on the mixing vane (R) side. This leads the flow towards this mixing vane. Compared with Figure 71, the results are in coherence with the velocity field where the flow is moving in the same direction of the mixing vane.

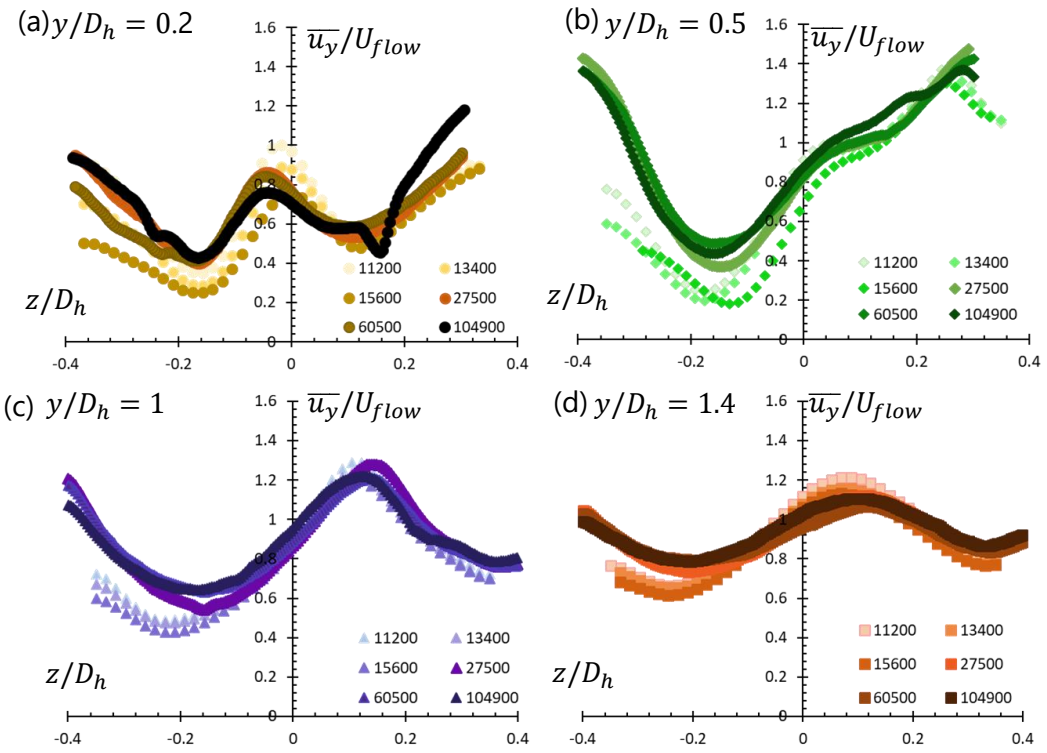

Figure 81: WMV configuration velocity profiles of $\overline{u_y}/U_{flow}$ of $Re_{Dh} = 11200, 13400, 15600, 27500, 60500, 104900$for $y/D_h =$ (a)0.2, (b)0.5, (c)1 and (d)1.4

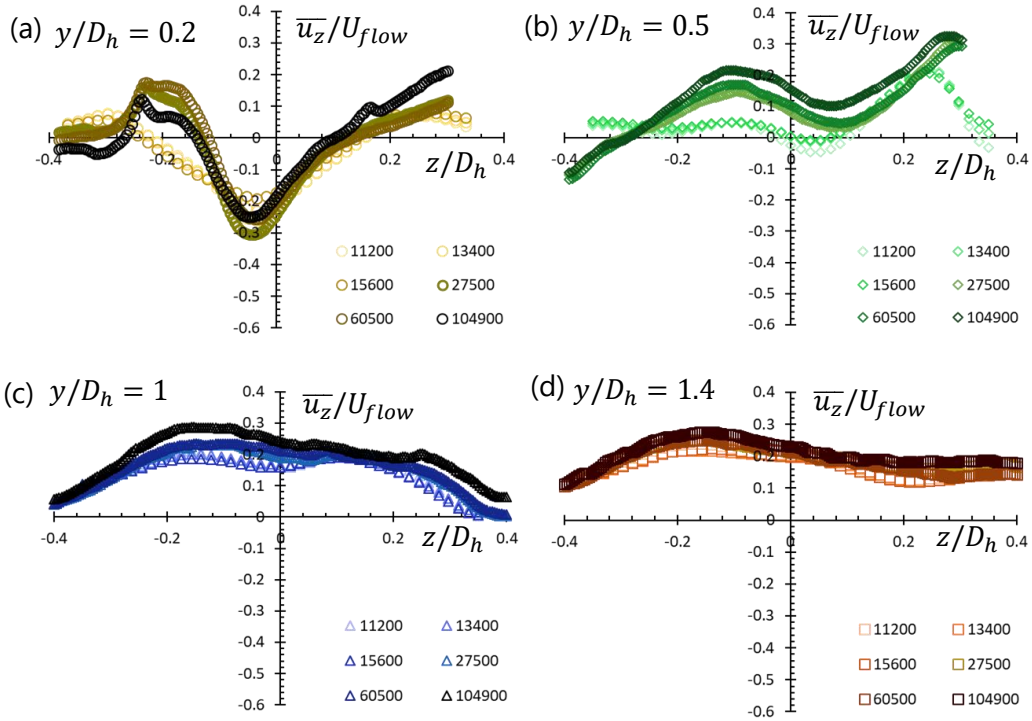

Figure 82: WMV configuration velocity profiles of $\overline{u_z}/U_{flow}$ of $Re_{Dh} = 11200, 13400, 15600, 27500, 60500, 104900$for $y/D_h =$ (a)0.2, (b)0.5, (c)1 and (d)1.4

9.2.7 Velocity fluctuations for the configuration With Mixing Vane

Velocity fluctuations are described using U'_{RMS}. Figure 83 shows the result for $Re_{Dh} = 20125$. Figure 83(a) shows the U'_{RMS}/U_{flow} field for measurement domain $0 \leq y/D_h \leq 1.4$. The fluctuations are 21% lower in average compared to the fluctuation for NMV configuration. From the field, it is observed that the velocity fluctuations are higher around the shear layer.

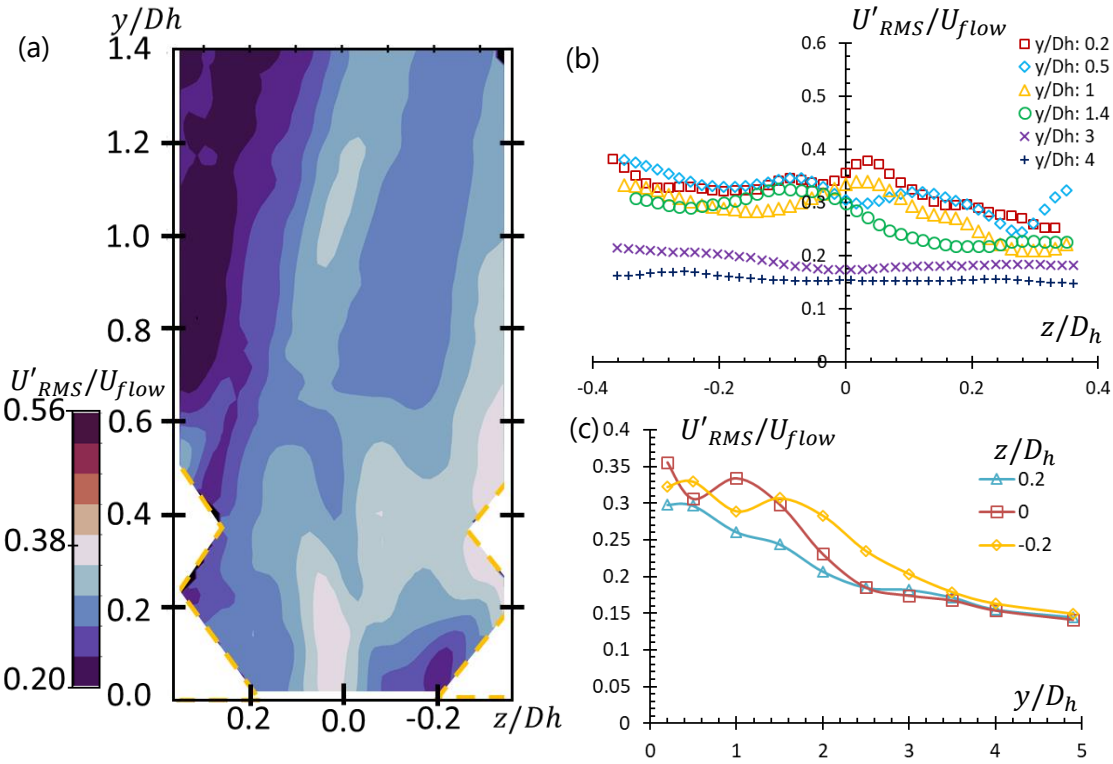

Figure 83: (a) U'_{RMS}/U_{flow} for $0 \leq y/D_h \leq 1.4$ and (b) U'_{RMS}/U_{flow} profile with different distances of Re=20125 for WMV (c) Intensity of U'_{RMS}/U_{flow}

Figure 83(b) shows the U'_{RMS}/U_{flow} profiles for different distances as $y/D_h = 0.2, 0.5, 1, 1.4, 3$ and 4.

- The highest U'_{RMS}/U_{flow} is 0.38 for $y/D_h = 0.2$ at $z/D_h = 0.03$. With the increasing distance, the intensity of the velocity fluctuations is decreased. For $y/D_h = 1.4$ the U'_{RMS}/U_{flow} are 14% lower and for $y/D_h = 4$ the fluctuations becomes 56% lower in average compared to the highest U'_{RMS}/U_{flow}.
- For NMV configuration, the fluctuations are observed to have similar to "M" shape with decreasing intensity for increasing distance. For WMV configuration no particular shape is observed.
- Between $0.2 \leq y/D_h \leq 1.4$, local maximum of the fluctuations are about 0.35 ± 0.02 , around the centre of the measurement domain, i.e. $-0.08 \leq z/D_h \leq 0.04$. The local minimum of the fluctuations are 0.23 ± 0.02 and detected around the $z/D_h = 0.21$.
- For $y/D_h > 3$, the velocity fluctuations are about 0.18 ± 0.02 at $z/D_h = -0.2$.
- The difference between the local maximum and the local minimum is decreased from 34% to 13% with the increasing distance from $0.2 \leq y/D_h \leq 4$.

This change in U'_{RMS}/U_{flow} is plotted for the distances $0.2 \leq y/D_h \leq 5$ in Figure 83(c). Three different z/D_h is selected as $-0.2, 0$ and 0.2 according to the maximum and minimum velocity fluctuations in Figure 83(b). For all profiles after $y/D_h \geq 3.5$, the U'_{RMS}/U_{flow} are stabilize about 0.18. The minimum

fluctuations are detected at $z/D_h = 0.2$, i.e. the neighbour mixing vane (R) side. For $z/D_h = 0$, the maximum decrease of the intensity of fluctuations are 38% around $1.5 \leq y/D_h \leq 2.5$.
U'_{RMS}/U_{flow} field for WMV configuration is investigated for different Reynolds numbers. Figure 84 shows the U'_{RMS}/U_{flow} for $Re_{Dh} = 11200, 15600, 60500$ and 104900. Close to the grid, i.e. $y/D_h \leq 0.5$, the intensity of velocity fluctuations are increasing with the increasing Reynolds number.

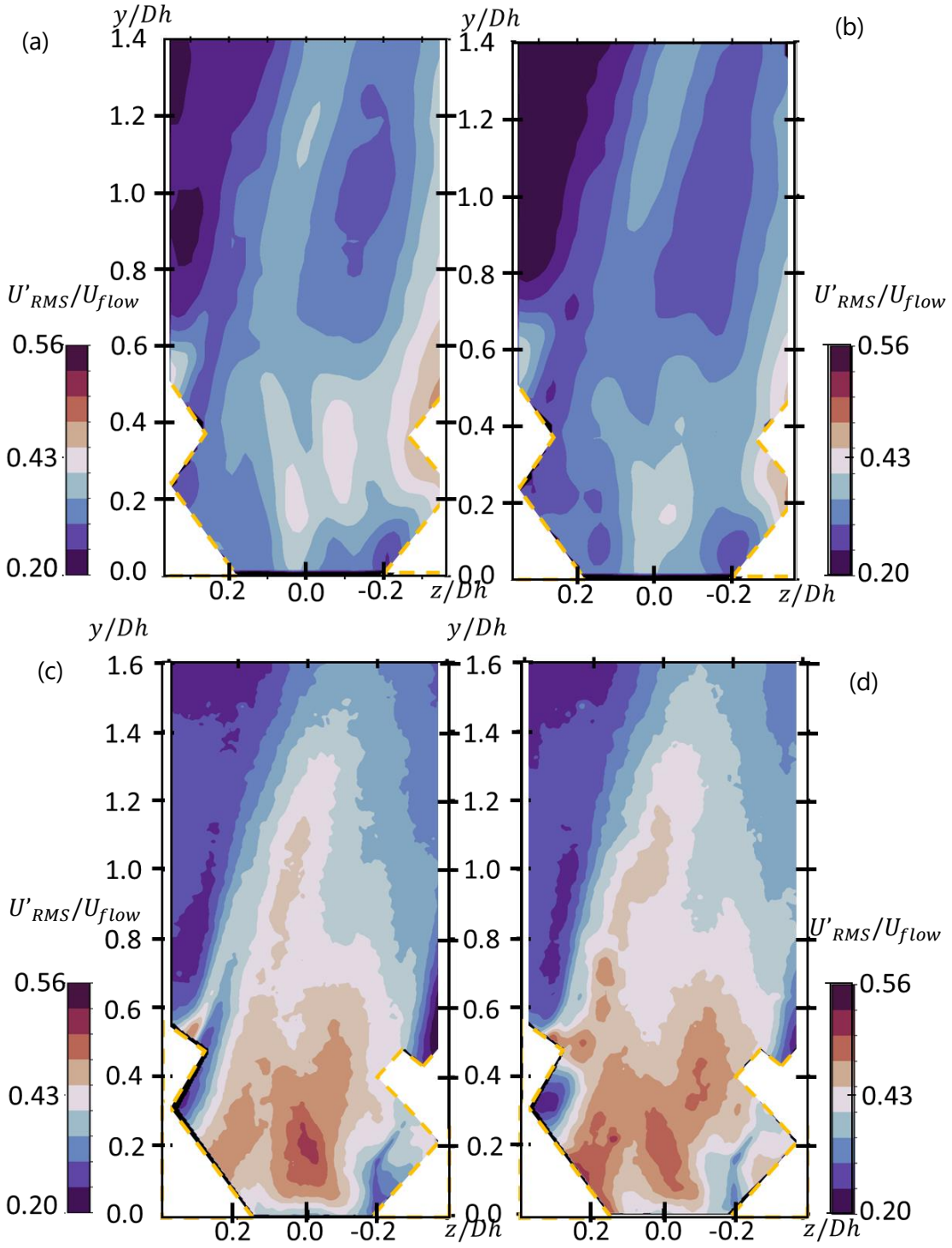

Figure 84: U'_{RMS}/U_{flow} field for WMV at measurement domain $0 \leq y/D_h \leq 1.4$ for $Re_{Dh} = (a)11200,\ (b)15600$ and at $0 \leq y/D_h \leq 1.6$ for $Re_{Dh} = (c)\ 60500, (d)104900$

To quantify these changes in velocity fluctuations, U'_{RMS}/U_{flow} are plotted in Figure 85 for different distances from the grid, i.e. $y/D_h = 0.2, 0.5, 1, 1.4$ and different Reynolds number, i.e. $Re_{Dh} = 11200, 13400, 15600, 27500, 60500$ and 104900.

The profiles confirm the trend of higher intensity of the fluctuations with the increasing Reynolds numbers. The intensity difference of fluctuation between $Re_{Dh} \leq 15600$ and $Re_{Dh} \geq 27500$ is spotted highest about 34%, at $z/D_h = 0.2$ for $y/D_h = 0.2$. The intensity differences are observed to decrease with the increasing distance. The lowest fluctuation intensity difference between the Reynolds numbers is 16% in average at $z/D_h = -0.2$ for $/D_h = 1.4$.

The difference between the local minimum and the local maximum is found $37\% \pm 4\%$ in average for $0.2 \leq y/D_h \leq 1.4$. The highest difference is 42% at $y/D_h = 0.5$, i.e. the tip of the mixing vane. The lowest difference is 32% at $y/D_h = 1.4$.

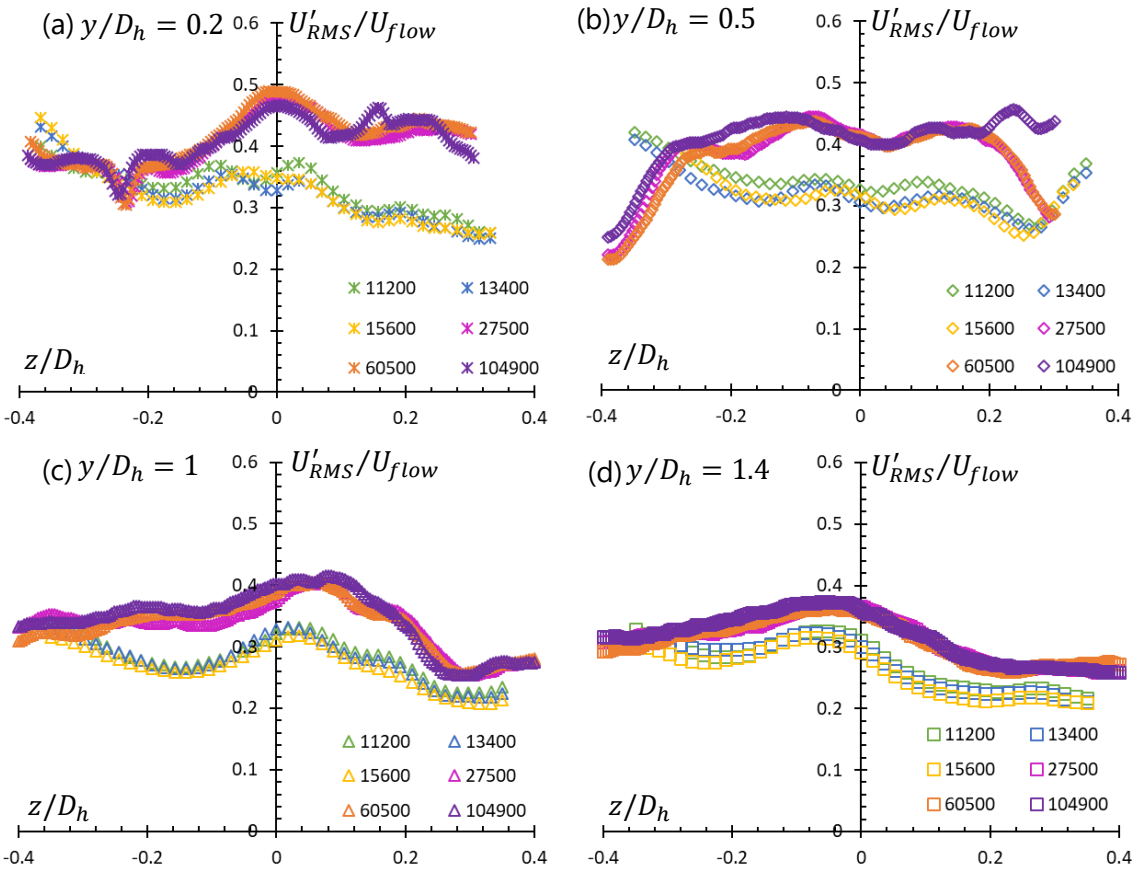

Figure 85 : U'_{RMS}/U_{flow} profiles for WMV of $Re_{Dh} = 11200, 13400, 15600, 27500, 60500, 104900$ for $y/D_h =$ (a)0.2, (b)0.5, (c)1 and (d)1.4

Figure 86 shows the U'_{RMS}/U_{flow} field for $Re_{Dh} = 11200$ and 15600 for $3 \leq y/D_h \leq 4.4$. Between $-0.2 \leq z/D_h \leq 0.2$, the fluctuations are observed minimum and outside this region relatively high fluctuations in the reference frame are spotted. These results are coherent with the $0 \leq y/D_h \leq 1.4$ region. In Figure 84 the fluctuations are observed higher in the direction of the mixing vane. This direction is observed to continue towards $z/D_h = -0.2$ side.

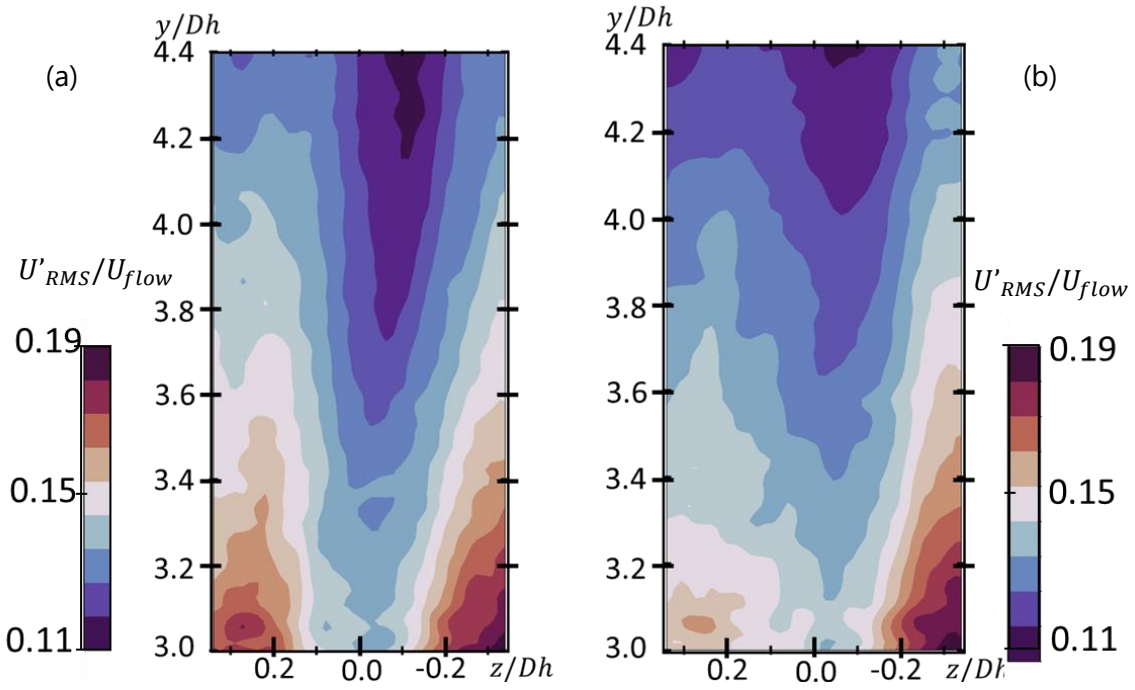

Figure 86: U'_{RMS}/U_{flow} field for WMV at measurement domain $3 \leq y/D_h \leq 4.4$ for $Re_{Dh} = (a)11200$ and $(b)15600$

CHAPTER 10
EXISTANCE OF FREQUENCY PEAKS

10. EXISTANCE OF FREQUENCY PEAKS

The excitation of the rod is the starting point of the Grid-to-Rod Fretting which is connected to the Fluid-Structure Interaction. To understand the mechanism behind the forces leading the excitation of rod, fluctuations are studied by frequencies. For this Fast Fourier Transform (FFT) is used.
For the investigation of pressure fluctuations, the measurements are performed around the rod with two measurement campaigns, i.e. SPS and MPS for both NMV and WMV configurations.
To investigate the energy of the velocity fluctuations, PIV and LDV-2019 measurements are used.
LDV-2019 measurements are performed downstream the dimple and spring for different distances by using the WMV configuration.
PIV measurements are performed downstream the dimple for both NMV configuration and WMV configuration.

10.1 Frequency peak on pressure spectra

10.1.1 Pressure spectra around the rod at Reynolds number 66000

The main aim of the SPS-2016 and SPS-2018 measurement campaigns are to investigate pressure fluctuations related to forces exciting the central rod with different types of grids, i.e. NMV and WMV. Figure 87 shows the dimensionless energy spectra averaged over around the central rod, i.e. $E^* = \langle E(f) \rangle_\theta / E_{total}$, for Re_{Dh} 66000.
The results cover different distances, i.e. $y/D_h = 0.5, 1, 2, 3, 4, 5, 10$ and 20, away from the grid, for both NMV and WMV configuration.
At $y/D_h = 0.5$, a clear frequency peak is observed for both configuration with 69Hz (Turankok, et al., 2020). This peak is observed to stay persisting until $y/D_h = 3$ for both configuration.
After $y/D_h = 3$ two different behaviour are observed on the spectra. For NMV configuration, the peak stays persisting until $20D_h$. For WMV configuration, it is observed that after $3D_h$, the peak starts to dissolve.
This frequency peak represents a periodic event connected to pressure fluctuations around the rod for $Re_{Dh} = 66000$. The results show that for NMV configuration, this periodic event can be observed up to $y/D_h = 20$. On the other hand, WMV configuration results show that with the mixing vanes these periodic events are disturbed and can't persist after $y/D_h = 3$.
To ensure these frequency peaks are connected to flow phenomena while performing the measurements an accelerometer is connected to surface of CALIFS. In the recorded signal, no similar frequency peaks are observed. This removes the possibility of the vibrations on CALIFS being the possible source of frequency peak.

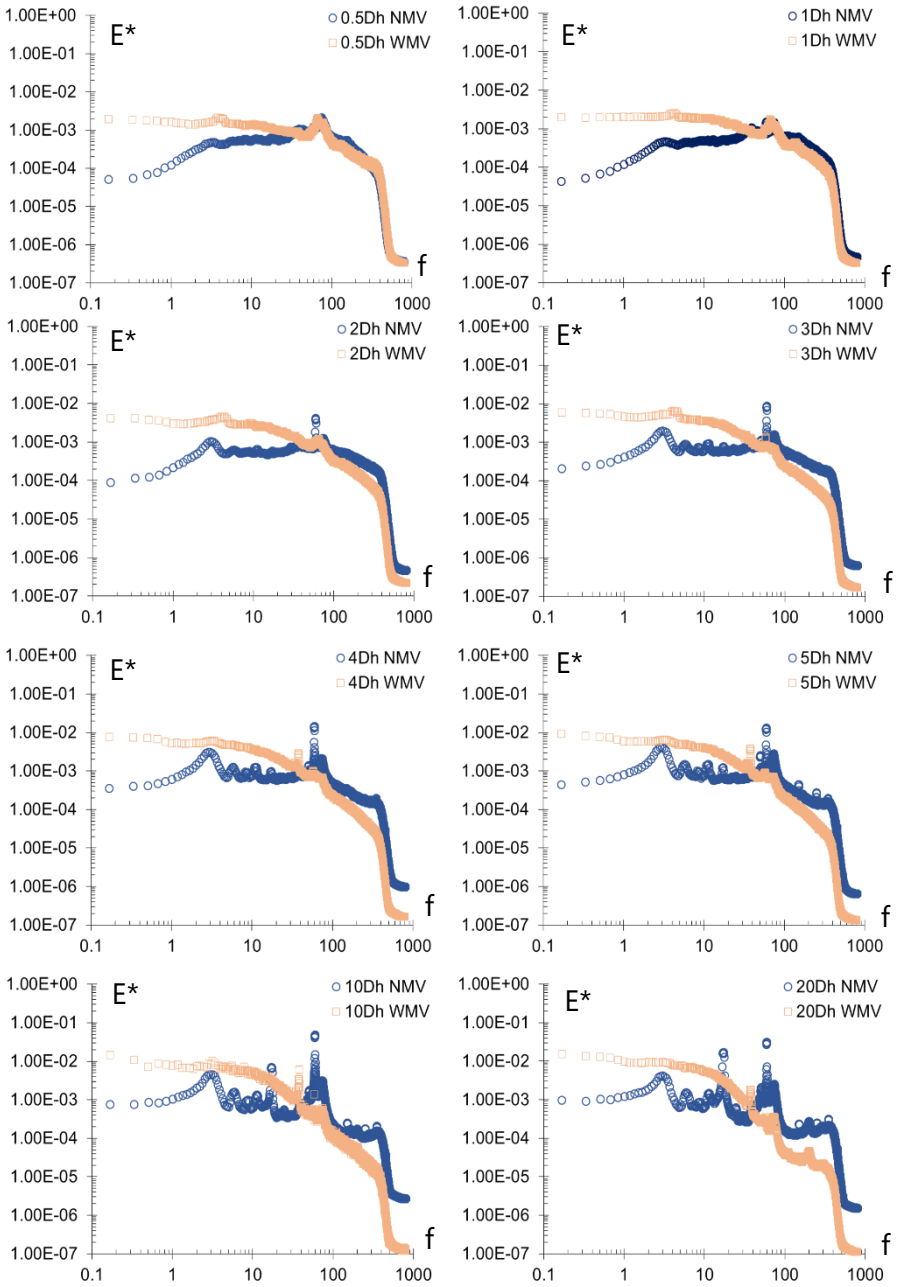

Figure 87: Azimuthal average of the pressure fluctuation spectra for NMV (blue) and WMV (orange) with different distance away from the grid

10.1.2 Pressure spectra with multisensor pressure measurements

The pressure measurements with multisensor device are performed to investigate a broad range of the Reynolds number where the periodic phenomena can be observed.

For this investigation, the multisensor pressure device is installed in the central rod downstream the dimple and the sensors are aligned vertically, i.e. with the same angle. The installed multisensor device can be seen in Chapter 7.

Different Reynolds numbers are obtained by changing the temperature and the velocity of the flow. Due to the disappearance of the frequency peaks after $y/D_h = 3$, i.e. results from SPS-2016 and SPS-2018, the multisensor device is installed at $y/D_h = 0$, i.e. same level as the exit of the spacer grid. Four pressure sensors are installed to the multisensor device, i.e. the measurements are performed up to 1.5Dh.

The pressure fluctuation data are obtained from different experimental campaigns. The experimental campaign with multisensor device is performed firstly with WMV configuration for $13200 \leq Re_{Dh} \leq 109000$, i.e. MPS-2019. For NMV configuration, the pressure data is obtained from the MPS-2020 and MPS-2021 for $14000 \leq Re_{Dh} \leq 47000$.

Figure 88 shows pressure measurements performed instantaneously with multisensor device for WMV and NMV configuration as Figure 88(a) and (b), respectively. The results show similar frequency peak values for both configuration. For NMV configuration, the peaks are observed about 19Hz and for WMV configuration the frequency peaks are observed about 23hz. For sensor 3 and 4, an electrical noise is observed on spectra at 50Hz. This electrical noise is deleted from the spectra for representation Figure 88(b).

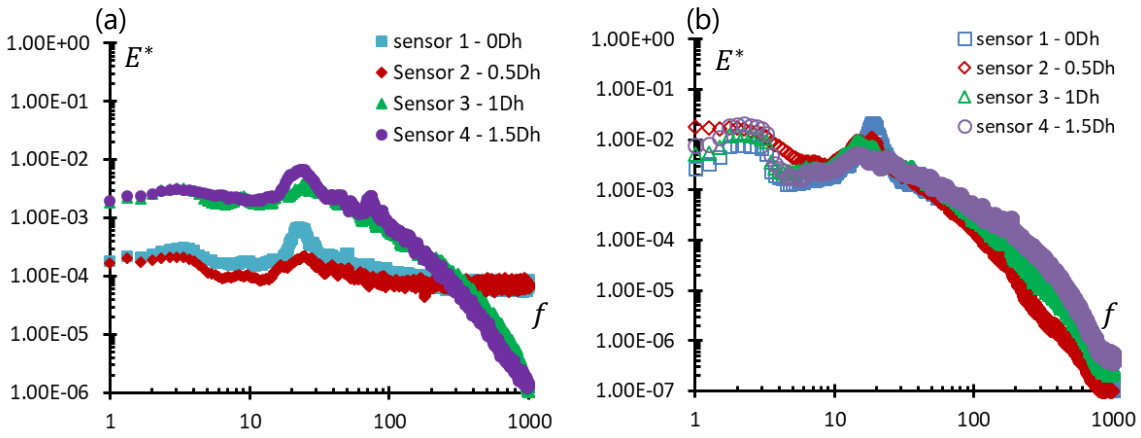

Figure 88: Multisensor result for (a) WMV configuration (b) NMV configuration at $Re_{Dh} = 20000$

In Figure 88(a), after the frequency peak a difference is observed on high frequencies for $Sensor_1$ and $Sensor_2$. The possible explanation for this difference might be connected to the sensor quality. Soon after the measurements are performed, these sensors are observed to lose their sensitivity.

Figure 89 shows 3D waterplot of Strouhal number with normalized energy for WMV configuration. The x-axis shows the Strouhal number, the y-axis shows the dimensionless energy spectra and the z-axis shows the Reynolds number.

The results show frequency in form of Strouhal number for the range of $13200 \leq Re_{Dh} \leq 109000$. The temperature range of the measurements varies from 12°C to 55°C. The existence of the frequency peaks are detected for $y/D_h = 0.5, 1, 1.5$ and 2.

By using the peaks of Strouhal number, the map of Strouhal versus Reynolds number is built. Figure 90 shows the map of Strouhal-Reynolds numbers downstream the dimples for the distance $y/D_h = 0.5, 1, 1.5$ and 2. The plots include different temperature, i.e. $12°C, 26°C, 32°C, 41°C, 47°C$ and $55°C$, for each distance. From the result, the average of Strouhal number of pressure spectra is found as 0.25 ∓ 0.006.

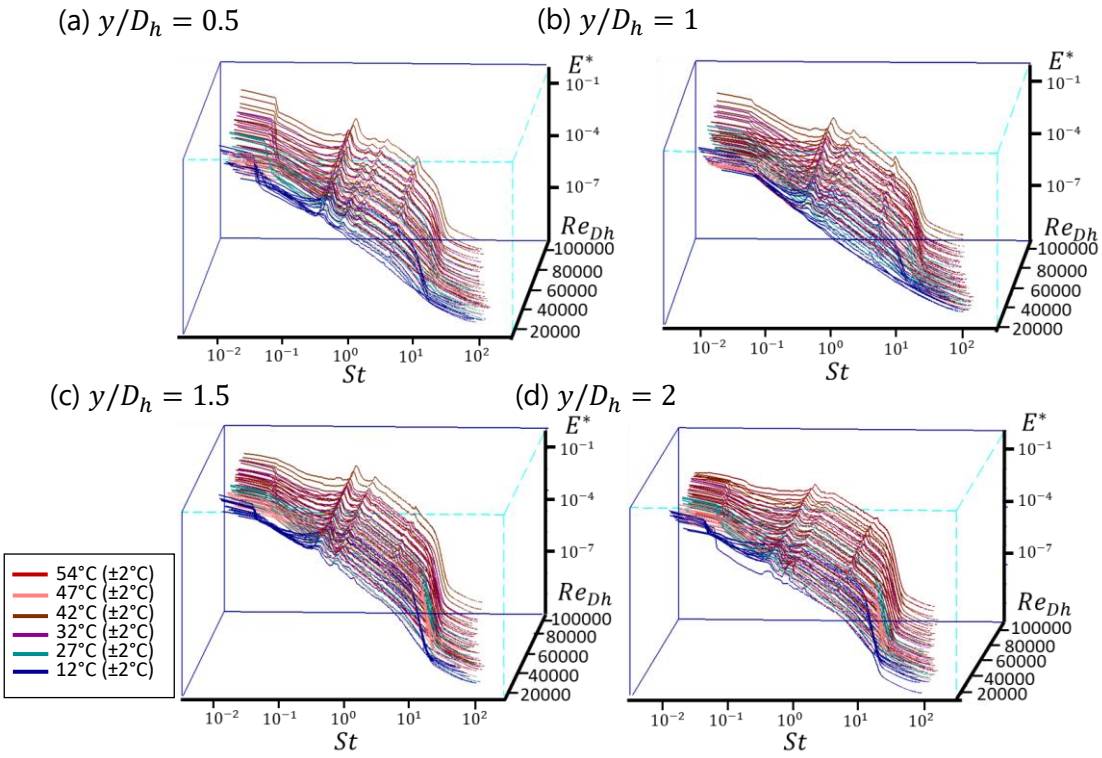

Figure 89: Pressure spectra of WMV configuration for Reynolds number range 13200-109000 at (a) $y/D_h = 0.5$ (b) $y/D_h = 1$ (c) $y/D_h = 1.5$ (d) $y/D_h = 2$

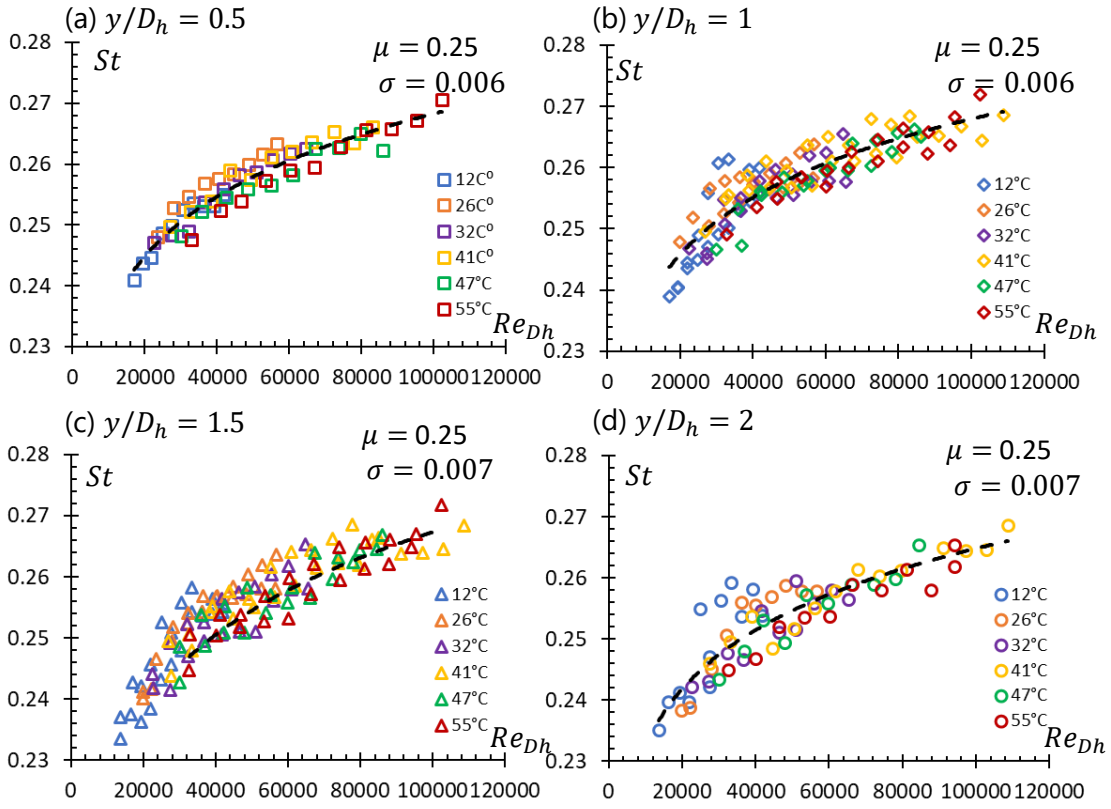

Figure 90: Strouhal versus Reynolds map for (a) $y/D_h = 0.5$ (b) $y/D_h = 1$ (c) $y/D_h = 1.5$ (d) $y/D_h = 2$ with different temperatures for WMV configuration

Figure 91 shows the Strouhal versus Reynolds map downstream the dimples for NMV configuration. For the measurements at $y/D_h = 0$, the average Strouhal number is found 0.27 ± 0.007. With the increasing distance from the spacer grid, the average Strouhal number is decreased from $St_{0Dh} = 0.26 \pm 0.013$ to $St_{1.5Dh} = 0.22 \pm 0.02$.

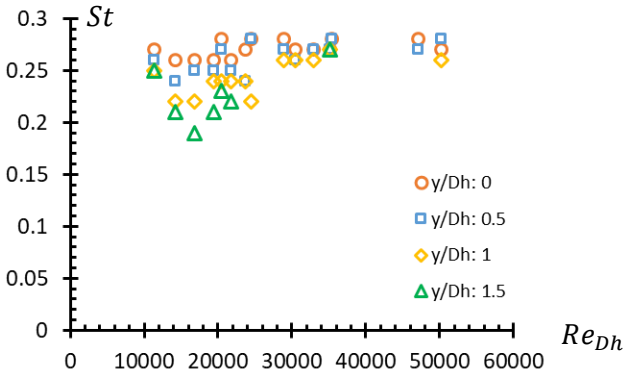

Figure 91: Strouhal versus Reynolds map for $y/D_h = 0, 0.5, 1, 1.5$ for NMV configuration

10.2 Frequency peak on velocity spectra

10.2.1 LDV measurements

LDV measurements are performed along two vertical lines placed, i.e. downstream the middle of the dimple and the spring for the WMV configuration. The aim of these measurements is to explore the effect of the grids elements on the frequency peak of velocity fluctuations.

Figure 92 shows the existence of the frequency peaks for different distances downstream the dimple and spring for $Re_{Dh} = 53600$. The plot is built according to the dimensionless energy, E^*, in a function of a dimensionless frequency built with associated Strouhal numbers.

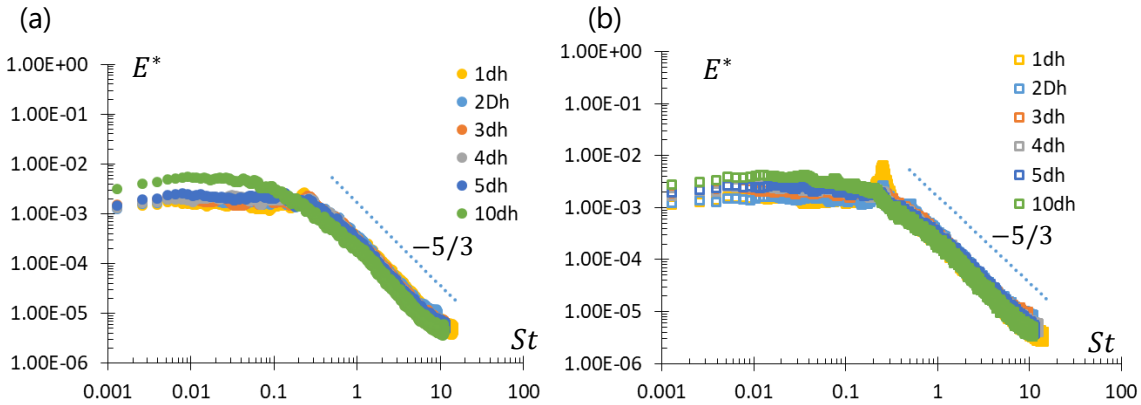

Figure 92: LDV velocity spectra with different distances for $Re_{Dh} = 53600$ downstream (a) spring and (b)dimple

Downstream $y/D_h = 1$, a frequency peak at 66Hz is observed for both geometry. This frequency peak is marked more for dimples compared to the springs. The E^* value is 68% higher at this peak for dimples.

Figure 93 is plotted with zoom-in view of Figure 92 to have a clear vision of the peaks for the distances $1 \leq y/D_h \leq 3$.

Downstream the spring, i.e. Figure 93(a), the peak at $y/D_h = 1$ is observed to be disappear at $y/D_h = 2$. For $y/D_h = 3$, this peak reappear with the E^* value 17% lower compared to E^* value at $y/D_h = 1$. After $y/D_h > 3$, no peak is observed on the spectra.

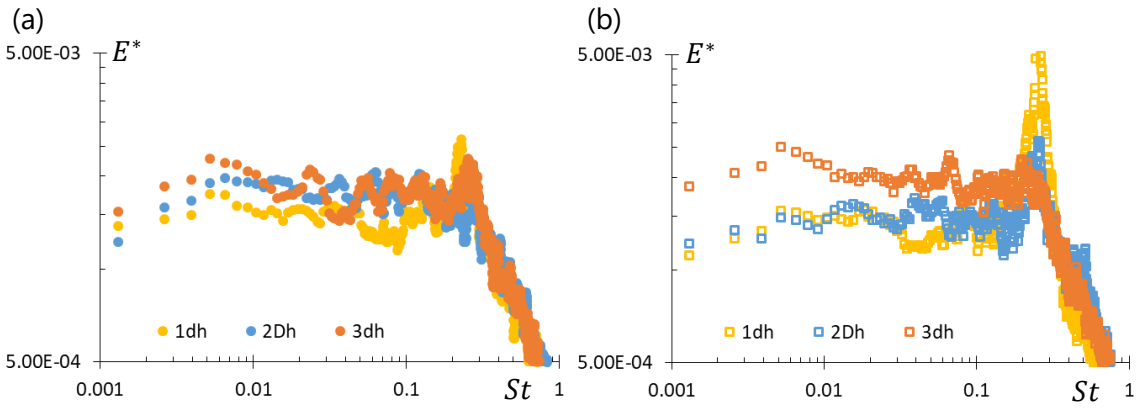

Figure 93: Zoom in to LDV velocity spectra for $Re_{Dh} = 53600$ downstream (a)spring (b)dimple for $1 \leq y/D_h \leq 3$

Downstream the dimple for $y/D_h = 1$ and $y/D_h = 2$, the peak is observed to persist but with the decrease of 53% on the E^* value. After $y/D_h = 2$ the peak is observed to be less pronounced.
For both dimple and spring, with the increasing distance from the spacer grid higher energies are detected for lower frequencies.
For all the spectra, a -5/3 power law decrease of energy spectra is observed over more than one decade for frequencies higher than the peak. The combination of peaks and -5/3 power law ranges is plausibly due to the presence of large scale eddies shedding within the turbulent flow.
Figure 94 shows the velocity spectra for $Re_{Dh} = 13400, 26800, 40200$ and 53600 with normalized energy versus Strouhal number.

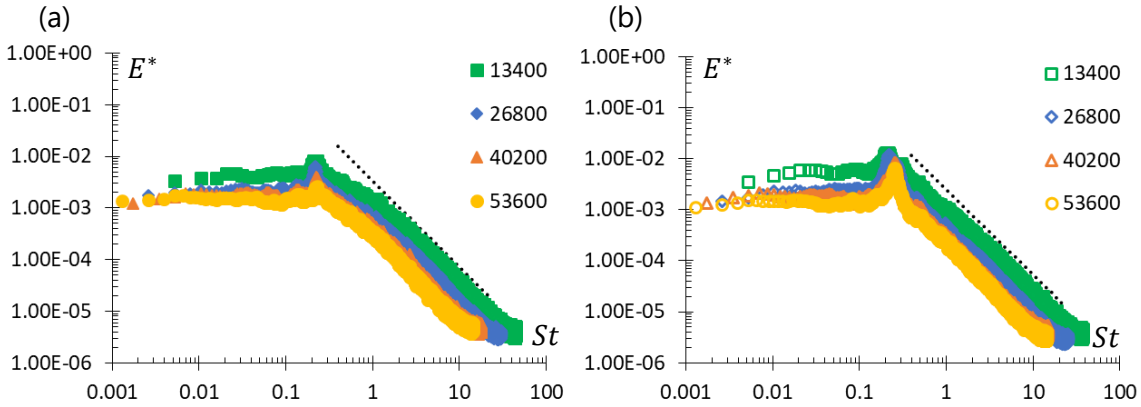

Figure 94: LDV velocity spectra of (a) spring and (b)dimple at $y/D_h = 1$ for $Re_{Dh} = 13400, 26800, 40200, 53600$

The results show the existence of the frequency peak for all the Reynolds numbers close to the spacer grid, i.e. $y/D_h = 1$. Figure 94(a) and Figure 94(b) shows the frequency peaks with the springs and dimple, respectively. As seen in Figure 92, the frequency peaks are more pronounced downstream the dimples.

In Figure 94(a), the sharpness of the peaks is observed to be higher with the decrease of the Reynolds number. This behaviour is observed to be opposite for the dimple where in Figure 94(b), increase of the Reynolds number leads to a sharper frequency peak.
The total energy under the frequency peak is observed to be similar for all the Reynolds numbers. For spring, $\langle E^* \rangle_{Re_{Dh}}$ is 0.24 ± 0.02 and for dimple this value is 0.4 ± 0.05. This shows that the periodic events are more pronounced on the downstream the dimples for different Reynolds numbers.
In the results, the -5/3 power law is observed for all the Reynolds numbers.
Figure 95 shows the relation between the Strouhal and Reynolds numbers for both geometries where the frequency peak is visible. From the result, the average of Strouhal number is found about 0.22 ∓ 0.01 for spring and 0.23 ∓ 0.02 for dimple.

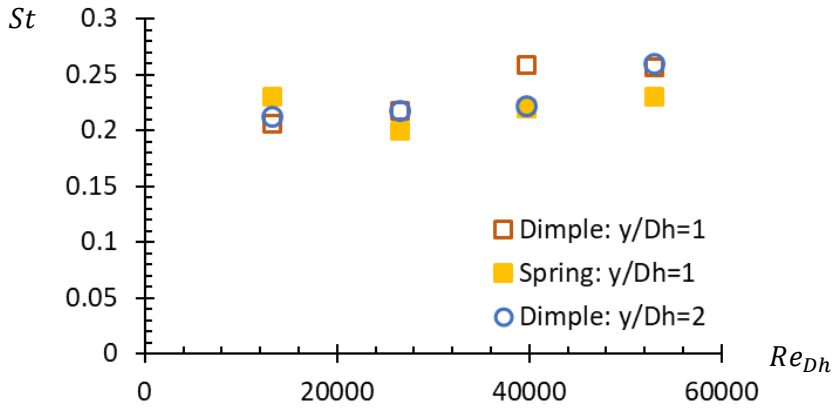

Figure 95: Strouhal versus Reynolds map built from LDV results for downstream the dimple and spring

10.2.2 High-speed PIV measurements

High-speed PIV results downstream the dimple are used to compute frequency spectra in the laser plane. The existence of the frequency peak is searched in the velocity field for both NMV and WMV configurations.
In Chapter 9.2, different velocity regions are measured. To search the frequency peaks in the velocity fluctuations, different points are selected from each region for the investigation of spectra.
Figure 96(a) shows the mean velocity field for $Re_{Dh} = 20125$ for NMV configuration. For the spectral analysis, 5 points are selected, i.e. $z/D_h = 0.30, 0.16, 0, -0.16$ and -0.30 for $y/D_h = 0.5$. Figure 96(b) shows the normalized energy spectra versus the frequency for the selected points. From the results it is observed that each point has different intensity of energy.
The highest energy of the fluctuations are observed on the shear layers, i.e. $z/D_h = 0.16$ and -0.16, with the $f_{peak} = 24Hz$. These points corresponds to the maximum velocity fluctuations on u'_{RMS}/U_{flow} field.
In the centre of the measurement domain, i.e. $z/D_h = 0$, the frequency peak at 24Hz disappears and instead, this peak is observed at 42Hz, i.e. $2 * fpeak_{0.16}$. In Chapter 9, the velocity profiles for NMV configuration show that the flow is moving towards the centre from the sides of the dimple. This might lead to the signatures of the fluctuations with less energy for higher frequencies downstream the dimple.
To be able to capture the position of the maximum energy observed, the energy values are isolated for the f_{peak} observed on Figure 96(b).
Figure 97 shows the normalized energy values of $f_{peak} = 24Hz$ and $f_{peak} = 48Hz$ for different distance away from the grid. The result shows the energy intensity of the selected frequency per z/Dh. The maximum intensity of energy is at $z/D_h = -0.2$ and 0.2 with 24Hz. The position of the

highest intensity of energy corresponds to shear layer on the mean velocity field which is expected since the spectra captures the energy of the fluctuations.

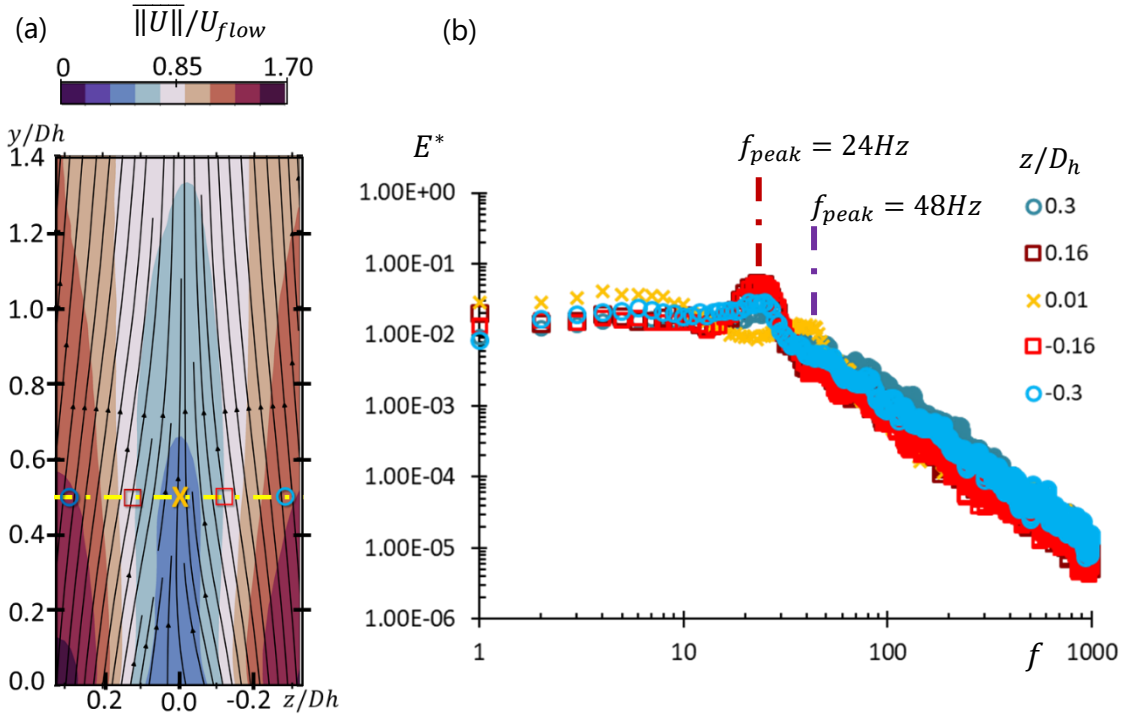

Figure 96: (a) $\|\overline{U}\|/U_{flow}$ field (b) Dimensionless velocity spectra at $y/D_h = 0.5$ for NMV configuration at $Re_{Dh} = 20100$

In addition to 24Hz energy intensity, 48Hz is also investigated as shown in Figure 97(b). The maximum energy for 48Hz is detected in the centre of the measurement domain. The energy intensity is found 72% lower compared to the 24Hz. This shows the dominant periodic frequency is 24Hz.
For both frequency peak, with the increasing distance from the grid, the intensity of the energy is decreasing.

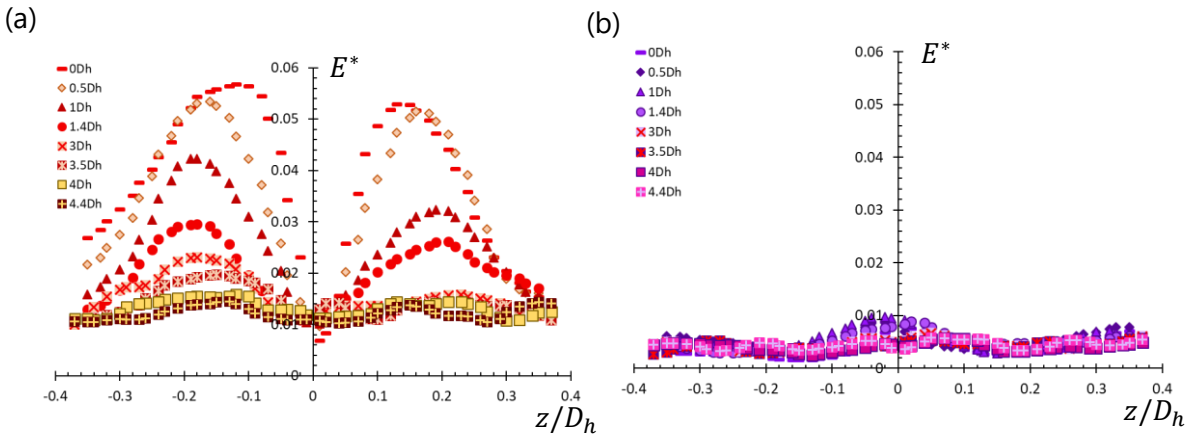

Figure 97: Normalized energy for (a)$f_{peak} = 24Hz$ and (b) $f_{peak} = 48Hz$ for NMV configuration $Re_{Dh} = 20100$

Figure 98(a) shows the mean velocity field of $Re_{Dh} = 20100$ for the WMV configuration. For spectral analysis same positions are selected as NMV configuration. Figure 98(b) shows the normalized energy spectra versus the frequency for the selected points. Compared to NMV configuration, the

frequency peaks on spectra are observed between $19Hz$ and $26Hz$ for the selected points. Between these different frequency peaks similar to NMV configuration, 24Hz is found as the frequency peak with maximum intensity for the distance $y/D_h = 0.5$.
Figure 99 shows normalized energy level for z/D_h position where $f_{peak} = 24Hz$. Compared to NMV

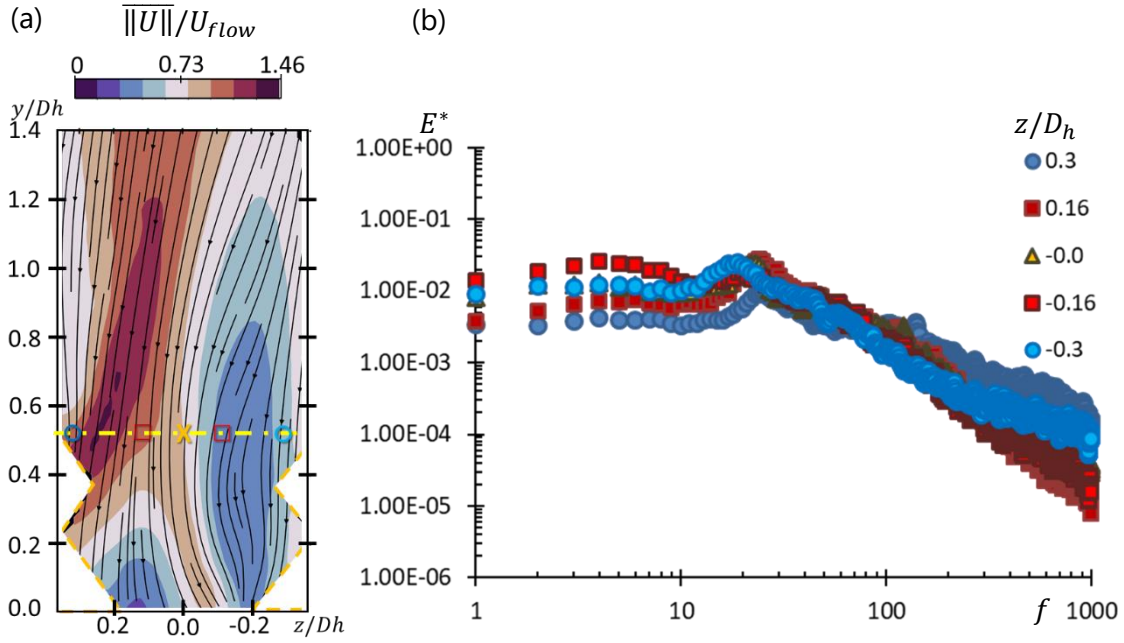

Figure 98: (a) $\|\bar{U}\|/U_{flow}$ field (b) Dimensionless velocity spectra at $y/D_h = 0.5$ for WMV configuration at $Re_{Dh} = 20100$

configuration, the highest energy level corresponds to $z/D_h = 0$. The maximum energy intensity of the $f_{peak} = 24Hz$ is found 24% lower compared to the maximum energy intensity of NMV configuration.

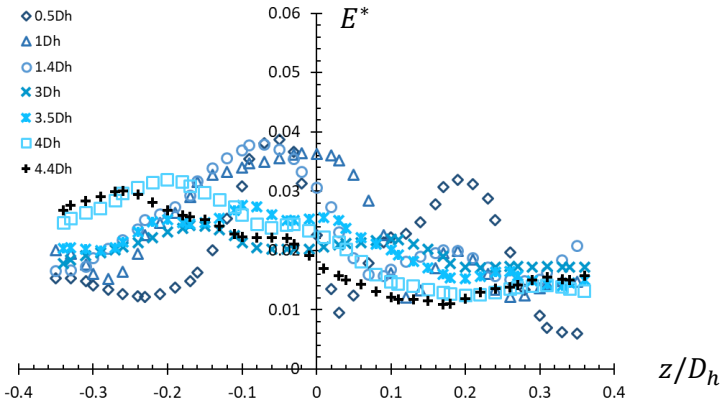

Figure 99: Normalized energy for $f_{peak} = 24Hz$ for WMV configuration $Re_{Dh} = 20100$

According to the results of Figure 97 and Figure 99, to investigate the frequency peak $z/D_h = 0.2$ and $z/D_h = 0$ is selected for NMV and WMV, respectively.
Figure 100 shows the normalized energy spectra for different distances at $Re_{Dh} = 20100$ for both NMV and WMV. Figure 100(a) shows the spectra of NMV for $z/D_h = 0.2$ and Figure 100(b) shows the spectra of WMV for $z/D_h = 0$.
The existence of the frequency peaks is plotted as in form of Strouhal number for $0 \leq y/D_h \leq 4.4$.
For NMV configuration the maximum energy intensity is observed at $y/D_h = 0$. In case of WMV configuration, this maximum value is observed about $y/D_h = 1.4$.

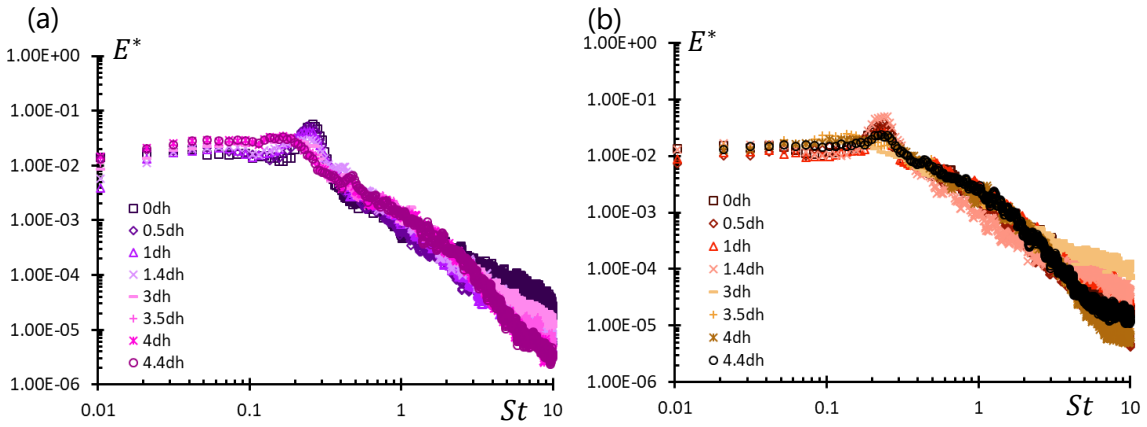

Figure 100: PIV spectra for (a) NMV and (b) WMV configuration for $Re_{Dh} = 20100$

Figure 101 shows the normalized energy spectra for different Reynolds number, i.e. $Re_{Dh} = 11200, 13400, 15600, 17900$ and 20100 at $y/Dh = 0.5$ with both configuration. From the result, the frequency peaks are observed with higher energy for NMV configuration.

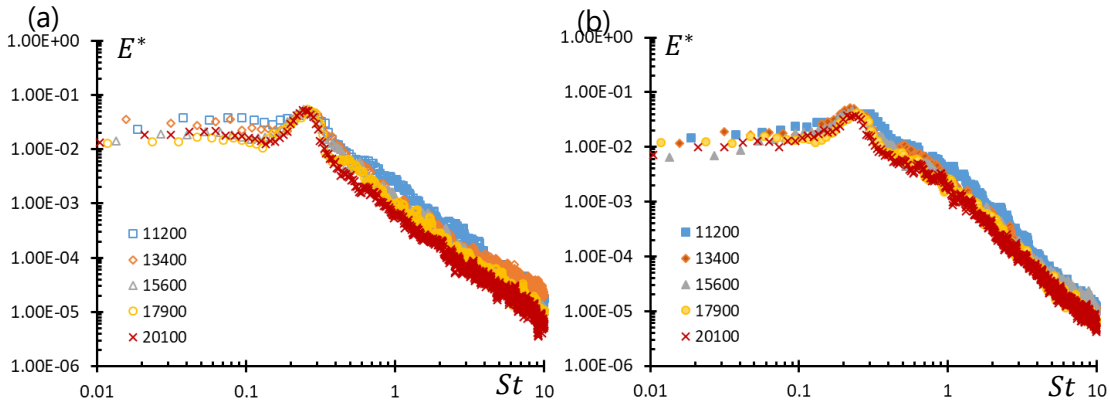

Figure 101: PIV spectra for $Re_{Dh} = 11200, 13400, 15600, 17900, 20100$ at $y/D_h = 0.5$ for (a) NMV and (b)WMV configuration

Figure 102 shows the Strouhal-Reynolds map built from the frequency peaks of PIV velocity spectra. The average Strouhal number for NMV is found as 0.26 ± 0.015. Similarly, for WMV this value is found about 0.23 ± 0.010.

All the quantification of these frequencies with different measurement techniques and configurations are summarised in Chapter 10.3.

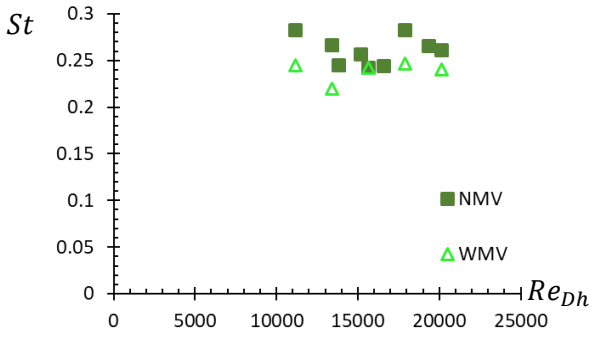

Figure 102: Strouhal versus Reynolds map built from High-speed PIV results

10.3 St-Re map

Figure 103 is built Strouhal-Reynolds map to summarize the frequency peaks measured using pressure, LDV and PIV measurements.
The Reynolds number range is from 13200 to 109000. The Strouhal values are observed to vary from 0.2 to 0.28. The average of Strouhal is about 0.25 with standard deviation as 0.9.
The investigated periodic phenomena is observed for $13200 \leq Re_{Dh} \leq 109000$.

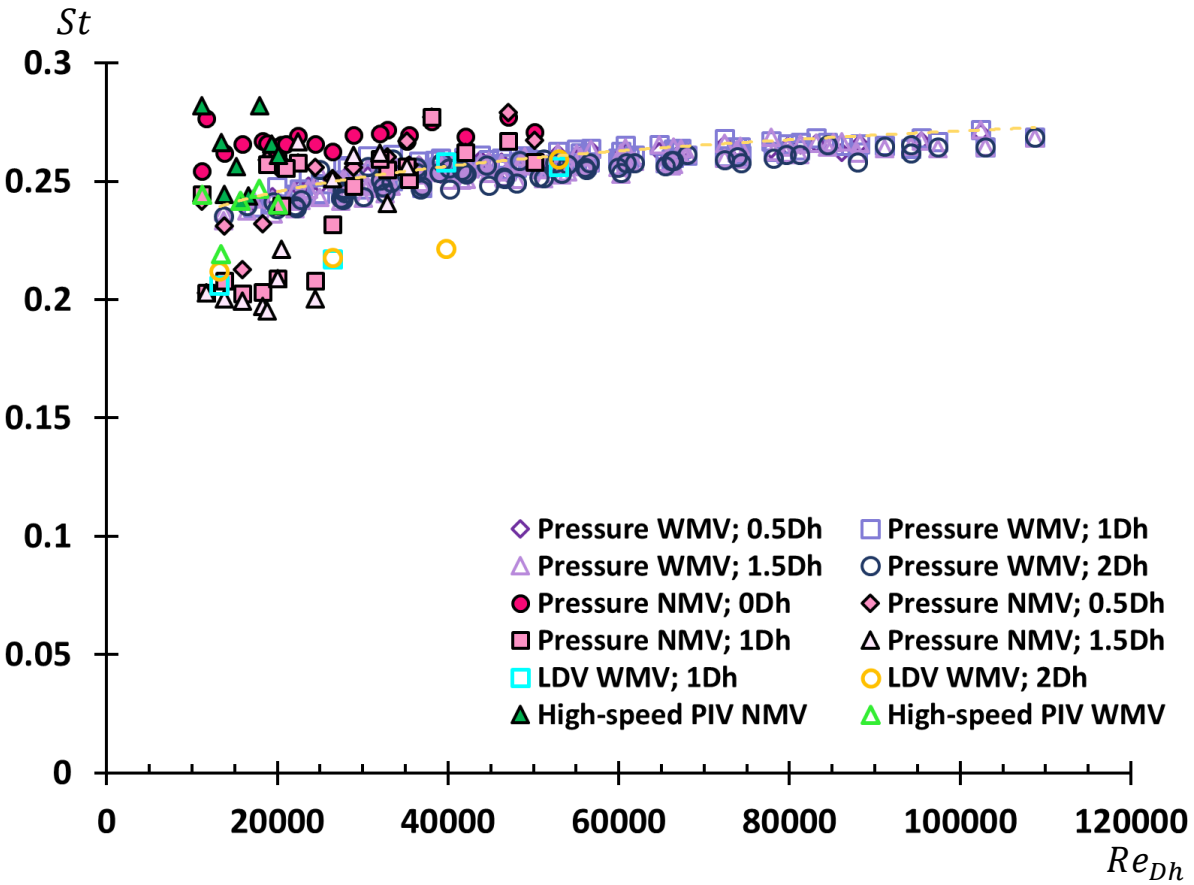

Figure 103. Strouhal-Reynolds Map

The Strouhal number is built by using the U_{flow}. It can be noted that the velocity flow rate within the grid is about $1.14U_{flow}$.

CHAPTER 11
STRUCTURES AND SCALES OF FLOW

11. STRUCTURES AND SCALES OF THE FLOW

In Chapter 10, the periodic signature of the wake flow is observed on pressure and velocity spectra downstream the dimple.

To investigate the source of this periodic signature, the existence of coherent structures is investigated using PIV measurements. The visualization of the structures is based on the streamlines in the frame moving with U_{flow}. The results are supported by the swirling function which is Galilean invariant where the streamlines are not (Jeong & Hussain, 1995). As discussed in Chapter 3.3, swirling function corresponds to the part of vorticity associated with the rotation. It sets apart the contribution of the shear. (Adrian, 2007)

In the first part, the existence of the structures are searched for different configurations and different distances for $11200 \leq Re_{Dh} \leq 152000$ and different range of Reynolds numbers, i.e..

After the observation of the structures, a movie is generated from the streamlines and swirling functions. In the movie, the generation of structures are observed to be quasi-periodic.

To check the periodicity and estimate its characteristic frequency, the energy spectra is used on the selected positions from the PIV measurements. According to the frequency obtained, the periodicity is confirmed by the searching the displacement of the structures within the expected frame.

In the eddy street, two different length scales are defined: the integral length scale and the periodic length scale. The integral length scale represents the size of eddies and the periodic length scale represents the distance between main large eddies.

For the calculation of the integral length scales, autocorrelation function is applied on pressure fluctuations and velocity fluctuations. For the periodic length scales, the frequency peak is used from spectra of fluctuations.

11.1 Visualization of the Structures

Figure 104 and Figure 105 show the visualization of the structures for $Re_{Dh} = 20100$ with NMV and WMV configuration, respectively.

The Figure 104(a) and Figure 105(a) show the velocity in the reference frame of U_{flow} , i.e. $\|U^{\Delta}\|/U_{flow}$, with the streamlines in the frame moving with U_{flow}. This parameter shows the corrected velocity.

The Figure 104(b) and Figure 105(b) show the swirling function results with the same streamlines. According to swirling function, the dark blue should represents the core of structures.

For NMV configuration, i.e. Figure 104, the swirling streamlines are observed on both side of the dimples. With WMV configuration, i.e. Figure 105, these streamlines are observed on the centre of the measurement domain.

In Figure 104(a) and Figure 105(a), the magnitude of the corrected velocities are observed as $\|U^{\Delta}\|/U_{flow} = 0$ in the centre of each swirling streamlines. High magnitude of velocities are detected, around the centre of the streamlines. This is coherent with the swirling function where for the same positions the centre of these streamlines are dark blue, i.e. $S^{*}\sim 1$.

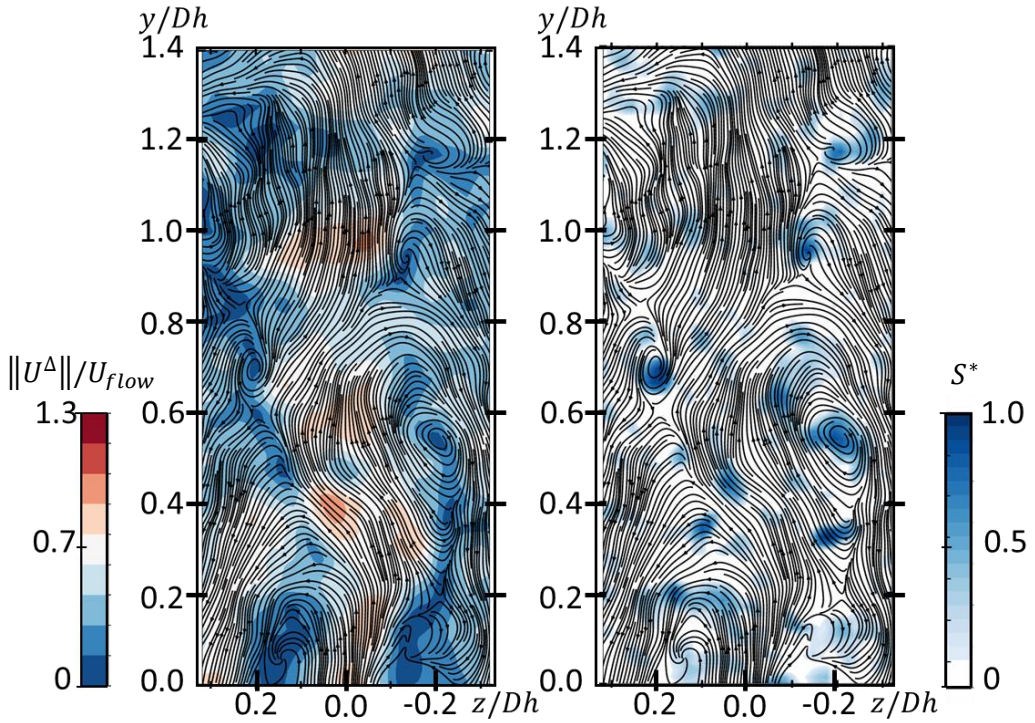

Figure 104: $\|U^{\Delta}\|/U_{flow}$ and swirling function with streamlines in referance frame moving with U_{flow} for $Re_{Dh} = 20100$ for NMV configuration

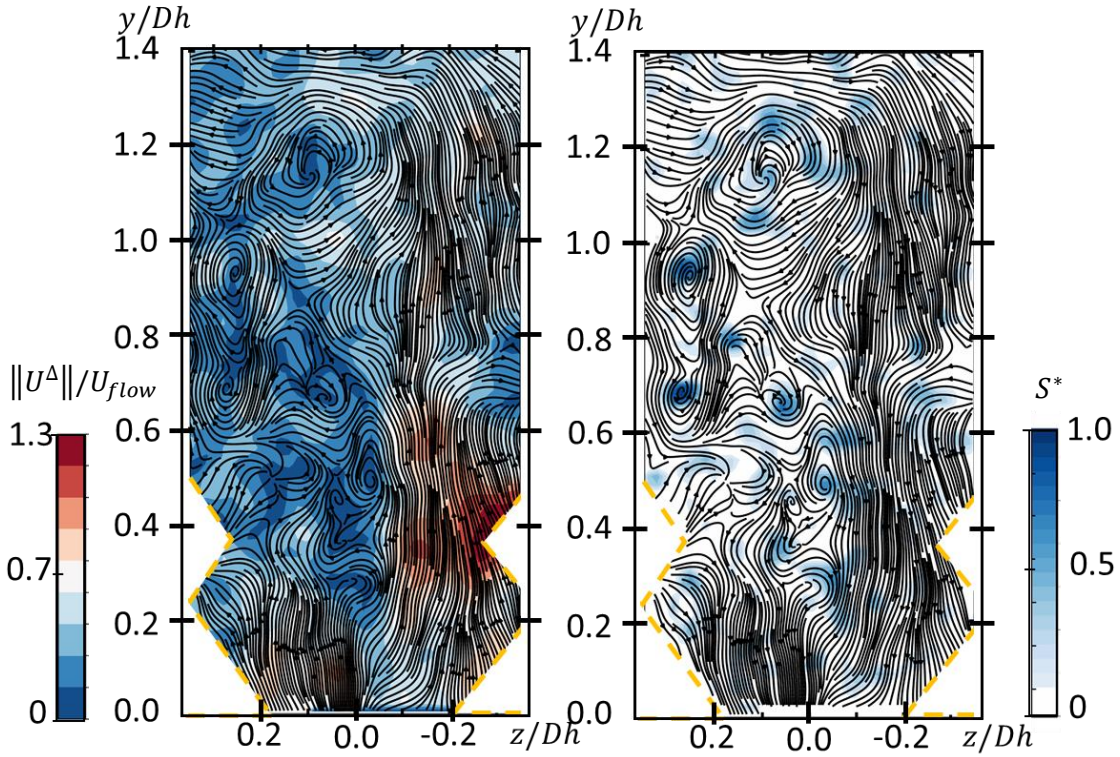

Figure 105: $\|U^{\Delta}\|/U_{flow}$ and swirling function with streamlines in referance frame moving with U_{flow} for $Re_{Dh} = 20100$ for WMV configuration

Figure 106 shows the $\|U^{\Delta}\|/U_{flow}$ and the swirling function for the Reynolds numbers $11200, 15600, 33000, 49500, 86400$ and 152000 with NMV configuration.

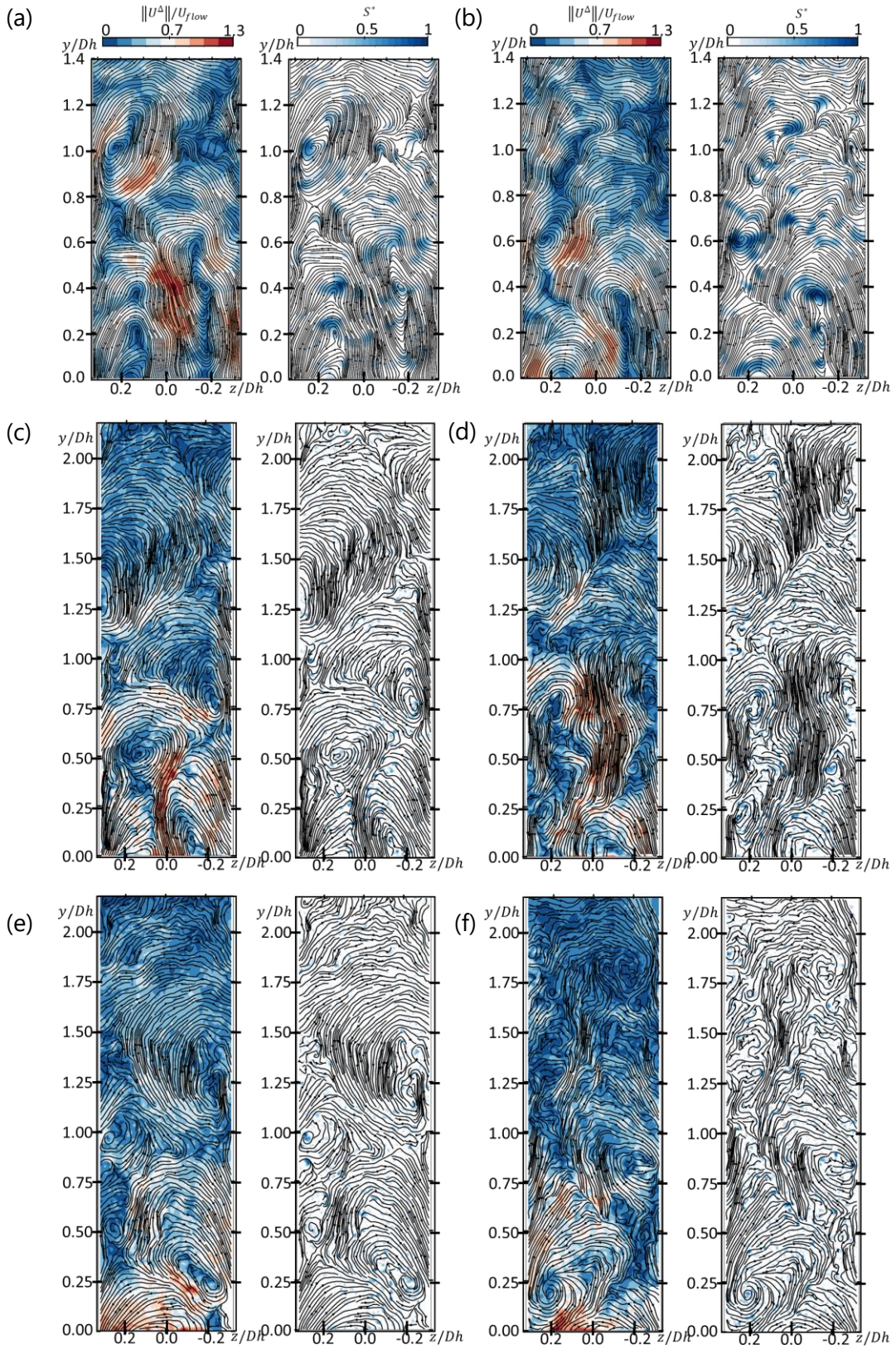

Figure 106: $\|U^{\Delta}\|/U_{flow}$ and swirling function with streamlines for $Re_{Dh} = (a)11200 (b)15600\ (c)33000\ (d)49500\ (e)86400\ (f)151200$

The existence of the coherent structures is experimentally demonstrated for the measured range of Reynolds number. Figure 106(a) and Figure 106(b) is the results of High-speed PIV measurements. The rest of the figures, i.e. from Figure 106(c) to Figure 106(f), show the results from Low-speed PIV. The results from Figure 106(c) to Figure 106(f) are with higher spatial resolution measurements, i.e. the flow can be examine for longer distances from the spacer grids, y/D_h~2.1.
Similar to the results $11200 \leq Re_{Dh} \leq 20100$, the stagnation points are observed in the heart of the structures. The existence of the structures persists up to the measurement domain, i.e $y/D_h = 1.75$. High intensity of velocities are presented around the structures.

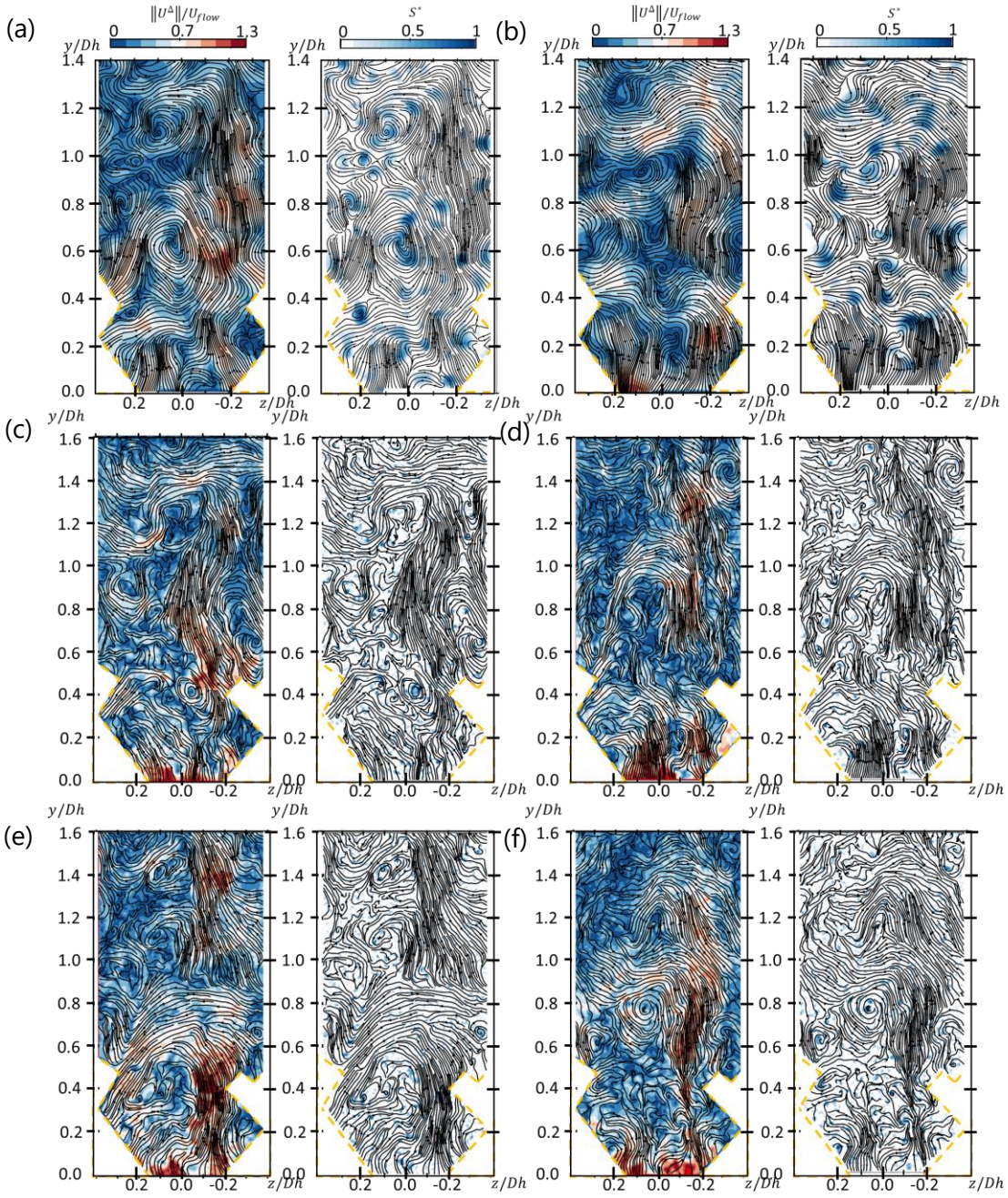

Figure 107: $\|U^{\Delta}\|/U_{flow}$ and swirling function with streamlines for $Re_{Dh} = (a)11200(b)15600\ (c)44000\ (d)60500\ (e)105000\ (f)118000$

Figure 107 shows the existence of the coherent structure for WMV configuration for the Reynolds numbers 11200, 15600, 44000, 60500, 105000 and 118000. The results show coherent behaviour with the Figure 105.
For higher Reynolds numbers, with the increased distance from the spacer grid, the intensity of the velocities around the structures is higher than for NMV configuration.

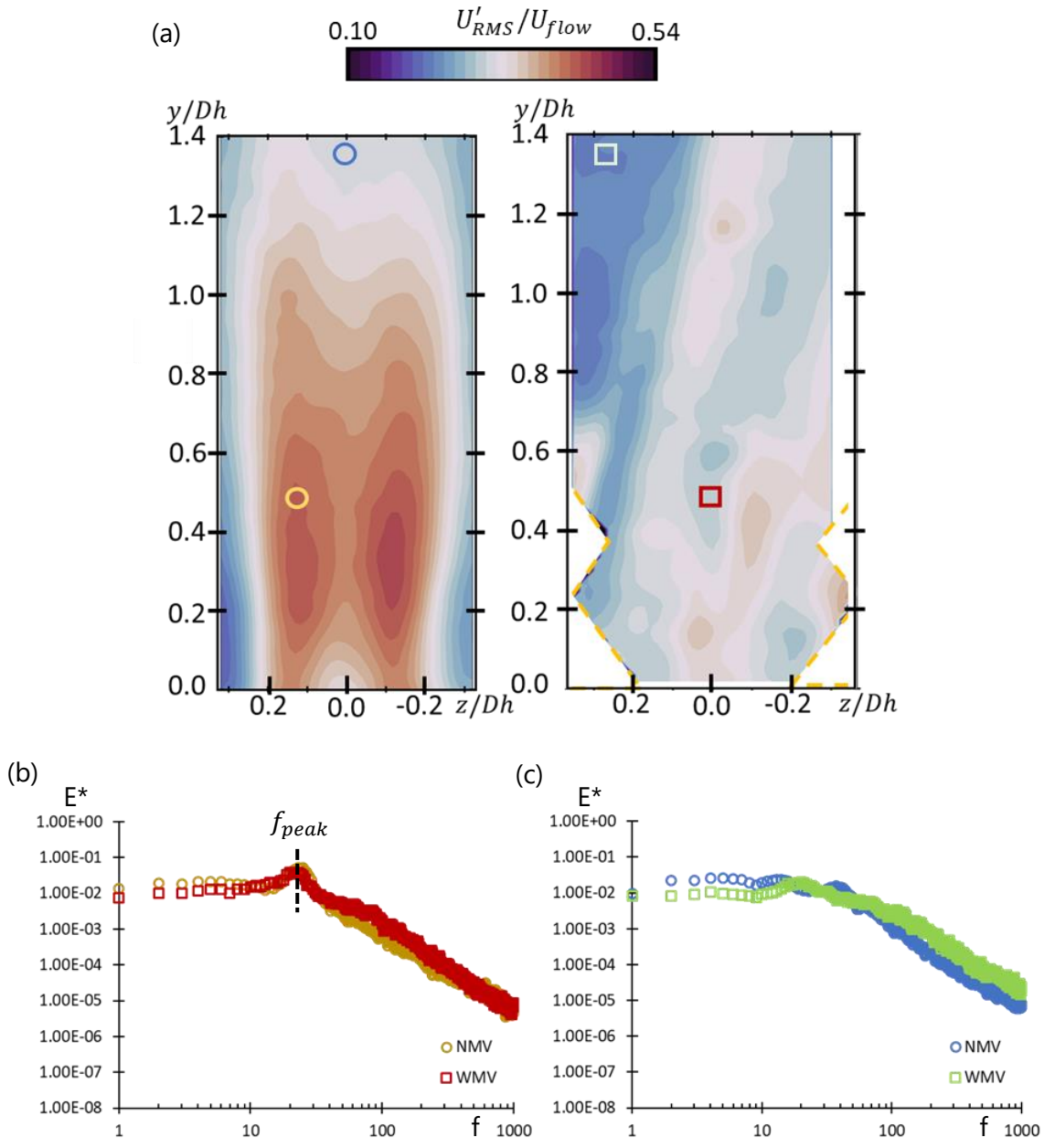

Figure 108: (a) U'_{RMS}/U_{flow} field for NMV and WMV, respectively (b) Velocity spectra at $y/D_h = 0.5$ (c) Velocity spectra at $y/D_h = 1.4$ for $Re_{Dh} = 20100$

Figure 108(a) shows the U'_{RMS}/U_{flow} for NMV and WMV configurations at $Re_{Dh} = 20100$.
In Figure 108(b) and Figure 108(c), E^* spectra is plotted for two horizontal positions, i.e. $y/D_h = 0.5$ and $y/D_h = 1.4$, respectively.
In Figure 108(b) the frequency peak can be seen for both NMV and WMV configuration. For NMV configuration the highest energy contribution is found on the sides of the dimples, i.e. $z/D_h = 0.2$

and -0.2. For WMV configuration, this contribution is observed maximum in the centre of the measurement domain, i.e. $z/D_h = 0$.

Figure 108(c) shows the E^* spectra for the points where the velocity fluctuations have low values, i.e. $0.10 \leq u'_{RMS}/U_{flow} \leq 0.15$, with darker blue colour. Compared to Figure 108(b), the frequency peaks are not present in the spectra. This result demonstrates the existence of frequency peaks in the eddy streets. The peak represent the quasi-periodic properties of these eddies in the wake of the dimples. A periodic time scale is calculated from the peak of the velocity spectra, i.e. $T = 1/f_{peak}$.

In Figure 108(c), f_{peak} is about 24Hz, i.e. T=0.041sec and 22Hz, i.e. T=0.045sec, for NMV and WMV configuration respectively.

Figure 109 and Figure 110 show the snapshot of these coherent structures downstream the dimple for $Re_{Dh} = 20100$ for NMV and WMV configurations, respectively. To show the periodicity of these structures, the frames are chosen according to the periodic time scale as 0, T/2, T, 2T, 4T and 60T.

For NMV configuration, the structures are presented in downstream the dimple on both sides. In Figure 109 the structures on the left-hand side, i.e. $0 \leq z/D_h \leq 0.3$ is marked as "L" and the right-hand side, i.e. $-0.3 \leq z/D_h \leq 0$, the structures are marked as "R". The structures are numbered according to their appearance.

From Figure 109(a) to Figure 109(c), the appearance of L_0 and L_1 is spotted to have the periodicity that is coherent with the f_{peak} in spectra. This appearance is detected for the whole duration of the measurements, i.e. ~ 25000 images. It is also noticed that the structures are following the same pattern on right-hand side with the same periodicity.

For WMV configuration the structures are seen downstream the dimple on the centre of the measurement domain and marked as "M". The structures are numbered according to their order of appearance. The periodic appearance of the structures that is remarked for NMV configuration is also noticed for WMV configuration.

To investigate if these structures persist through the space, the PIV results from higher distances, i.e. $y/D_h \geq 3$ is studied. Figure 111 shows $\|U'\|/U_{flow}$ with the swirling function at $Re_{Dh} = 20100$ for NMV and WMV, respectively, in the $3 \leq y/D_h \leq 4.4$ measurement domain.

From Figure 111(a), the coherent structures are observed to persist for NMV configuration. Compared $0 \leq y/D_h \leq 1.4$ range, the structures are noticed to be more disordered.

In Chapter 10, according to the average around the rod for NMV configuration, the frequency peak on pressure spectra is persisting up to $y/D_h = 20$. For the PIV spectra, this frequency peak is detected to persist with an intensity loss for the increased distance from the grid. This shows coherent behaviour as presented in Figure 111(a). With the increasing distance from the spacer grid, the structures keep persisting although the position of the structures become irregular compared to lower distances. This leads to the persisting frequency peaks on the average of the pressure spectra up to $y/D_h = 20$. On the other hand, in PIV spectra depending on the selected positions, i.e. $z/D_h = 0.2$, the peak becomes less pronounced.

For WMV configuration, i.e. Figure 111(b), the structures are spotted around $z/D_h = -0.2$ in the measurement domain $3 \leq y/D_h \leq 4.4$. This shows a shift on the path of the eddies compared to the measurement domain $0 \leq y/D_h \leq 1.4$. The shift present coherent behaviour with the velocity field where the same kind of direction is detected in the shear layer with the increasing distance from the grid. The size of the structures is observed to be smaller than the ones in measurement domain $0 \leq y/D_h \leq 1.4$.

For WMV configuration, with the increasing distance from the grid, the decreasing presence of the f_{peak} on pressure, LDV and PIV energy spectra, are presented in Chapter 10. Figure 111(b) shows coherent behaviour where the persisting structures are noticed to disappear for the measurement region $3 \leq y/D_h \leq 4.4$.

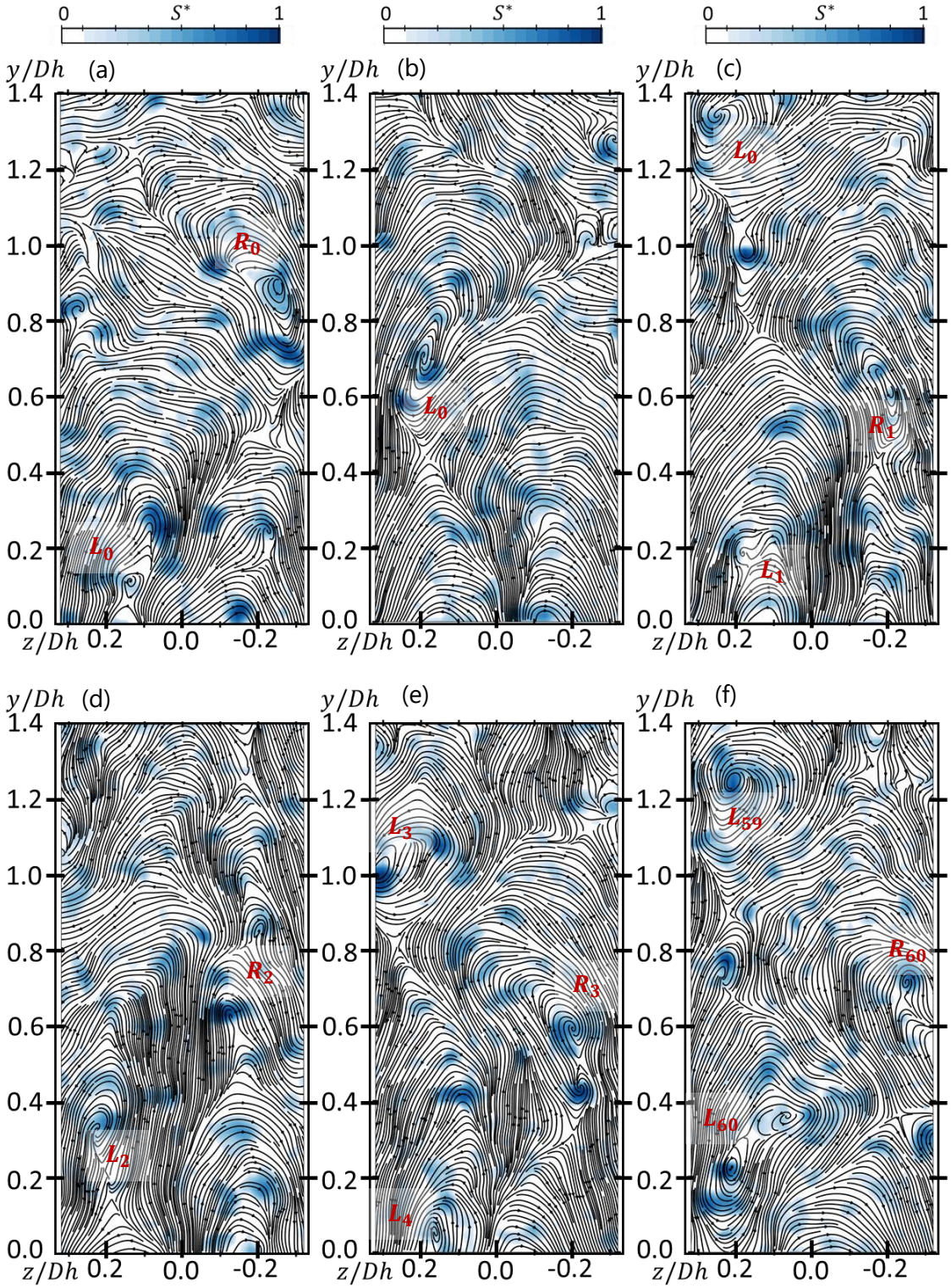

Figure 109: Displacement of main eddies at time (a) 0, (b) T/2, (c) T, (d) 2T, (e) 4T and (f) 60T for NMV configuration

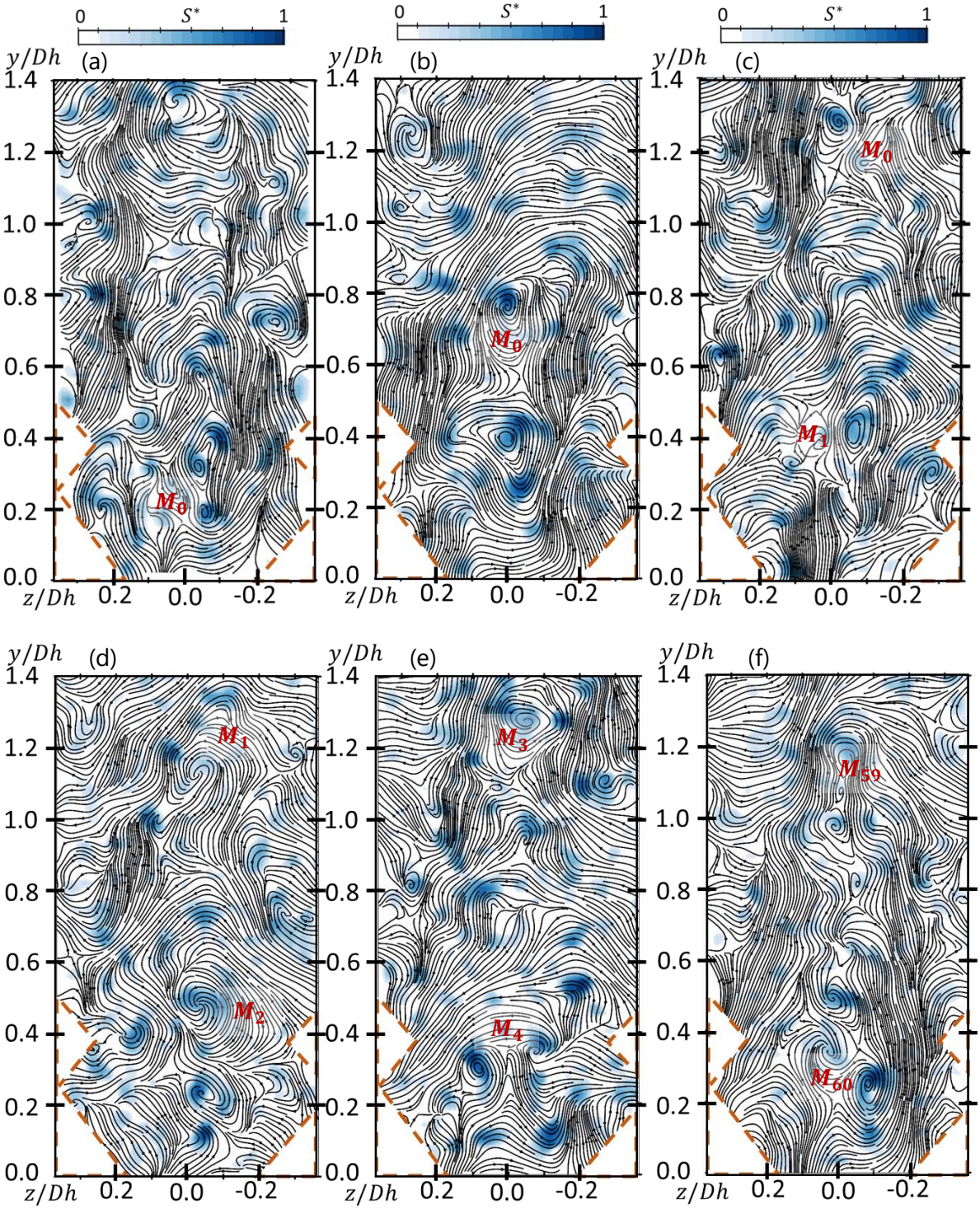

Figure 110: Displacement of main structure at time (a) 0, (b) T/2, (c) T, (d) 2T, (e) 4T and (f) 60T for WMV configuration

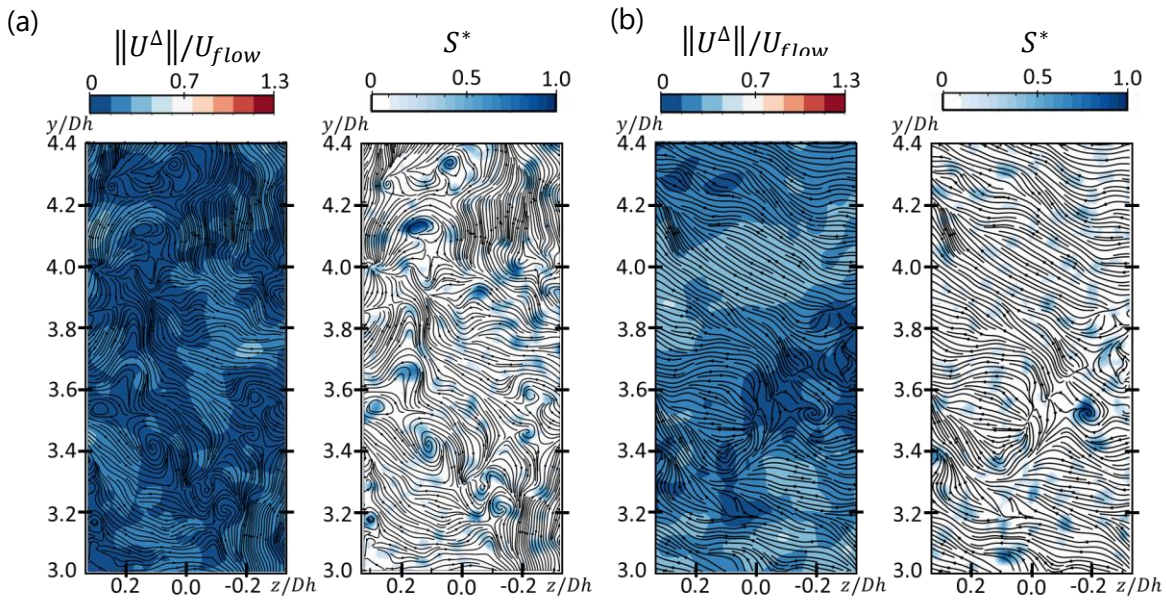

Figure 111: $\|U^{\Delta}\|/U_{flow}$ with S^* for $Re_{Dh} = 20100$ for (a) NMV configuration (b) WMV configuration

11.2 Periodic Length Scales

The periodic length scale is defined Eq.(56) where f_{peak} is the frequency peak on the spectra. It is used to estimate the distance between each periodic structure.

$$L_p = \frac{U_{flow}}{f_{peak}} \tag{56}$$

Figure 112 shows the periodic length scale of $Re_{Dh} = 13300$ for both configurations. Figure 112(a) includes the results obtained by different measurement techniques. According to pressure fluctuations, f_{peak} is found around 16Hz for NMV configuration and 15Hz for WMV configuration. For PIV measurements, the f_{peak} is measured around 17 Hz and 18Hz for NMV and WMV configurations, respectively. In LDV measurements of WMV configuration, the f_{peak} value is 12Hz where and an extra 16Hz peak is detected. The average of the f_{peak} is $15.6 \pm 2.3Hz$, i.e. $St = 0.24 \pm 0.03$.

Figure 112(b) and Figure 112(c) shows the structures with the calculated periodic length scales. For pressure length scale $L_{p_{pressure}}$ is used and for PIV length scale $L_{p_{PIV}}$ is used.

For NMV configuration, the periodic length scales of pressure and velocity are similar to each other, i.e. $1.35D_h$ and $1.27D_h$ respectively. From Figure 112(b), the calculated scales give coherent results with the distance between two structures. The selected structures are marked with red circle.

For WMV configuration the periodic length scales are $1.44D_h$ and $1.20D_h$, respectively for pressure and PIV. The coherent structures in PIV result are marked with red circles. The velocity periodic length scale is closer to the distance between the structures compared to the pressure periodic length scale. This is an expected output since the pressure sensors are measuring the signature of the structures whereas the PIV is measuring the velocity fluctuations that are related directly to the structures.

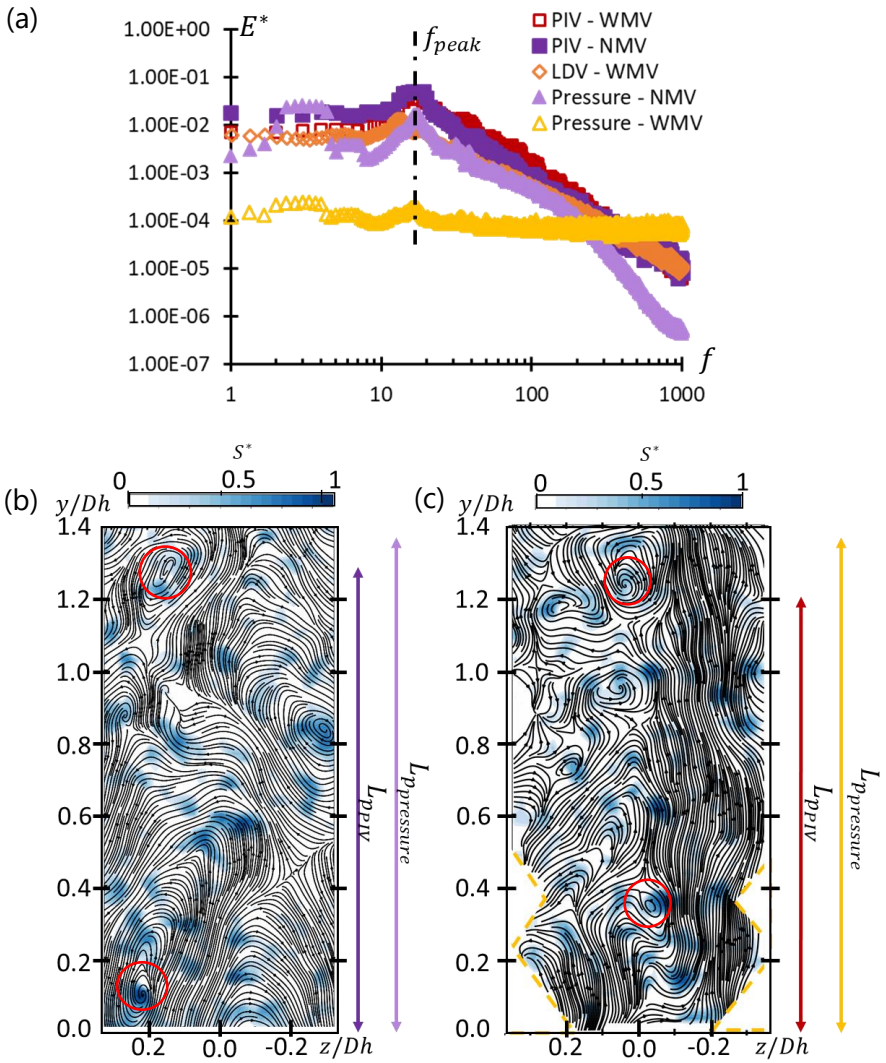

Figure 112: (a) Spectra for NMV and WMV configuration with pressure, LDV and PIV measurements (b) Periodic length scale for NMV configuration (c) Periodic length scale for WMV configuration at $Re_{Dh} = 13300$

11.3 Integral Length Scale

The integral length scale represents the size of the large scale fluctuations. For the calculation of this scale, the autocorrelation function is used. Autocorrelation functions are represents the fit between the past observations and the future predicted values (Bendat & Piersol, 1993).

The implementation of autocorrelation in Chapter 3 for the calculation of integral length scale is given in Eq. (57). F' represents the fluctuation of the signal, i.e. velocity or pressure fluctuation, t represents the point in time and τ represents the time shift. σ shows the standard deviation of the signal.

$$R_{xx}(\tau) = \lim_{T\to\infty} \frac{1}{T} \int_0^T \frac{F'(t)F'(t+\tau)}{\sigma_{F'(t)}\sigma_{F'(t+\tau)}} dt$$

$$L_i = U_{flow} * \int_0^{T_{R(T)=0}} R(t)\, dt \qquad (57)$$

11.3.1 Integral length scale for pressure measurements

11.3.1.1 Integral length scale calculation for Re 66000

Figure 113 shows the correlation function averaged over θ and noted as $\overline{R_{xx}\theta}$, with NMV configuration and WMV configuration for $Re_{Dh} = 66000$, respectively. τ^* shows the dimensionless time shift, i.e. $\tau * U_{flow}/D_h$. The both configurations the correlation functions are plotted up to $\tau^* = 3$.

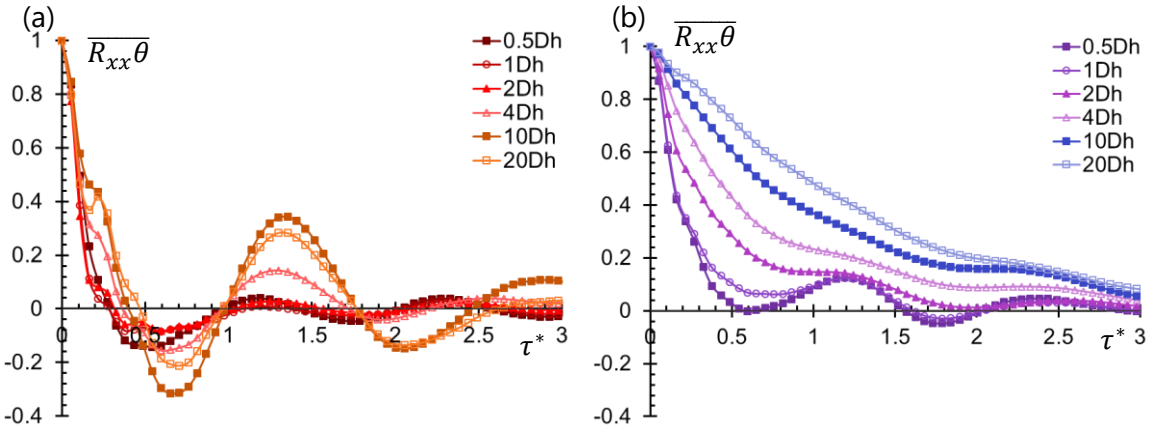

Figure 113: Correlation functions of pressure with (a) NMV configuration (b) WMV configuration for $Re_{Dh} = 66000$

For NMV configuration, the existence of anti-correlation is detected for the distances $0.5 \leq y/D_h \leq 20$. This shows that the structures persist up to $y/D_h = 20$. This is in coherence with PIV results where the structures are able to detected until the maximum PIV measurement distance, i.e. $y/D_h = 4.4$.
The most visible anti-correlation domain is spotted between $0.3 \lesssim \tau^* \lesssim 1$ for all the distances. After $\tau^* \gtrsim 1.7$, for distances $0.5 \leq y/D_h \leq 5$ the correlation values are stabilizing around 0 with standard deviation 0.01. For $y/D_h > 5$, the correlation and anti-correlation regions stay more pronounced with standard deviation 0.1, i.e. an order of magnitude higher compared to $0.5 \leq y/D_h \leq 5$.
For WMV configuration, the anti-correlation profiles are noticed between $1.5 \lesssim \tau^* \lesssim 2$ only for the distances $y/D_h < 2$. After $\tau^* \gtrsim 2$, the correlation function is remarked to start oscillate around 0. The maximum standard deviation is found 0.01 for $y/D_h = 20$.
The overall behaviour show more pronounced oscillations and clear zero-crossing values for NMV configuration compared to WMV configuration.
Figure 114 shows the integral length scale calculated from Figure 113 with the single sensor pressure measurements. The results includes both configuration for different distances away from the grid, i.e. $0.5D_h - 20D_h$.
For NMV case, the integral length scale stays persisting with the increasing distance from the grid. The size of the large scales are smaller than the hydraulic diameter, i.e. 27.7mm. The large scales vary from 0.13Dh to 0.2Dh. For $0.5 \leq y/D_h \leq 1$, 13% decrease is observed on the large scales. Between $1 \leq y/D_h \leq 2$, the scale is observed to stay stable around $0.12D_h$. With the increasing distance from $y/D_h \geq 2$, an increase around 38% is observed up to $y/D_h = 5$. After $y/D_h \geq 5$, the large scales are observed to stabilize around $0.20D_h$.
For the configuration WMV, the scales are observed larger than hydraulic diameter. These scales are increasing from 0.26Dh to 1.73Dh with the distance away from the spacer grid. The variation of the large scales are found as 84%.

The ratio of the integral length scales, i.e. $(\overline{\aleph_p\theta})_{WMV}/(\overline{\aleph_p\theta})_{NMV}$ is about 2 close to the grid and about 9 times far from the grid. These differences can be attributed to the locking of pressure fluctuations to a given size, possibly eddies.

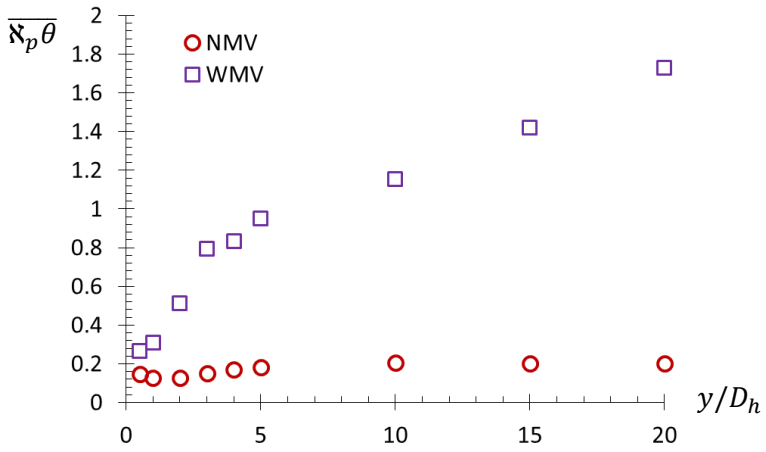

Figure 114: Dimensionless pressure integral scale averaged $\overline{\aleph_p}$over θ versus y/Dh for NMV and WMV configuration from pressure measurements

11.3.1.2 Integral length scale for broad range of Reynolds number

The integral length scale is calculated with the MPS-2021 for Reynolds number range 12800 to 20600 with NMV configuration. Figure 115 shows the integral length scale for MPS-2021 with the calculated scales from SPS-2016 at $Re_{Dh} = 66000$ for comparison.

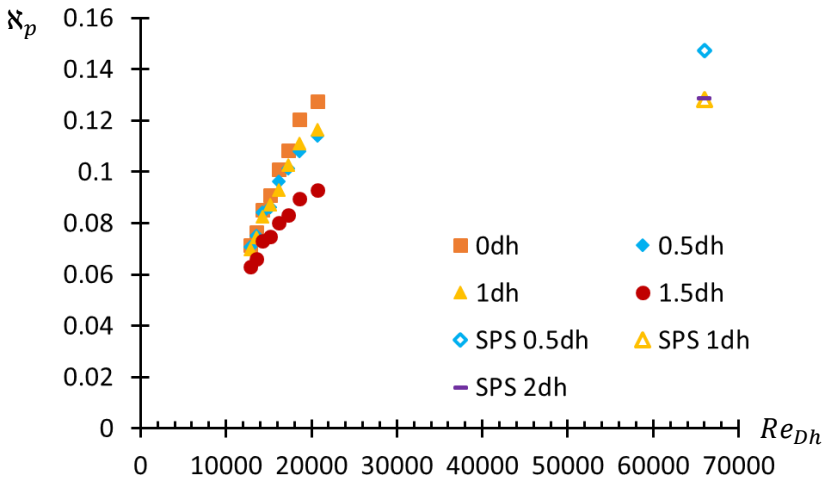

Figure 115: Pressure length scale with NMV configuration for $Re_{Dh} = 12800 - 66000$

The integral length scales are found 0.09 ± 0.008 for the Reynolds numbers $12800 \leq Re_{Dh} \leq 66000$. The smallest $\aleph_p$ is around 0.07 for $Re_{Dh} = 13000$ at $y/D_h = 1.5$.

The length scales are noticed to increase with the increasing Reynolds number and with the decreasing distance.

The increase connected to the Reynolds number is found as 51% for $12800 \leq Re_{Dh} \leq 66000$. From MPS-2021 results, the integral length scales are observed to vary from 0.06Dh to 0.12Dh. The average variation between the length scale from difference distances, i.e. $0 \leq y/D_h \leq 1.5$, is found as 19%.

In coherence with the results of $Re_{Dh} = 66000$, the size of the large scales is observed to be smaller than the hydraulic diameter, i.e. 27.7mm.

11.3.2 Integral length scale for velocity measurements

11.3.2.1 Velocity integral length scales from LDV results

Figure 116(a) shows an example autocorrelation function for $Re_{Dh} = 53600$ with WMV configuration. For all the distances, zero-crossing values are observed with oscillations on the correlation function. Figure 116(b) shows a comparison for WMV configuration with the length scales calculated from LDV velocity scales and pressure scales for $Re_{Dh} = 66000$, i.e. SPS-2018 campaign.

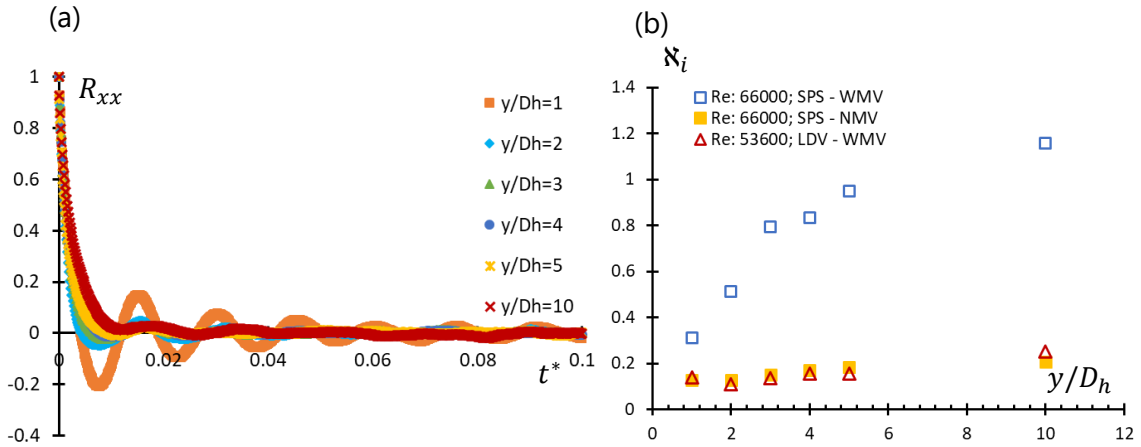

Figure 116: (a) Autocorrelation plot for $Re_{Dh} = 53600$ (b) Comparison of scales with SPS-2018 pressure results and LDV velocity results for WMV configuration

The results shows two different behaviour for velocity fluctuations and pressure fluctuations. The average difference between the integral length scales calculated from LDV-2019 velocity fluctuations and SPS-2018 pressure fluctuations are calculated as 76% for WMV configuration. This difference between length scales is decreased around 6% comparison with SPS-2016 pressure length scales with NMV configuration and LDV-2019 velocity length scale with WMV configuration. The details about possible source of this difference between pressure and velocity integral length scale is discussed in Chapter 11.3.2.2 with quantification of structures by using PIV measurements.

The LDV-2019 integral length scales of velocity fluctuation are decreased by 21% from 0.12 to 0.08 between $1 \leq y/D_h \leq 2$. Starting from $y/D_h = 3$, these scales are increases from 0.10 to 0.25 at $y/D_h = 10$.

Figure 117 shows the LDV-2019 integral length scales of velocity fluctuations with different distances, i.e. $1 \leq y/D_h \leq 10$ for Reynolds number range $13400 \leq Re_{Dh} \leq 53600$.

For all the Reynolds number, between $1 \leq y/D_h \leq 2$, a decrease is observed on the length scales. After $y/D_h \geq 3$, the scales are observed to increase.

Between $1 \leq y/D_h \leq 3$ to $y/D_h = 3$, the standard deviation is observed to increase with the distance, i.e. 0.007 to 0.021. After $y/D_h \geq 3$, the standart deviation of the lengths scales are stabilize around 0.013.

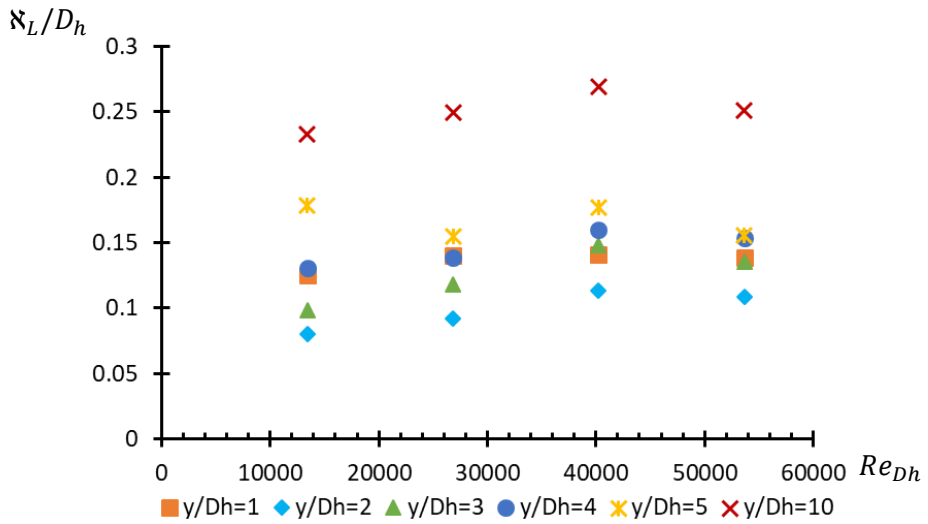

Figure 117: Zero-crossing length scales with WMV configuration for $13400 \leq Re_{Dh} \leq 53600$

11.3.2.2 PIV velocity integral length scales

By using the autocorrelation, the integral length scales are calculated for two components of the flow, i.e. $\aleph_{i_{uu}}$ and $\aleph_{i_{vv}}$. The characteristic length scale for PIV is calculated as Eq. (58) by using these components of the flow. (Matozinhos, et al., 2021)

$$\aleph_{i_{mag}} = \sqrt{\aleph_{i_{uu}}^2 + \aleph_{i_{vv}}^2} \tag{58}$$

Figure 118 shows the integral length scale field with NMV configuration for u component, v component and magnitude of the length scale, respectively as Figure 118(a), Figure 118(b) and Figure 118(c). The figure includes different Reynolds number as $11200, 15700$ and 20125.

For Figure 118(a), high-length scales are observed downstream the dimples. This zone corresponds to no-structure zone which can be seen in Chapter 11.1. With the increasing Reynolds number it is observed that the intensity of $\aleph_{i_{uu}}/D_h$ is increasing around this zone.

On two side of the dimple the length scales are observed close to $\aleph_{i_{uu}} \sim 0.2 D_h$.

Figure 118(b) shows the results for $\aleph_{i_{vv}}/D_h$ component where the length scale is around $\aleph_{i_{vv}}/D_h \sim 0.2$.

Figure 118(c) shows similar results as Figure 118(a) which is expected where the dominant component of the flow is u-component.

Figure 119 shows the same length scales for WMV configuration. Compared to NMV configuration, no high-scale zone is observed. The scale difference is spotted with the orientation of the tip of mixing vanes, i.e. presence of smaller scales with the mixing vane angle.

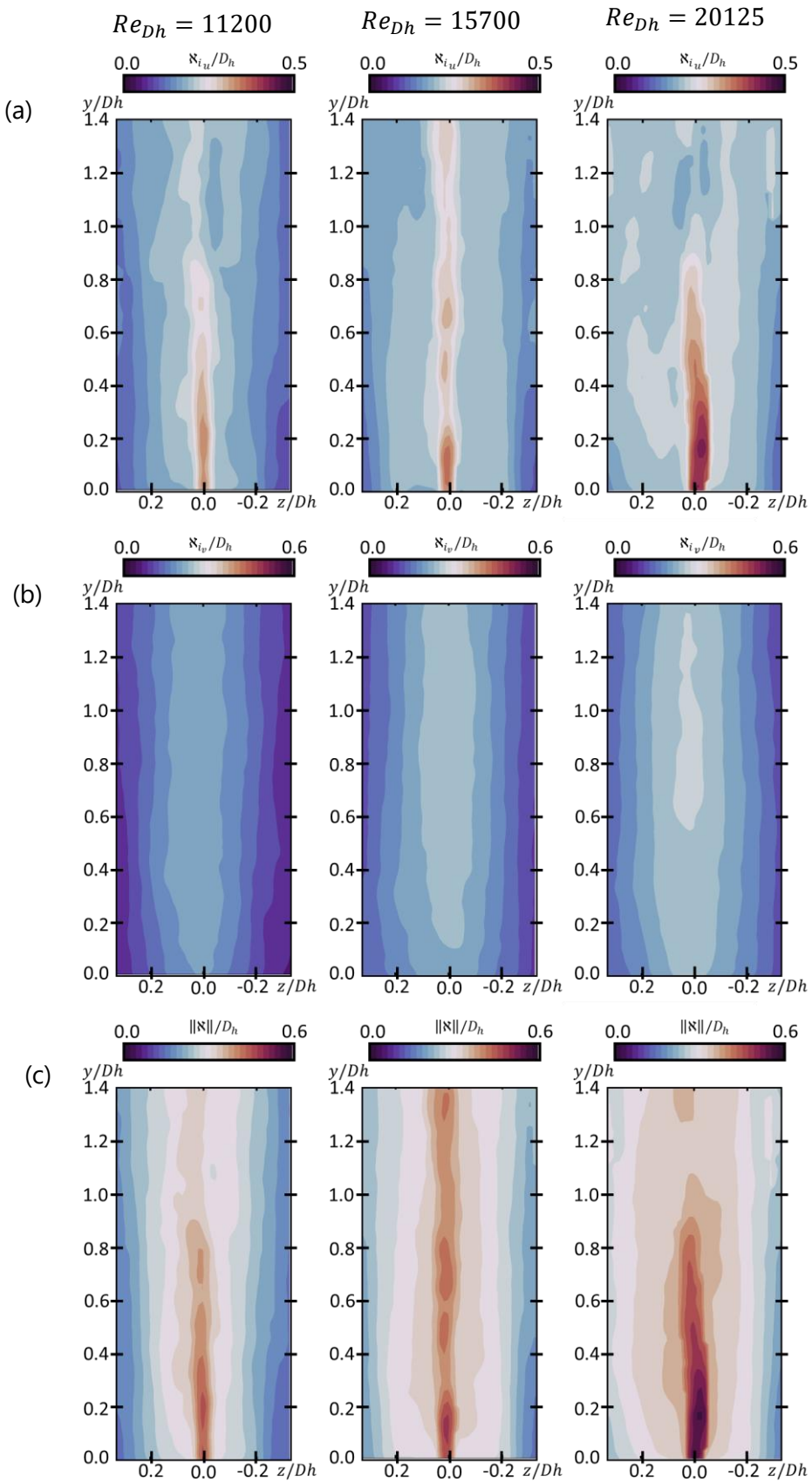

Figure 118: (a) integral length scale of u component (b) integral length scale of v component (c) integral length scale magnitude for $Re_{Dh} = 11200, 15700, 20100$ respectively for NMV configuration

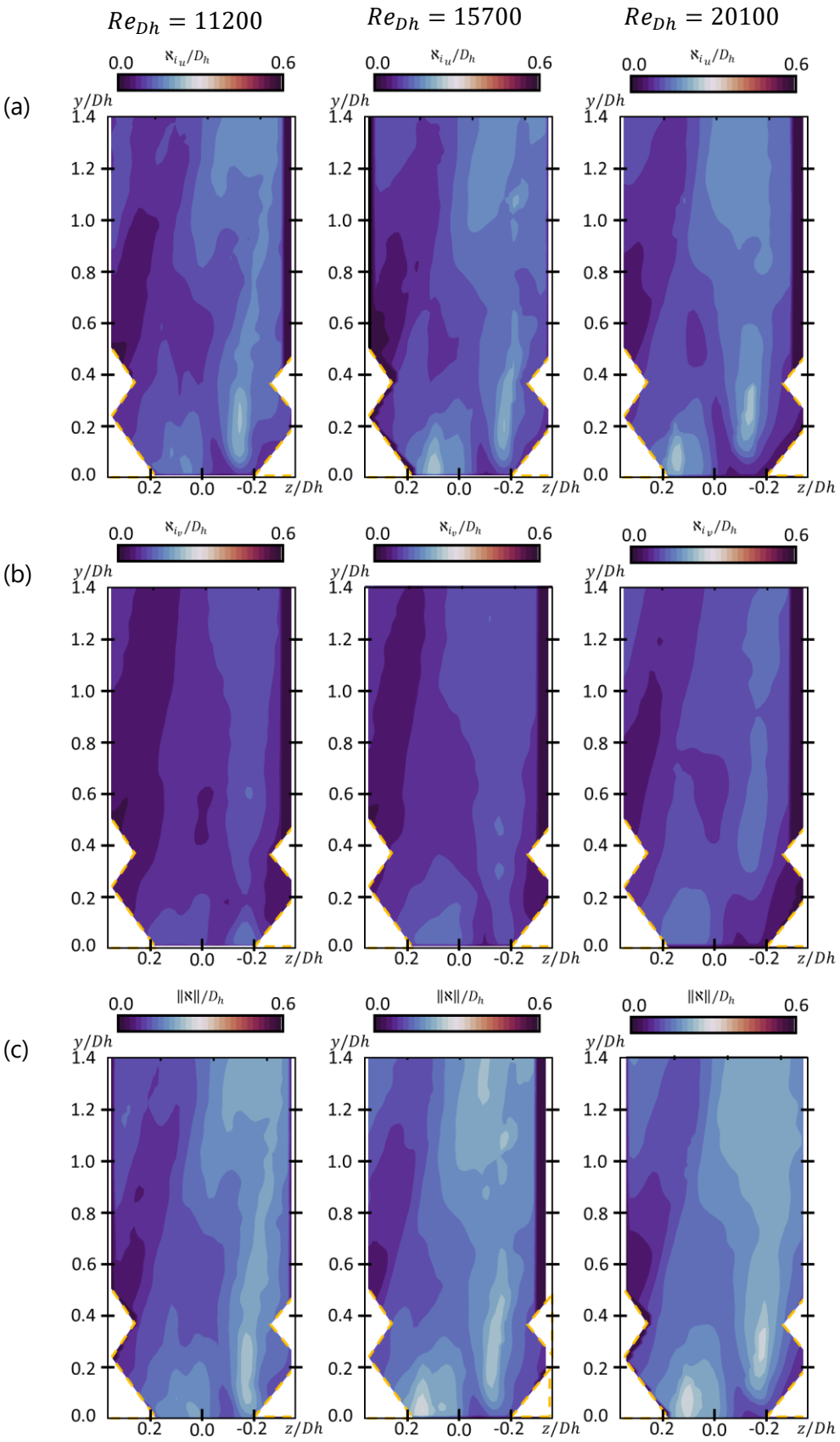

Figure 119: (a) integral length scale of u component (b) integral length scale of v component (c) integral length scale magnitude for $Re_{Dh} = 11200, 15700, 20100$ respectively for WMV configuration

To quantify the length scales, the profile of dimensionless length scale magnitude, $\aleph_i^* = \aleph_{i_{mag}}/D_h$, is plotted in Figure 120. For the profiles, the z/D_h is selected according to the structure region, i.e. $z/D_h = 0.2$ and $z/D_h = 0$, respectively for NMV and WMV configurations.
The $\langle \aleph_i^* \rangle$ values are $0.20, 0.23$ and 0.25 with NMV configuration for Reynolds number values of $11200, 15700$ and 20100, respectively.

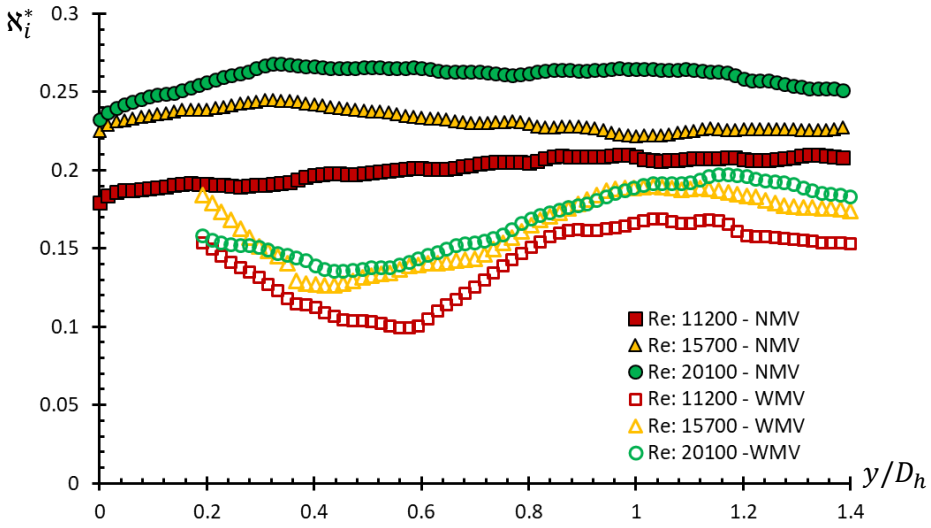

Figure 120: PIV integral length scale for $Re_{Dh} = 11200, 15700, 20100$ for NMV and WMV configurations. For NMV profile is selected at $z/D_h = 0.2$, for WMV profile is selected at $z/D_h = 0$

For WMV configuration, the measurement domain $y/D_h < 0.2$ is discarded in the profile due to uncertainties of the results which is discussed in Chapter 9. The $\langle \aleph_i^* \rangle$ values are $0.14, 0.16$ and 0.16, for Reynolds number values of $11200, 15700$ and 20100, respectively. In average the PIV velocity length scales are found 32% higher than WMV configuration.
For NMV configuration, the profile of $\langle \aleph_i^* \rangle$ is observed more stable than WMV configuration. The standard deviation is 0.007 and 0.02 for NMV and WMV configuration, respectively. This corresponds lower than 96% and 84% of the mean value for NMV and WMV configuration, respectively.
Figure 121(a) and Figure 121(b) is the swirling function for NMV configuration and WMV configuration, respectively for $Re_{Dh} = 17900$. On the figure, calculated PIV length scale magnitude is marked as $\aleph_{NMV}^*$ and $\aleph_{WMV}^*$ where $\aleph^* = \langle \aleph_{i_{mag}} \rangle / D_h$. $\aleph_{NMV}^*$ is 0.22 ± 0.02 and $\aleph_{WMV}^*$ is 0.17 ± 0.03.
The captured structures are coherent with the length scale calculated from PIV velocity fluctuations. It is also observed that the length scale corresponds to the dark blue part of the core of the structure.

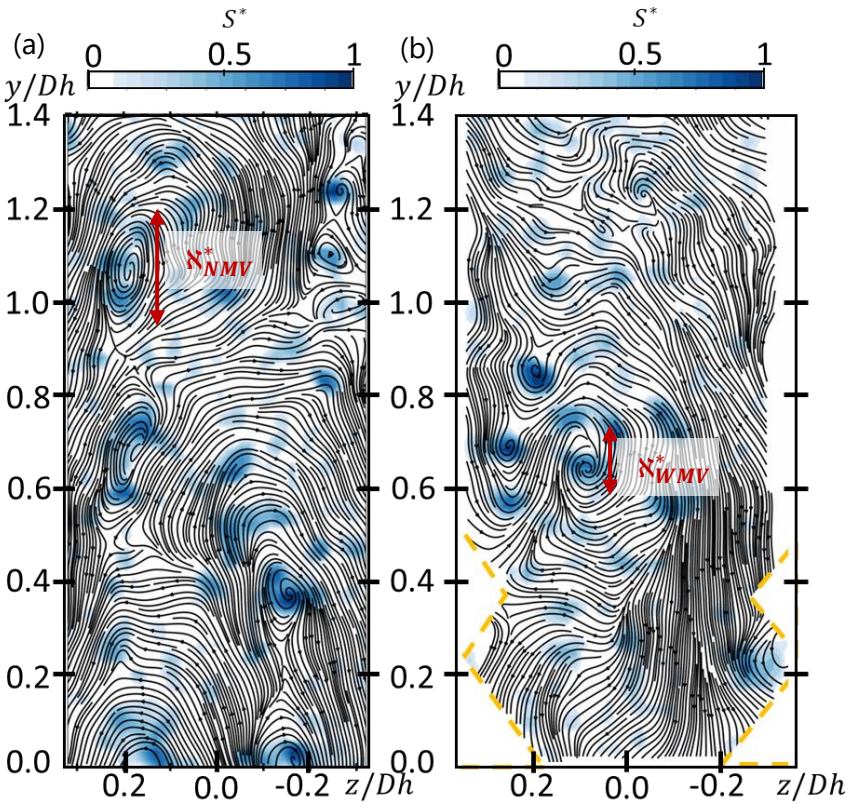

Figure 121: (a) Swirling function for NMV configuration (b) Swirling function for WMV configuration for $Re_{Dh} = 17900$

To explore the connection with other length scales, i.e. pressure length scale and LDV velocity length scale, PIV swirling function is plotted for $Re_{Dh} = 66000$ as Figure 122.

Figure 122(a) and Figure 122(b) show the swirling function for NMV and WMV configuration, respectively. In both configuration, the dimensionless pressure length scale is marked as $\aleph^*_p$.

For NMV configuration, only the pressure length scale is compared with the structure size. The pressure length scales are in coherence with the structures downstream the dimples. These structures are observed as one core for $Re_{Dh} = 66000$ similarly to Figure 121(a). For WMV configuration, these structures have multiple cores for increased Reynolds number.

For WMV configuration, two different length scales are used as $\aleph^*_p$ and the dimensionless LDV velocity length scale which is marked as $\aleph^*_L$.

In Chapter 11.3.2.1, the difference between two length scales are shown in Figure 116(b). From those results, the difference between pressure and velocity scales were found as 76%. According to the Figure 122(b), the pressure length scale includes a larger area of the structure where for LDV velocity length scale is matching with the cores of the structure.

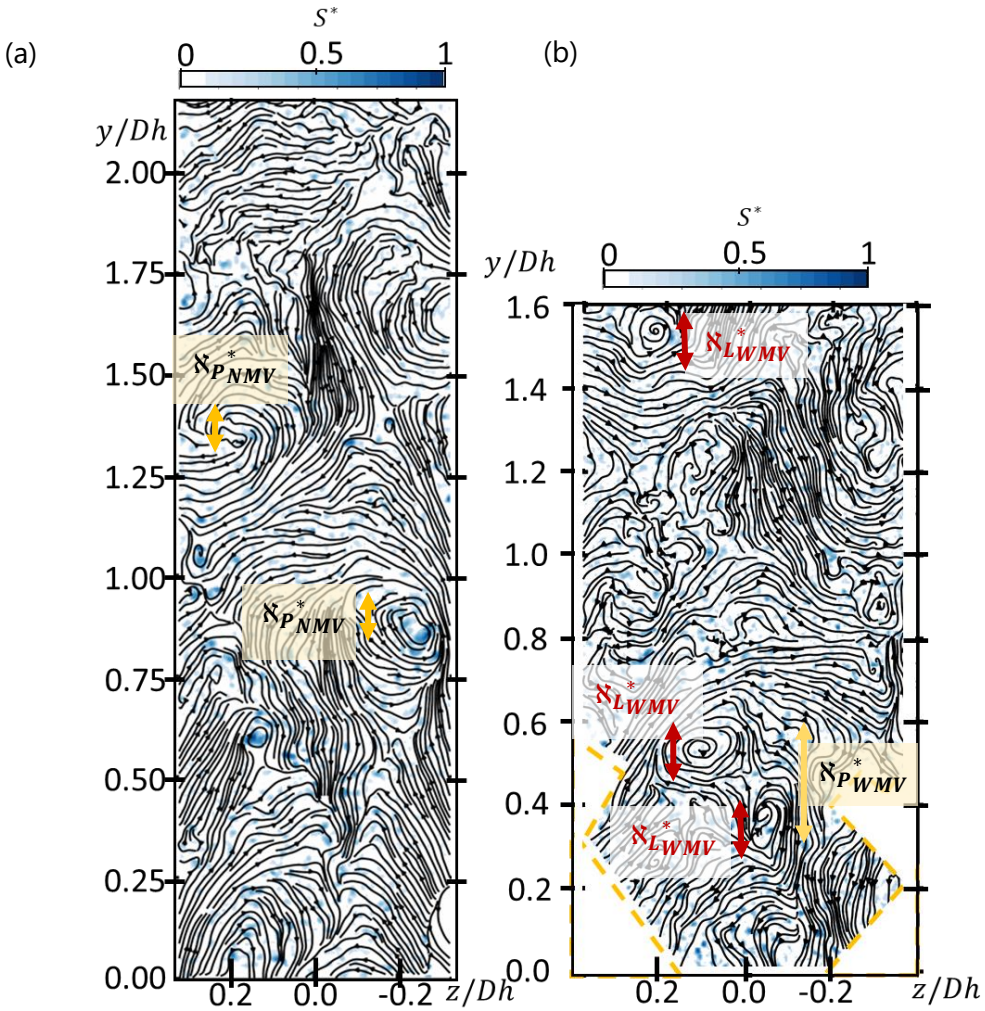

Figure 122: Swirling function for $Re_{Dh} = 66000$ with (a) NMV configuration (b) WMV configuration

In Figure 123, different frames are plotted with $\|U^{\Delta}\|/U_{flow}$ for WMV configuration. In the figure, the pressure integral scale is shown with yellow arrow and LDV length scale is shown with red arrow next to the identified structures according to the swirling streamlines.

The core of the identified structures, the $\|U^{\Delta}\|/U_{flow}$ is zero. These structures are surrounded by the high velocity zones which are marked with yellow dotted circles. The pressure length scales are noticed to have similar size with this high velocity zones.

The reason of the difference between pressure and velocity length scales might be explained by the properties of eddies. In Chapter 3, the turbulent flow is identified with eddies which are stretched and twisted by the velocity field. This leads, the eddies to inducing their own velocity field while generating pressure waves (Davidson, 2004). Since the pressure sensors are measuring these generated waves, i.e. signatures of the structures, it can be possible that the sensors are less sensitive to the core of the structures. In coherence with this, LDV integral scales of velocity fluctuations shows the cores of the structures, i.e. as a consequence of the direct relation between the eddies and the velocity field.

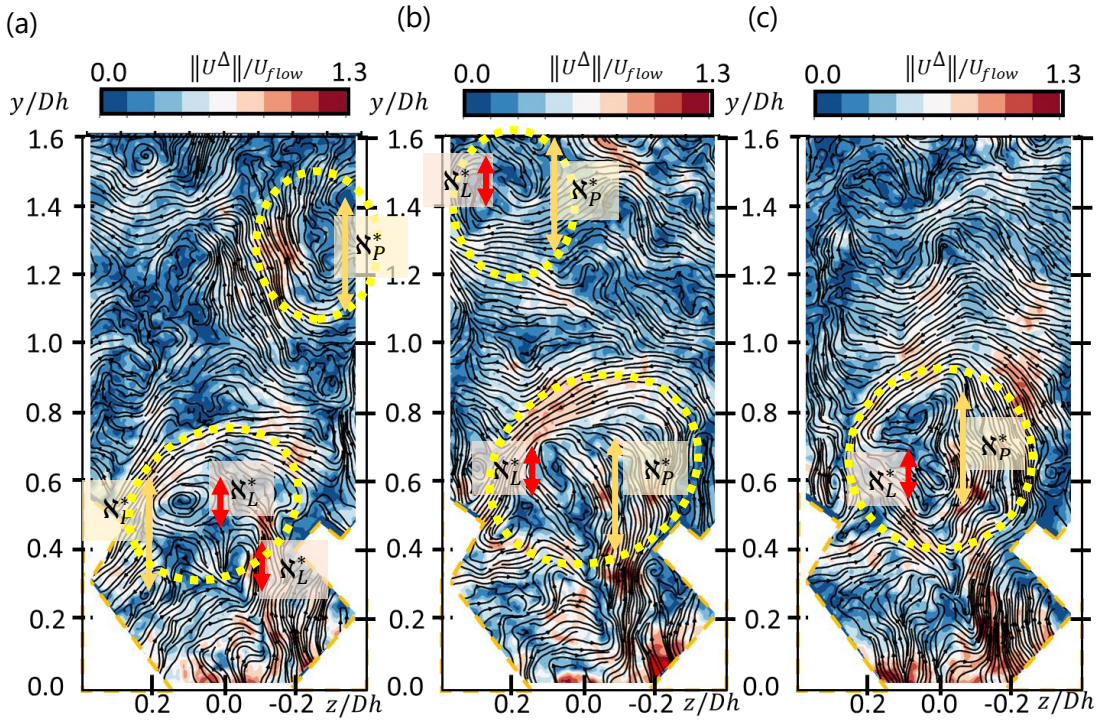

Figure 123: $\|U^{\Delta}\|/U_{flow}$ field for $Re_{Dh} = 66000$ for two PIV frame intervals (F) (a) $F = F_0$ (b)$F_0 + 2$ (c) $F_0 + 4$ with WMV configuration. The pressure and LDV integral length scale is shown in yellow and red arrow. The high velocity zones are marked with yellow dotted circle.

CHAPTER 12
TRANSPORT OF FLUCTUATIONS

12. TRANSPORT OF PRESSURE FLUCTUATIONS

A frequency peak is present in both velocity and pressure fluctuations spectra. In this chapter the transport of the pressure fluctuations are explored using the multi-sensor device and direct correlation between simultaneous velocity and pressure measurements.

Transport velocity represents the speed at which a disturbance is transported downstream. This information can be obtained by the space-time correlation data of the fluctuations that are connected to wall turbulence (Bakewell, 1968). To investigate the transport velocity of the pressure events, cross-correlation is used.

Figure 124 shows the schematic of the transport of flow structures compared to the position of the pressure sensors. The structure passing though the pressure sensors can be seen in this schematics.

In the first part, the transport velocity of pressure events is investigated. For this, the pressure results that is obtained from multisensor device are used for pressure-pressure correlation.

In the second part, the transport of pressure fluctuations are investigated using cross-correlation between velocity and pressure signal measured simultaneously.

The parameters for application of the cross-correlation between pressure-pressure and pressure-velocity depends on the phenomena investigated. For pressure-pressure cross-correlation the aim is to track the pressure event sensor by sensor. For pressure-velocity cross-correlation, the aim is to track the periodicity of the fluctuations and measure the phase shift in function of the distance between pressure and velocity measurements.

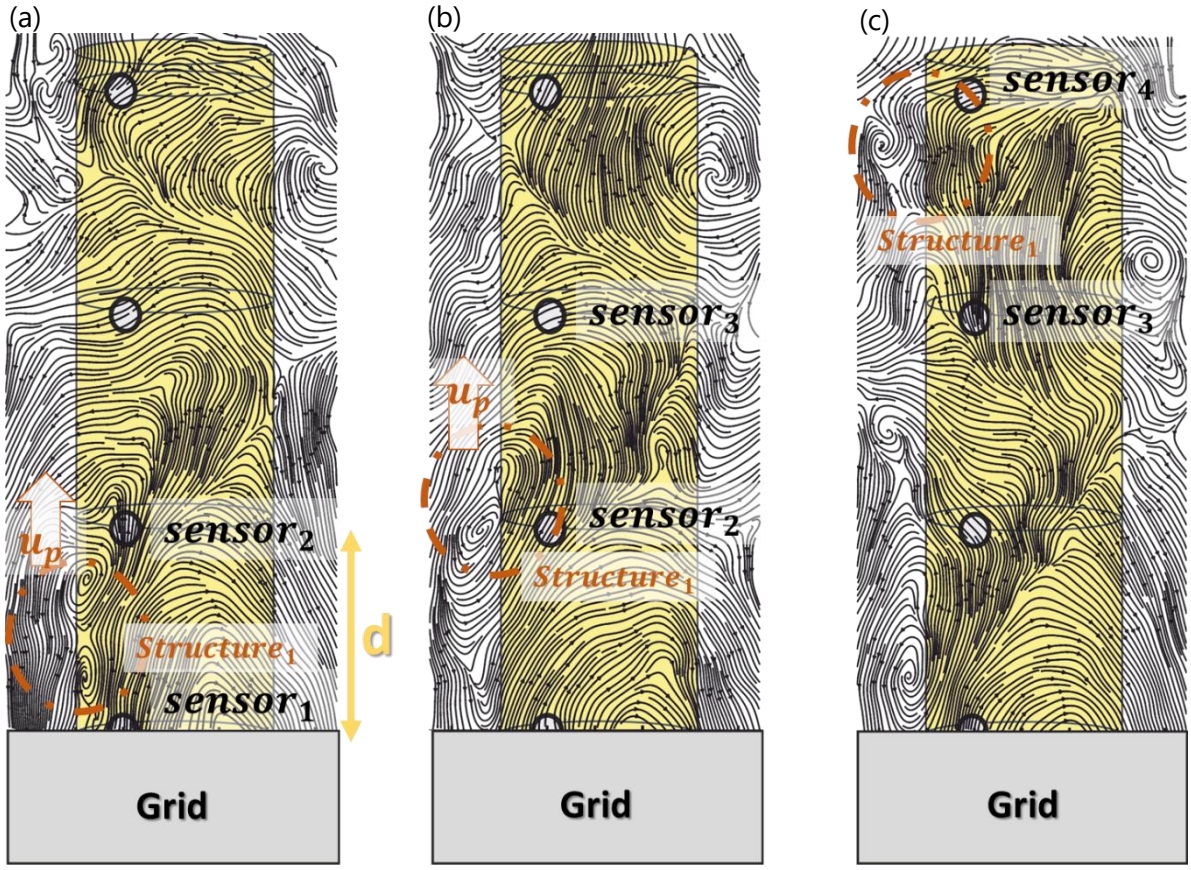

Figure 124 : Schematics of transport of fluctuations. The streamlines are taken from PIV results. (a) $t_0 = 0$ (b)$t_1 = t + t_0$ (c)$t_2 = t + t_1$ where $t = 1/(2 * f_{peak})$

12.1 Tracking events between different pressure sensors

The aim of the simultaneous pressure measurements is to catch the transport of pressure events that are related to frequency peak on the pressure spectra.
The high cross-correlation coefficient between the pressure sensors represents the similarity between the pressure events which is assumed to corresponds to signature of the same structure.
The time delay, τ, corresponds to the time information of the highest correlation coefficient, i.e. time lag between similarity of different sensors. This τ shows the time difference of the signature created by the same structure.
Since the distance between each sensor, d, is known, the transport velocity of the pressure fluctuation can be found as Eq.(59)

$$u_\tau = \frac{d}{\tau} \tag{59}$$

12.1.1 Application of pressure-pressure cross-correlation

12.1.1.1 Parameters for pressure cross-correlation

In order to track a selected event, two parameters are selected:

- window size
- searching area

The aim is to have a correlation window that is large enough to permit to capture a single event meanwhile the searching area includes this single event.
The correlation window is selected according to the periodicity of one event, i.e. $1/f_{peak}$. For the result of the correlation, high correlation coefficient is expected when the selected two sensors observe similar events.
The searching area needs to be short enough to avoid multiple events in the correlation results. In Chapter 9, the velocity field is observed as non-uniform. In Chapter 11, the structures are observed where the velocity values are found about U_{flow}. To ensure to capture the signatures of these structures, the limit of searching area, τ_{limit}, is selected according to Eq.(60).

$$\tau_{limit} = 2 * \left(\frac{d_{sensors}}{U_{flow}} \right) \tag{60}$$

In Eq.(60), $d_{sensors}$ is the distance between selected sensors. Since the velocity of the structures are not expected to be faster than U_{flow}, the velocity is selected as U_{flow}.
The selected correlation window is moved point by point on the selected signals. This moving points shows the time lag which is defined as τ. For every point the cross-correlation is calculated as Eq. (61) that is implemented from Chapter 3.

$$R_{xy}(\tau) = \frac{\overline{(P_1'(t) * P_2'(t+\tau))}}{\sigma_{P_1'(t)} \sigma_{P_2'(t+\tau)}} \tag{61}$$

In Eq. (61) P_1' and P_2' show the selected two signals, t shows the selected time range and σ is the standard deviation of the signals.
Figure 125 shows the dimensionless pressure fluctuations, i.e. P^*, from pressure sensor 1 and pressure sensor 2 for the selected case. To illustrate the procedure, Re_{Dh} is selected as 19400 for NMV configuration. The frequency peak is observed as $\sim 20 - 21\, Hz$ on the pressure spectra. According to this peak, the correlation window size is selected as 0.05sec. τ_{limit} is found as 0.0307sec. For sensor 1, same section of time is selected from $t = 0.03 - 0.08\, sec$ for all the plots. For sensor 2, the section of time is selected with different time delays relative to the presented correlation window, i.e. different τ values. τ shows the time shift relative to the selected window.

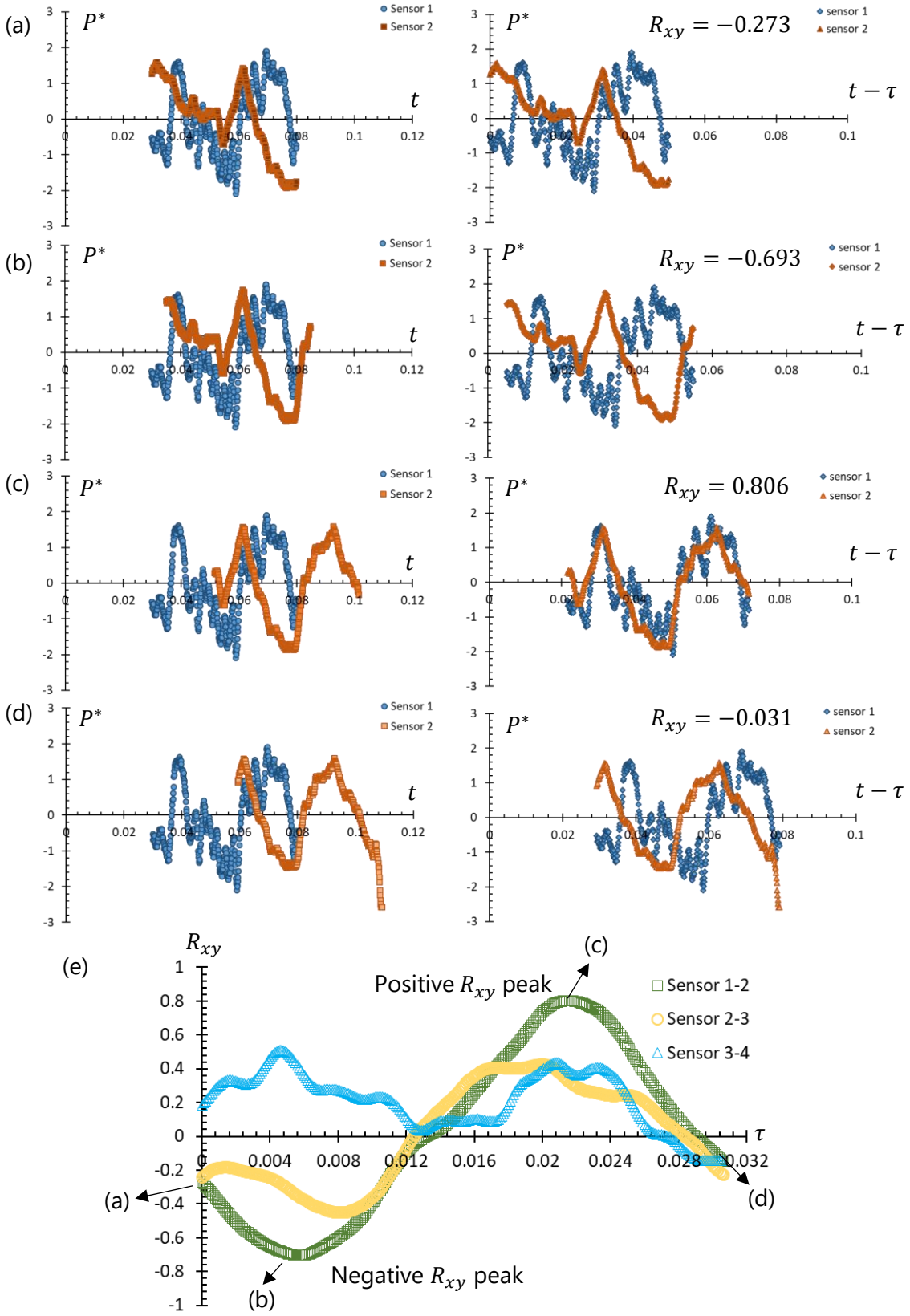

Figure 125: Dimensionless pressure fluctuation for real time and normalized time respectively for (a) $\tau = 0sec$ (b) $\tau = 0.005sec$ (c) $\tau = 0.0216sec$ (d) $\tau = 0.0293sec$ (e) Correlation result of window t=0.03-0.08sec for sensors 1-2, sensors 2-3 and sensors 3-4

In each plot of Figure 125(a) to Figure 125(d), the calculated correlation coefficient can be seen as R_{xy} for different τ values. The left-hand side of the plots give the real time of the selected signals. On the right-hand side, the selected signals are shown in normalized time, i.e. $t - \tau$. This gives the superposed plots of the selected signals.

Figure 125(e) shows the result of the cross-correlation which is the R_{xy} values plotted according to τ values for the $t = 0.03 - 0.08\ sec$. The plot includes the correlation results between sensor 1-2, sensor 2-3 and sensor 3-4 for same section of time.

All the selected cases, i.e. Figure 125(a) to Figure 125(d), are shown with their corresponding letters for sensor1-2 case. The highest R_{xy} value is 0.80 for $\tau = 0.0216$. The similarity of the signals can be seen in Figure 125(c).

For same selected window, the R_{xy} values are decreasing with the increased distance, i.e. correlation between sensor 2-3, where the highest correlation value is observed around same values. The correlation result is observed to be different for sensor 3-4 where no negative correlation coefficient is found.

12.1.1.2 Time lag between pressure sensors

To have the cross-correlation result, the correlation coefficient is calculated point by point for time section between $t = 0 - 20sec$. For each window, the peaks of positive R_{xy} and negative R_{xy} is found as shown in Figure 125(e). These peaks correspond to Figure 125(c) and Figure 125(b), respectively.

The highest positive and negative R_{xy} values per window is detected in order to find the time information of the pressure events. The results are filtered according to maximum R_{xy} of all the windows, i.e. $|R_{xy}|_{max}$. All the coefficients that are $|R_{xy}| < 0.8|R_{xy}|_{max}$, are removed.

The R_{xy} values that fulfil the conditions are recognized as "identified event". The time information, i.e. τ, corresponds to the "identified event" are gathered. The histogram of the time information is

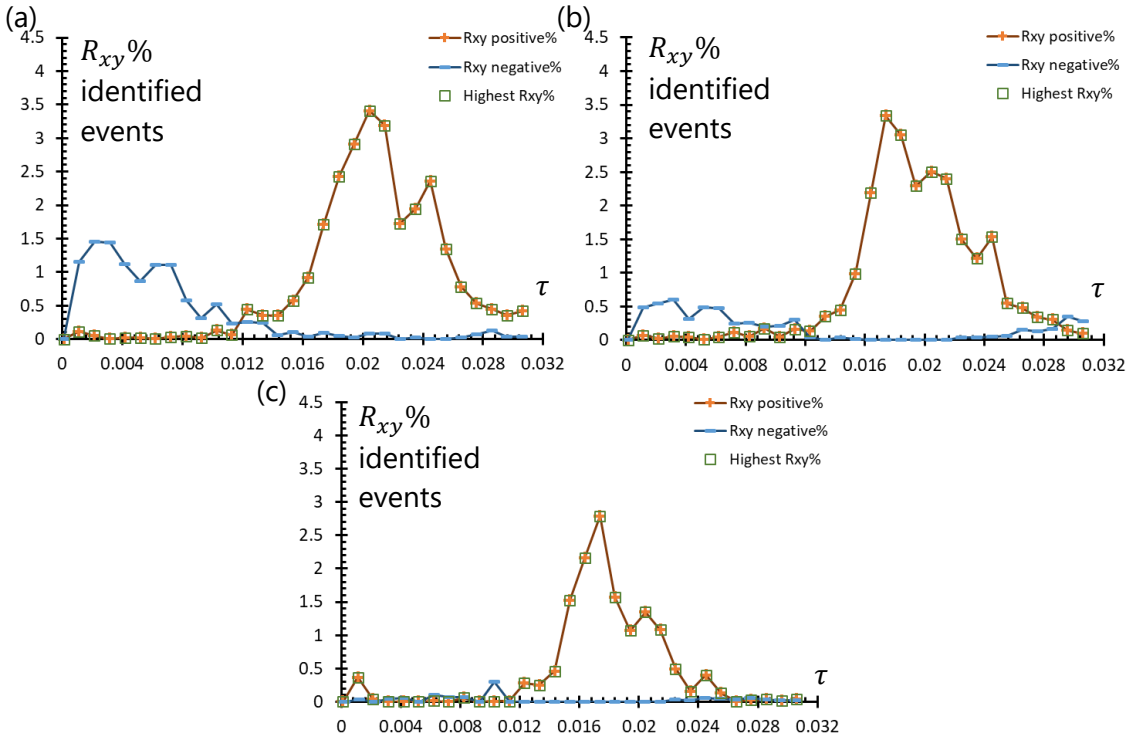

Figure 126: $\%R_{xy}$ results for correlation between (a) sensor 1-2 (b) sensor 2-3 (c) sensor 3-4 for NMV configuration $Re_{Dh} = 19400$

plotted according to the percentage of identified events. The percentage is calculated for ~200000 windows.

Figure 126 shows the identified events for sensor 1-2, sensor 2-3 and sensor 3-4 with NMV configuration.

In the plots, both positive and negative R_{xy} which is higher than $0.8|R_{xy}|_{max'}$ are given as identified "R_{xy} positive%" and "R_{xy} negative%", respectively.

The "Highest R_{xy}%" shows the comparison between the absolute value of negative R_{xy} and positive Rxy values for each window. In each correlation window, the correlation values are observed higher for positive R_{xy} values, i.e. for pressure, the sensors are positively correlated.

For $Re_{Dh} = 19400$, the τ values are found as 0.0204 sec, 0.0173 sec and 0.0173 sec for sensor 1-2, sensor 2-3 and sensor 3-4, respectively. The distance between each sensor is $0.5D_h$ and the U_{flow} is 0.9m/s. By applying the Eq.(59), the transport velocity of pressure events are found as 0.67m/s, 0.79m/s and 0.79m/s for sensor 1-2, sensor 2-3 and sensor 3-4, respectively.

The same procedure of pressure-pressure cross-correlation is performed for WMV configuration. For WMV, two different types of data set are used. For the cross-correlation between sensor1-sensor2, the data is taken from the MPS-2021, i.e. same as the NMV pressure sensors. The correlation between the other sensors couldn't investigated due to loss of sensor3. For the correlation between sensor2-3 and sensor3-4, the data is used is from MPS-2020 where the sensor1 was broken.

Figure 127 shows the percentage of correlation results which have higher correlation coefficient than $0.8|R_{xy}|_{max'}$ i.e. R_{xy} identified events, for sensor 1-2, sensor 2-3 and sensor 3-4 for WMV configuration. The Reynolds number is selected as $Re_{Dh} = 19800$. The percentage is calculated according to all the window number. i.e. ~200000 windows.

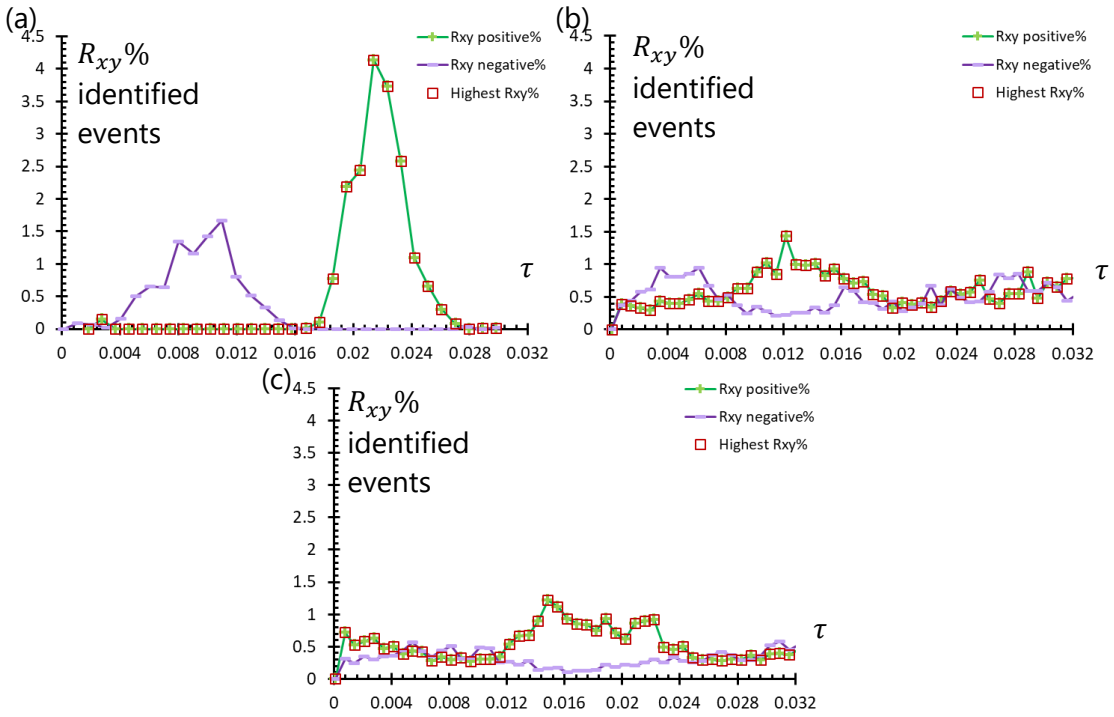

Figure 127: $\%R_{xy}$ results for correlation between (a) sensor 1-2 (b) sensor 2-3 (c) sensor 3-4 for WMV configuration $Re_{Dh} = 19400$

The results show peaks on the identified events values between the sensors. The sensor2-3 and sensor3-4 shows lower peaks compared to the sensor1-2 where the difference can be seen in Figure

127(a) and Figure 127(b) - Figure 127(c). For the data MPS-2021, the peak of the valid results are observed around 4.5% where for the data MPS-2020 the peaks are observed to have lower identification amount, i.e. around 1.5%. This difference can be due to the different pressure sensor conditions where for MPS-2021 the sensors are more robust compared to MPS-2020.
For sensor 1-2 the τ is found as 0.021 sec and for sensor2-3 and sensor3-4, the τ is found as 0.012 sec and 0.014 sec, respectively. Applying the Eq.(59), the transport velocity of pressure events between sensor1-2, sensor 2-3 and sensor 3-4, is found as 0.64m/s, 1.13m/s and 0.93m/s, respectively.

12.1.2 Transport of pressure events

The transport of pressure events for NMV configuration is performed for Reynolds number as $14000, 15800, 18400$ and 19500. Since for WMV configuration different data set is used the Reynolds number range is different for the different distances. The Reynolds numbers for the $0 \leq y/D_h \leq 0.5$ are selected as 17700 and 19800. For the distance range $0.5 \leq y/D_h \leq 1.5$, the Reynolds numbers are $19400, 25000, 30600$ and 39155. The correlations are performed between each sensor with the distances $0.5D_h$.
The position of the pressure measurements are selected according to the high fluctuation region, i.e. $20°$ and $0°$, respectively for NMV and WMV configuration. These zones can be seen in Chapter 9.2.
For each correlation results, the positive correlation coefficient is used. The corresponding time lag, τ, to the highest peak of the $R_{xy}\%$ identified events is selected as the time information for the transportation of pressure events.
Figure 128 shows the result of normalized the transportation velocity of periodic pressure events, i.e. U_e/U_{flow} versus the Reynolds number for both NMV and WMV configuration. The results includes different distances away from the spacer grid, i.e. the correlation between $0 \leq y/D_h \leq 0.5, 0.5 \leq y/D_h \leq 1$ and $1 \leq y/D_h \leq 1.5$.

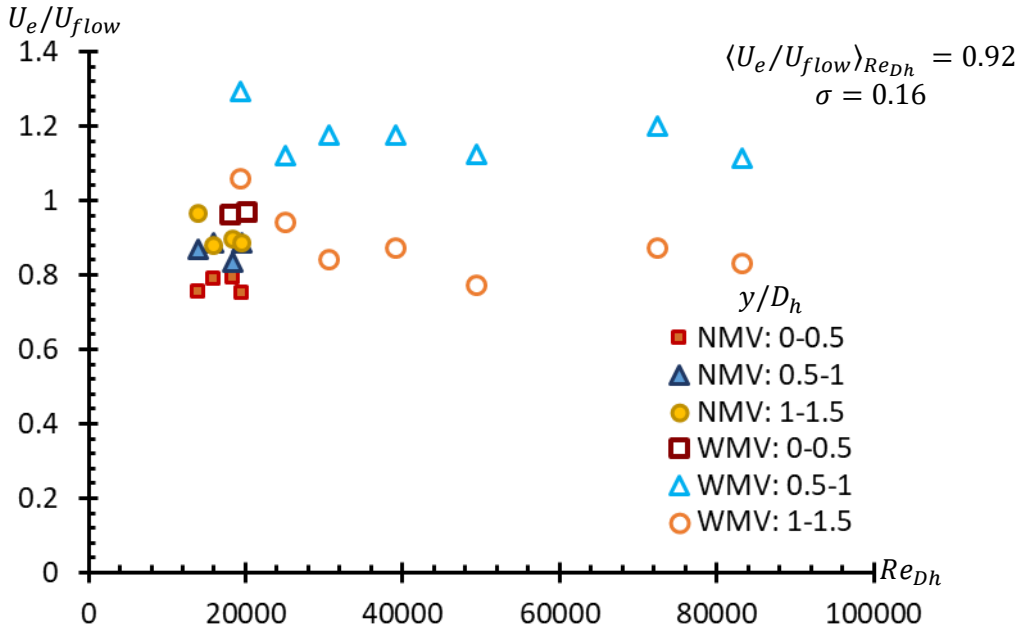

Figure 128: U_e/U_{flow} for different Reynolds number and different distances away from the spacer grid

The results shows the ratio of U_e values to U_{flow}. For NMV configuration, the transport of pressure events are found lower than U_{flow}. With the increasing distance, U_e is observed to increase and around $1 \leq y/D_h \leq 1.5$, the $\langle U_e/U_{flow}\rangle_{Re_{Dh}}$ is found 0.90 ± 0.03 in average of the different Reynolds

numbers. For $0 \leq y/D_h \leq 0.5$, this ratio is 0.77 ± 0.02 and for $0.5 \leq y/D_h \leq 1$, it is found as 0.86 ± 0.02. This shows 14% increase of U_e/U_{flow} for the distance range $0 \leq y/D_h \leq 1.5$.

For WMV configuration at $0 \leq y/D_h \leq 0.5$, U_e/U_{flow} is about 1 ± 0.005 . With the mixing vane, i.e. the tip of the mixing vane is at $y/D_h = 0.5$, an increase on the U_e values is observed, i.e. $U_e/U_{flow} = 1.17 \pm 0.06$. The difference between $0 \leq y/D_h \leq 0.5$ and $0.5 \leq y/D_h \leq 1$ is 17%. This increase in coherence with the flow field where the maximum velocities are observed within the tip of the mixing vanes. After $y/D_h \geq 1$, the U_e/U_{flow} is decreased by 11%, i.e. $\langle U_e/U_{flow} \rangle_{Re_{Dh}} = 0.88 \pm 0.09$.

From these results the overall behaviour is that for both configuration the pressure events are observed to transported about U_{flow}.

For the distances close to grid, i.e. $y/D_h < 0.5$, this transportation is observed slower compared to the other distances.

For $0.5 \leq y/D_h \leq 1$, an increase in U_e is observed for both configuration. For NMV configuration this increase, i.e. 11%, is lower compared to WMV configuration, i.e. 17%.

After $y/D_h \geq 1$, the difference of U_e/U_{flow} between NMV and WMV configuration is 2%.

For NMV configuration, the standard deviation of U_e/U_{flow} is noticed about 0.06 including the results from different distances. This value reaches to 0.15 for WMV configuration. The average of all the Reynolds number including both configuration and different distances is $\langle U_e/U_{flow} \rangle_{Re_{Dh}} = 0.92 \pm 0.16$. The average shows that the pressure events are transported with the velocities close to the U_{flow}. The $\pm 16\%$ difference in U_e/U_{flow} can be explained with the mixing vanes where for NMV the transportation velocities are observed to vary less.

12.2 Tracking events between velocity fluctuations and pressure fluctuations

In pressure cross-correlation, the transport of pressure events are searched through the signature of structures. The aim of the simultaneous pressure-PIV measurements is to investigate the relation between the structures by using the velocity fluctuations and pressure fluctuations.

12.2.1 Application of pressure-velocity cross-correlation

12.2.1.1 Parameters for pressure-velocity cross-correlation

To capture the periodicity of the correlated events, different than pressure-pressure correlation the correlation window is selected accordingly to capture multiple events, i.e. larger than $1/f_{peak}$. To achieve this, the window sizes are selected as, $6 * 1/f_{peak}$.

Figure 129 shows the signals that is used for the cross-correlation. Figure 129(a) shows the signal from second pressure sensor as volt which is propositional to pressure fluctuations. Figure 129(c) is the velocity fluctuation which is selected for the same position as second sensor during simultaneous measurements. Figure 129(b) and (d) shows an example of the pressure and velocity fluctuation in correlation window, respectively.

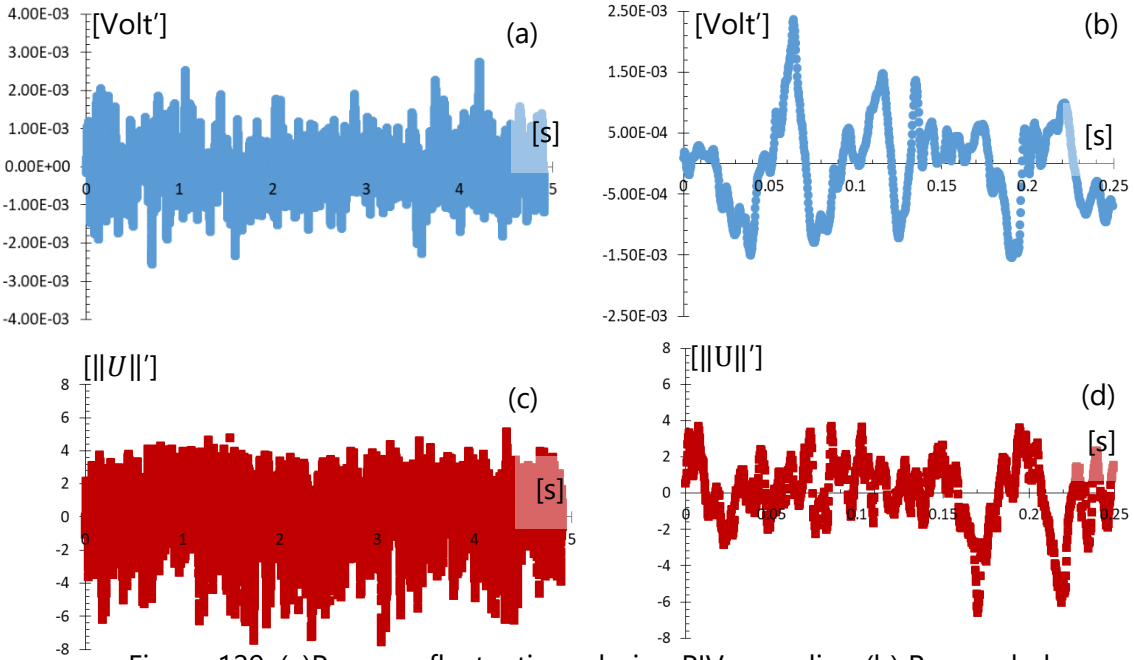

Figure 129: (a)Pressure fluctuations during PIV recording (b) Resampled pressure fluctuation according to PIV data during one correlation window (c) Velocity fluctuation (d) Velocity fluctuation during one correlation window

For the cross-correlation of pressure-velocity, similar to pressure-pressure cross-correlation, the Eq.(62) is used. $R_{PV}(\tau)$ is the correlation coefficient where τ defined as time lag. P' represents the pressure fluctuation from a selected sensor of coordinates $y0z0$ and V'represents the velocity fluctuation from a selected point of coordinates y1z1. t shows the selected time range and σ is the standard deviation of the signals. The two selected signal is moved point by point until the end of the searching area. This moving points shows the τ.

$$R_{PV}(\tau) = \frac{\overline{\left(P'_{y0z0}(t) * {V_{y1z1}}'(t+\tau)\right)}}{\sigma_{P'_{y0z0}(t)}\sigma_{{V_{y1z1}}'(t+\tau)}} \tag{62}$$

The cross-correlation between velocity and pressure depends on the selected points. Each time a structure is passing from a velocity point which is selected around the same position as a pressure

sensor, the correlation coefficient between pressure and velocity is expected to increase. With the increased distance between the velocity point and the selected sensor, this correlation coefficient is expected to be decrease since the signature of the structure will disappear with the transportation of the structure.

To be able to capture this transportation, the searching area is selected from $-window\ size/2$ to $+window\ size/2$. This gives the opportunity to search the phase shift between the velocity and pressure fluctuations backwards and forwards in time.

Figure 130 shows an example cross-correlation between the same selected point in velocity field and the pressure sensors.

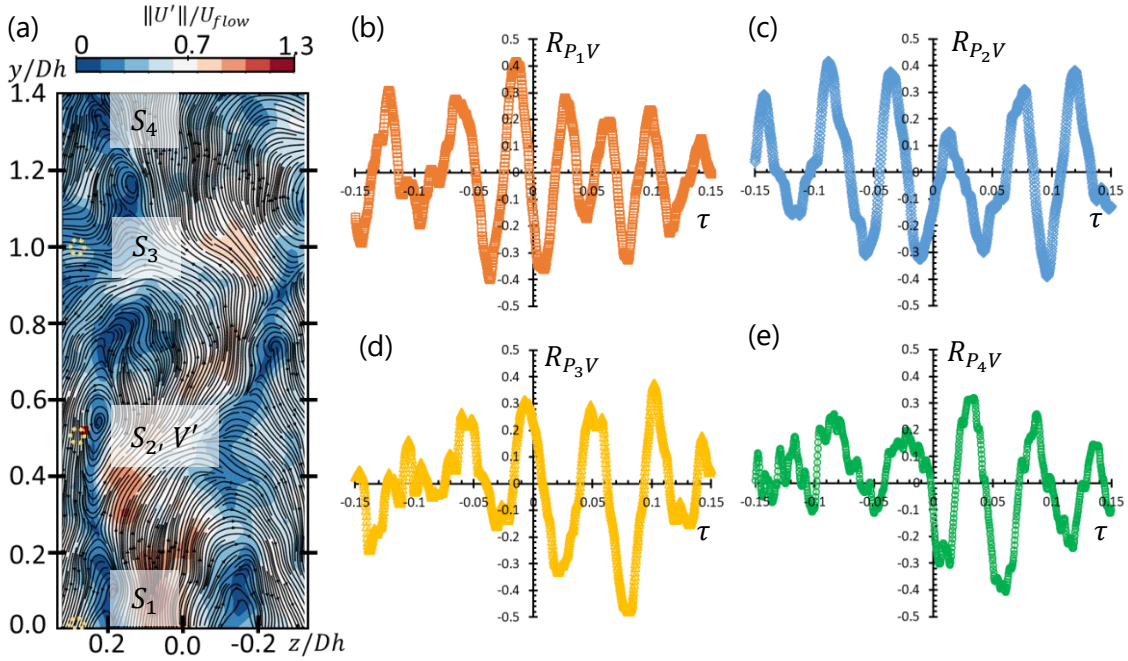

Figure 130: (a) $\|U'\|/U_{flow}$ with swirling function streamlines for $Re_{Dh} = 20125$. The position of the selected velocity point shown in red square, i.e. $y/D_h = 0.5$ and $z/D_h = 0.25$, and the sensors are shown with yellow circle. The correlation result of window t=1-1.24sec between velocity point, i.e. position of sensor2 and (b) sensor1 (c)sensor2 (d)sensor3 and (e)sensor 4.

The pressure position, $P'(y_0, z_0)$, is varied as S_1, S_2, S_3 and S_4, respectively from sensor 1 to 4. The vertical position is same for all the sensors, i.e. $z_0 = z_{0_{S1}} = z_{0_{S2}} = z_{0_{S3}} = z_{0_{S4}}$. The velocity position is $V'(y_1, z_1)$ where $y_1 = y_{0_{S2}}$ and $z_1 = z_{0_{S2}}$, i.e. the position of the sensor2. The positions of the sensors and the selected point of velocity are shown in Figure 130(a) with yellow circles and red square, respectively. The correlation window size is selected as 0.25sec. The results for each sensor with one selected correlation window are presented in Figure 130(b) to Figure 130(e) for sensor 1 to sensor 4, respectively.

The $V'(y_1, z_1)$ is selected according to the positions where the structures is observed on the swirling function. The periodicity of the correlation can be seen in the results. The peaks of R_{PV} values are observed to be less defined with the increased distance from the selected point, i.e. sensor 3 and sensor 4. These signals are not correlated to the same event but correlated to the periodicity of the events in the flow.

To have the complete correlation result between the pressure and velocity fluctuations, Eq. (62) is applied to rest of the signals point by point using the correlation windows.

Figure 131 shows the results of correlation processed over 5sec signal.

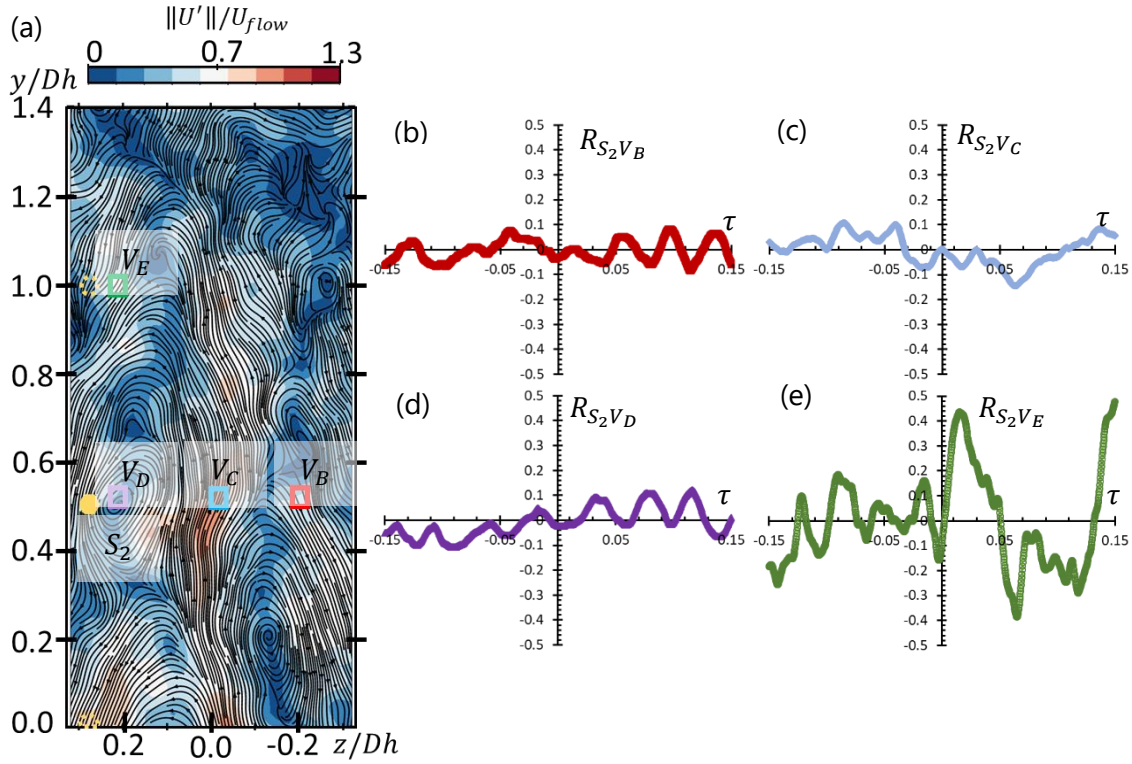

Figure 131: (a) $\|U'\|/U_{flow}$ with swirling function streamlines for $Re_{Dh} = 20125$, the selected sensor is shown with yellow circle and the selected velocity points are shown with squares. Correlation results between sensor 2 and (b) $y/D_h = 0.5, z/D_h = -0.2$ (c) $y/D_h = 0.5, z/D_h = -0.03$ (d) $y/D_h = 0.5, z/D_h = +0.2$ (e) $y/D_h = 1, z/D_h = +0.2$

The Figure 131(a) shows the position of the correlation points. Correlation is performed between the P'_{S2}, i.e. sensor 2, and different velocity fluctuation points as V_B, V_C, V_D and V_E. The exact positions are:

- $R_{S_2V_B}$ as Figure 131(b): $y/D_h = 0.5, z/D_h = -0.2$
- $R_{S_2V_C}$ as Figure 131(c): $y/D_h = 0.5, z/D_h = -0.03$
- $R_{S_2V_D}$ as Figure 131(d): $y/D_h = 0.5, z/D_h = +0.2$
- $R_{S_2V_E}$ as Figure 131(e): $y/D_h = 1, z/D_h = +0.2$

For all the points, the correlation window is selected as 0.25sec where the searching area is selected between $-0.15sec$ to $0.15sec$.

From the results, the effect of the position of selected velocity fluctuation can be seen.

For Figure 131(b), ~7 events of periods is detected even the correlation peaks are not very well defined. Each period is related to a large-scale event. The loss of the definition on correlation is observed due to the signature of the structures are on the other side of the dimple. This position is far away from the signals that is captured with pressure sensors.

On Figure 131(c), the correlation peaks can't be defined. The loss of the peaks are expected since for $z/D_h = 0$, no persisting structures are observed.

The Figure 131(d) and Figure 131(e), shows the result from the same side of the sensor 2. The peaks are defined clearly where the velocity point is selected next to sensor 2 as shown in Figure 131(d).

On Figure 131(e), the correlation peaks are observed with high correlation coefficient compared to the rest of the results with lower definition of the correlation peaks.

Compare to the pressure cross-correlation, the correlation coefficients are expected to be lower since pressure and velocity are two different physical values. Additionally the measurement techniques are different where the contribution of the noise is expected to affect different.

12.2.1.2 Time shift between velocity and pressure fluctuations

Figure 132 shows the periodic cross-correlation result between velocity fluctuations and pressure fluctuations.

The R_{PV} peak shows that a moving structure downstream the dimple is effecting both velocity fluctuation in the selected position and the pressure fluctuation. Since these structures are observed as periodic, each peak is related to the periodicity of the velocity and pressure fluctuations. The Figure 132(a) and Figure 132(c) shows the full range of the results where ~7 periodic events can be seen.

The Figure 132(b) and Figure 132(d) show a zoomed-in view to the cross-correlation results. The first extrema before and after the zero-crossing value represents the time shift between the velocity and pressure fluctuations. Figure 132(b) and Figure 132(d) show these points for $y/D_h = 0.5, z/D_h = -0.13$ and $y/D_h = 0.5, z/D_h = +0.2$, respectively. τ^- represents the negative lag and τ^+ represents the positive lag of the periodic cross-correlations.

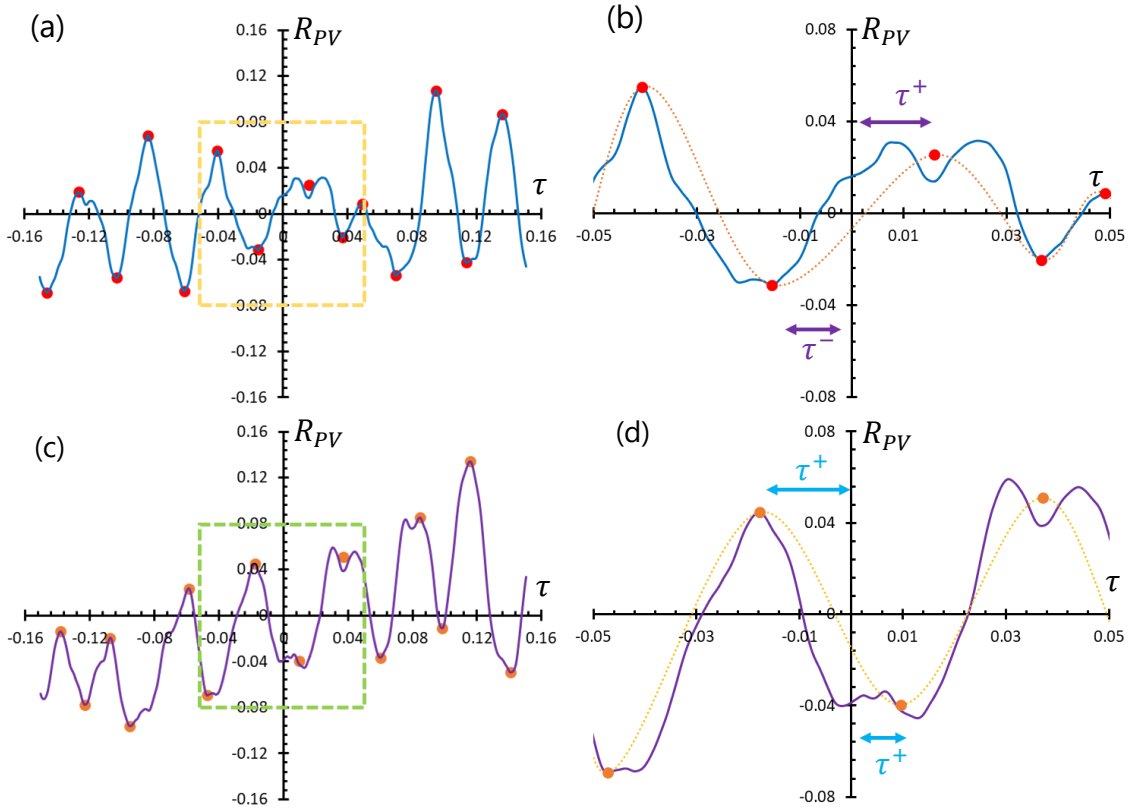

Figure 132: (a)Cross-correlation result between sensor 2 and $y/D_h = 0.5, z/D_h = -0.13$ (b) zoom-in to the marked area of (a) (c) Cross-correlation result between sensor 2 and $y/D_h = 0.5, z/D_h = +0.2$ (d) zoom-in to the marked area of (c)

12.2.2 Convection velocity deduced from time shift

To find the velocity of pressure fluctuation transportation, the time shift is measured between pressure sensors and selected points in the velocity field. The time shift represents the time information where similar periodic events are present in both velocity and pressure signals.
Figure 133 shows the positions of the pressure points, i.e. pressure sensors and the velocity points for NMV and WMV configuration, respectively as Figure 133(a) and Figure 133(b).
The positions of the velocities are selected where the eddies are observed on the swirling function, i.e. $y/D_h = 0.2$ and $y/D_h = 0$, respectively for NMV and WMV configuration.

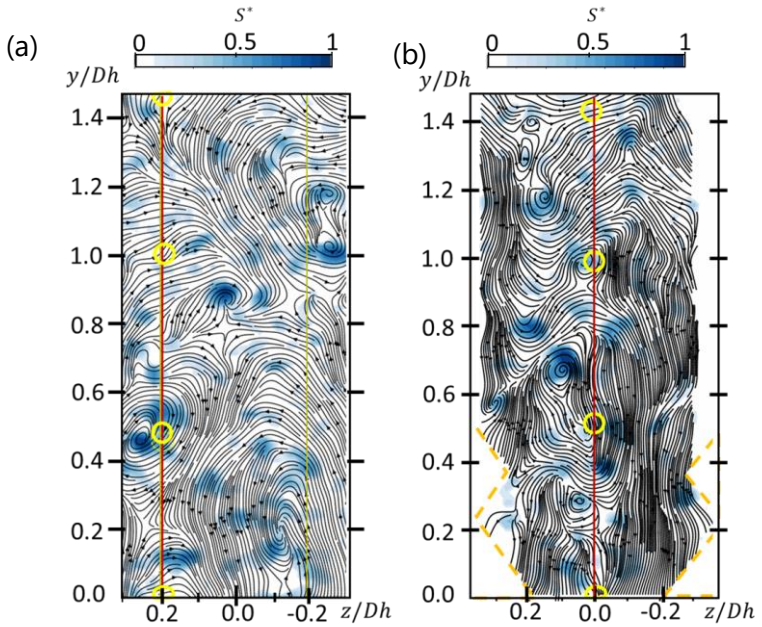

Figure 133: Position of the sensors (yellow circles) and velocity points positions(red lines) for (a) NMV condiguration and (b) WMV configuration

12.2.2.1 Convection velocity for NMV configuration

Figure 134 shows the results for NMV configuration for $Re_{Dh} = 20100$.
The abscissa of the plot is the normalized time shift, i.e. $\tau^* = \tau * U_{flow}/D_h$ and the ordinate is the distance between the selected velocity point and the selected sensor d^*. The plots are separated according to the selected sensor from $y/D_h = 0$ to $y/D_h = 1.5$. The results show both negative shifts and positive shifts according to the distance.
The average U_c/U_{flow} is found as 0.98, 1.08, 1.17 and 1.01, respectively from $y/D_h = 0$ to $y/D_h = 1.5$ with 0.5 intervals. The average over different distance is $\langle U_c/U_{flow}\rangle_{y/D_h} = 1.06 \pm 0.08$. The results are in agreement with the transportation of pressure events where the convection of pressure fluctuations are detected around the U_{flow} for NMV configuration.

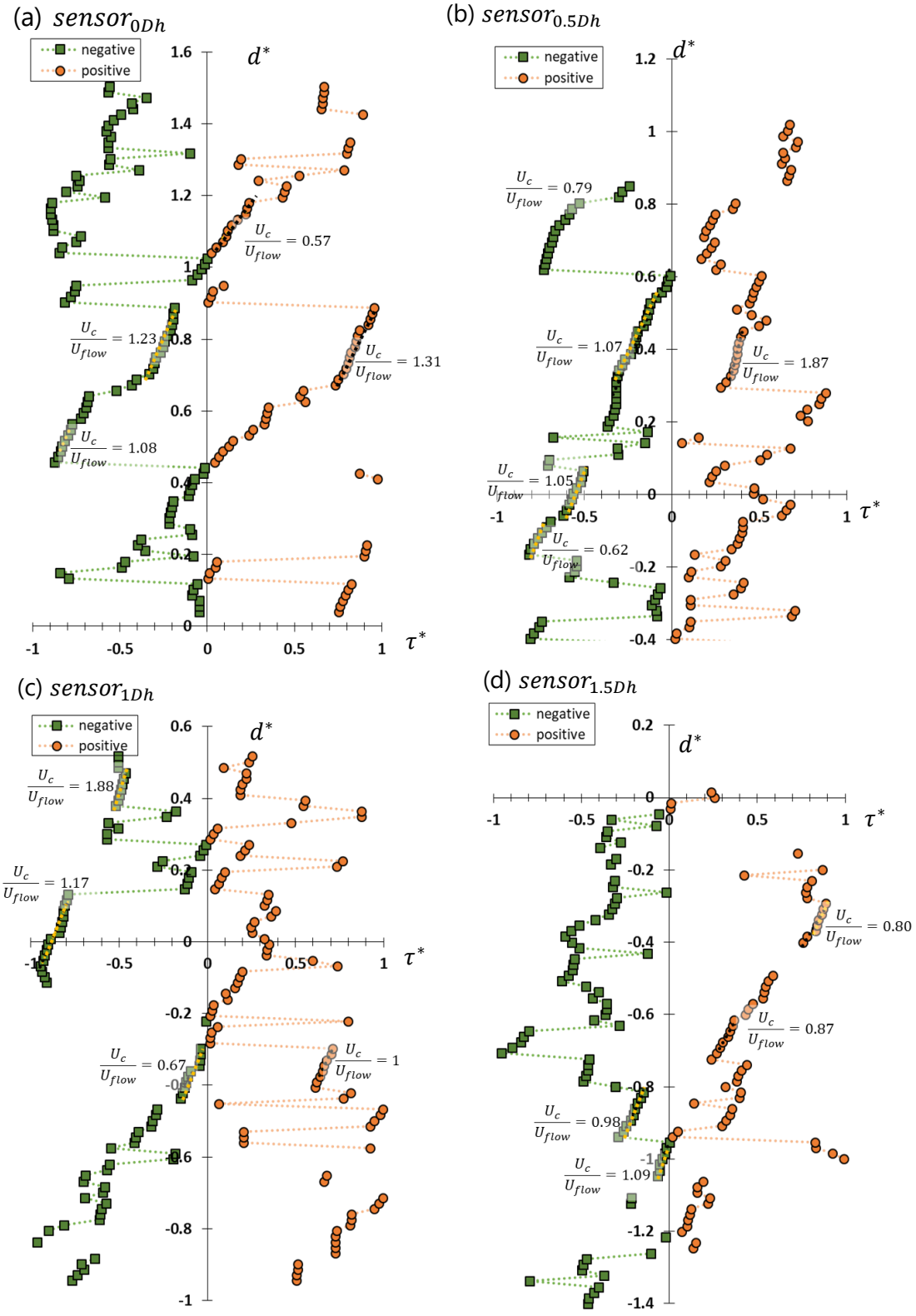

Figure 134: Normalized time shift τ^* versus distance between selected velocity point and pressure point d^* for (a) sensor $0D_h$ (b) sensor $0.5D_h$(c) sensor $1D_h$(d) sensor $1.5D_h$. Slope shows the U_c/U_{flow} values for NMV configuration at $Re_{Dh} = 20100$

12.2.2.2 Convection velocity for WMV configuration

Figure 135 shows the result for WMV configuration for $Re_{Dh} = 20100$ for different sensors.

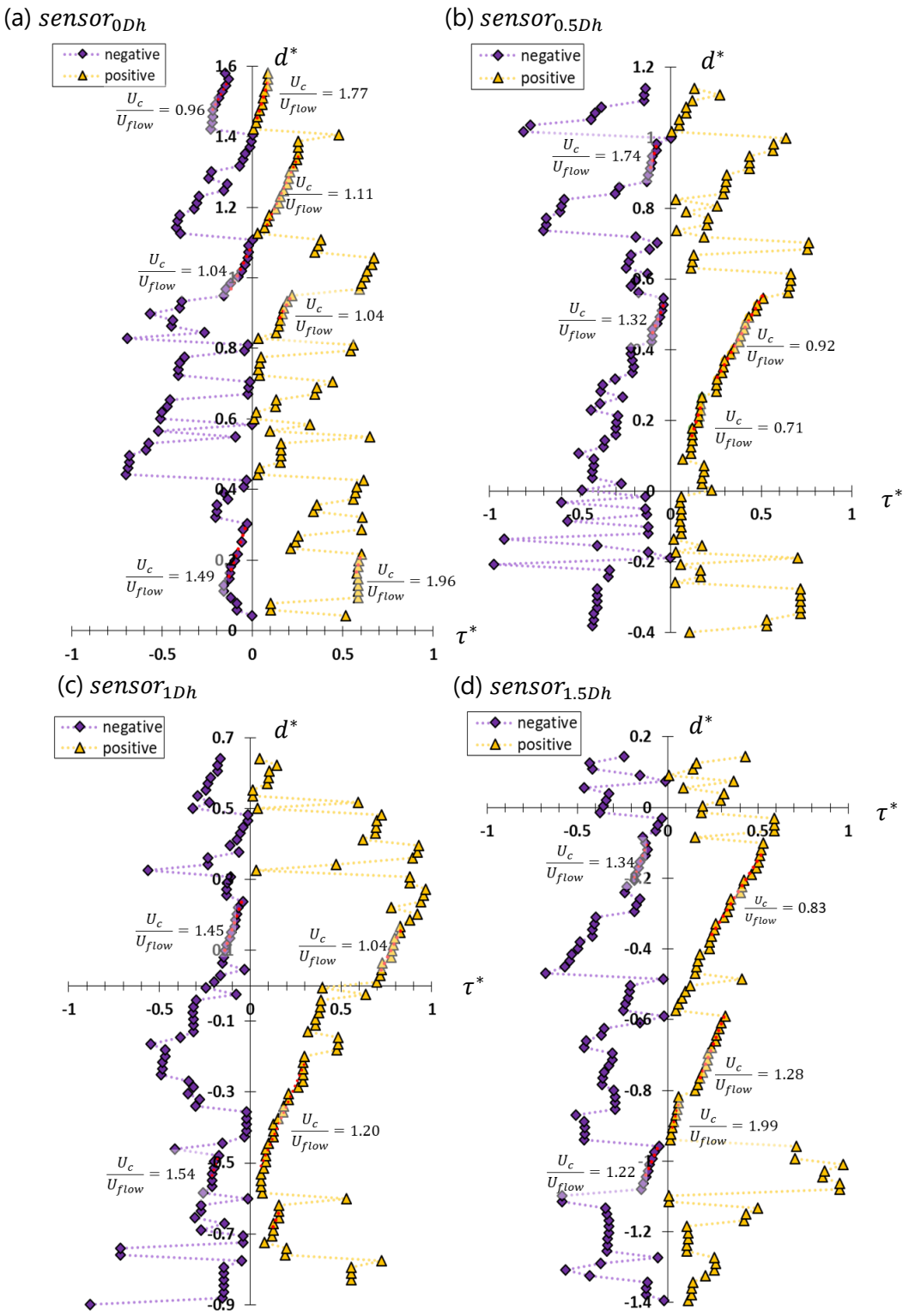

Figure 135: Normalized time shift τ^* versus distance between selected velocity point and pressure point d^* for (a) sensor $0D_h$ (b) sensor $0.5D_h$(c) sensor $1D_h$(d) sensor $1.5D_h$. Slope shows the U_c/U_{flow} values for WMV configuration at $Re_{Dh} = 20100$

From the results the average U_c/U_{flow} is found as 1.33, 1.36, 1.31 and 1.33, respectively from $y/D_h = 0$ to $y/D_h = 1.5$ with 0.5 intervals. This shows that the pressure fluctuations are transported faster than the U_{flow}. The increase on the U_c is observed especially for $y/D_h = 0.5$, i.e. tip of the mixing vane. This also shows coherent behaviour with the pressure-pressure correlation results where the transport of pressure events are observed with higher velocity between $y/D_h = 0.5 - 1$ for WMV configuration. After $/D_h > 1$, U_c is observed to slow down and with the increasing distance U_c/U_{flow} is observed around ~ 1.

12.2.3 Convection velocity of pressure fluctuations

Figure 136 is the results of the convection velocity built by taking the average of the slopes per sensors. The plot includes results from different sensor distances, i.e. $y/D_h = 0, 0.5, 1, 1.5$, for Reynolds number range $14100 \leq Re_{Dh} \leq 20100$. The measurements are performed for the temperature 12°C for both NMV and WMV configuration.

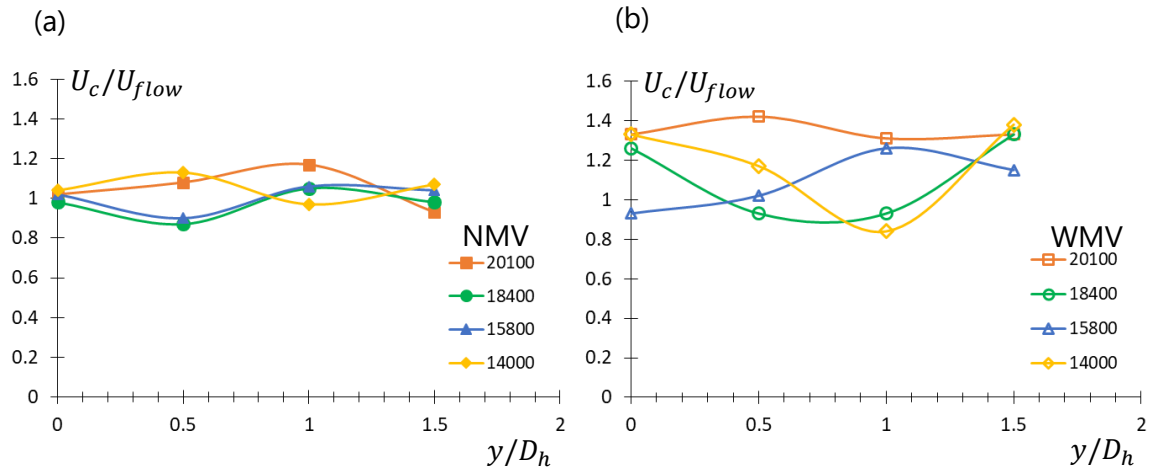

Figure 136: U_c/U_{flow} with different Reynolds number and different distances away from the spacer grid for (a) NMV configuration (b) WMV configuration

Figure 136(a) shows the results for NMV configuration and Figure 136(b) shows the results for WMV configuration. For NMV configuration the average of $\langle U_c/U_{flow} \rangle_{Re_{Dh}}$ including different distances is 1.02 ± 0.07. For WMV configuration this value is 1.17 ± 0.18. This shows the effect of the mixing vanes which leads to variation on the U_c/U_{flow}.

12.3 Transport velocity map

Figure 137 shows the summary map for transport velocity of pressure fluctuations, $\langle U_c/U_{flow}\rangle_{y/D_h}$, and pressure events, $\langle U_e/U_{flow}\rangle_{y/D_h}$, versus Reynolds number. These values are plotted together as transport velocity, i.e. u_t/U_{flow}. "SM" is results from simultaneous pressure-velocity measurements and "Pressure" is from pressure-pressure measurements.

Even though in the previous section similar trends are observed for both methods, for NMV configuration between $\langle U_e/U_{flow}\rangle_{y/D_h}$ and $\langle U_c/U_{flow}\rangle_{y/D_h}$is found about 13%. Similarly, for WMV configuration this difference is about 15%.

Even with the variations on the transport velocities, the $\langle u_t/U_{flow}\rangle_{Re_{Dh}}$, is 1.03 with standard deviation 0.17. This shows that the pressure fluctuation are transported by the mean flow with 17% variations. There might be different sources of these variations on u_t/U_{flow}.

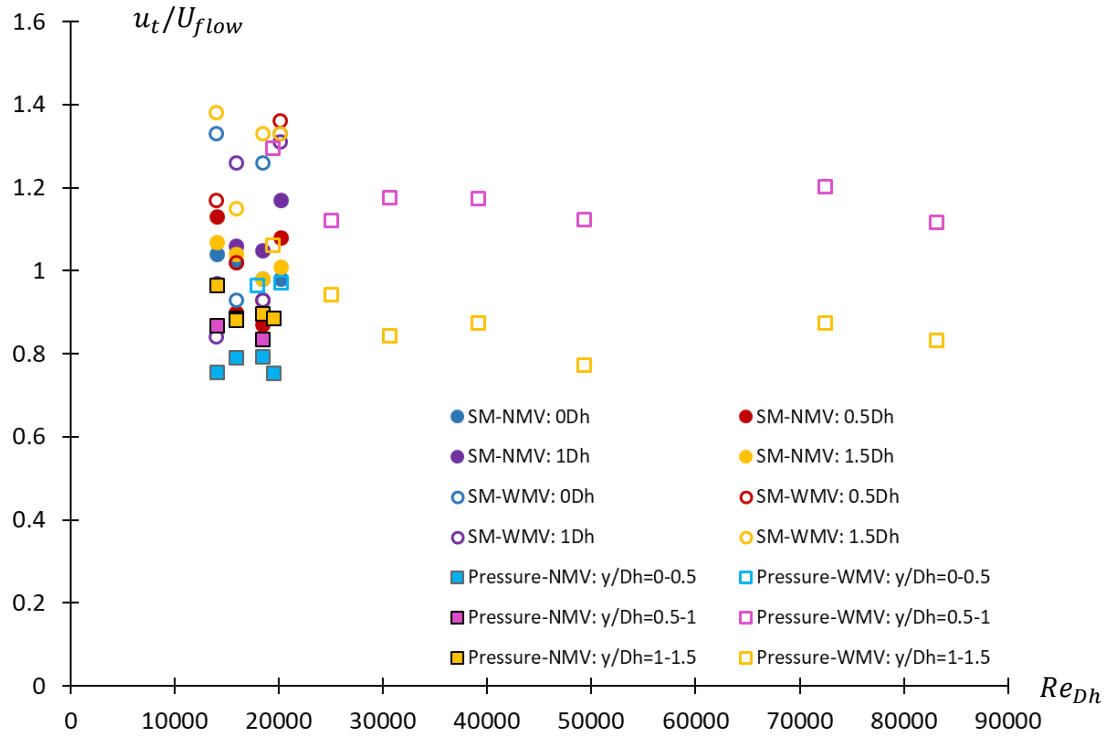

Figure 137: Summary of transport velocity for NMV and WMV configuration with multisensor pressure measurements and simultaneous pressure - PIV measurements

One explanation can be due to the uncertainties connected to pressure measurements, i.e. 8%, and PIV measurements, 3%.

Another possible explanation might be the variation of the flow velocity downstream the grids. In the previous chapters, different velocity regions are detected in the velocity field. After the distance corresponds to the tip of mixing vane the transport of velocities are increasing. For velocity field, this region has the highest velocity. This might show that the velocity field is coherent with the transport velocities and since there is variations on velocity field, it might be expected to have variations on the transport velocities.

Another explanation can be connected to the structure itself. According to the experiments performed in wall turbulence by (Adrian, et al., 2000) the packets that consist of eddies are observed in the outer region of the turbulent boundary layer. These eddies are observed to propagate together with packet convection velocity. In the results, the small packets are found to transport slower compared to the big packets. With the increase distance from the boundary layer, the convection velocities are observed to get closer to the mean velocity of the flow.
For measurements performed in CALIFS, the flow is more complex compared to horizontal flat plate, i.e. (Adrian, et al., 2000), with additional geometrical elements such as dimples, springs and mixing vanes. That being said, it might be one of the explanation for the variation of the transportation of fluctuations.

CHAPTER 13
CONCLUSION AND PERSPECTIVES

13. CONCLUSION AND PERSPECTIVES

13.1 Main results

First measurements performed on CALIFS 5x5 have shown the existence of frequency peak on pressure spectra for both NMV and WMV configuration for $Re_{Dh} = 66000$. One of the beginning idea was that these frequency peaks might be related to the large scale structures, possibly eddies, in the flow.

In consequence, one of the initial goal of my PhD was to investigate the origin of these frequency peaks and demonstrate the limits of related phenomena in terms of Reynolds numbers.

The main new results of this manuscript show that:

1. The phenomena, i.e. existence of a frequency peak, exist over a broad range of Reynolds numbers, i.e. $13200 \leq Re_{Dh} \leq 108000$.
2. These peaks are observed on both pressure and velocity fluctuation spectra
3. Large scale eddies are shaded downstream the dimples with scale and frequencies in agreement with the one deduced from pressure measurement
4. The Strouhal number of the shaded eddies is quantified about 0.25, i.e. $13200 \leq Re_{Dh} \leq 108000$.
5. The pressure fluctuations are transported with the mean flow similarly to the large-scale eddies.
6. This fully support the point that the measured pressure fluctuations exiting the rods downstream CALIF spacer grids are issued from eddies streets.

These structures are transported with the mean flow. To reveal the transport of these large scale structures, the cross-correlation method is realized between the different pressure sensors, i.e. pressure-pressure fluctuations, and PIV-pressure sensors, i.e. velocity-pressure fluctuations.

These main results are achieved by performing different measurement techniques.

13.2 Experimental and technical approaches supporting these results

To study the pressure fluctuation around the rod single pressure measurements were performed for both NMV and WMV configuration. In addition to the existence of frequency peak, the results show maximum pressure fluctuations downstream the dimples.

To investigate further the pressure fluctuation, a new multisensor device is designed. With the new multisensor device, the pressure fluctuations are measured instantaneously with four piezoresistive pressure sensor. The phenomena related to these pressure fluctuations, the measurements are performed for a broad range of Reynolds number, i.e. $13000 \leq Re_{Dh} \leq 120000$ downstream the dimples. In order to vary the Reynolds number, the measurements are performed with different velocities and temperature. The results confirm the existence of the phenomena for different Reynolds number that leads to frequency peak on pressure spectra for both NMV and WMV configuration.

The measurements regarding velocity fluctuations are performed by LDV with WMV configuration. The aim of this study is to characterize the dominant geometry downstream the spacer grid. The results reveal that, coherent to pressure results, the maximum contribution is downstream the dimple. Additionally, the existence of the frequency peak for $13000 \leq Re_{Dh} \leq 66000$ is confirmed for velocity fluctuations downstream the dimple.

In order to demonstrate the origin of these frequency peaks the planar PIV measurements are performed with two different PIV setting, i.e. High-speed PIV and Low-speed PIV.

To be able to perform the PIV technique, the optical access to the measurement domain is achieved by RIM method. The two INOX rod in front of the central rod, i.e. the measurement domain, is changed with FEP transparent rods.
The flow is characterized in 2D for both NMV and WMV configuration.
The results from PIV measurements demonstrate different velocity zones for each configuration. These velocity zones are identified according to the local velocities that are higher and lower than the U_{flow}. Between the interaction of each high/low velocity region, shear layers are detected. For NMV configuration, the shear layer is found on both side of the dimple with a quasi-straight linear behaviour. For WMV a λ shape is observed with high velocity region. The shear layers are observed coherent with this λ shape in the flow.
For NMV configuration, highest velocity fluctuations are within the shear layer on both side of the dimple with maximum intensity around $0.2 < y/D_h < 0.4$. With the increasing distance from the spacer grids, the velocity fluctuations start to become more homogeneous. This shows coherent results with LDV and pressure results for $Re_{Dh} = 66000$.
With WMV configuration, high velocity fluctuations are all around the frame for the measurement range $0 < y/D_h < 1.4$. This high velocity fluctuation zone follows with the direction of the mixing vane. Coherently with the LDV and pressure results for $Re_{Dh} = 66000$, the velocity fluctuations are more heterogeneous with WMV configuration than NMV configuration.
To investigate the source of the frequency peaks of these fluctuations, the flow is studied for a broad range of Reynolds number. The shedding phenomena that is related to these frequency peaks, are estimated by the Strouhal number. The Strouhal-Reynolds number map is built including the measurements of pressure, LDV and PIV. The Strouhal number is determined to be in range of 0.20 to 0.28.
The demonstration of the shedding phenomena is shown with the streamlines in the frame moving with U_{flow} and swirling function on PIV results. From results, the structures are detected with the shear layer. For NMV configuration, these structures persist on both side of the dimples up to $y/D_h = 1.4$. These structures are observed downstream the dimple on the centre of the measurement domain for WMV configuration.
With the increased distance from the spacer grid, for NMV configuration these structures persist, on the other hand for WMV configuration these periodic structures disappear after $y/D_h > 2$.
To characterize these large scale structures two different length scales are used. Integral length scale shows the size of these large scale structure and periodic length scale shows the distance between each periodic structure.
The integral length scale is calculated with the autocorrelation function. The scales that are calculated from LDV and PIV velocity fluctuations, correspond to the size of the structures highlighted by the swirling function for both NMV and WMV configuration.
For NMV configuration the pressure integral length scale are detected close to the velocity length scales. On the other hand, for WMV configuration, these scales are 60% longer compared velocity integral length scales. These pressure length scales correspond to the low intensity velocity region that is captured high intensity velocity region.
To confirm the periodicity of the structures, the periodic length scale is calculated according the f_{peak} value observed in the velocity spectra. The periodic length scale shows coherent results with the distance between each structure identified on the PIV results for both configuration.
To investigate the transportation of these periodic events, the simultaneous pressure measurements with multisensor device are used. For this investigation the pressure fluctuations are tracked event by event between two pressure sensors by using cross-correlation. The results show the periodic events are moving with the U_{flow} where the standard deviation is 0.16.

To study the relation of pressure transport with velocity fluctuations, the simultaneous PIV-pressure measurements are performed. Instead of tracking the fluctuations event by event, the relation built up from the periodicity of the fluctuations. Similarly to previous measurement, results show that the pressure fluctuations are transported with a velocity close to U_{flow} with a standard deviation $0.17U_{flow}$.
The structures are transported faster with the existence of the mixing vane. Therefore the variation of this transport velocity can be explained by the variation of the velocity field downstream the grid. It can be also connected to the structural information of the large scale eddies. The variation of the size of eddies can lead to variation of generated pressure fluctuation which can be another explanation.

13.3 Perspectives

13.3.1 Refinement of CALIFS experiments

CALIFS has 5x5 rod bundle which creates a higher spatial resolution of the phenomena investigated compared to PWR fuel assemblies, i.e. 17x17 rod bundle.
The number of rods change the effect of boundaries where with 5x5 rod bundle the central rod is closer to the edge of the fuel assembly compared to the 17x17. Also in PWR these fuel assemblies are side by side with each other where in CALIFS, these kind of effects are not investigated.
Addition to the rod bundle, the spacer grids that is used in CALIFS is analytical grid. This is also to create a simplified geometry where it makes the manufacturing process easier and cheaper. Additionally since one of the aim is creating a database for simulations, the simplified geometry decreases the computational costs.
A noticeable difference in the analytical grid is the dimples. In PWR the dimples have a bridge type of a geometrical shape. In CALIFS to simplify this geometry, the dimple used as a cube shape. This also give the advantage of simplifying the phenomena.
For future experiments, the design of the dimples can be changed with a bridge type of dimple. This can give a better representation of the flow downstream the dimple in PWR.

13.3.2 Experiments with low Reynolds numbers using water-glycerine mixtures

The relation between the velocity and pressure can be represented by Bernoulli's law as Eq.(63).

$$\mathrm{p_{dyn}} = \frac{1}{2}\rho \mathrm{u}^2 \tag{63}$$

In Eq.(63), p_{dyn} is the dynamic pressure, ρ is the density and u is the velocity. This equation shows that the pressure increase when the fluid is in motion and when the flow is at rest the dynamic pressure become zero (Masterson, 2020).
The contribution that is coming from the environment and electrical devices as noise is calculated around 1-2 Pa. The details about noise measurements can be found in Appendix.
Since when the velocity is decreasing to reach the low Reynolds numbers, according to Eq.(63), the pressure fluctuations are also decreasing. The pressure results close to the noise levels leads to high uncertainties of the measurements or non-extractable pressure results.
Addition to fluctuations, the minimum Reynolds number that can be achieved depends on the working range of the pump of the loop. Working with water where the minimum temperature in the loop is $12°C$, the minimum achievable Reynolds number is around 11000.
The Reynolds number could smaller by using water-glycerine mixture which will change the density of the fluid. A 50%-50% water-glycerine mixing will lead to increase on the kinematic viscosity. With

the increased viscosity the measurements could be performed for lower Reynolds numbers for the same range of velocities, i.e. 0.5m/s-2.8m/s, without decreasing the pressure fluctuation intensity.

13.3.3 PIV measurements downstream the spring

In current manuscript, the periodic events are observed downstream the dimple. Downstream the springs, the intensity of the energy of frequency peaks are observed to be lower than the frequency peaks connected to the dimples. Even though the contribution of the springs are lower compared to dimples, it can be interesting to visualize and quantify the flow downstream the spring.

13.3.4 3D-PIV measurements

For NMV configuration, planar-PIV method is observed to be sufficient where the structures, the velocity profiles and the velocity fluctuations show coherent behaviour.
On the other hand for WMV, the results on the grid levels are observed to be not-consistent throughout the measurements. This is explained with the strong 3D effect of the flow where the out-of-motions lead to inconsistent velocity profiles for $0 < y/D_h < 0.2$.
By using Tomographic PIV, the third component can be measured while the volume of the measurement is increased. Additionally, it can give the results for the shape of the eddies transported downstream the spacer grid which will enlighten the different measurement of integral length scales of velocity and pressure.

13.3.5 Experiments with transparent grids

Downstream the dimples, the wake flow is observed. There is a set of two dimple in the spacer grids. One of the dimple is on the bottom side of the spacer grid and one is the top side of the spacer grid with 6.5cm distance.
With a grid which is designed with a transparent material, interaction of the flow with the first dimple can be investigated. This could show the evolution of the eddies passing through the grid.

13.3.6 Generation of pressure field

Beside direct pressure measurements, pressure can be also estimated by using indirect methods.
PIV measurements gives opportunity to reconstruct the pressure field from the velocity field by using different methods, i.e. Poisson equation or industrial software such as LaVision. Different than local pressure measurements, this method gives the pressure as a volume whereas the implementation is highly depend on the available velocity data which has an impact on the accuracy of the pressure reconstruction (van Oudheusden, 2013). Some examples can be found in literature as (van Gent, et al., 2017) (Ghaemi, et al., 2012)
For the determination of the Poisson equation, Navier-Stokes equation adapted to incompressible fluids without external forces considering two-dimensional flow. Eq.(64) shows the Poisson approach applied to three-dimensional flow (van Oudheusden, 2013).

$$\begin{aligned}\frac{\partial^2 P}{\partial x^2}+\frac{\partial^2 P}{\partial y^2} = &-\rho\left\{\left(\frac{\partial u}{\partial x}\right)^2+2\frac{\partial u}{\partial y}\frac{\partial v}{\partial x}+\left(\frac{\partial v}{\partial y}\right)^2\right\}\\ &-\rho\left\{\frac{\partial div_{xy}}{\partial t}+u\frac{\partial div_{xy}}{\partial x}+v\frac{\partial div_{xy}}{\partial y}\right\}+\mu\left\{\frac{\partial^2 div_{xy}}{\partial x^2}+\frac{\partial^2 div_{xy}}{\partial y^2}\right\}\\ &-\rho\left\{\frac{\partial w}{\partial x}\frac{\partial u}{\partial z}+\frac{\partial w}{\partial y}\frac{\partial v}{\partial z}+w\frac{\partial div_{xy}}{\partial z}\right\}\end{aligned} \tag{64}$$

This relation includes different terms. The left-hand side represents the in-plane divergence component of the pressure gradient.

The left-hand side of the equation can be divided into three main terms.

The first term , $\left(\frac{\partial u}{\partial x}\right)^2 + 2\frac{\partial u}{\partial y}\frac{\partial v}{\partial x} + \left(\frac{\partial v}{\partial y}\right)^2$ obtained according to the Poisson equation under the assumption of two-dimensional flow.

The second term $\left\{\frac{\partial div_{xy}}{\partial t} + u\frac{\partial div_{xy}}{\partial x} + v\frac{\partial div_{xy}}{\partial y}\right\} + \mu\left\{\frac{\partial^2 div_{xy}}{\partial x^2} + \frac{\partial^2 div_{xy}}{\partial y^2}\right\}$ is the in-plane divergence where $div_{xy} = \frac{\partial u}{\partial x} + \frac{\partial v}{\partial y}$. This term is neglected under two-dimensional assumptions but in three-dimensional flow it can be evaluated from the planar PIV data.

Lastly the term $\left\{\frac{\partial w}{\partial x}\frac{\partial u}{\partial z} + \frac{\partial w}{\partial y}\frac{\partial v}{\partial z} + w\frac{\partial div_{xy}}{\partial z}\right\}$ is the out-of-plane element and not accessible with the planar PIV data.

To resolve the out-of-plane element volumetric techniques are needed. From the other studies (van Oudheusden, 2013), it is observed that *ad hoc* modifications to correct this out-of-plane motion does not provide essential improvements but for the simulations this small to moderate degree of out-of-plane doesn't affect the pressure field determination.

After the generation of pressure field via the Poisson equation, the results can be compared with LaVision software generation, i.e. Eulerian commercial approach. Additionally comparisons with Particle Tracking Velocimetry and Accelerometry (PTVA) can be performed as Lagrangian approach (Ferrari & Rossi, 2008).

With the generated pressure field, it will be possible to perform cross-correlation process with pressure sensors and the pressure field using the same method as in Chapter 13. This will give the possibility to study the evolution of the pressure fluctuations. Additionally it will provide a refined comparison with CFD where the pressure terms are important to estimate the fluctuating forces exerted on the rods.

BIBLIOGRAPHY

14. BIBLIOGRAPHY

Abramovich, G. N., 1963. *The Theory of Turbulent Jets.* Cambridge: M.I.T. Press .

Adrian, R. J., 1991. Particle Imaging Techniques for Experimental Fluid Mechanics. *Annu. Rev. Fluid Mech.,* Volume 23, pp. 261-304.

Adrian, R. J., 2007. Hairpin vortex organization in wall turbulence. *Physics of Fluids,* Volume 19, pp. 041301.

Adrian, R. J., Meinhart, C. & Tomkins, C., 2000. Vortex organization in the outer region of the turbulent boundary layer. *Journal of Fluid Mechanics,* Volume 422, pp. 1-54.

Amini, N. & Hassan, Y. A., 2009. Measurements of jet flows impinging into a channel containing a rod bundle using dynamic PIV. *International Journal of Heat and Mass Transfer,* Volume 52, pp. 5479–5495.

Aziz, A. R. & Wong, K. F., 2003. Velocity Measurements Across Fluid-Porous Medium Interface using Particle Image Velocimetry. *International Journal of Modelling and Simulation,* Volume 23:3, pp. 179-186.

Bakewell, H., 1968. Turbulent Wall-Pressure Fluctuations on a Body of Revolution. *The journal of the Acoustical Society of America,* 43(6), pp. 1358-1363.

Bakosi, J., Christon, M., Lowrie, R., Pritchett-Sheats, L., & Nourgaliev, R., 2013. Large-Eddy Simulations of Turbulent Flow for Grid-to-Rod Fretting in Nuclear Reactors. *Nuclear Engineering and Design*, Volume 262.

Baldwin, A., Mears, L., Arora, N., Kumar, R., Alvi, F., & Naughton, J., 2018. Skin Friction Measurements Using Oil Film Interferometry in a 3-D Supersonic Flowfield. *AIAA*, Volume 57, pp.1-10.

Bartzis, J. G. & Todreas, N. E., 1979. Turbulence Modeling of Axial Flow in a Bare Rod Bundle. *ASME J. of Heat Transfer,* Volume 101, pp. 628-634.

Bastos, F. C. & Carajilescov, P., 2000. Experimental analysis of pressure drop and flow redistribution in axial flows in rod bundles. *Journal of the Brazilian Society of Mechanical Sciences,* Volume 22.

Batchelor, G., 1967. *An introduction to fluid dynamics.* Cambridge: Cambridge University Press.

Batsanov, S. S., Ruchkin, E. D. & Poroshina, I. A., 2016. *Refractive Indices of Solids.* Singapore: Springer.

Bendat, J. S. & Piersol, A. G., 1993. *Engineering Applications of Correlation and Spectral Analysis.* New York: Wiley-Interscience .

Berdahl, C. & Thompson, D., 1993. Eduction of swirling structure using the velocity gradient tensor. *AIAA Journal,* 31(1), pp. 97-103.

Beresh, S. J., Henfling, J. F., Spillers, R. W. & Pruett, B. O., 2011. Fluctuating wall pressures measured beneath a supersonic turbulent boundary layer. *Physics of Fluids,* 23(7), pp. 075110.

Berger, E., 1967. Suppression of Vortex Shedding and Turbulence behind Oscillating Cylinders. *The Physics of Fluids,* Volume 10, pp. 191.

Bertocchi, F., Rohde, M. & Kloostermen, J., 2018. LDA measurements of coherent flow strucutres and cross-flow across the gap of a compound channel with two half-rods. *Neclear Engineering and Design,* Volume 2018, pp. 17-30.

Bhattacharjee, S., Ricciardi, G. & Viazzo, S., 2017. Comparative study of the contribution of various PWR spacer grid components to hydrodynamic and wall pressure characteristics. *Nuclear Engineering and Design,* Volume 317, pp. 22-43.

Bieder, U., Falk, F. & Fauchet, G., 2014. LES analysis of the flow in simplified PWR assembly with mixing grid. *Progress in Nuclear Energy,* Volume 75, pp. 15-24.

Bigillon, F., Nino, Y. & Garcia, M. H., 2006. Measurements of turbulence characteristics in an open-channel flow over a transitionally-rough bed using particle image velocimetry. *Experiments in Fluids,* Volume 41, pp. 857–867.

Blinde, P., 2018. *From Particle to Pressure PIV-based pressure reconstruction for base flows,* Thesis: TUDelft.

Bordet, A., Poncet, S., Poirier, M. & Galanis, N., 2018. Flow visualizations and pressure drop measurements of isothermal ice slurry pipe flows. *Experimental Thermal and Fluid Science,* Volume 99, pp. 595-604.

Borowsky, J. & Wei, T., 2006. Simultaneous velocimetry/accelerometry measurements. *Experiments in Fluids,* Volume 41, pp. 13-20.

Bovati, O., Yildiz, M., Hassan, Y. & Vaghetto, R., 2021. RANS simulations for transition and turbulent flow regimes in wire-wrapped rod bundles. *International Journal of Heat and Fluid Flow,* Volume 90, pp. 108838.

Breeze, P., 2014. *Power Generation Technologies (Second Edition).* United Kingdom: Newnes.

Bruchhausen, M., Guillard, F. & Lemoine, F., 2005. Instantaneous measurement of two-dimensional temperature distributions by means of two-color planar laser induced fluorescence (PLIF). *Experiments in Fluids,* Volume 38, pp. 123-131.

Camussi, R., Felli, M., Pereria, F., Aloisio, G., & Di Marco, A., 2008. Statistical properties of wall pressure fluctuations over a forward-facing step. *Physics of Fluids*, 20(7).

Carajilescov, P. & Todreas, N. E., 1976. Experimental and analytical study of axial turbulent flows in an interior subchannel of a bare rod bundle. *Journal of Heat Transfer,* Volume 98, pp. 262-268.

Chang, S. K., Kim, S. & Song, C. H., 2014. Turbulent mixing in a rod bundle with vaned spacer grids: OECD/NEA-KAERI CFD benchmark exercise. *Nuclear Engineering and Design,* Volume 279, pp. 19-36.

Chang, S. K., Moon, S. K., Baek, W. P. & Choi, Y. D., 2008. Phenomenological investigations on the turbulent flow structures in a rod bundle array with mixing devices. *Nuclear Engineering and Design,* Volume 238, pp. 600-609.

Chapra, S. & Canale, R., 2009. *Numerical methods for engineers.* New York: McGraw-Hill.

Chen, S. K., Chen, Y. M. & Todreas, N. E., 2018. The upgraded Cheng and Todreas correlation for pressure drop in hexagonal wire-wrapped rod bundles. *Nuclear Engineering and Design,* Volume 335, pp. 356-373.

Choi, S. K., Choi, I. K., Nam, H. Y., Choi, J. H., & Choi, H. K., 2003. Measurement of Pressure Drop in a Full-Scale Fuel Assembly of a Liquid Metal Reactor. *Journal of Pressure Vessel Technology*, Volume 125, pp.233-238.

Chong, M., Perry, A. & Cantwell, B., 1990. A general classification of threedimensional flow fields. *Physics of Fluids A: Fluid Dynamics,* 2(5), pp. 765-777.

Chun, M. H., Seo, K. W., Choi, S. K. & Num, H. Y., 2001. An experimental study of pressure drop correlations for wire-wrapped fuel assemblies. *Journal of Mechanical Science and Technology,* Volume 15, pp. 403-409.

Cinosi, N., Walker, S., Bluck, M. & Issa, R., 2014. CFD simulation of turbulent flow in a rod bundle with spacer grid (MATHIS-H) using STAR-CMM+. *Nuclear Engineering and Design,* Volume 279, pp. 37-49.

Colin, S., 2010. *Microfluidics.* United Kingdom: Wiley.

Conner, M. E., Hassan, Y. A. & Dominguez-Ontiveros, E. E., 2012. Hydraulic benchmark data for PWR mixing vane grid. *Nuclear Engineering and Design,* Volume 264.

Coolen, M. C. J., Kieft, R. N., Rindt, C. C. M. & van Steenhoven, A. A., 1999. Application of 2-D LIF temperature measurements in water using a Nd : YAG laser. *Experiments in Fluids,* Volume 27, pp. 420-426.

David, L., Jardin, T., Braud, P. & Farcy, A., 2012. Time-resolved scanning tomography PIV measurements around a flapping wing. *Experiments in fluids,* Volume 52, pp. 857-864.

Davidson, P. A., 2004. *Turbulence.* United Kingdom: Oxford.

Dey, S., Swargiary, D., Sarkar, S., Fang, H., & Gaudio, R., 2018. Turbulence features in a wall-wake flow downstream of a wall-mounted vertical cylinder. *European Journal of Mechanics - B/Fluids*, Volume 69, pp.46–61.

Dimotakis, P. E. & Brown, G. L., 1976. The mixing layer at high Reynolds number: large-structure dynamics and entrainment. *Journal of Fluid Mechanics,* Volume 78, pp. 535-560.

Doll, J. C. & Pruitt, B. L., 2013. *Piezoresistor Design and Applications.* New York: Springer.

Dominguez-Ontiveros, E. E. & Hassan, Y. A., 2009. Non-intrusive experimental investigation of flow behavior inside a 5×5 rod bundle with spacer grids using PIV and MIR. *Nuclear Engineering and Design,* Volume 239, pp. 888-898.

Dominguez-Ontiveros, E. E. & Hassan, Y. A., 2014. Experimental study of a simplified 3x3 rod bundle using DPTV. *Nuclear Engineering and Design,* Volume 279, pp. 50-59.

Dong, P., Hsu, T. Y., Atsavapranee, P. & Wei, T., 2001. Particle Image Accelerometry. *Experiments in Fluids,* Issue 30, pp. 626-632.

Dracos, T., 1996. *Three-Dirnensional Velocity and Vorticity Measuring and Image Analysis Techniques.* United Kingdom:Springer-Science+Business Media, B.Y..

Duderstadt, J. J. & Hamilton, L. J., 1976. *Nuclear reactor analysis.* New York: Wiley.

Elsinga, G. E., Scarano, F., Wieneke, B. & van Oudheusden, B. W., 2006. Tomographic particle image velocimetry. *Experiments in Fluids,* Volume 17, pp. 209-219.

Epps, B., 9 - 13 January 2017. *Review of Vortex Identification Methods.* Grapevine, Texas.

Farges, B., Gauffre, M., Benhamadouche, S., Badel, P., Faucher, V., & Ricciardi, G., 2021. Advanced benchmark of the flow through a mixing vane grid - Large Eddy Simulation validation. *Nuclear Engineering and Design*, Volume 381, pp.111335.

Ferrari, G., Franchini, G., Balasubramanian, P., Giovanniello, F., Le Guisquet, S., Karazis, K., & Amabili, M., 2020. Nonlinear vibrations of a nuclear fuel rod supported by spacer grids. *Nuclear Engineering and Design*, Volume 361, pp.110503.

Ferrari, S. & Rossi, L., 2008. Particle tracking velocimetry and accelerometry (PTVA) measurements applied to quasi-two-dimensional multi-scale flows. *Exp Fluids,* Volume 44, pp. 873-886.

Frisch, U., 1995. *Turbulence.* Cambridge: Cambridge University Press.

Ganapathisubramani, B., Lakshminarasimhan, K. & Clemens, N. T., 2007. Determination of complete velocity gradient tensor by using cinematographic stereoscopic PIV in a turbulent jet. *Experiments in Fluids,* Volume 42, pp. 923-939.

Gauffre, M., Benhamadouche, S. & Badel, P., 2020. Wall-Modeled Large Eddy Simulation of the Flow Through PWR Fuel Assemblies at ReH=66 000—Validation on CALIFS Experimental Setup. *Nuclear Technology,* Volume 206, pp. 255-265.

Ghaemi, S., Ragni, D. & Scarano, F., 2012. PIV-based pressure fluctuations in the turbulent boundary layer. *Experiments in Fluids,* Volume 53, pp. 1823–1840.

Green, S. J. & Hetsroni, G., 1995. PWR Steam Generators. *Int. J. Multiphase Flow,* Volume 21, pp. 1-97.

Hassan, Y. A. & Chaplin, R. A., 2010. *Nuclear Energy Materials And Reactors - Volume I.* United Kingdom: EOLSS Publications.

He, G. S., Qin, H. Y. & Zheng, Q., 2009. Rayleigh, Mie, and Tyndall scatterings of polystyrene microspheres in water: Wavelength, size, and angle dependences. *Journal of Applied Physics,* Volume 105, pp. 023110.

Herrin, J. L. & Dutton, J. C., 1993. An investigation of LDV velocity bias correction techniques for high-speed separated flows. *Experiments in Fluids,* Volume 15, pp. 354–363.

Hooper, J. D. & Rehme, K., 1984. Large-scale structural effects in developed turbulent flow through closely-spaced rod arrays. *Journal of Fluid Mechanic,* Volume 145, pp. 305-337.

Hosokawa, S., Yamamoto, T., Okajima, J. & Tomiyama, A., 2012. Measurements of turbulent flows in a 2x2 rod bundle. *Nuclear Engineering and Design,* Volume 249, pp. 2-13.

Hultmark, M., Vallikivi, M., Bailey, S. C. C. & Smits, A. J., 2012. Turbulent Pipe Flow at Extreme Reynolds Numbers. *Physical Review Letters,* Volume 108, pp. 094501.

Hu, Z., 2018. Developments of analyses on grid-to-rod fretting problems in pressurized water reactors. *Progress in Nuclear Energy,* Volume 106, pp. 293-299.

Ikeda, K. & Hoshi, M., 2006. Development of rod-embedded fiber LDV to measure velocity in fuel rod bundles. *Journal of Nuclear Science and Technology,* Volume 43, pp. 150-158.

International Atomic Energy Agency, 2010. *Review of Fuel Failures in Water Cooled Reactors, Nuclear Energy Series No. NF-T-2.1,* Vienna, Austria: IAEA.

In, W. & Chun , T., 2005. Assessment of the RANS Turbulence Models for a Turbulent Flow and Heat Transfer in a Rod Bundle. *Nuclear Technology,* 150(3), pp. 231-250.

Jakobsen, M. . L., Dewhirst, T. P. & Greated, C. A., 1997. Particle image velocimetry for predictions of acceleration fields and force within fluid flows. *Meas. Sci. Technol.,* Issue 8, pp. 1502–1516.

Jeong, J. & Hussain, F., 1995. On the identification of a vortex. *Journal of Fluid Mechanics,* Volume 285, pp. 69-94.

Johansson, G., Naughton, J., Mehdi, F. & Shiri, F., 2005. *Skin Friction Measurements using Oil Film Interferometry and Laser Doppler Anemometry*. Ontario, Canada, 4th AIAA Theoretical Fluid Mechanics Meeting

Ju, H., Wang, M., Wang, Y., Zhao, M., Tian, W., Liu, T., Su, G.H., Qiu, S., 2020. Large Eddy Simulation on turbulent mixing phenomena in 3x3 bare thight lattice rod bundle using spectral element method. *Nuclear Engineering and Technology*, Volume 52, pp.1945-1954.

Keane, R. D., Adrian, R. J. & Zhang, Y., 1995. Super-resolution particle imaging velocimetry. *Meas. Sci. Technol.,* Volume 6, pp. 754-768.

Kraus, A., Merzari, E., Norddine, T., Marin, O., & Benhamadouche, S., 2021. Large Eddy Simulation of a 5 × 5 rod bundle: Impacts of a central control rod thimble tube. *Nuclear Engineering and Design*, Volume 381, pp.111337.

Kurtulus, D. F., Scarano, F. & David, L., 2007. Unsteady aerodynamic forces estimation on a square cylinder by TR-PIV. *Experiments in Fluids,* Volume 42, pp. 185-196.

LaVision GmbH, n.d. *DaVis – Software Solution for Intelligent Imaging*. [Online] Available at: http://www.lavision.de/en/products/davis-software [Accessed 17 10 2021].

Lee, J., Lee, J. & Park, H., 2020. Modified mixing coefficient for crossflow between subchannels in a 5x5 rod bundle geometry. *Nuclear Engineering and Design,* Volume 52, pp. 2479-2490.

Lee, S. J. & Lee, J. Y., 2008. PIV measurements of the wake behind a rotationally oscillating circular cylinder. *Journal of Fluids and Structures,* Volume 24, pp. 2-17.

Lindner, G., Devaux, Y. & Miskovic, S., 2020. VortexFitting: A post-processing fluid mechanics tool for vortex identification. *SoftwareX,* Volume 12, pp. 100604.

Liu, Z., Adrian, R. J. & Hanratty, T. J., 2001. Large-scale modes of turbulent channel flow: transport and structure. *Journal of Fluid Mechanics,* Volume 448, pp. 53-80.

Lofdahl, L., Kalvesten, E. & Stemme, G., 1994. Small silicon based pressure transducers for measurements in turbulent boundary layers. *Experiments in Fluids,* Volume 17, pp. 24-31.

Martinez-Padilla, L. P., Arzate-Lopez, A. C. & Delgado-Reyez, V. A., 1997. Measurement and Prediction of the Pressure Drop Inside a Pipe: The Case of a Model Food Suspension with a Newtonian Phase. *Journal of Food Process Engineering,* Volume 20, pp. 477-497.

Masterson, R. E., 2019. *Nuclear Reactor Thermal Hydraulics - An Introduction to Nuclear Heat Transfer and Fluid Flow.* Boca Raton: CRC Press.

Matozinhos, C. F., Gabriel, G. C. Q., Nguyen, T. & Hassan, Y., 2021. Experimental investigation of turbulent flow characteristics in cross-flow planes of a 5x5 rod bundle with spacer grid. *International Journal of Heat and Fluid Flow,* Volume 87, pp. 108757.

McClusky, H. C., Holloway, M. V., Beasley, D. E. & Conner, M. E., 2002. Development of swirling flow in a rod bundle subchannel. *Journal of Fluids Engineering,* Volume 124, pp. 747-755.

McClusky, H. L., Holloway, M. V., Beasley, D. E., & Conner, M. E., 2002. Development of swirling flow in a rod bundle subchannel. *Journal of Fluids Engineering*, Volume 124, pp. 747-755.

Moin, P. & Mahesh, K., 1998. Direct Numerical Simulation : A tool in turbulence research. *Annual Review of Fluid Mechanics,* Volume 30, pp. 539-578.

Moller, S. V., 1991. On phenomena of turbulent flow through rod bundles. *Experimental Thermal and Fluid Science,* Volume 4, pp. 25-35.

Moreno, F., Bantiche, S., Bazin, F., Lohez, T., Picard, D., Testaniere, S., & Rossi, L., 2019. *Unsteady pressure and velocity measurements in 5x5 rods bundle using grids with and without mixing vanes*. Juan-les-pins, France: ICAPP 2019.

Moreno, F., Collard, B. & Faucher, V., 2016. *Measurement of fluctuating fluid pressure exerted on the walls of a tube bundle*. Hague, Netherlands: 11th International Conference on Flow-Induced Vibration.

Nicoud, F., 2007. *Unsteady flows modeling and computation.* Belgium, Von Karman Institude.

Ohmi, K. & Li, H., 2000. Particle-tracking velocimetry with new algorithms. *Meas. Sci. Technol.,* Volume 11, pp. 603–616.

Okubo, A., 1970. Horizontal dispersion of floatable particles in the vicinity of velocity singularities such as convergences. *Deep-Sea Research and Oceanographic Abstracts,* Volume Vol. 17, pp. 445-454, .

Ozalp, C., Pınarbası, A. & Sahin, B., 2010. Experimental measurement of flow past cavities of different shapes. *Experimental Thermal and Fluid Science,* Volume 34, pp. 505-515.

Palik, E. D., 1998. *Handbook of Optical Constants of Solids.* s.l.:Academic Press.

Panda, P. P., Busari, O., Lucht, R. P. & Laster, W. R., 2017. Effect of the nature of vitiated crossflow on the flow-field of a transverse reacting jet. *Experiments in Fluids,* 58(9), pp. 1-16.

Pedocchi, F., Martin, J. E. & Garcia, M. H., 2008. Inexpensive fluorescent particles for large-scale experiments using particle image velocimetry. *Exp Fluids,* Volume 45, pp. 183–186.

Pfund, D., Rector, D. & Shekarriz, A., 2000. Pressure Drop Measurements in a Microchannel. *AIChE Journal,* 46(8), pp. 1496-1507.

Qu, W., Xiong, J., Chen, S. & Cheng, X., 2019 (a). High-fidelity PIV measurement of cross flow in 5x5 rod bundle with mixing vane grids. *Nuclear Engineering and Design,* Volume 344, pp. 131-143.

Qu, W., Xiong, J., Chen, S., Qiu, Z., Deng, J., & Cheng, X., 2019 (b). PIV measurement of turbulent flow downstream of mixing vane spacer grid in 5x5 rod bundle. *Annals of Nuclear Energy*, Volume 132, pp.277-287.

Raffel, M., Willert, C., Wereley, S. & Kompenhans, J., 2007. *Particle Image Velocimetry.* s.l.:Springer.

Rehme, K., 1972. Pressure drop performance of rod bundles in hexagonal arrangements. *International Journal of Heat and Mass Transfer,* Volume 15, pp. 2499-2517.

Rehme, K., 1978. The structure of turbulent flow through a wall subchannel of a rod bundle. *Nuclear Engineering and Design,* Volume 45, pp. 311-323.

Rehme, K., 1987. The structure of turbulent flow through rod bundles. *Nuclear Engineering and Design,* Volume 99, pp. 141-154.

Rehme, K. & Trippe, G., 1980. Pressure drop and velocity distribution in rod bundles with spacer grids. *Nuclear Engineering and Design,* Volume 62, pp. 349-359.

Reynolds, O., 1883. An Experimental Investigation of the Circumstances Which Determine Whether the Motion of Water Shall Be Direct or Sinuous, and of the Law of Resistance in Parallel Channels. *Philosophical Transactions of the Royal Society of London,* Volume 174, pp. 935-982.

Rossi, L., Doorly, D. & Kustrin, D., 2013. Lamination, stretching, and mixing in cat's eyes flip sequences with varying periods. *Physics of Fluids,* Volume 25, pp. 073604.

Rossi, L., Doorly, D. & Kustrin, D., 2012. Lamination and mixing in three fundamental flow sequences driven by electromagnetic body forces. *Phys. Rev. E,* Volume 86, pp. 026313.

Rossi, L., Vassilicos, J. & Hardalupas, Y., 2006. Electromagnetically controlled multiscale flows. *Journal of Fluid Mechanics,* Volume 558, pp. 207-242.

Rowe, D. S., Johnson, B. M. & Knudsen, J. G., 1974. Implications Concerning Rod Bundle Crossflow Mixing Based on Measurements of Turbulent Flow Structure. *Int. J. Heat Mass Transfer,* Volume 17, pp. 407-419.

Saddoughi, S. G. & Veeravalli, S. V., 1994. Local isotropy in turbulent boundary layers at high Reynolds number. *Journal of Fluid Mechanics,* Volume 268, pp. 333-372.

Saffman, P., 1993. Vortex Dynamics. *Journal of Fluid Mechanics,* Volume vol. 256, pp. 720–722.

Satake, S., Aoyagi, Y., Unno, N., Yuki, K., Seki, Y., & Enoeda, M., 2015. Three-dimensional flow measurement of a water flow in asphere-packed pipe by digital holographic PTV. *Fusion Engineering and Design*, Volume 98-99, pp.1864–1867.

Schroder, A., Geisler, R., Elsinga, G., Scarano, F., & Dierksheide, U., 2008. Investigation of a turbulent spot and a tripped turbulent boundary layer flow using time-resolved tomographic PIV. *Experiments in Fluids*, Volume 44, pp.305-316.

Sergeenko, K. M., Chulyunin, B. I. & Krasnopolsky, B. I., 2019. Direct numerical simulation of turbulent flow and heat transfer in a hexagonal rod bundle. *Journal of Physics: Conference Series,* Volume 1369, pp. 012045.

Shen, H., Cheng, A., Wang, K., Teng, M., & Liu, C., 2002. *Environmental Fluid Mechanics: Theories and Applications*. Reston, Virginia: American Society of Civil Engineers.

Sridhar, G. & Katz, J., 1995. Drag and lift forces on microscopic bubbles entrained by a vortex. *Physics of Fluids,* 7(2), pp. 389-399.

Stacey, W. M., 2007. *Nuclear Reactor Physics.* United Kingdom: Wiley.

Tardu, S., 2014. *Transport and Coherent Structures in Wall Turbulence.* United Kingdom: Wiley-ISTE.

Tasic, A. Z., Djordjevic, B. D., Grozdanic, D. K. & Radojkovic, N., 1992. Use of mixing rules in predicting refractive indexes and specific refractivities for some binary liquid mixtures. *Journal of Chemical and Engineering Data,* Volume 37, pp. 310-313.

Tennekes, H. & Lumley, J., 1972. *A first course in turbulence.* Cambridge Massachusetts: The MIT Press.

Townsend, A., 1949. The Fully Developed Wake of a Circular Cylinder. *Australian Journal of Scientific Research, Series,* Volume 2, pp. 451.

Tritton, D. J., 1988. *Physical Fluid Dynamics.* United Kingdom: Oxford University Press.

Tropea, C., Yarin, A. & Foss, J. F., 2007. *Springer Handbook of Experimental Fluid Mechanics.* Berlin: Springer.

Tsuji, Y. & Ishihara, T., 2003. Similarity scaling of pressure fluctuation in turbulence. *Physical Review E.,* Volume 68, pp. 026309.

Tummers, M. & Passchier, P., 1998. *Spectral Analysis of Individual Realization LDA Data.* Netherlands: Delft University Press.

Turankok, N., Lohez, T., Bazin, F., Biscay, V., & Rossi, L., 2021. Exploration of Frequencies Peaks Observed On Local Wall Pressure Measurements by Time Resolved Velocity Fields Measurements in Complex Flows. *Experiments in Fluids*, Volume 62(38).

Turankok, N., Moreno, F., Bantiche S., Bazin, F., Biscay, V., Lohez, T., Picard, D., Testaniere, S., Rossi, L., 2020. Unsteady pressure and velocity measurements in 5x5 rods bundle using grids with and without mixing vanes. *Nuclear Engineering and Design*, Volume 364, pp. 110687.

Uzol, O., Chow, Y. C., Katz, J. & Meneveau, C., 2001. *Unobstructed PIV measurements within an axial turbo-pump using liquid and blades with matched refractive indices.* Göttingen, Germany, 4th International Symposium on Particle Image Velocimetry.

van Gent, P. L., Michaelis, D., van Oudheusden, B. W., Weiss, P., de Kat, R., Laskari, A., Jeon, Y. J., David, L., Schanz, D., Huhn, F., Gesemann, S., Novara, M., McPhaden, C., Neeteson, N. J., Rival, D. E., Schneiders, J.F.G., Schrijer, F.F.J., 2017. Comparative assessment of pressure field reconstructions from particle image velocimetry measurements and Lagrangian particle tracking. *Experiments in Fluids*, 58(33), pp. 1-23.

van Oudheusden, B. W., 2013. PIV-based pressure measurement. *Measurement Science and Technology,* Issue 24, pp. 1-32.

Waxler, R. & Weir, C., 1963. Effect of Pressure and Temperature on the Refractive Indices of Benzene, Carbon Tetrachloride and Water. *Journal of Research of the National Bureau of Standards-A. Physics and Chemistry,* 67A(2), pp. 163-171.

Weiss, J., 1991. The dynamics of enstrophy transfer in two-dimensional hydrodynamics. *Physica D: Nonlinear Phenomena,* Vol. 48(2-3), pp. 273–294.

Wendt, J. F., 2009. *Computational Fluid Dynamics - An Introduction.* Berlin: Springer.

Wilson, J. F., Cobb, E. D. & Kilpatrick, F. A., 1986. *Fluorometric Procedures for Dye Tracing,* Washington, U.S.: U.S. Geological Survey.

Wiltschko, F., Qu, W. & Xiong, J., 2021. Validation of RANS models and Large Eddy Simulation for predicting cross flow induced by mixing vanes in rod bundle. *Nuclear Engineering and Technology,* Volume 53, pp. 3625-3634.

World Nuclear Association, 2021. *World Nuclear Performance Report 2021 COP26 Edition,* World Nuclear Association.

Wright, F. S., Zadrazil, I. & Markides, C. N., 2017. A review of solid–fluid selection options for optical-based measurements in single-phase liquid, two-phase liquid–liquid and multiphase solid–liquid flows. *Experiments in Fluids,* pp. 58-108.

Xiong, J., Qu, W., Zhang, T., Chai, X., Liu, X., & Yang, Y., 2020. Experimental investigation on split-mixing-vane forced mixing in pressurerized water reactor fuel assembly. *Annals of Nuclear Energy*, Volume 143, pp.107450.

Xiong, J., Yu, N., Yu, Y., Fu, X., Cheng, X., & Yang, Y., 2014. Experimental investigation on anisotropic turbulent flow 6x6 rod bundle with LDV. *Nuclear Engineering and Design*, Volume 278, pp. 333-343.

Xue, Z., Charonko, J. & Vlachos, P., 2013. *Signal-to-noise ratio, error and uncertainty of PIV measurement.* Netherlands, 10th International symposium on particle image velocimetry.

Yang, S. K. & Chung, M. K., 1998. Turbulent flow through spacer grids in rod bundles. *Journal of Fluids Engineering,* Volume 120, pp. 786-791.

Zang, Z., Gao, F. & Cui, J., 2013. Physical modeling and swirling strength analysis of vortex shedding from near-bed piggyback pipelines. *Appl. Ocean Res.,* Volume 40, pp. 50-59.

Zhiyin, Y., 2015. Large-Eddy Simulation: Past, present and the future. *Chinese Journal of Aeronautics,* Volume 28, pp. 11-24.

Zhou, J., Adrian, R., Balachandar, S. & Kendall, T., 1999. Mechanisms for generating coherent packets of hairpin vortices in channel flow. *J Fluid Mecg,* Volume 96, pp. 387-353.

Zhu, W., Knapp, Y. & Deplano, V., 2016. Low hazard refractive index and density-matched fluid for quantitative imaging of concentrated suspensions of particles. *Experiments in Fluids,* pp. 57-68.

APPENDIX

15. APPENDIX

15.1 Sensor data sheet

kulite

SUBMINIATURE PRESSURE TRANSDUCER

XTL-140 (M) SERIES

- Easy Installation
- Smallest Threaded Device Available
- Patented Leadless Technology VIS®
- High Natural Frequency
- Suitable For Use in Most Conductive Liquids and Gases

The XTL-140 Series utilizes Kulite's Patented Leadless Technology to obtain extremely high natural frequencies in the smallest thread mount available.

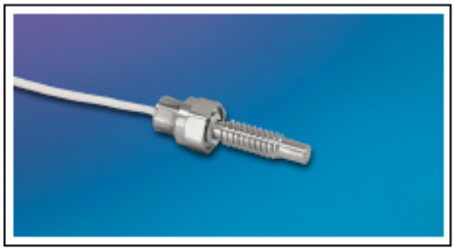

Kulite recommends the KSC Series of signal conditioners to maximize the measurement capability of the XTL-140 transducer.

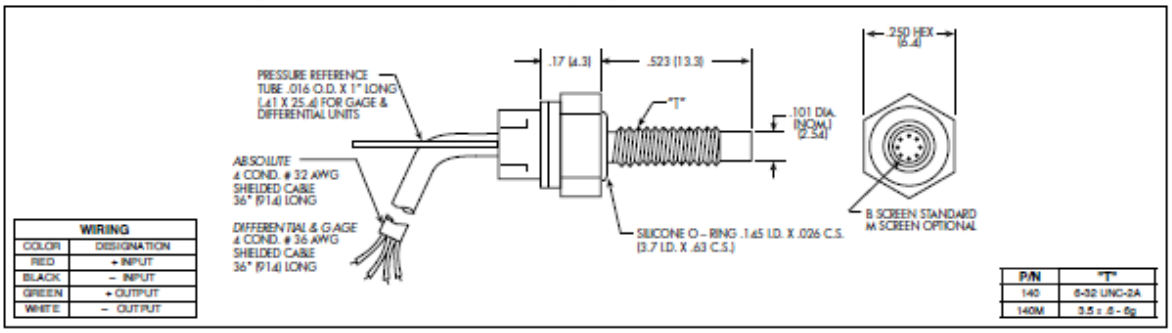

WIRING	
COLOR	DESIGNATION
RED	+ INPUT
BLACK	– INPUT
GREEN	+ OUTPUT
WHITE	– OUTPUT

P/N	"T"
140	6-32 UNC-2A
140M	3.5 x .6 - 6g

INPUT	Pressure Range	0.7 10	1.0 15	1.7 25	3.5 50	7 100	17 250	35 BAR 500 PSI
	Operational Mode	Absolute, Gage, Differential		Absolute, Gage, Sealed Gage, Differential			Absolute, Sealed Gage	
	Over Pressure	2 Times Rated Pressure						
	Burst Pressure	3 Times Rated Pressure						
	Pressure Media	Most Conductive Liquids and Gases - Please Consult Factory (All Media May Not Be Suitable With O-Ring Supplied)						
	Rated Electrical Excitation	10 VDC/AC						
	Maximum Electrical Excitation	12 VDC/AC						
	Input Impedance	1000 Ohms (Min.)						
OUTPUT	Output Impedance	1000 Ohms (Nom.)						
	Full Scale Output (FSO)	100 mV (Nom.)						
	Residual Unbalance	± 5 mV (Typ.)						
	Combined Non-Linearity, Hysteresis and Repeatability	± 0.1% FSO BFSL (Typ.), ± 0.5% FSO (Max.)						
	Resolution	Infinitesimal						
	Natural Frequency of Sensor Without Screen (KHz) (Typ.)	175	200	240	300	380	550	700
	Acceleration Sensitivity % FS/g Perpendicular	$1.0x10^{-3}$	$6.5x10^{-4}$	$5.0x10^{-4}$	$3.0x10^{-4}$	$1.5x10^{-4}$	$1.0x10^{-4}$	$6.0x10^{-5}$
	Insulation Resistance	100 Megohm Min. @ 50 VDC						
ENVIRONMENTAL	Operating Temperature Range	-65°F to +350°F (-55°C to +175°C)						
	Compensated Temperature Range	+80°F to +180°F (+25°C to +80°C) Any 100°F Range Within The Operating Range on Request						
	Thermal Zero Shift	± 1% FS/100°F (Typ.)						
	Thermal Sensitivity Shift	± 1% /100°F (Typ.)						
	Steady Acceleration	10,000 g. (Max.)						
	Linear Vibration	10-2,000 Hz Sine, 100g. (Max.)						
PHYSICAL	Electrical Connection	Absolute (4 Conductor 32 AWG Cable 36" Long) Differential and Gage (4 Conductor 36 AWG Cable 36" Long)						
	Weight	3 Grams (Nom.) Excluding Cable						
	Pressure Sensing Principle	Fully Active Four Arm Wheatstone Bridge Dielectrically Isolated Silicon on Silicon Patented Leadless Technology						
	Mounting Torque	15 Inch-Pounds (Max.) 1.7 Nm						

Note: Custom pressure ranges, accuracies and mechanical configurations available. Dimensions are in inches. Dimensions in parenthesis are in millimeters. All dimensions nominal. (N) Continuous development and refinement of our products may result in specification changes without notice.
Kulite miniature pressure transducers are intended for use in test and research and development programs and are not necessarily designed to be used in production applications. For products designed to be used in production programs, please consult the factory.

KULITE SEMICONDUCTOR PRODUCTS, INC. • One Willow Tree Road • Leonia, New Jersey 07605 • Tel: 201 461-0900 • Fax: 201 461-0990 • http://www.kulite.com

MINIATURE LEADLESS PRESSURE TRANSDUCER

XCL-072 SERIES

- Designed For Harsh Environments
- Ideal For Turbine Engine Probes and Wind Tunnel Applications
- Patented Leadless Technology VIS®
- Designed For Both Static and Dynamic Response
- Suitable For Use in Most Conductive Liquids and Gases

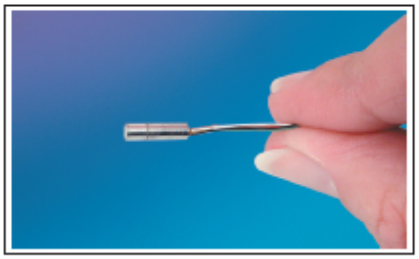

The XCL-072 design features Kulite's patented leadless technology. This allows for a very rugged package suited for probes, pressure rakes and other similar test set ups. This transducer is well suited for both dynamic and static pressure measurements in benign or harsh environments.

Kulite recommends the KSC Series of signal conditioners to maximize the measurement capability of the XCL-072 transducer.

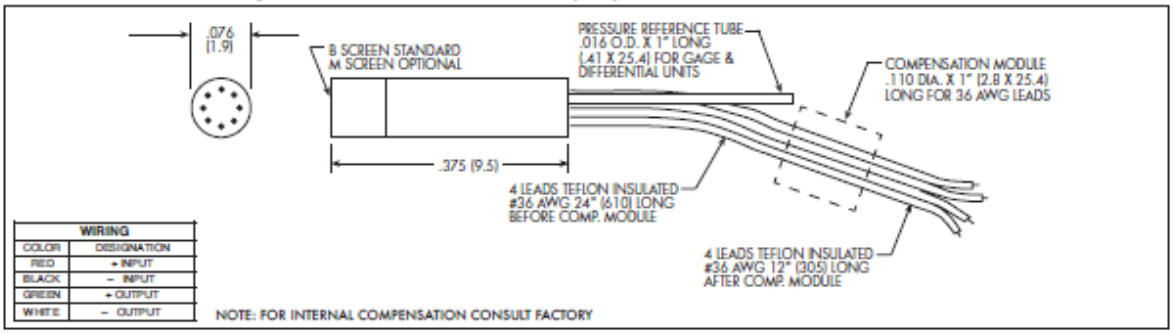

WIRING	
COLOR	DESIGNATION
RED	+ INPUT
BLACK	– INPUT
GREEN	+ OUTPUT
WHITE	– OUTPUT

NOTE: FOR INTERNAL COMPENSATION CONSULT FACTORY

INPUT	Pressure Range	1.0 15	1.7 25	3.5 50	7 100	14 200	21 300	35 500	70 BAR 1000 PSI
	Operational Mode	Absolute, Gage, Differential	Absolute, Gage, Sealed Gage, Differential			Absolute, Sealed Gage			
	Over Pressure	2 Times Rated Pressure to 500 PSI (35 BAR), 1.5 Times Rated Pressure Above 500 PSI (35 BAR)							
	Burst Pressure	3 Times Rated Pressure							
	Pressure Media	Most Conductive Liquids and Gases - Please Consult Factory							
	Rated Electrical Excitation	10 VDC/AC							
	Maximum Electrical Excitation	12 VDC/AC							
	Input Impedance	1000 Ohms (Min.)							
OUTPUT	Output Impedance	1000 Ohms (Nom.)							
	Full Scale Output (FSO)	100 mV (Nom.)							
	Residual Unbalance	± 5 mV (Typ.)							
	Combined Non-Linearity, Hysteresis and Repeatability	± 0.1% FSO BFSL (Typ.), ± 0.5% FSO (Max.)							
	Resolution	Infinitesimal							
	Natural Frequency of Sensor Without Screen (KHz) (Typ.)	175	200	240	300	380	550	575	700	1000
	Acceleration Sensitivity % FS/g Perpendicular	$1.0x10^{-3}$	$6.5x10^{-4}$	$5.0x10^{-4}$	$3.0x10^{-4}$	$1.5x10^{-4}$	$1.1x10^{-4}$	$9.0x10^{-5}$	$6.0x10^{-5}$	$4.0x10^{-5}$
	Insulation Resistance	100 Megohm Min. @ 50 VDC							
ENVIRONMENTAL	Operating Temperature Range	-65°F to +250°F (-55°C to +120°C)							
	Compensated Temperature Range	+80°F to +180°F (+25°C to +80°C) Any 100°F Range Within The Operating Range on Request							
	Thermal Zero Shift	± 1% FS/100°F (Typ.)							
	Thermal Sensitivity Shift	± 1% /100°F (Typ.)							
	Steady Acceleration	10,000g. (Max.)							
	Linear Vibration	10-2,000 Hz Sine, 100g. (Max.)							
PHYSICAL	Electrical Connection	4 Leads 36 AWG 36" Long							
	Weight	.2 Gram (Nom.) Excluding Module and Leads							
	Pressure Sensing Principle	Fully Active Four Arm Wheatstone Bridge Dielectrically Isolated Silicon on Silicon Patented Leadless Technology							

Note: Custom pressure ranges, accuracies and mechanical configurations available. Dimensions are in inches. Dimensions in parenthesis are in millimeters. All dimensions nominal. (Q) Continuous development and refinement of our products may result in specification changes without notice.
Kulite miniature pressure transducers are intended for use in test and research and development programs and are not necessarily designed to be used in production applications. For products designed to be used in production programs, please consult the factory.

KULITE SEMICONDUCTOR PRODUCTS, INC. • One Willow Tree Road • Leonia, New Jersey 07605 • Tel: 201 461-0900 • Fax: 201 461-0990 • http://www.kulite.com